SIEMENS

MAGNETOM Flash

The Magazine of MRI

Issue Number 5/2013 | RSNA Edition

Not for distribution in the US

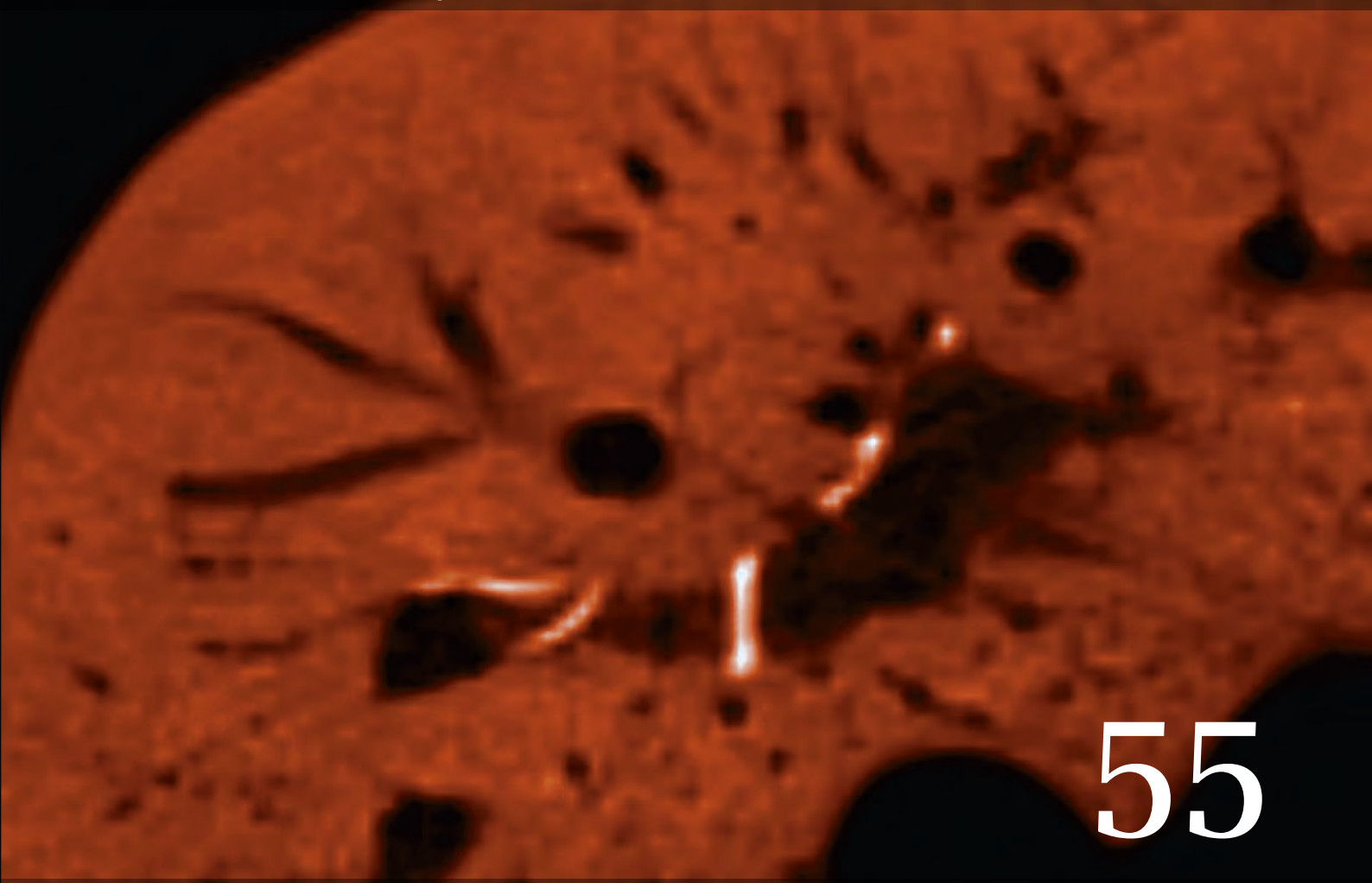

55

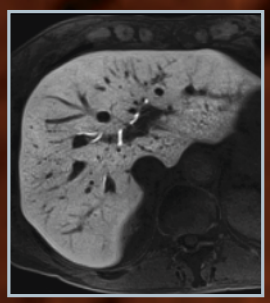

Clinical T1w MRI using Radial VIBE
Page 6

Acute MR Stroke Protocol in 6 Minutes
Page 44

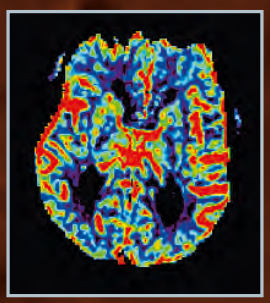

New Generation Cardiac Parametric Mapping: The Clinical Role of T1 and T2 Mapping
Page 104

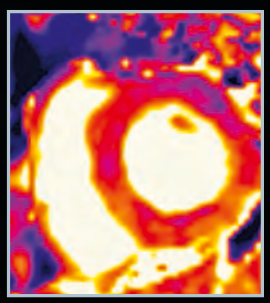

Mustafa R. Bashir, M.D., is an Assistant Professor of Radiology at Duke University Medical Center, Durham, USA. He joined the faculty at Duke in 2010, and serves as the Director of MRI and Director of Body MRI. In 2012, he was named the Medical Director of the Center for Advanced Magnetic Resonance Development, Duke Radiology's MRI research and development facility. He has been awarded several industry research grants as principal investigator and serves as site imaging principal investigator on several NIH-funded grants. Dr. Bashir serves as a working group chair for the Liver Imaging Reporting and Data System (LI-RADS) committee for the American College of Radiology and is a site radiologist for the NIH-funded Non-Alcoholic Steatohepatitis Clinical Research Network. His clinical and research interests include abdominal MRI, liver imaging, quantitative imaging, and novel contrast mechanisms.

Working Together

The theme of the 99th Annual Meeting of the Radiological Society of North America is "The Power of Partnership". Nowhere is this concept better exemplified than in the cooperation between academic medical centers and industry partners in the development and improvement of diagnostic imaging. This issue of MAGNETOM Flash contains a wealth of examples of how such collaborations have advanced the discipline of MRI.

As the world population's healthcare needs grow, so must diagnosis and disease management continue to advance. Diagnostic imaging plays an increasingly central role in detecting and characterizing disease, and guiding therapy. In particular, MRI remains a cornerstone of neurologic, orthopedic, oncologic, and cardiovascular imaging.

MRI has long had advantages in leveraging useful contrast mechanisms for visualization of anatomy and pathology. This is well-demonstrated in articles describing visualization of diffusion-weighted imaging data [Doring et al. page 12], spectroscopic imaging of prostate cancer [Scheenen et al. page 16], susceptibility-weighted imaging [Ascencio et al. page 52], and quantitative myocardial relaxivity mapping [Moon et al. page 104].

However, gone are the days when lengthy examinations producing inconsistent image quality were considered acceptable. In an atmosphere of rising cost and diminishing resources, all imaging is under pressure to demonstrate consistent examination quality, despite increasing use in challenging populations, such as the obese and those with diminished breath-holding capacity. In their article on the New York University-Langone Medical Center experience using Radial VIBE*, Tobias Block et al. show the power of a motion-robust non-Cartesian strategy to obtain free-breathing, artifact-free, volumetric T1-weighted image sets in the body [page 6]. Such paradigms can be applied to improve image quality in patients unable to hold their breath, and to enhance the MRI experience by providing healthier patients with a more comfortable examination with fewer breath-holds. In addition, colleagues at the University Hospital of Lausanne and Northwestern University demonstrate the feasibility of rapid cardiac acquisition using compressed sensing* methods [page 108 and 117]. Such techniques are shown to produce high-resolution, multiplanar acquisitions in single breath-holds, which can both shorten total examination time and provide comparable or more accurate measurements of left ventricular ejection fraction and stroke volume, compared with conventional methods.

The broad availability of commercial wide-bore systems with high channel counts makes clinical MR imaging a reality in a larger portion of the population. Particularly in the United States, where over 35% of the population is obese [http://www.cdc.gov/obesity/data/adult.html], high-quality imaging is now available to more patients than ever, with greater physical comfort. In addition to comfort, turnaround time is also considered an important measure of examination quality, and as a first-line diagnostic modality, MRI must provide rapid, definitive diagnosis in order for appropriate treatment to be rendered in a timely manner.

*WIP, the product is currently under development and is not for sale in the US and other countries. Its future availability cannot be ensured.

"In an atmosphere of rising cost and diminishing resources, all imaging is under pressure to demonstrate consistent examination quality, despite increasing use in challenging populations, such as the obese and those with diminished breath-holding capacity."

Mustafa R. Bashir, M.D.

This is exemplified in the article by Kambiz Nael et al., who describe a six-minute comprehensive acute stroke protocol, combining brain structure imaging, functional measures including diffusion- and perfusion-weighted imaging, and MR angiography [page 44]. This 'one-stop-shop' approach can facilitate rapid triage of appropriate patients to endovascular management while avoiding unnecessary, and potentially dangerous, delays in diagnosis.

Finally, Mark Griswold et al. and Masahiro Ida address another important element of a comfortable MRI experience, as they discuss simple methods for optimizing frequently-used pulse sequences to reduce acoustic noise [page 30 and 35].

In the following pages, fifteen high-quality articles from a diverse group of authors are presented. These highlight important advances that build on the excellent contrast/visualization capabilities of MRI, strengthen image quality and robustness, or that improve the patient experience and throughput. Importantly, they show the success that can be realized by bringing innovators from academia and industry together into cooperative teams.

Happy reading, and see you at RSNA!

Editorial Board

We appreciate your comments.
Please contact us at magnetomworld.med@siemens.com

Antje Hellwich
Associate Editor

Wellesley Were
MR Business Development Manager Australia and New Zealand

Ralph Strecker
MR Collaborations Manager, São Paulo, Brazil

Sven Zühlsdorff, Ph.D.
Clinical Collaboration Manager, Chicago, IL, USA

Gary R. McNeal, MS (BME)
Advanced Application Specialist, Cardiovascular MR Imaging Hoffman Estates, IL, USA

Peter Kreisler, Ph.D.
Collaborations & Applications, Erlangen, Germany

Review Board

Lisa **Chuah**, Ph.D.
Global Segment Manager Neurology
Lars **Drüppel**, Ph.D.
Global Segment Manager Cardiovascular MR
Wilhelm **Horger**
Application Development Oncology
Michelle **Kessler**
US Installed Base Manager
Berthold **Kiefer**, Ph.D.
Oncological and Interventional Applications
Sunil **Kumar** S.L., Ph.D.
Senior Manager Applications
Reto **Merges**
Head of Outbound Marketing MR Applications
Heiko **Meyer**, Ph.D.
Neuro Applications
Edgar **Müller**
Cardiovascular Applications
Nashiely Sofia **Pineda Alonso**, Ph.D.
Global Segment Manager Men's and Women's Health
Silke **Quick**
Global Segment Manager Body Imaging
Heike **Weh**
Clinical Data Manager

Content

24

Positioning and immobilization of RT patients

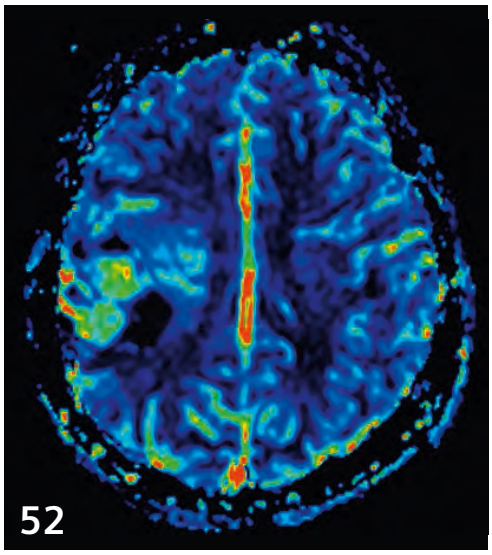

52

SWI with MAGNETOM ESSENZA

Cover

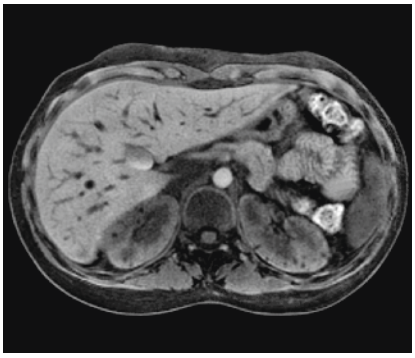

Growth with Body MRI.

New Certainty in Liver MRI.

Already today, many important staging and treatment decisions are taken on the basis of Body MRI. By using MRI for your body imaging examinations you can profit from excellent soft tissue contrast, high spatial and temporal resolution, as well as 3D and 4D data acquisition. Siemens Healthcare enables you to expand your Body MRI services.

www.siemens.com/growth-with-BodyMRI

Clinical Head-to-Toe Imaging

6 Improving the robustness of clinical T1-weighted MRI using Radial VIBE*
Tobias Block, et al.

12 New features of *syngo* MR D13 for improved whole-body DWI
Thomas Doring, et al.

Clinical Oncology

16 The metabolite ratio in spectroscopic imaging of prostate cancer
Tom Scheenen, et al.

24 Evaluation of the CIVCO Indexed Patient Position System (IPPS) MRI-overlay for positioning and immobilization of radiotherapy patients
Thomas Koch, et al.

Technology

30 Making MRI quieter: Optimizing TSE with parallel imaging
Eric Y. Pierre, et al.

35 Quiet T1-weighted 3D imaging of the central nervous system using PETRA*
Masahiro Ida, et al.

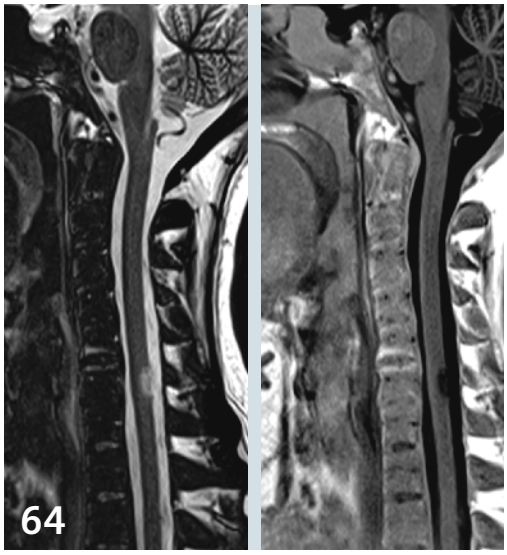

Imaging MS lesions in the cervical spinal cord

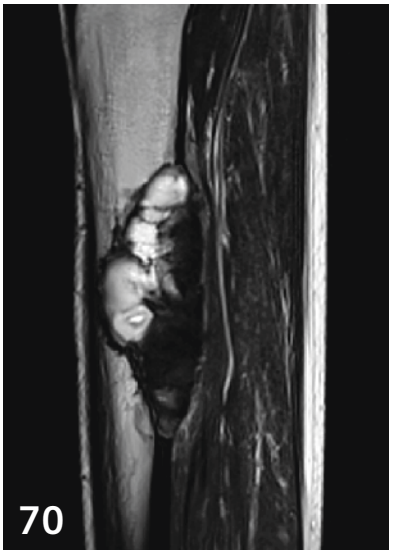

Pictorial essay: Benign and malignant bone tumors

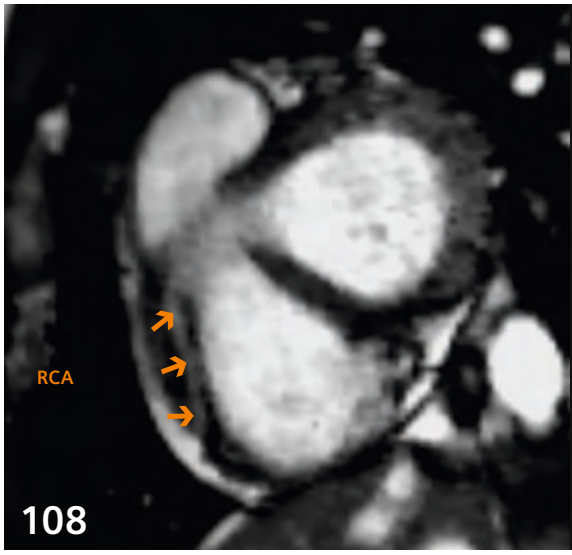

Compressed sensing*

Clinical Neurology

44 **How I do it:** Acute stroke protocol in 6 minutes
Kambiz Nael, et al.

52 SWI with 1.5T MAGNETOM ESSENZA
José L. Ascencio, et al.

58 **How I do it:** Curve fitting of the lipid-lactate range in an MR Spectrum: Some useful tips
Helmut Rumpel, et al.

64 T1w PSIR for imaging multiple sclerosis in the cervical spinal cord
Bart Schraa

Clinical Orthopedic Imaging

70 Pictorial Essay: Benign and malignant bone tumors
Katharina Gruenberg, et al.

Clincial Cardiovascular Imaging

100 Combined ^{18}F-FDG PET and MRI evaluation of a case of hypertrophic cardiomyopathy using Biograph mMR
Ihn-ho Cho, et al.

104 New generation cardiac parametric mapping: The clinical role of T1 and T2 mapping
James C. Moon, et al.

108 Preliminary experiences with compressed sensing* multi-slice cine acquisitions for the assessment of left ventricular function
J. Schwitter, et al.

117 Accelerated segmented cine TrueFISP of the heart on a 1.5T MAGNETOM Aera using *k-t*-sparse SENSE*
Maria Carr, et al.

The information presented in MAGNETOM Flash is for illustration only and is not intended to be relied upon by the reader for instruction as to the practice of medicine.
Any health care practitioner reading this information is reminded that they must use their own learning, training and expertise in dealing with their individual patients. This material does not substitute for that duty and is not intended by Siemens Medical Solutions to be used for any purpose in that regard. The treating physician bears the sole responsibility for the diagnosis and treatment of patients, including drugs and doses prescribed in connection with such use. The Operating Instructions must always be strictly followed when operating the MR System. The source for the technical data is the corresponding data sheets.

* WIP, the product is currently under development and is not for sale in the US and other countries. Its future availability cannot be ensured.

Improving the Robustness of Clinical T1-Weighted MRI Using Radial VIBE

Kai Tobias Block[1]; Hersh Chandarana[1]; Girish Fatterpekar[1]; Mari Hagiwara[1]; Sarah Milla[1]; Thomas Mulholland[1]; Mary Bruno[1]; Christian Geppert[2]; Daniel K. Sodickson[1]

[1] Department of Radiology, NYU Langone Medical Center, New York, NY, USA
[2] Siemens Medical Solutions, New York, NY, USA

Introduction

Despite the tremendous developments that MR imaging has made over the last decades, one of the major limitations of conventional MRI is its pronounced sensitivity to motion, which requires strict immobility of the patient during the data acquisition. In clinical practice, however, suppression of motion is often not possible. As a consequence, MR images frequently show motion artifacts that appear as shifted object copies, which are well-known as 'ghosting' artifacts and which, depending on the artifact strength, can potentially obscure important diagnostic information. Ghosting artifacts pose a particular problem for abdominopelvic exams that need to be performed during suspended respiration. Because many patients struggle to adequately hold breath during the scan, the number of exams with suboptimal image quality is relatively high. This has impaired the acceptance of MRI as an imaging modality of choice in many abdominopelvic indications. Other widely utilized MRI applications such as head and neck imaging are also often affected by motion-induced ghosting artifacts, e.g., if patients are anxious, or if wthey cannot suppress swallowing or coughing during the exam.

Radial *k*-space acquisition scheme

The high sensitivity to motion results from the data-sampling strategy used in conventional MR imaging to spatially resolve the object. Conventional sequences acquire the data space (*k*-space) using a sampling scheme along parallel lines (Fig. 1A), which is usually referred to as 'Cartesian' sampling. The acquired parallel lines differ by a fixed difference in the signal phase, which is why the scheme is also called 'phase encoding' principle. However, if the object moves during the exam, phase offsets are created that disturb the phase-encoding scheme. In a simplified view, it can be thought of as jittering of the sampled lines, which causes gaps in the *k*-space coverage and results in aliasing artifacts along the phase-encoding direction from improper data sampling. Hence, the Cartesian geometry is inherently prone to motion-induced phase distortions. Even if navigation or triggering techniques are used to minimize phase inconsistencies within the acquired data, a certain amount of residual ghosting artifacts is almost always present.

The situation can be improved when changing the *k*-space acquisition to a different sampling geometry. One promising alternative is the 'radial' sampling scheme, which acquires the data along rotated spokes (Fig. 1B). Due to the overlap of the spokes in the center, gaps in the *k*-space coverage cannot occur if individual spokes are 'jittered' and, therefore, appearance of ghosting artifacts is not possible with this scheme. Furthermore, the overlap has a motion-averaging effect. Data inconsistencies can instead lead to 'streak' artifacts. However, in most cases the streaks have only a mild effect on the image quality, and they can easily be identified as artifacts due to their characteristic visual appearance (e.g., Fig. 3B). Because the artifacts appear mainly as 'texture' added to the underlying object, the likelihood that lesions get obscured is significantly lower than for the more dominant Cartesian ghosting artifacts.

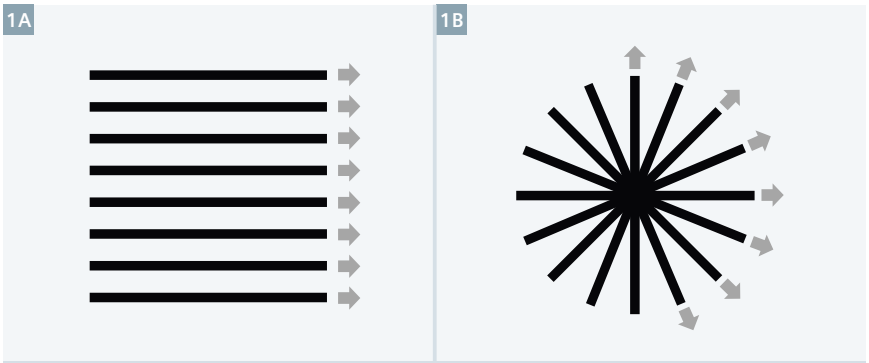

1 **(1A)** Conventional 'Cartesian' MRI sampling scheme along parallel lines, and **(1B)** radial sampling scheme along rotated spokes that overlap in the center of *k*-space.

Interestingly, although the advantages for clinical applications seem clear and although the idea of radial sampling has been known since the early days of MRI, the technique has not been widely employed in clinical practice so far. Radial sampling was first described by Lauterbur in his seminal MRI paper from 1973 [1]. However, because practical implementation required coping with a number of technical complexities, it was soon replaced by the Cartesian acquisition scheme which could be more easily and more robustly implemented on early MRI systems. These technical complexities include a more sophisticated image reconstruction, higher required homogeneity of the magnetic field, and the need for much more accurate and precise generation of time-varying gradient fields. Consequently, radial sampling has only been used sporadically in research projects while clinically established techniques are currently almost exclusively based on the Cartesian scheme.

Over the last several years, however, it has become possible to resolve the majority of issues that prevented a practical application of radial sampling, in part through improvements of the MR hardware designs and in part through new algorithmic developments. Therefore, it is now for the first time feasible to utilize radial acquisitions routinely on unmodified clinical MRI systems, with sufficient reliability and robustness for clinical applications and with image quality comparable to that of the conventional Cartesian scans.

Radial VIBE sequence

The Radial VIBE sequence* is the first available works-in-progress sequence for Siemens MR systems that integrates these developments for volumetric acquisitions and provides radial *k*-space sampling in a fully seamless way, aiming at achieving higher robustness to motion and flow effects in daily practice. It is based on the conventional product VIBE sequence, which is an optimized T1-weighted 3D gradient echo sequence (3D FLASH) with various fat-saturation options. Radial sampling has been implemented using a 3D 'stack-of-stars' approach, which acquires the k_x-k_y plane along radial spokes and the k_z dimension with conventional sampling, resulting in cylindrical *k*-space coverage (see Fig. 2). This trajectory design enables use of time-efficient fat-saturation methods, such as Quick FatSat or SPAIR, with minimal artifact strength, which is important as radial scans should be performed with fat suppression for most applications. Although Cartesian acquisition steps are employed along the k_z dimension, a high degree of motion robustness is achieved due to the use of an incoherent temporal acquisition order. The Radial VIBE sequence can be used on the full range of Siemens MR systems, including systems from the B-line generation (e.g., MAGNETOM Avanto, Trio, Verio) and D-line generation (e.g., MAGNETOM Skyra, Aera), and it can also be used on the Biograph mMR MR-PET system as well as Siemens' 7T** systems. Because the sequence does not require any modification of the MR hardware or reconstruction system, it can be deployed to installed systems and used clinically for fat-saturated T1-weighted exams as a motion-robust alternative to 3D GRE, VIBE, MPRAGE, or 2D TSE sequences.

2

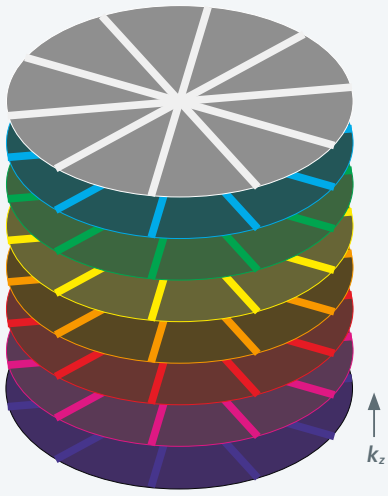

2 Stack-of-stars trajectory as implemented by Radial VIBE, which employs radial *k*-space sampling in the k_x-k_y plane and Cartesian sampling along k_z.

* Radial VIBE is a prototype for StarVIBE. StarVIBE is now 510k released and is available for 1.5T MAGNETOM Aera and 3T MAGNETOM Skyra. Radial VIBE is work in progress.

** The product is under development and not commercially available yet. Its future availability cannot be ensured. This research system is not cleared, approved or licensed in any jurisdiction for patient examinations. This research system is not labelled according to applicable medical device law and therefore may only be used for volunteer or patient examinations in the context of clinical studies according to applicable law.

Clinical applications and results

Over the last two years, the sequence has been tested extensively at NYU Langone Medical Center to evaluate the achievable image quality across various MR systems in daily routine applications. Radial VIBE scans were added to clinical protocols under IRB approval in more than 5000 patient exams and compared to established reference protocols. Several clinical studies have been performed or are ongoing that investigate the improvement in diagnostic accuracy resulting from the absence of ghosting artifacts.

Free-breathing abdominal imaging

A key application of the Radial VIBE sequence is imaging of the abdomen and/or pelvis before and after injection of a contrast medium, which is conventionally performed during suspended respiration. With Radial VIBE, it is possible to acquire the data during continued shallow breathing, which therefore can be the preferred exam strategy for patients who are unable to sustain the normally

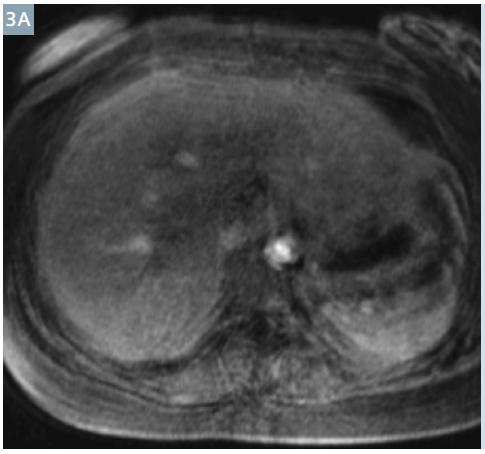

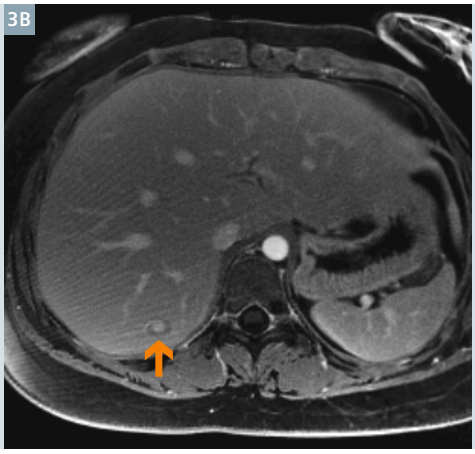

3

(3A) Conventional VIBE exam of a patient failing to hold breath during the acquisition and **(3B)** Radial VIBE acquisition during free breathing. Radial VIBE provides significantly higher image quality and reveals a lesion in the liver (arrow) not seen on the conventional scan

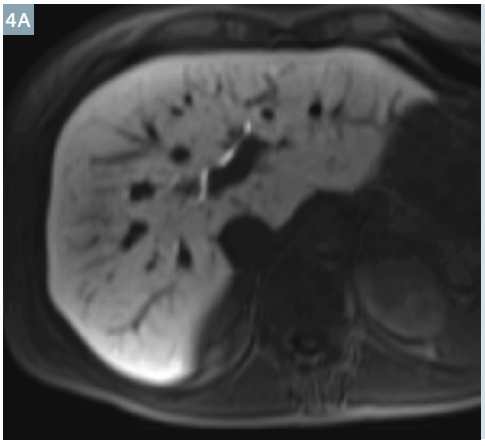

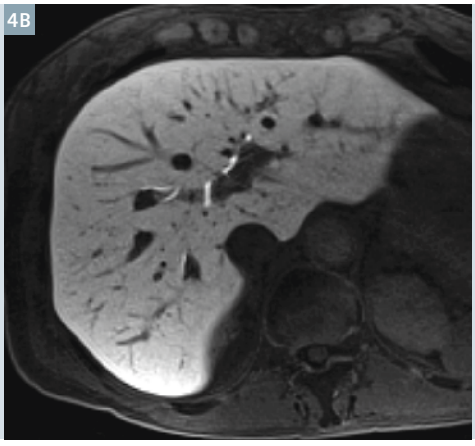

4

(4A) Conventional breath-hold VIBE exam of a patient 20 min after injection of Gadoxetate Disodium. **(4B)** Because Radial VIBE exams can be performed during continued respiration, data can be acquired over longer time, resulting in clearly improved resolution (here 1.0 mm isotropic).

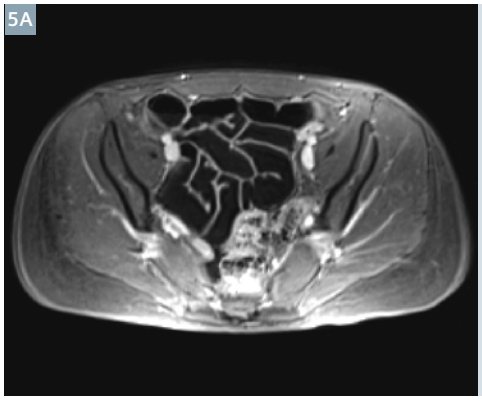

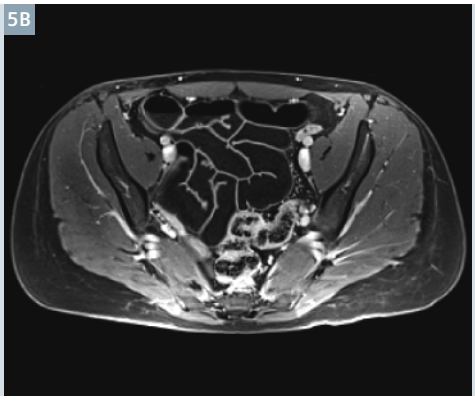

5

MR enterography using **(5A)** conventional VIBE and **(5B)** Radial VIBE acquisition. The higher motion robustness achieved with Radial VIBE leads to sharper images and improved resolution.

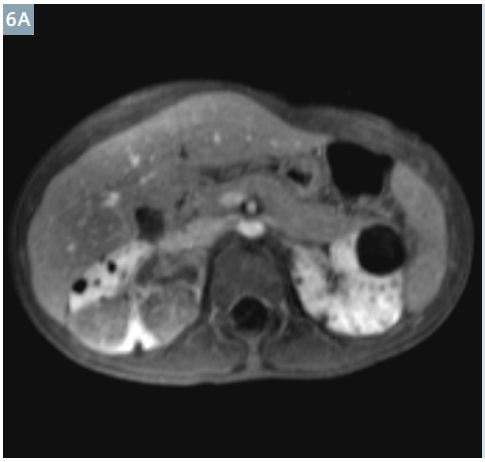

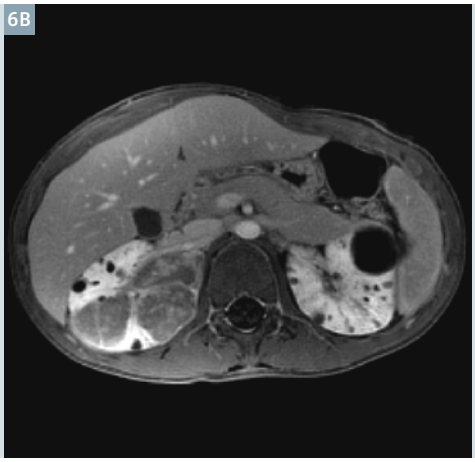

6

Abdominopelvic exam of a sedated pediatric patient with Tuberous Sclerosis. **(6A)** Because suspending respiration is not possible under deep sedation, conventional exams are affected by respiration artifacts. **(6B)** Radial VIBE provides significantly sharper images with improved spatial resolution, as visible from the small cysts in the kidneys.

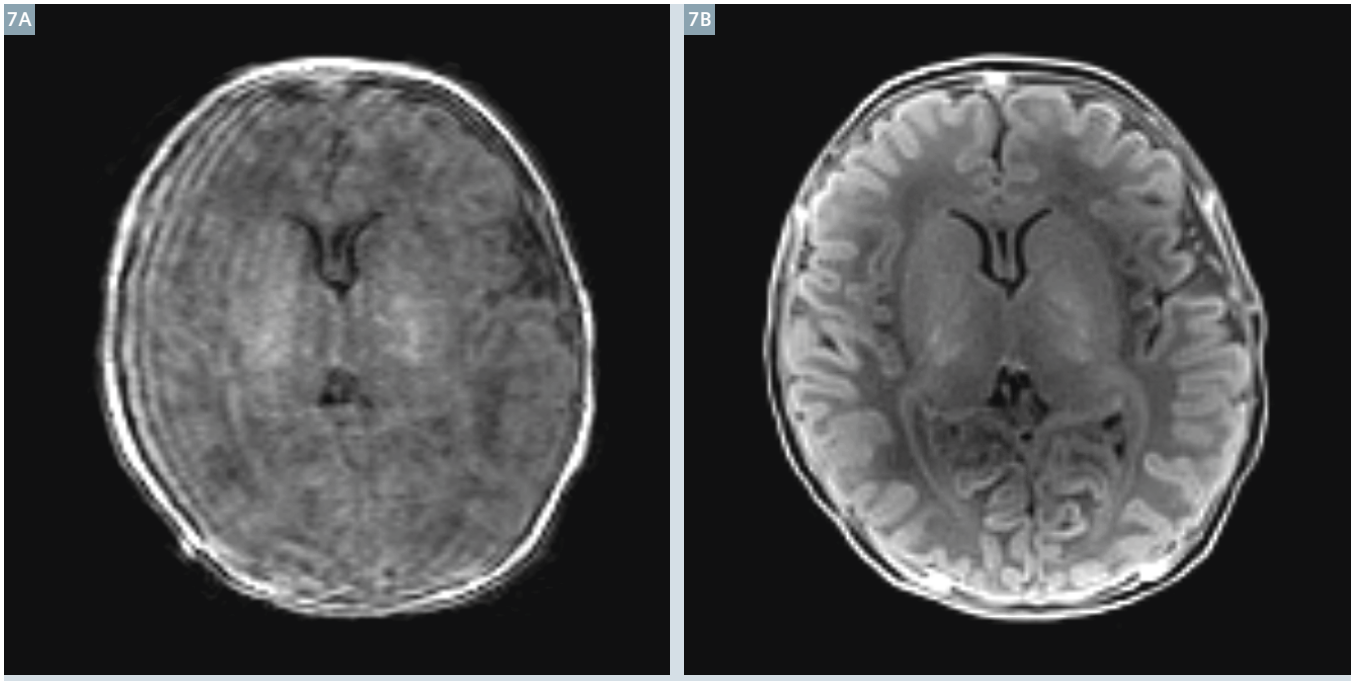

7 Brain exam of a 4-day-old* patient using **(7A)** conventional MPRAGE and **(7B)** Radial VIBE sequence. Due to vigorous patient activity, the MPRAGE scan is affected by strong ghosting artifacts, while Radial VIBE provides diagnostic image quality.

*MR scanning has not been established as safe for imaging fetuses and infants less than two years of age. The responsible physician must evaluate the benefits of the MR examination compared to those of other imaging procedures.

required breath-hold time, such as elderly or severely sick patients. A blinded-reader study by Chandarana et al. demonstrated that the average image quality obtained with free-breathing radial acquisition is comparable to conventional breath-hold exams and significantly better than free-breathing exams with Cartesian acquisition [2]. As an example, figure 3 compares a free-breathing Radial VIBE exam to a conventional Cartesian exam of a patient with insufficient breath-hold capability. The Radial VIBE image is affected by a certain amount of streak artifacts but clearly depicts a lesion in the right lobe of the liver, which is fully obscured in the Cartesian scan.

High-resolution abdominopelvic imaging

The ability to acquire data during continued respiration also has advantages for the examination of patients with proper breath-hold capacity. With conventional Cartesian sequences, the achievable spatial resolution in abdominopelvic exams is limited by the amount of *k*-space data obtainable within typical breath-hold durations of less than 20 sec. Because Radial VIBE eliminates the need for breath holding, it is possible to sample data over several minutes and, thus, to increase the spatial resolution by a significant factor. Figure 4 demonstrates this possibility for an isotropic 1 mm high-resolution scan of the liver 20 min after injection of Gadoxetate Disodium, which provides clearly sharper visualization of the biliary duct compared to the corresponding Cartesian protocol. In figure 5, the achievable resolution improvement is shown for the case of MR enterography, which is another good candidate for Radial VIBE due to the higher overall robustness to the bowel motion.

Pediatric imaging

During the clinical evaluation phase, Radial VIBE demonstrated particular value for the application in pediatric* patients. Pediatric exams are often conducted under general anesthesia or deep sedation, which makes active breath holding impossible. Therefore, conventional abdominopelvic scans are in most cases affected by respiration artifacts that impair the achievable effective resolution and diagnostic accuracy. Due to the inherent motion robustness, much sharper and crisper images are obtained with Radial VIBE, as evident from the depiction of small cysts in the kidneys of a patient with Tuberous Sclerosis shown in figure 6. A retrospective blinded-reader study of our case collection revealed that 8% of all lesions were only identified with Radial VIBE but missed in the corresponding Cartesian reference exams [3].

In young neonatal patients, sedation is usually avoided due to the higher risk of potential adverse effects. Imaging these patients is challenging because they often move spontaneously in the scanner. Also in this patient cohort Radial VIBE provides improved image quality and reliability, which is demonstrated in figure 7 for a brain exam of a 4-day-old patient, in this case compared to a Cartesian MPRAGE protocol.

*MR scanning has not been established as safe for imaging fetuses and infants less than two years of age. The responsible physician must evaluate the benefits of the MR examination compared to those of other imaging procedures.

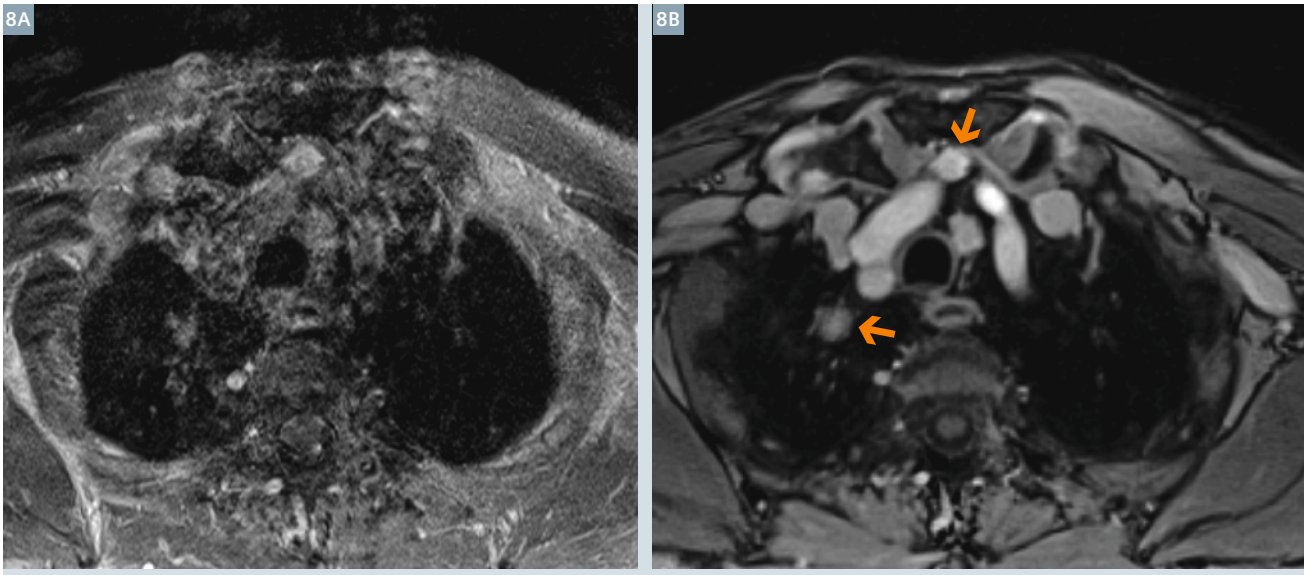

8 Examination of the neck and upper chest using **(8A)** a conventional 2D TSE sequence and **(8B)** Radial VIBE. Because of the respiration and strong blood flow, the TSE scan shows drastic artifacts. Two suspicious lesions are more clearly visible on the Radial VIBE exam (arrows).

Imaging of the neck and upper chest

Although imaging of the head and neck region appears less critical at first glance, severe motion-related artifacts occur quite often in routine exams. Conventional neck protocols usually include slice-selective T1-weighted TSE sequences, which are especially sensitive to motion and flow. If patients are unable to suppress swallowing or coughing during the acquisition, images are rendered non-diagnostic. Furthermore, adequate examination of the upper chest region is often not possible because of drastic artifacts from respiration and strong blood flow in the proximity of the heart. Radial VIBE exams are a promising alternative for this application and are largely unaffected by swallowing, minor head movements, or flow, which is illustrated in figure 8. The sequence also maintains a convincing sensitivity to chest lesions in the presence of respiratory motion [4]. Because Radial VIBE scans are immune to ghosting artifacts, exams can be performed with high isotropic spatial resolution, which allows for retrospective reconstruction in multiple planes (MPRs). In this way, it is possible to substitute multiple conventional slice-selective protocols in varying orientation with a single Radial VIBE high-resolution scan. A representative example is shown in figure 9.

Imaging of the orbits, inner auditory canal, and full brain

Finally, the sequence also offers improved sharpness and clarity for the examination of the orbits. When patients move the eyes or change the position of the eyelids during the exam, conventional protocols show a band of strong ghosting artifacts along the phase-encoding direction, which can make identifying pathologies a difficult task. Radial VIBE provides cleaner depiction of the optic nerves and improved suppression of intra- and extraconal fat [5]. Flow effects from surrounding larger blood vessels can lead to mild streak patterns but are less prominent than for most Cartesian protocols and can be additionally attenuated with the use of parallel saturation bands. The possibility to create high-resolution MPRs is another advantage of using Radial VIBE for this application, which is demonstrated in figure 10 for a patient with optic nerve sheath meningioma. In a similar way, the sequence can be applied for examinations of the inner auditory canal (IAC) or the full brain, in which a particularly high sharpness of vessel structures is achieved.

Conclusion

The large number of successful patient exams of various body parts conducted with Radial VIBE over the last two years demonstrates that radial sampling is now robust and reliable for routine use on standard clinical MR systems. Due to the higher resistance to patient motion and the absence of ghosting artifacts, improved image quality can be obtained in applications where motion-induced image artifacts are a common problem. In particular, the Radial VIBE sequence enables exams of the abdomen and upper chest during continued shallow respiration, which can be a significant advantage for patients that struggle to adequately hold breath. Furthermore, the sequence enables reconfiguring exam protocols towards higher spatial resolution and allows consolidating redundant acquisitions into MPR-capable isotropic scans. Because the sequence works robustly on existing MRI hardware, Radial VIBE has the potential to find broad application as motion-robust T1-weighted sequence alternative and will complement the spectrum of clinically established imaging protocols.

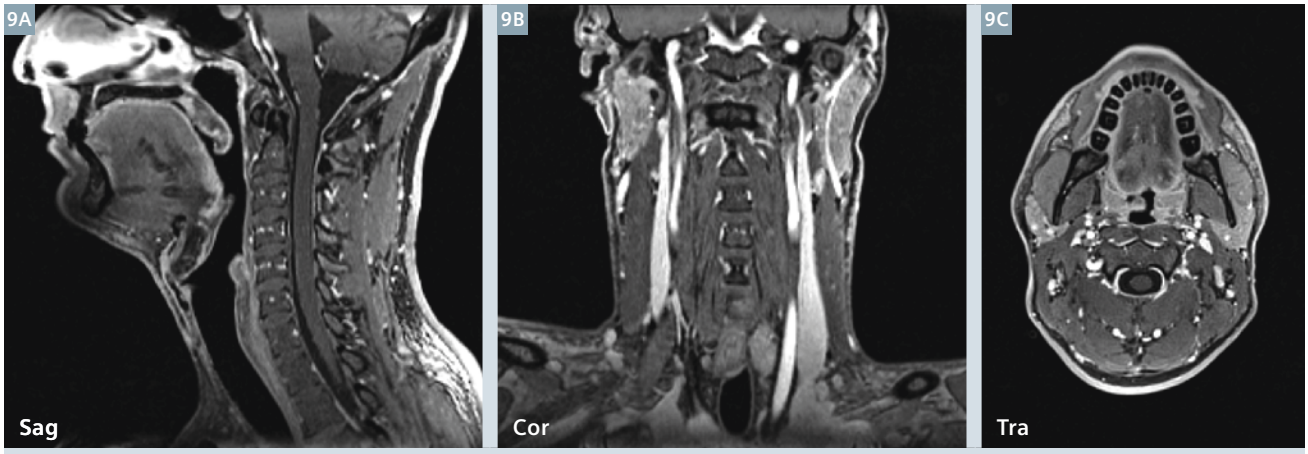

9 Neck exam using transversal Radial VIBE acquisition with 1 mm isotropic resolution. Due to the robustness to swallowing and minor head motion, high quality 3D scans are possible that can be reconstructed in multiple planes (MPR). This enables consolidating redundant 2D protocols with varying scan orientation.

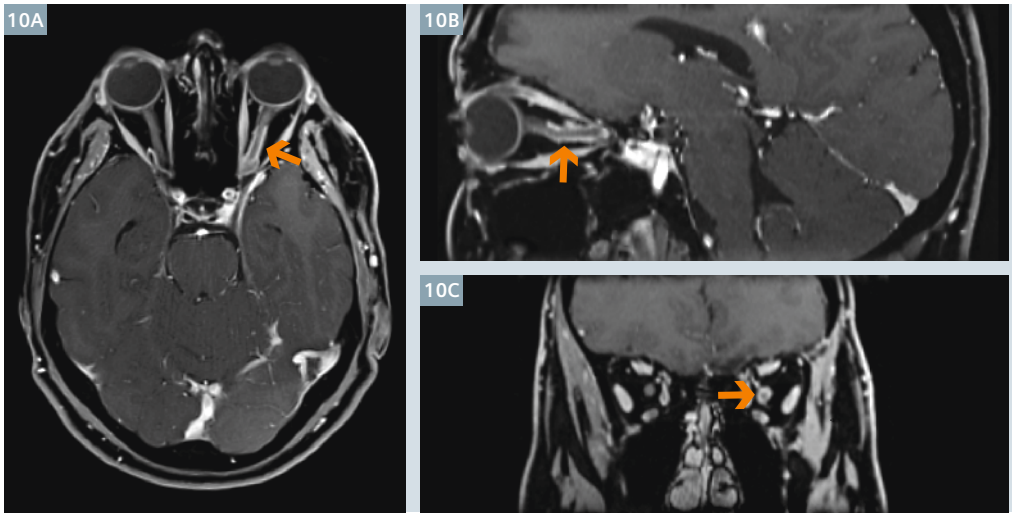

10 Multiplanar reconstructions of a transversal Radial VIBE exam with 0.8 mm resolution. The sequence achieves good fat suppression and provides sharp depiction of the optic nerves without artifacts from eye motion. An abnormal contrast enhancement of the left optic nerve is clearly visible (arrows), which is indicative of an optic nerve sheath meningioma.

References

1 Lauterbur PD. *Image formation by induced local interactions: Examples employing nuclear magnetic resonance.* Nature 242:190–191, 1973.

2 Chandarana H, Block KT, Rosenkrantz AB, Lim RP, Kim D, Mossa DJ, Babb JS, Kiefer B, Lee VS. *Free-breathing radial 3D fat-suppressed T1-weighted gradient echo sequence: a viable alternative for contrast-enhanced liver imaging in patients unable to suspend respiration.* Invest Radiology 46(10):648-53, 2011.

3 Chandarana H, Block KT, Winfeld JM, Lala SV, Mazori D, Giuffrida E, Babb JS, Milla S. *Free-breathing contrast-enhanced T1-weighted gradient-echo imaging with radial k-space sampling for paediatric abdominopelvic MRI.* European Radiology, September 2013.

4 Chandarana H, Heacock L, Rakheja R, Demello LR, Bonavita J, Block KT, Geppert C, Babb JS, Friedman KP. *Pulmonary Nodules in Patients with Primary Malignancy: Comparison of Hybrid PET/MR and PET/CT Imaging.* Radiology 268(3):874-81, 2013.

5 Bangiyev L, Raz E, Block KT, Hagiwara M, Yu E, Fatterpekar GM. *Contrast-enhanced radial 3D fat-suppressed T1-weighted gradient echo (Radial-VIBE) sequence: A viable and potentially superior alternative to conventional T1-MPRAGE with water excitation and fat-suppressed contrast-enhanced T1W sequence for evaluation of the orbit.* ASNR Annual Meeting 2013: O-413.

Contact

Tobias Block, Ph.D.
Assistant Professor of Radiology
New York University
School of Medicine
Center for Biomedical Imaging
New York, NY 10016
USA
tobias.block@nyumc.org

New Features of *syngo* MR D13 for Improved Whole-Body Diffusion-Weighted MRI

Thomas Doring[1]; Ralph Strecker[2]; Michael da Silva[1]; Wilhelm Horger[3]; Roberto Domingues[1]; Leonardo Kayat Bittencourt[1]; Romeu Domingues[1]

[1] CDPI and Multi-imagem (DASA), Rio de Janeiro, Brazil
[2] Siemens Ltda, São Paulo, Brazil
[3] Siemens Healthcare, Erlangen, Germany

Backround

Whole-body diffusion-weighted imaging (WB-DWI) is gaining in clinical importance for oncological imaging. It has been shown to be a promising tool principally for tumor detection, tumor characterization, and therapy monitoring of bone metastases [1, 2]. The clinical implementation of WB-DWI aims for standardization of the acquisition protocol. For this reason, further improvements of data acquisition, analysis and display of the results are requested.

The recently launched new software version *syngo* MR D13 provides several new features for WB-DWI such as variable averaging of the b-values, inline composing, and a Bias Field Correction (BiFiC) filter in order to overcome previously existing limitations such as long acquisition times, mis-registration between, and intensity inhomogeneities across image stations.

New features in *syngo* MR D13 b-value specific averaging

One limitation of the broader clinical usability is the long acquisition time of over 25 minutes for head-to-pelvis WB-DWI MRI. For more efficient scanning the new feature b-value specific averaging was developed: This allows us to set the number of averages (NEX) for each b-value individually. The current product protocol uses a b-value of 50 with NEX 2, and a

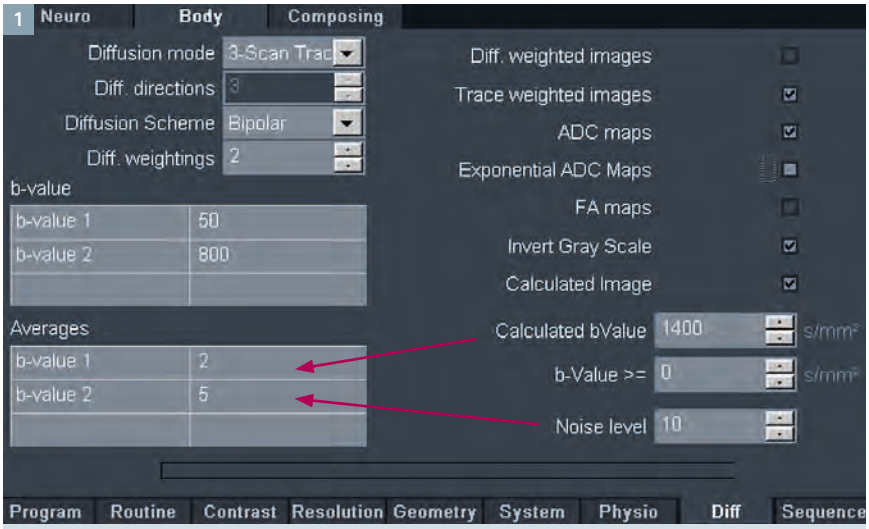

1 In the Diffusion taskcard it is now possible to select the number of averages for each b-value individually (Here: b50 NEX 2, b800 NEX 5, red arrows).

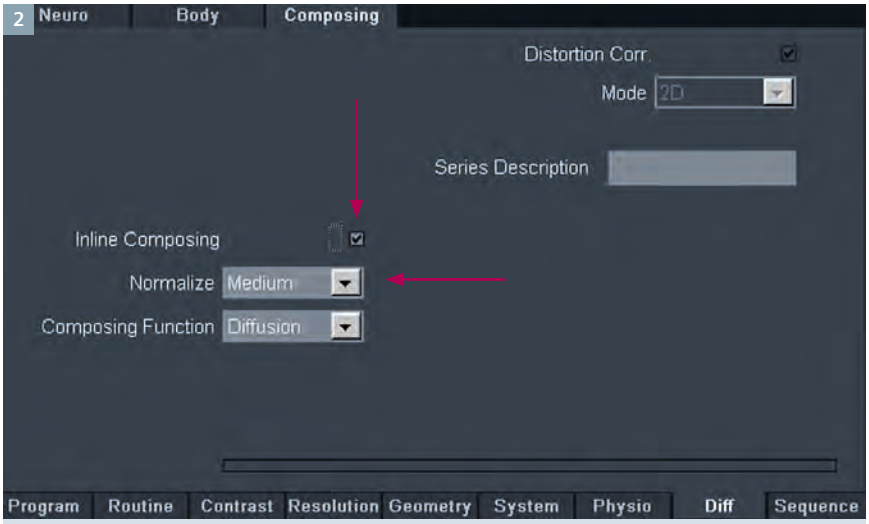

2 By checking the Inline Composing box in the diffusion taskcard of the sequence the automatic composing modus is activated. The strength of the BiFiC filter can be set to weak, medium or strong (red arrows).

b-value of 800 with NEX 5, resulting in a reduction of scan time of 30%, when compared to the previously used NEX 5 for all b-values (Fig. 1). A similar image quality can be achieved for lower b-value images with lower NEX with almost no impact on the signal-to-noise ratio (SNR) for the calculated ADC.

New composing mode diffusion

An inline composing filter can be activated within the diffusion sequence of *syngo* MR D13 on the diffusion taskcard of the sequence (Fig. 2). The composing itself is a fully automatic process and creates for each b-value a continuous stack of composed images as an individual new series. Similarly a new series for the optional calculated b-value images is generated. Depending on the local shim situation the frequency differences between neighbored stations can lead to discontinuities of anatomical structures like the 'broken-spine' artifact. During the composing step a correction is applied showing a much smoother transition of local anatomy (Fig. 2).

In older software versions (*syngo* MR D11) composing had to be done manually within the *syngo*.3D taskcard by dragging and dropping all trace-weighted series at once with no possibility to correct for any discontinuities in the anatomy. The new inline composing feature significantly improves the acquisition workflow of the technologist as it allows to load the single composed series to *syngo*.3D for the generation of the 3D reformatted maximum intensity projection (MIP) images.

Bias Field Correction (BiFiC) filter

The BiFiC filter as a homomorphic filter aims to normalize inhomogeneities in image intensities from multi-station measurements such as whole-spine imaging. After completing the inline composing step the filter is automatically applied to the composed 3D continuous image stack and saved as the new composed series. The strength of the filter (weak, medium, strong) can be set within the diffusion task card (Fig. 2, arrow).

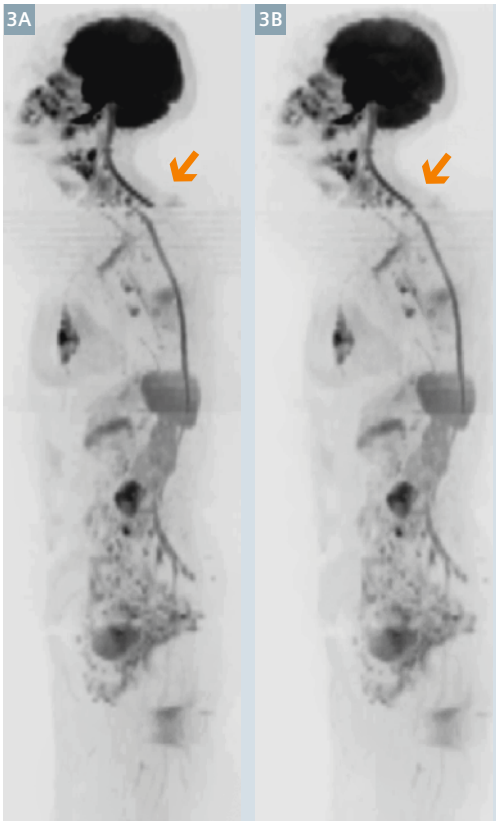

3 64-year-old female patient, after surgery, with endometrial stromal sarcoma, that has evolved with bony metastases. Acquisition parameters: 1.5T MAGNETOM Aera, echoplanar imaging diffusion sequence with fat suppression (STIR), TR 14100 ms, TE 79 ms, TI 180 ms, 4 stations, 50 slices with 5 mm slice thickness, no gap, voxel size $1.7 \times 1.7 \times 5$ mm^3, b50 with 2 and b800 with 5 averages. **(3A)** b800 manually composed images within the *syngo*.3D tool shows the artifact in the neck shoulder transition where the stations are joined (arrows). **(3B)** The new inline composing feature demonstrates significantly better composing of the neck and shoulder transition.

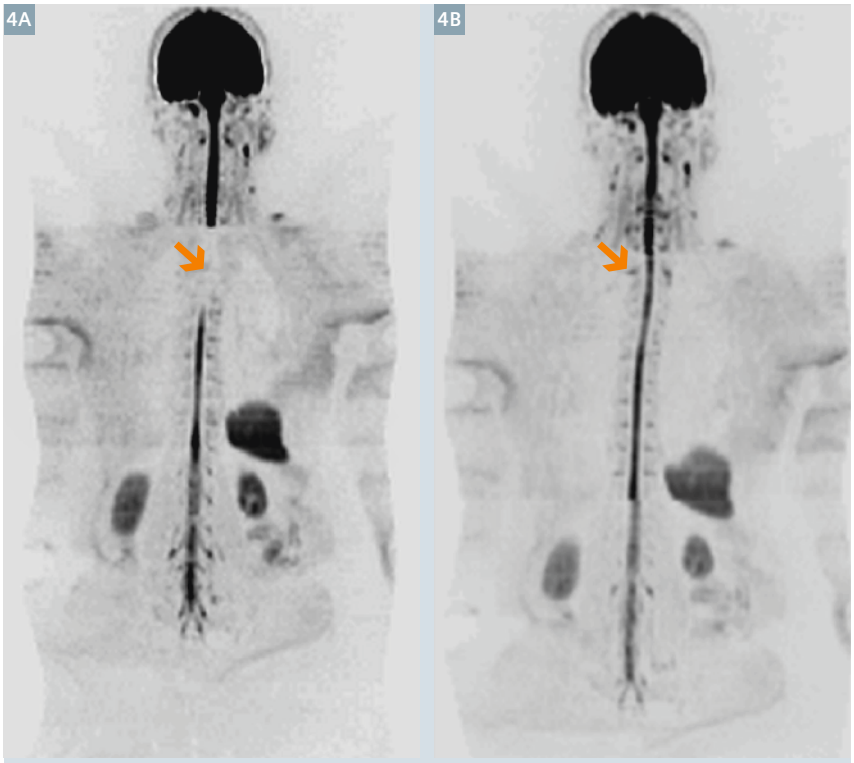

4 Same patient as in figure 3 with curved reconstructed MPRs in the coronal plane. **(4A)** Clearly visible the discontinuity in the spinal cord due to composing errors. **(4B)** Significantly better registration of the stations.

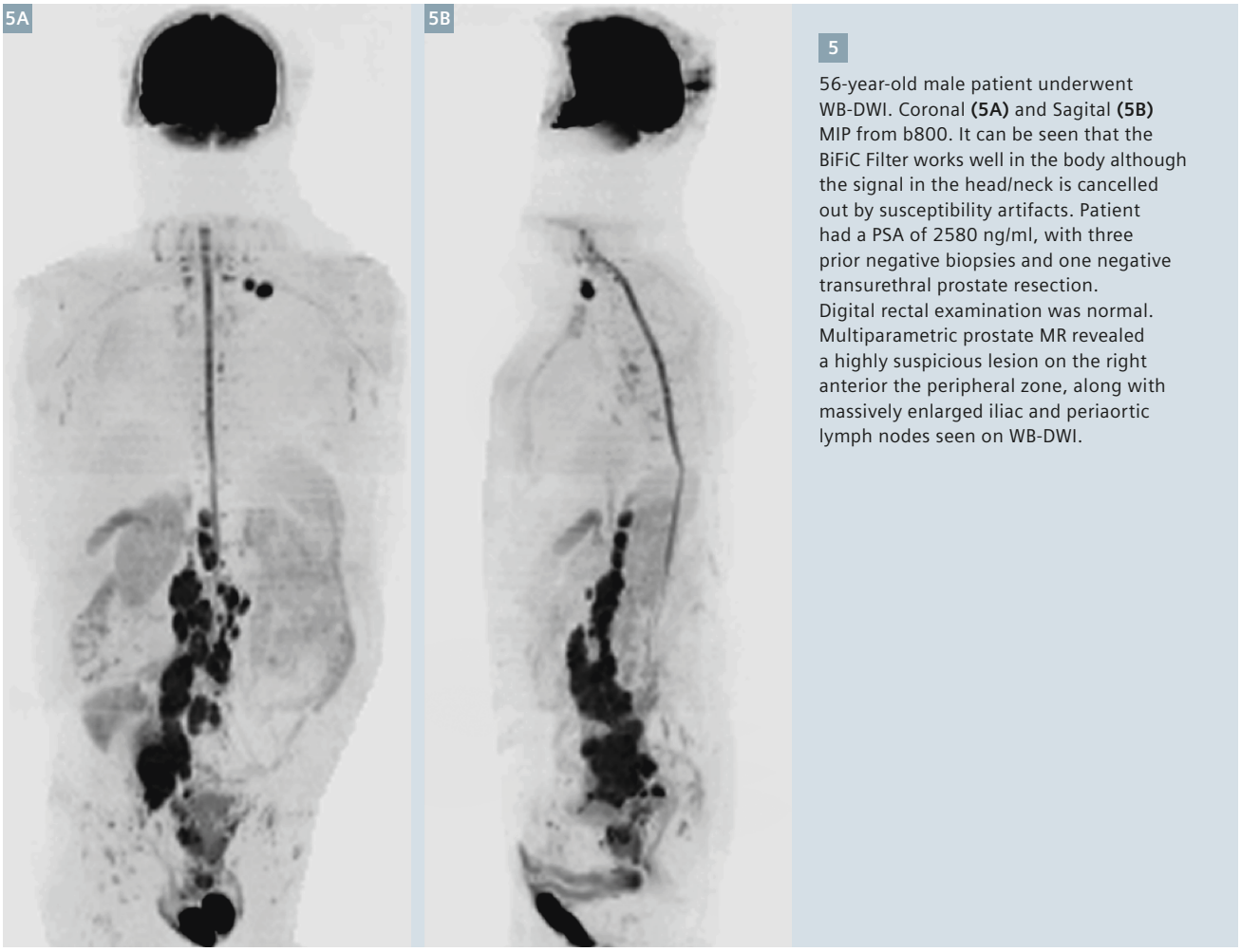

5

56-year-old male patient underwent WB-DWI. Coronal **(5A)** and Sagital **(5B)** MIP from b800. It can be seen that the BiFiC Filter works well in the body although the signal in the head/neck is cancelled out by susceptibility artifacts. Patient had a PSA of 2580 ng/ml, with three prior negative biopsies and one negative transurethral prostate resection. Digital rectal examination was normal. Multiparametric prostate MR revealed a highly suspicious lesion on the right anterior the peripheral zone, along with massively enlarged iliac and periaortic lymph nodes seen on WB-DWI.

Conclusion

The new features within the product sequence of *syngo* MR D13 improve the image quality of whole-body DWI when compared to older software versions. The new inline composing filter, in particular, shows good results in the neck-shoulder transition compared to the previously manual technique in *syngo* MR D11 that was not able to recover discontinuities in the spine. Improvements in the clinical workflow are also addressed.

References

1 Padhani AR, Koh DM, Collins DJ. Whole-Body Diffusion-weighted MR Imaging in Cancer: Current Status and Research Directions. Radiology. 2011 Dec; 261(3): 700-718.

2 Initial Experience with Whole-Body Diffusion-Weighted Imaging in Oncological and Non-Oncological Patients. Marcos Vieira Godinho, Romulo Varella de Oliveira, Clarissa Canella, Flavia Costa, Thomas Doring, Ralph Strecker, Romeu Cortes Domingues, Leonardo Kayat Bittencourt. MAGNETOM Flash 2/2013: 94-102.

Contact

Thomas Doring, Ph.D.
Clínica de Diagnóstico por Imagem
Rio de Janeiro
Brazil
thomas.doring@gmail.com

Growth with Body MRI.

New Certainty in Liver MRI.

Are you striving to always
catch the correct timepoint
of lesion enhancement
throughout the arterial phase?

With **TWIST-VIBE** you can!

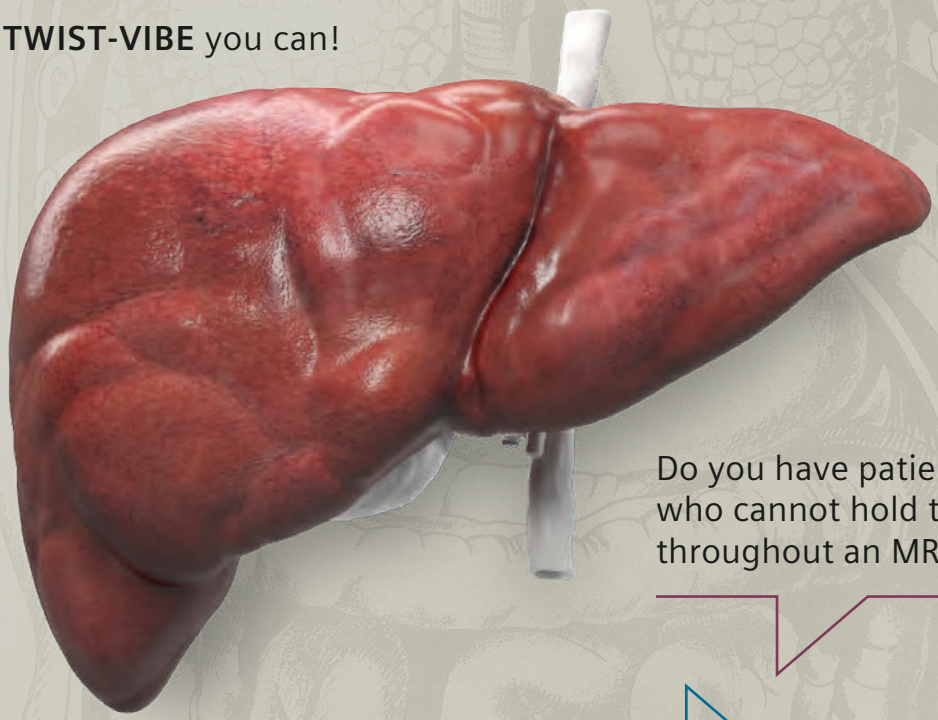

Do you have patients
who cannot hold their breath
throughout an MRI scan?

With **StarVIBE** they don't
need to!

Are you facing challenges in Body MRI? With us you will be able to solve them!
Find out how we do that and see what other users say:

www.siemens.com/growth-with-bodyMRI

The Metabolite Ratio in Spectroscopic Imaging of Prostate Cancer

Alan J. Wright; Thiele Kobus; Arend Heerschap; Tom W. J. Scheenen

Radboud University Nijmegen Medical Centre, Radiology Department, Nijmegen, The Netherlands

Introduction

Prostate cancer is the second leading cause of cancer related death in Western countries [1]. The prevalence of the disease is very high, but many men diagnosed with the disease will die from unrelated causes. This is because prostate cancer very often is a disease of old age that grows slowly. Common treatment for prostate cancer in clinical practice involves radical resection of the entire gland or radiotherapy with a dose distributed over the whole organ. Provided that the cancer has not metastasized, these therapies are curative, though concern over their side effects has led to patients and their doctors delaying this treatment and, instead, entering into active surveillance or watchful waiting programs. In order for patients to safely forgo curative treatment, it is essential to characterize their disease: to determine that it is sufficiently benign that growth will be slow and metastasis improbable. Selecting these patients, with low risk disease, that are appropriate for active surveillance requires accurate diagnosis of not just the presence of tumor, but how aggressive it is: i.e. how fast it is growing and how likely it is to metastasise to the lymphatic system. Magnetic resonance imaging (MRI) is an emerging technique for making this patient selection. It can diagnose the presence of tumor, localize it in the organ and provide information as to how aggressive it is. The MRI exams employed for this purpose usually involve multiple imaging sequences including a T2-weighted sequence, diffusion-weighted imaging (DWI) and one or more further techniques such as dynamic contrast enhanced MRI (DCE-MRI) or Proton Magnetic Resonance Spectroscopic Imaging (^{1}H MRSI) [2].

Radiologists can read the different imaging modalities to decide the location, size and potential malignancy of the tumor which are all indicators of its metastatic potential. Acquiring and reporting imaging data in this way is known as multiparametric (mp) MRI. MRSI is the only mpMRI methodology that acquires data from molecules other than water [19]. A three dimensional (3D) ^{1}H MRSI data set consists of a grid of spatial locations throughout the prostate (see Fig. 1) called voxels. For each voxel a spectrum is available. Each spectrum consists of a number of peaks on a frequency axis, corresponding to resonances from protons with a certain chemical shift in different molecules. The size of a peak at a certain frequency (chemical shift) corresponds to the amount of the metabolite present in the voxel. In this way MRSI measures the bio-chemicals in regions of tissue *in vivo* without the need for any external contrast agent or invasive procedures. Examples of spectra from two voxels, acquired at a magnetic field strength of 3 Tesla (3T), are given in figure 1B, C, which clearly shows the differing profiles that are characteristic of benign prostate tissue and its tumors.

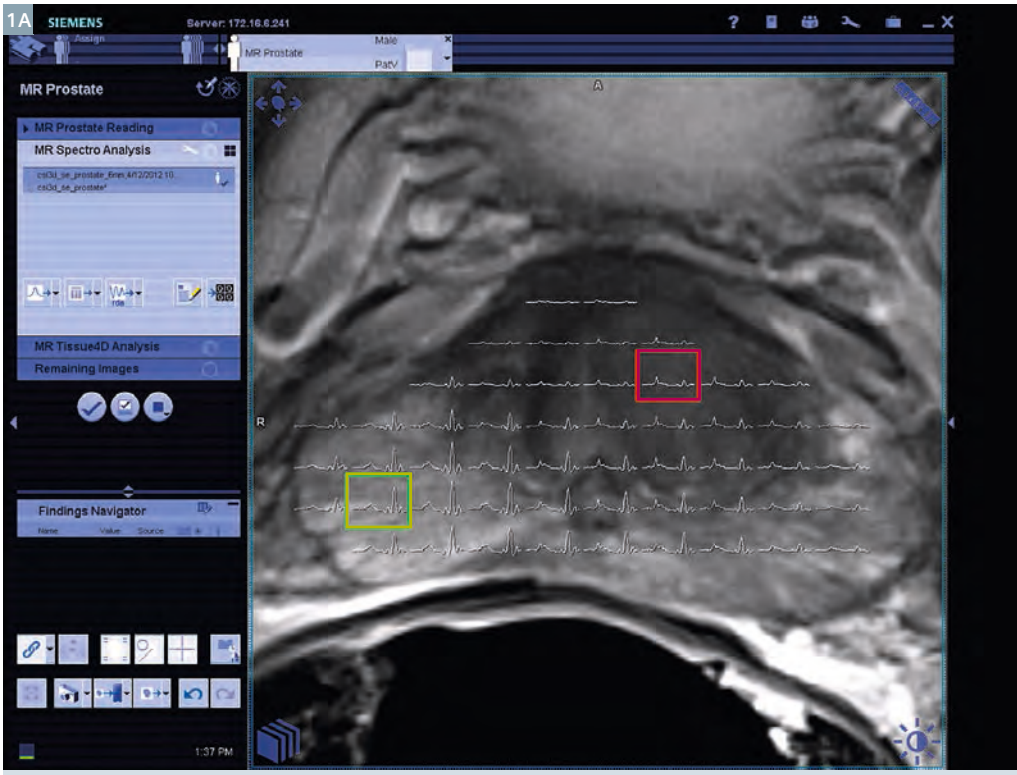

1 **(1A)** T2-weighted MR image of a transverse section through a prostate with an overlaid grid of MRSI spectra from voxels within the prostate.

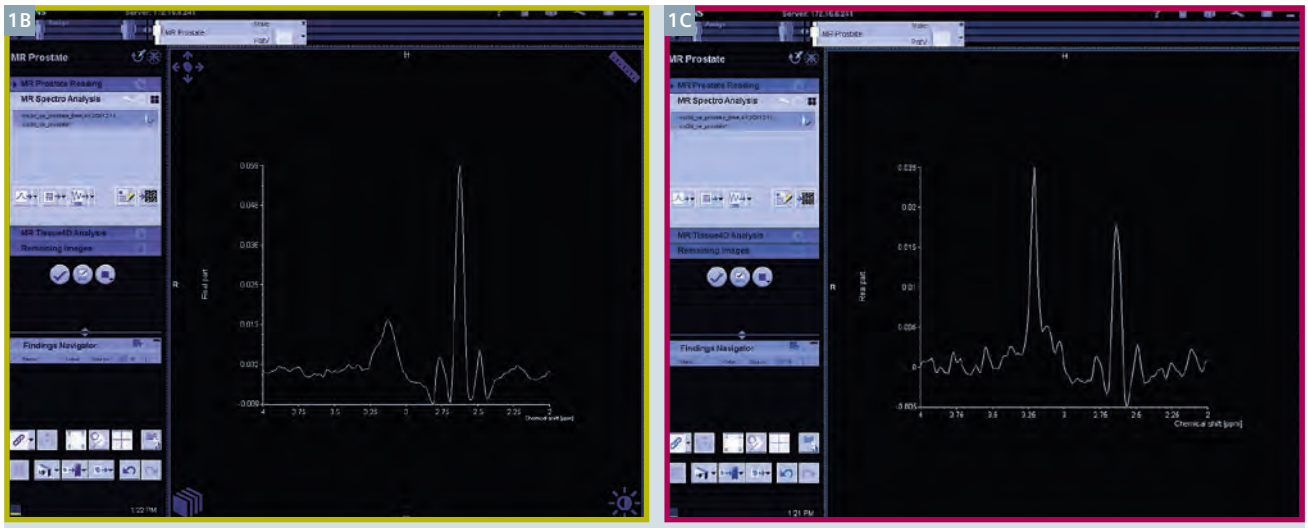

1 **(1B)** One example spectrum shown on a ppm scale from a region of benign prostate tissue. **(1C)** A spectrum from another voxel that, in this case, co-localises to a region of tumor.

Important metabolites in prostate MRSI

The initial papers on *in vivo* prostate MRSI were performed at a magnetic field strength of 1.5T [3-5], and three assignments were provided for the observed resonances: choline, creatine and citrate (Fig. 2). The small number of these assignments reflected the simplicity of the spectrum, which contained two groups of resonances: one in the region of 3.3 to 3 ppm, which will be referred to as the choline-creatine region, and another at 2.55–2.75 ppm, which shall be called the citrate group. These assignments related to what were believed to be the strongest metabolite resonances. People should be aware however, that the assignments are representative of multiple similar molecules. The choline assignment reflects the methyl resonances from multiple compounds containing a choline group (Fig. 4): choline, phosphocholine and glycerophosphocholine. Similarly, creatine refers to both creatine and phosphocreatine. In between the choline and creatine signals another group of resonances are present: the polyamines (mainly spermine and spermidine). The citrate resonances are from citrate only but can have a complicated shape, although *in vivo* at 1.5T they give the appearance of a single peak. Nowadays a magnetic field strength of 3T is used more and more for prostate spectroscopic imaging, which gives opportunities to better resolve the choline, polyamines, creatine resonances, but also changes the shape of the citrate signal.

Larger choline signals are associated with tumor in nearly all cancers [6]. High choline signals are interpreted as being evidence of rapid proliferative growth and, more directly, the increased membrane turnover required for cell division. Membranes contain phospholipids: phosphatidyl choline and phosphatidyl ethanolamine, which are synthesised by a metabolic pathway involving choline-containing metabolites known as the Kennedy pathway. It is in the synthesis and catabolism of these products, upregulated in proliferative tumor growth, that causes the increase in these signals.

The large amplitude of citrate resonances observed in prostate tissue is due to an altered metabolism particular to this gland. Prostate tissue accumulates high concentrations of zinc ions which inhibit mitochondrial aconitase, leading to a build up of citrate in the prostate's epithelial cells [7]. This citrate is further secreted into the ductal spaces of the prostate as

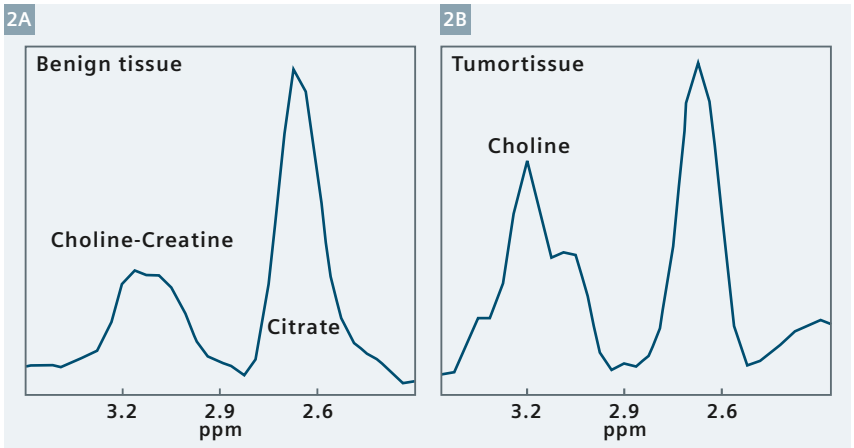

2 Examples of ^{1}H MRSI spectra acquired from benign prostate tissue and tumor at 1.5T.

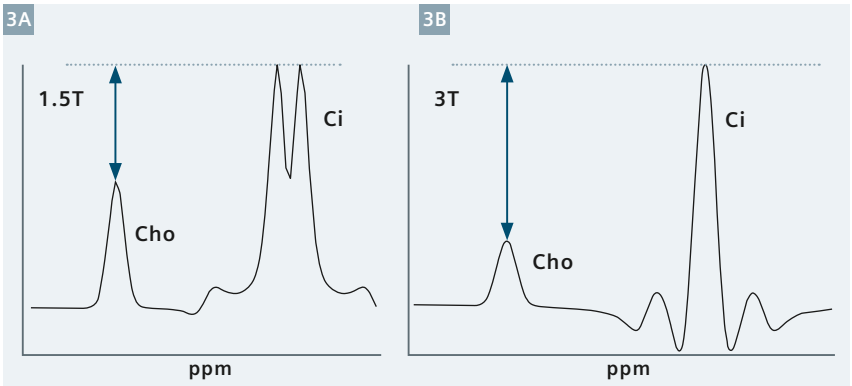

3 Simulated spectral shape of Cho and Ci for typical echo times (120 ms at 1.5T, 145 ms at 3T). Identical concentrations, i.e. scale factors, are applied, but different line broadening of the signals (4 Hz at 1.5T; 8 Hz at 3T). Note the difference in the spectral shape of Ci and the different peak amplitude ratios for Cho/Ci.

4

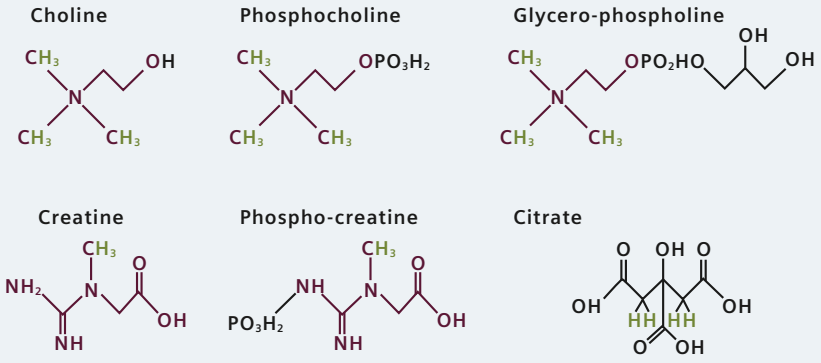

4 Structural formulas of the key small molecule metabolites observed in the spectra of prostate tissue. For each group, cholines and creatines, the common moiety is highlighted in red. The protons that give the MR spectral resonances present in the choline-creatine region are indicated in green. Choline-containing metabolites have 9 co-resonant protons in the region 3.2–3.25 ppm. Creatines have three co-resonant protons at 3.05 ppm. Citrate has four protons that resonate at two chemical shifts (2.6 and 2.7 ppm), one for each proton in a pair bonded to the same carbon. This pair also has a coupling between them and the symmetry of the whole molecule ensures that two protons co-resonate at each frequency.

part of prostatic fluid, which has a high concentration of this metabolite. Prostate carcinomas do not accumulate zinc ions, so they do not have this high citrate concentration. The increased presence of tumor cells within a ^{1}H MRSI voxel can, therefore, have two diminishing effects on the observed citrate signals: epithelial cells that accumulate citrate can transform into, or be replaced by, tumor which has low citrate, or the lesion can grow through the ductal spaces, thus displacing the prostatic fluid. The relative contribution of each of these two physiological changes, whether we are observing tumor formation and malignant progression or a histological change in tumor invasion of ductal structure, is not yet known. It is, however, clear that there is an inverse correlation of the levels of citrate metabolite and tumor cell density with some evidence to support a similar correlation with the aggressiveness of the tumor as well [8].

The introduction of a metabolite ratio

To transform the described changes in choline and citrate signals between benign (high citrate) and tumorous tissue (low citrate, high choline) into a marker for prostate cancer, the metabolite ratio was introduced [3-5]. The signal intensities of the different spectral peaks were quantified by simple integration of the two groups of resonances (the choline-creatine region and the citrate group), and the results were expressed as a ratio of the two. This gave the choline plus creatine over citrate ratio (abbreviated to CC/C [4]) or its inverse (with citrate as the numerator, [3, 5]). With choline in the numerator and citrate in the denominator, it became a positive biomarker for the presence of cancer.

Acquiring the MRSI data sets

As the prostate is embedded in lipid tissue, and lipids can cause very strong unwanted resonance artefacts in prostate spectra, the pulse sequence to acquire proton spectra is equipped with five properties to keep lipid signals out and retain optimal signals-of-interest in the whole prostate [9].

1. Localization of the signal with slice-selective pulses. The point resolved spectroscopy sequence (PRESS) is a combination of one slice selective excitation pulse and two slice selective refocusing pulses leading to an echo at the desired echo time. The three slices are orthogonal, producing an echo of the volume-of-interest (crossing of three slices) only.
2. Weighted acquisition and filtering. Proton MRSI data sets are acquired using a phase encoding technique where the gradients across spatial dimensions are varied with each repeat of the pulse sequence. By using weighted averaging of these phase encoding steps (smaller gradient steps are averaged more often than larger gradient steps) and adjusted filtering of the noise in these weighted steps, the resulting shape of a voxel after the mathematical translation of the signal into an image (Fourier Transform)

is a sphere. Contrary to conventional acquisition without filtering, the spherical voxels after filtering are not contaminated with signals from non-neighboring voxels.

3. Frequency-selective water and lipid suppression. The pulse sequence has two additional refocusing pulses that only touch upon water and lipid signals. Together with strong crushing gradients, signals from water and lipids are suppressed.
4. Outer volume suppression. Around the prostate, slice-selective pulses can be positioned to suppress all signals in the selected slabs. These slices can be positioned quite close to the prostate, even inside the PRESS-selected volume-of-interest.
5. Long echo time. To accommodate all localization and frequency selective pulses, the echo time of ^{1}H MRSI of the prostate is around 120 ms at 1.5T and 145 ms at 3T. At longer echo times, lipid signals decay due to their short T2 relaxation time.

The prostate is small enough (< 75 cubic centimetres) to allow a 3D ^{1}H MRSI data set to be acquired, with complete organ coverage, within 10 minutes of acquisition time. The nominal voxel size is usually around 6 × 6 × 6 mm, which after filtering as described above results in a true voxel size of 0.63 cm^{3}.

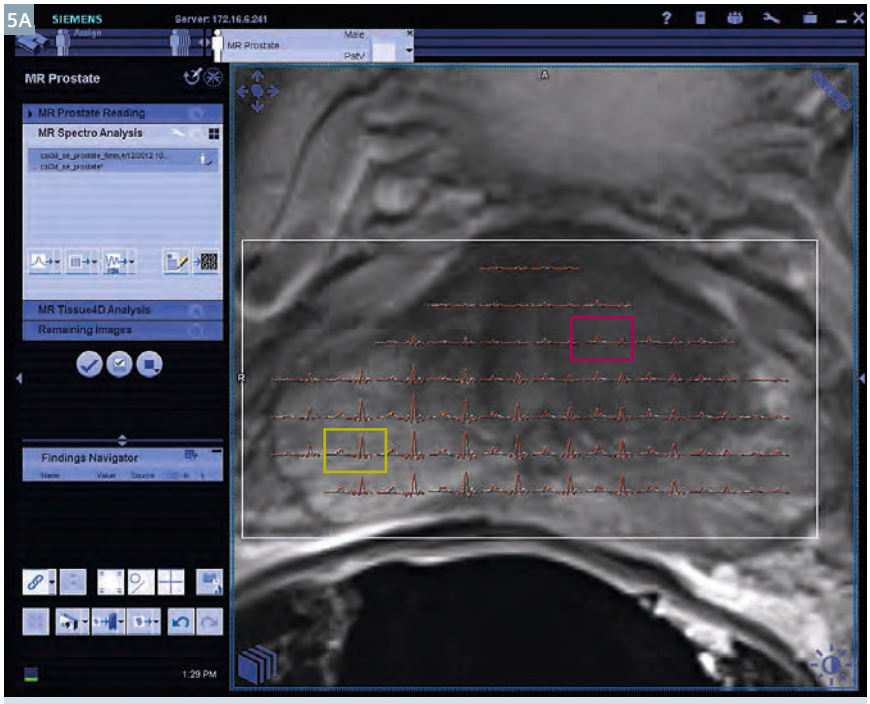

5 T2-weighted MRI image of a transverse section through a prostate as shown in figure 1 with an overlaid grid of MRSI-voxel data displayed as fitted spectra **(5A)**.

Spectral patterns

Due to multiple different protons in the molecule, a single metabolite can have multiple resonances. If interactions exist between protons within a metabolite, the shape of a spectral peak can be complicated. A resonance group of protons that has a mixture of positive and negative parts is said to have a dispersion component in its shape; a symmetrical-positive peak is referred to as an absorption shape. Choline and creatine resonances appear as simple peaks (singlets),

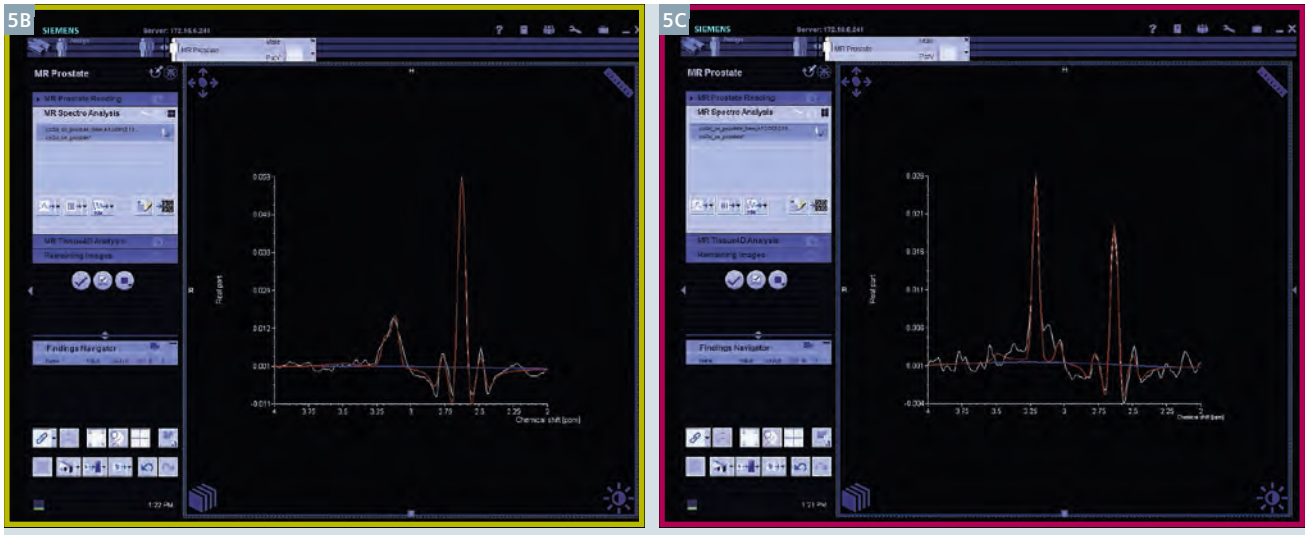

5 Two spectra (shown previously in figure 1) with their fitted model metabolite signals **(5B, C)**.

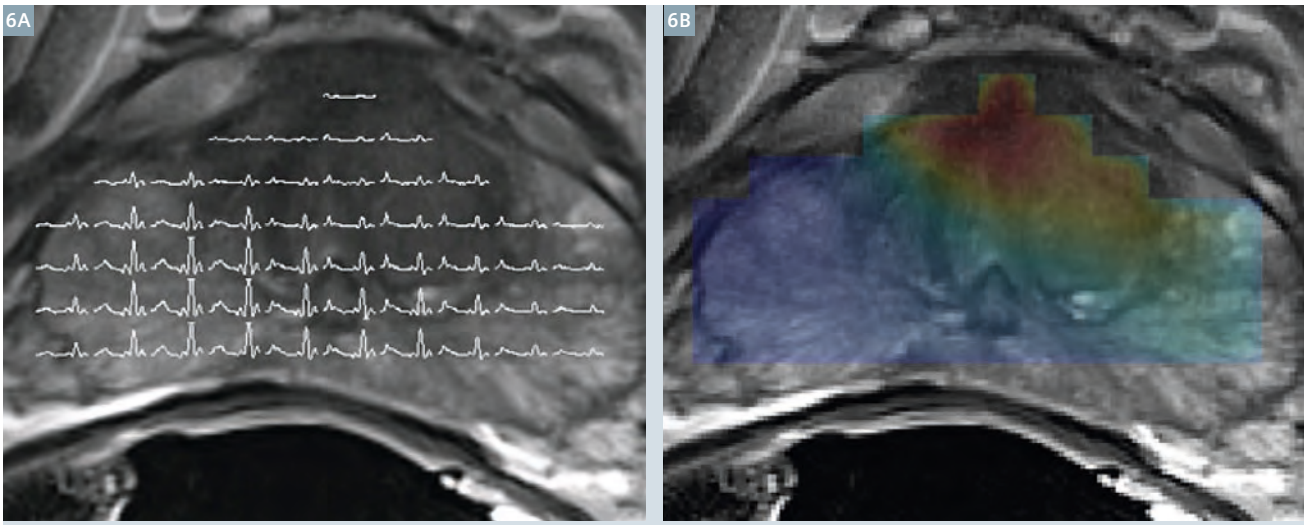

6 T2-weighted MR image of a transverse section through a prostate as shown in figure 1 with an overlaid grid of MRSI-voxel data displayed as spectra **(6A)** and as the pseudo integral CC/C ratio **(6B)** from metabolite fitting of the spectra. The ratio data points are interpolated and shown on a color scale of values from 0 (blue) to 3 (red). The tumor containing region of the prostate corresponds to the higher ratio values: the cyan-red area in the image.

although they very often cannot be separated from each other as they overlap within *in vivo* spectral linewidths. The structure of citrate, given in figure 4, results in protons at two different chemical shifts, with coupling between each proton and one other (a strongly coupled spin system). The spectral shape of these protons depends on their exact chemical shift, the coupling constant between them, the pulse sequence timing and the main magnetic field strength. At an echo time of 120 ms at 1.5T (and a very short delay between excitation and first 180 degree refocusing pulse), the spectral peaks of citrate are close to a positive absorption mode. The spectral shape consists mainly of an inner doublet with small side lobes on the outer wings. Together with line broadening the citrate protons quite closely resemble a single, somewhat broadened peak. The small side lobes around this peak are hardly detectable over the spectral noise *in vivo*. At 3T with an echo time of 145 ms (examples given in Fig. 1), the negative dispersion components of the citrate shape cannot be ignored. Its side lobes are substantially larger and reveal also some negative components [10]. Therefore the area under the curve, the integral, is substantially smaller at 3T than at 1.5T. Because of its complicated shape, it is essential at 3T to incorporate this shape in quantification of the signal.

Signal quantification by integration or metabolite fitting

The size of the peaks of the individual resonances represent the amount of the metabolite present in the voxel. Integration provides a simple method to quantify the spectra, as long as all signals have an absorption shape. Although it cannot discriminate between overlapping resonances, as long as overlapping signals (choline and creatine) are summed in a ratio this does not matter. With clear separation between citrate resonances and the choline-creatine region, the CC/C ratio can be calculated. However, as pointed out earlier, the spectral shape of citrate is not straightforward, and ignoring the small satellites at 1.5T, or simply integrating the large dispersion parts of the signal at 3T, would inevitably lead to underestimation of the total citrate signal intensity. An alternative is to fit the spectra with models of the citrate resonances with their expected shape. The shape can either be measured, using a solution of citrate placed in the MRI system and a spectrum acquired with the same sequence as the *in vivo* data, or it can be calculated using a quantum mechanical simulation (Fig. 3). By this process of spectral fitting, models of each metabolite's spectral peaks are fit to the total spectrum and the intensities of each fitted model are calculated. A linear combination of the metabolite models is found by the fitting routine such that

$$\text{Data} = C_1{}^{*}\text{choline model} + C_2{}^{*}\text{creatine model} + C_3{}^{*}\text{citrate model} + \text{baseline} \qquad \text{Eqn1.}$$

The coefficients $C_{1\text{-}4}$ give the relative concentrations of the individual metabolites.

When fitting with *syngo*.via, the result of a fit to a spectral peak can be expressed in two ways: as an integral value, which describes the area under the fitted spectral peak, or as a relative concentration (incorporating the number of protons in the corresponding peak) of the metabolite, called the scale factor (SF) of the metabolite.

As noted earlier, the integral value of citrate is different for 1.5 vs. 3 Tesla due to the different spectral patterns and would also change if pulse sequence timing other than standard

Table 1: Typical integral values of the CC/C ratio in prostate tissue at 1.5T [17] and pseudo integral values of CC/C at 3T [18]:

Tissue	1.5 Tesla*	3 Tesla**
Non-cancer peripheral zone	0.28 (0.21– 0.37)	0.22 (0.12)
Non-cancer central gland* **	0.36 (0.28–0.44)	0.34 (0.14)
Cancer	0.68 (0.43–1.35)	1.3 (3.7)

*median and 25th and 75th percentile **mean and standard deviation ***combined transition zone and central zone

would be used. If the scale factor is multiplied with the number of resonating protons (#H), it represents the intensity of a signal, in relation to the integral value of a pure singlet of one resonating proton in absorption mode. We call this entity pseudo integral, which is calculated as A.

pseudo integral (Metabolite) = #H * SF (Metabolite).

For citrate this pseudo integral is perhaps best described as the numerical integral of the magnitude (all negative intensity turned positive) of the citrate spectral shape, ignoring signal cancellations of absorption and dispersion parts of the shape.

The spectral fits are shown for the two spectra in figure 5 with model spectra of the three metabolites choline, creatine and citrate. It can be seen from these spectra that the relative amplitudes of the metabolites vary between the benign and the tumor spectrum. As expected, the benign spectrum has a higher citrate amplitude while the tumor has a greater choline amplitude, relative to the other metabolites. Combined in the CC/C ratio, the positive biomarker for the presence of tumor in the prostate is calculated.

Depending on the used quantification (spectral integration without fitting (a), fitted relative concentrations (b) or pseudo integrals (c)) the CC/C can be calculated by:

(a) {Integral(Choline) + Integral (Creatine)} / Integral(Citrate)

(b) {SF(Choline) + SF(Creatine) } / SF(Citrate)

(c) {9*SF(Choline) + 3*SF(Creatine)} / 4*SF(Citrate), respectively.

The numbers in the last equation correspond to the number of protons of the different signals. Generally, use of the pseudo integral ratio is strongly preferred, as it is least sensitive to large variations in individual metabolite fits in overlapping signals (choline and creatine). Note (again) that this pseudo integral ratio does not aim to provide a ratio of absolute metabolite concentrations, as this is very difficult with overlapping metabolite signals, partially saturated metabolite signals due to short TR (T1 effects), and variation in signal attenuation due to the use of a long echo time (T2 effects).

Now, what could be the effect on the ratio if further metabolites are included in the fitting? Could even polyamines be incorporated in the analysis [11]? After separate fitting, the main focus of the analysis could just be on choline and citrate, which have opposite changes in intensity with cancer, to make a simpler and potentially more sensitive choline/citrate ratio. Various metabolite ratios have been proposed [12, 13], and there is certainly value in using choline over creatine as a secondary marker of tumor malignancy that can give complementary information to the CC/C ratio [14-16]. However, any of these interpretations are limited by how well the individual metabolite resonances can be resolved. At 3T the choline, polyamines and creatine resonances all overlap (Figs. 1 and 5). In practice this lack of resolution in the spectrum translates to errors in the model fitting where one metabolite can be overestimated at the expense of another. For example a choline over citrate ratio could be underestimated if the polyamines fit was overestimated and accounted for some of the true choline signal. While acquisition and fitting methods are being actively researched to improve the individual quantification of these metabolites, it is more reliable to stick to the pseudo-integral CC/C ratio.

Once reliably calculated, the CC/C ratio combines the essence of the observable spectroscopic data into a single quantity that can be displayed on an image (Fig. 6), combining the key information into a simple to read form for radiological reporting.

Published values of the ratios for tumor and benign tissue, which are calculated in a similar way to the *syngo*.via fitting, are listed in table 1.

Future perspective of MRSI for prostate cancer

The CC/C ratio is the most used method for interpreting ^{1}H MRSI data of prostate and prostate cancer. It remains, essentially, the integral of the choline-creatine region divided by the citrate region, a simple combination of the metabolite information in a single-value marker that is sensitive to the presence of tumor. The use of areas under the resonances in the ratio has the implication that the absolute value of this biomarker is largely dependent on the acquisition sequence used. Any change in field strength, the pulses or pulse timings will change resonance amplitude and shape due to T1 and T2 relaxations and the scalar couplings of especially citrate. Values of the ratio quoted in the literature for tumor or benign tissues depend strongly on how the

ratio is actually calculated and are, therefore, often not directly comparable. However, using the Siemens-supplied default protocols for acquisition and *syngo*.via postprocessing enables one to make use of published values as given in table 1, and incorporate ^{1}H MRSI of the prostate into their clinical routine.

References

1 Siegel R, Naishadham D, Jemal A. Cancer statistics, 2012. CA Cancer J Clin 2012; 62(1):10-29.

2 Hoeks CMA, Barentsz JO, Hambrock T, Yakar D, Somford DM, Heijmink SWTPJ, Scheenen TWJ, Vos PC, Huisman H, van Oort IM, Witjes JA, Heerschap A, Fütterer JJ. Prostate Cancer: Multiparametric MR Imaging for Detection, Localization, and Staging. Radiology 2011; 261: 46 –66.

3 Heerschap A, Jager GJ, van der Graaf M, Barentsz JO, Ruijs SH. Proton MR spectroscopy of the normal human prostate with an endorectal coil and a double spin-echo pulse sequence. Magn Reson Med 1997;37(2):204-213.

4 Kurhanewicz J, Vigneron DB, Hricak H, Parivar F, Nelson SJ, Shinohara K, Carroll PR. Prostate cancer: metabolic response to cryosurgery as detected with 3D H-1 MR spectroscopic imaging. Radiology 1996;200(2):489-496.

5 Kurhanewicz J, Vigneron DB, Nelson SJ, Hricak H, MacDonald JM, Konety B, Narayan P. Citrate as an *in vivo* marker to discriminate prostate cancer from benign prostatic hyperplasia and normal prostate peripheral zone: detection via localized proton spectroscopy. Urology 1995;45(3):459-466.

6 Glunde K, Bhujwalla ZM, Ronen SM. Choline metabolism in malignant transformation. Nat Rev Cancer;11(12): 835-848.

7 Costello LC, Franklin RB. Novel role of zinc in the regulation of prostate citrate metabolism and its implications in prostate cancer. The Prostate 1998; 35(4):285-296.

8 Giskeodegard GF, Bertilsson H, Selnaes KM, Wright AJ, Bathen TF, Viset T, Halgunset J, Angelsen A, Gribbestad IS, Tessem MB. Spermine and citrate as metabolic biomarkers for assessing prostate cancer aggressiveness. PloS one;8(4):e62375.

9 Scheenen TW, Klomp DW, Roll SA, Futterer JJ, Barentsz JO, Heerschap A. Fast acquisition-weighted three-dimensional proton MR spectroscopic imaging of the human prostate. Magn Reson Med 2004;52(1):80-88.

10 Scheenen TW, Gambarota G, Weiland E, Klomp DW, Futterer JJ, Barentsz JO, Heerschap A. Optimal timing for *in vivo* ^{1}H-MR spectroscopic imaging of the human prostate at 3T. Magn Reson Med 2005;53(6):1268-1274.

11 Shukla-Dave A, Hricak H, Moskowitz C, Ishill N, Akin O, Kuroiwa K, Spector J, Kumar M, Reuter VE, Koutcher JA, Zakian KL. Detection of prostate cancer with MR spectroscopic imaging: an expanded paradigm incorporating polyamines. Radiology 2007;245(2):499-506.

12 Garcia-Martin ML, Adrados M, Ortega MP, Fernandez Gonzalez I, Lopez-Larrubia P, Viano J, Garcia-Segura JM. Quantitative (1) H MR spectroscopic imaging of the prostate gland using LCModel and a dedicated basis-set: correlation with histologic findings. Magn Reson Med; 65(2):329-339.

13 Heerschap A, Jager GJ, van der Graaf M, Barentsz JO, de la Rosette JJ, Oosterhof GO, Ruijter ET, Ruijs SH. *In vivo* proton MR spectroscopy reveals altered metabolite content in malignant prostate tissue. Anticancer research 1997; 17(3A): 1455-1460.

14 Jung JA, Coakley FV, Vigneron DB, Swanson MG, Qayyum A, Weinberg V, Jones KD, Carroll PR, Kurhanewicz J. Prostate depiction at endorectal MR spectroscopic imaging: investigation of a standardized evaluation system. Radiology 2004;233(3):701-708.

15 Futterer JJ, Scheenen TW, Heijmink SW, Huisman HJ, Hulsbergen-Van de Kaa CA, Witjes JA, Heerschap A, Barentsz JO. Standardized threshold approach using three-dimensional proton magnetic resonance spectroscopic imaging in prostate cancer localization of the entire prostate. Investigative radiology 2007;42(2):116-122.

16 Kobus T, Hambrock T, Hulsbergen-van de Kaa CA, Wright AJ, Barentsz JO, Heerschap A, Scheenen TW. *In vivo* assessment of prostate cancer aggressiveness using magnetic resonance spectroscopic imaging at 3 T with an endorectal coil. European urology;60(5):1074-1080.

17 Scheenen TWJ, Fütterer J, Weiland E and others. Discriminating cancer from noncancer tissue in the prostate by 3-dimensional proton magnetic resonance spectroscopic imaging: A prospective multicenter validation study. Invest Radiol 2011;46(1):25-33.

18 Scheenen TW, Heijmink SW, Roell SA, Hulsbergen-Van de Kaa CA, Knipscheer BC, Witjes JA, Barentsz JO, Heerschap A. Three-dimensional proton MR spectroscopy of human prostate at 3 T without endorectal coil: feasibility. Radiology 2007;245(2):507-516.

19 Kobus T, Wright AJ, Scheenen TW, Heerschap A. Mapping of prostate cancer by ^{1}H MRSI. NMR Biomed. 2013 Jun 13. doi: 10.1002/nbm.2973. [Epub ahead of print] PMID:23761200.

Contact

Tom Scheenen, Ph.D.
Radboud University Nijmegen
Medical Centre
Radiology Department
P.O. Box 9102
6500 HC Nijmegen
The Netherlands
Tom.Scheenen@radboudumc.nl

Alan Wright

Arend Heerschap

Thiele Kobus

Tom Scheenen

Get your free copy of the PI-RADS Scoring Image Atlas

Visit us at
www.siemens.com/magnetom-world
Go to > Publications > Subscriptions > MRI Poster

Read the comprehensive article

"PI-RADS Classification: Structured Reporting for MRI of the Prostate"

by Matthias Röthke et al.
in MAGNETOM Flash 4/2013
page 30-38.

Available for download at
www.siemens.com/magnetom-world

SIEMENS

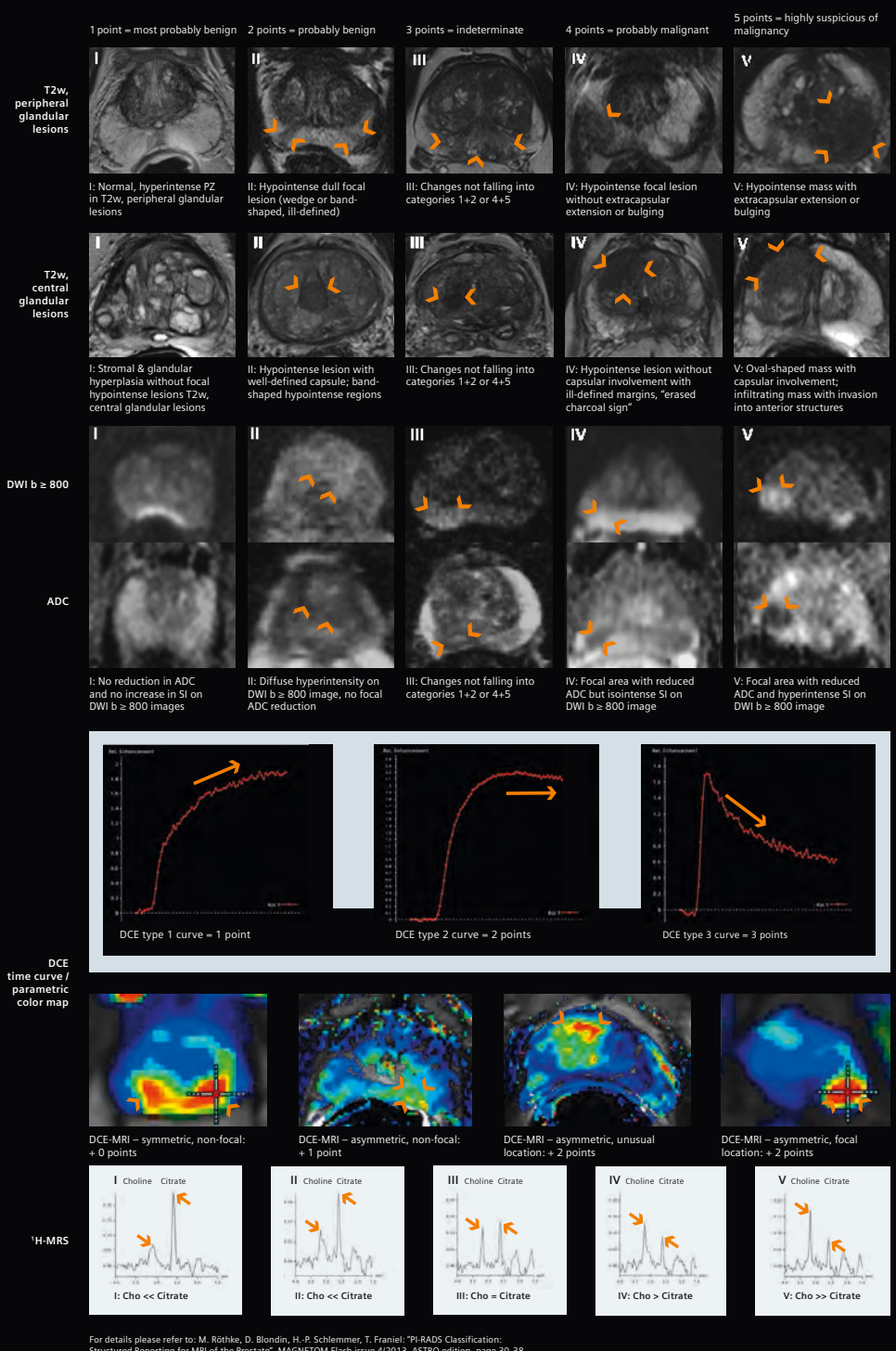

For details please refer to: M. Röthke, D. Blondin, H.-P. Schlemmer, T. Franiel: "PI-RADS Classification: Structured Reporting for MRI of the Prostate", MAGNETOM Flash issue 4/2013, ASTRO edition, page 30-38.

www.siemens.com/magnetom-world

PI-RADS SCORING Image Atlas

Prostate MRI

Answers for life.

Evaluation of the CIVCO Indexed Patient Position System (IPPS) MRI-Overlay for Positioning and Immobilization of Radiotherapy Patients

Th. Koch[1]; K. Freundl[1]; M. Lenhart[2]; G. Klautke[1]; H.-J. Thiel[1]

[1] Klinik und Praxis für Strahlentherapie und Radioonkologie, Sozialstiftung Bamberg, Germany
[2] Klinik für Diagnostische Radiologie, Interventionelle Radiologie und Neuroradiologie, Bamberg, Germany

Abstract

The emerging development in modern radiotherapy planning (RTP) requires sophisticated imaging modalities. RTP for high precision requires exact delineation of the tumor, but this is currently the weakest link in the whole RTP process [1]. Therefore Magnetic resonance imaging (MRI) is of increasing interest in radiotherapy treatment planning because it has a superior soft tissue contrast, making it possible to define tumors and surrounding healthy organs with greater accuracy. The way to use MRI in radiotherapy can be different. The MRI datasets can be used as secondary images to support the tumor delineation. This is routinely in use in many radiotherapy departments. Two other methods of MRI guidance in the RTP process are until now only research projects, but interest in them is increasing. The first method is to use MRI data as the primary and only image dataset and the second is the application of the MRI data as reference dataset for a so-called 'MRI-guided radiotherapy in hybrid systems' (Linear Accelerator (Linac) or Cobalt RT units combined with MRI). For all cases it is essential to create the MRI datasets in the radiotherapy treatment position. For this reason the CIVCO Indexed Patient Positioning System (IPPS) MRI-Overlay was introduced and tested with our Siemens MAGNETOM Aera MRI Scanner.

Introduction

Although computed tomography (CT) images are the current gold standard in radiotherapy planning, MRI becomes more and more interesting. Whilst CT has limitations in accuracy concerning the visualization of boundaries between tumor and surrounding healthy organs, MRI can overcome these problems by yielding superior soft tissue contrast. Currently there are three different possible strategies by which MRI can help to improve radiotherapy treatment planning:

The MRI datasets can be used as secondary images for treatment planning. These MR images can be used to delineate the tumor and the surrounding organs, whilst the CT images – the primary planning data – are necessary to calculate the 3D dose distribution. The two image datasets have to be co-registered thoroughly to ensure that the anatomy correlates (see for example [2]). The registration

1 1.5T MAGNETOM Aera with the standard cushion on the MRI couch.

2 After the removal of the standard cushion the CIVCO IPPS MRI-Overlay can be mounted.

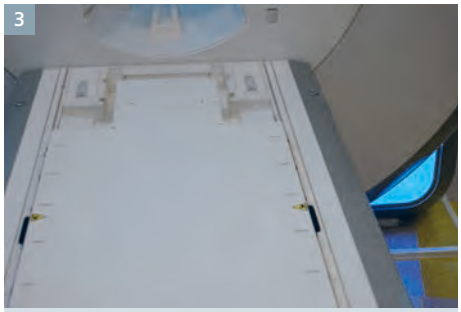

3 The lines indicate the position for the index bars.

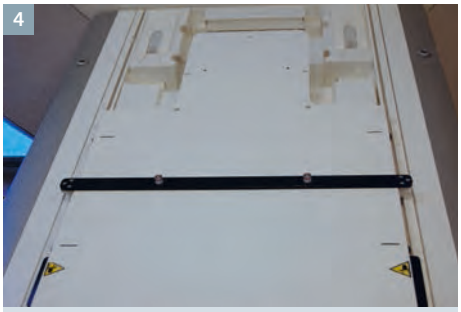

4 One index bar is latched to the MRI-Overlay.

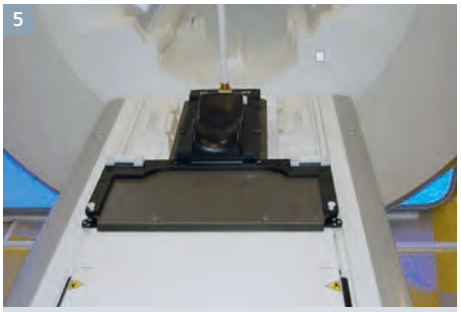

5 The mask system for head and neck fits to the index bar to avoid movement.

accuracy strongly depends on the MRI scan position. Hanvey et al. [3] and Brunt et al. [4] have shown that it is indispensable for the MRI dataset to be created in the treatment position which is primarily defined by the CT scan.

The MRI dataset can also feasibily be used as the only dataset. Because of the lack of electron density information, which is required for dosimetric calculations, bulk densities have to be applied to the MRI images. For this purpose the different anatomic regions like bone, lung, air cavities and soft tissue have to be overwritten with the physical densities. With this method it is possible to achieve dose calculation results quite similar to the calculation in the CT dataset in the head and neck region [5, 6] as well as in the pelvic region [7]. The advantage of this method is that by avoiding the CT scan you save some time and money. In this case it is necessary for the treatment position to be determined during the MRI scan, hence the MRI scanner has to be equipped with the same positioning and immobilization tools as the Linac. Further problems to overcome are the evaluation and correction of possible image distortions and the determination of accurate bulk densities.

After the RTP process there are a lot of remaining uncertainties such as set-up errors, motion of the target structures and during the treatment changes of the tumor volume and shrinking. This problem can be overcome with the so-called image-guided radiotherapy (IGRT). IGRT involves a periodical verification (weekly or more frequent) of tumor position and size with appropriate imaging systems. It is evident that IGRT is only as good as the accuracy with which the target structures can be defined. For this reason some groups try to develop hybrid systems, where a Linac or a cobalt treatment unit is combined with an MRI scanner for a so-called MR-guided radiotherapy [8-10]. Again: MR-guided radiotherapy can only be successful when the reference MRI dataset has been created in the treatment position.

In any of the above three cases, where MRI can be helpful to improve the accuracy of radiotherapy, it is strongly advised that one has a robust and reproducible patient positioning and immobilization system, mainly at the MRI scanner, which is used for MR-guided RTP. Siemens provides with the CIVCO IPPS MRI-Overlay a suitable solution. In our clinic we have introduced and tested this MRI-overlay, especially for patients with tumors in the pelvis and for brain tumors and metastasis.

Method

Our 1.5T MAGNETOM Aera system (Siemens Healthcare, Erlangen, Germany) is located in the radiology department and can temporarily be used by the staff of the radiotherapy department. For the purpose of MR-guided RTP we have equipped the MAGNETOM Aera with the CIVCO IPPS MRI-Overlay. This overlay enables the fixation of positioning and immobilization tools necessary for radiotherapy treatments. For our purpose we have used an MR compatible mask system for head and neck cases and vacuum cushions for patients with diseases in the pelvic region both from Medical Intelligence (Elekta, Schwabmünchen, Germany). These tools can all be fixed with so-called index bars (Figs. 4, 12) at the MRI-Overlay. These index bars are custom designed for our purpose by Innovative Technologies Völp (IT-V, Innsbruck, Austria) for the MRI-Overlay and for use in the high field magnetic environment. For the correct positioning of the patients, the laser system Dorado 3 (LAP, Lüneburg, Germany) was additionally installed in the MRI room. The preliminary modifications and the patient positioning is described in the following for two cases.

The first case describes the procedure for a patient with a head tumor. The first step is the removal of the standard cushion of the MRI couch and the mounting of the MRI-Overlay (Figs. 1–3). One index bar is necessary to fix the mask system on the overlay (Figs. 4, 5) to avoid movements and rotations during the scan. Because the standard head coil set cannot be used with the mask system, two flex coils (Flex4 Large) have to be prepared (Figs. 6–8). In figure 8 one can see, that the correct head angle could be adjusted. Now the patient is placed on the overlay and in the mask system. The patient's head can be immobilized with the real and proper mask made from thermoplastic material called iCAST (Medical Intelligence, Elekta, Schwabmünchen, Germany)

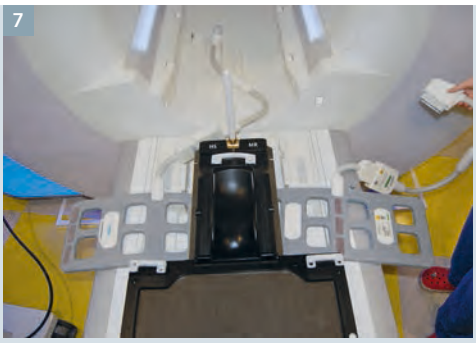

6
Two flex coils (Flex4 Large) are prepared.

7
The flex coils have to be positioned partly under the mask system, because the whole head of the patient should be covered.

8
It is possible to adjust the head angle in an appropriate and reproducible position that is comfortable for the patient.

9
Now the patient is immobilized using a custom-made mask made from thermoplastic material.

10
The flex coils are closed with hook-and-loop tapes.

11
The patient is ready for the scan.

12 A custom-made vacuum cushion for the lower extremities is latched to the MRI-Overlay with two index bars.

13 A second vacuum cushion is positioned on the table to fix the arms and shoulders and keep the patient in a comfortable position.

as can be seen in figure 9. Now the flex coils can be fixed with hook-and-loop tapes and placed very tight to the patient (Figs. 10, 11). Now the MRI scan can be started.

The second case describes the preparation before the MRI scan for a patient with a tumor in the pelvic region. The first two steps are identical, the remove of the standard cushion followed by the mount of the overlay (Figs.1, 2). Then a custom-made vacuum cushion for the lower extremities is attached to the overlay with two index bars (Figs. 12, 13). For a robust position of the patients with diseases in the pelvis it is very important to keep the legs in well-defined position – not only during imaging but also throughout the

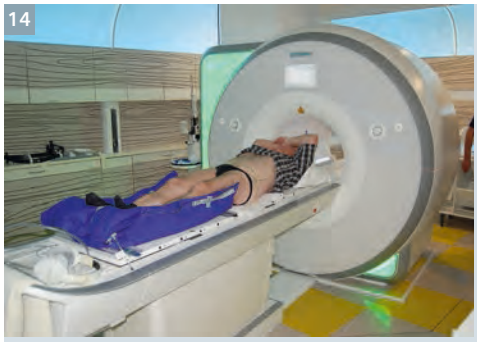

14
Now the patient can be positioned.

15
The accurate position of the patient can be adjusted with the LAP laser system.

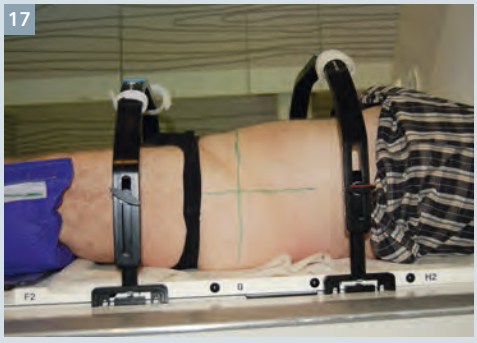

16
A mounting-frame for the flex coil has to attached to the MRI-Overlay.

17
The mounting-frame from a side view.

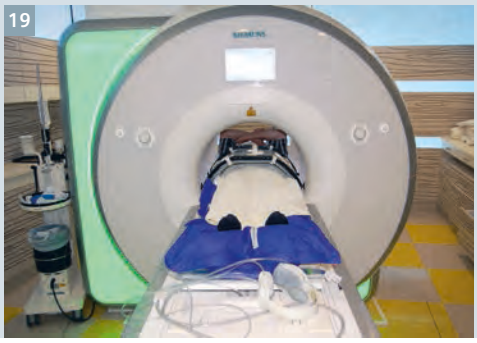

18
The flex coil is fixed to the mounting-frame with hook-and-loop tapes.

19
The patient is ready to start the scan.

whole treatment course, which spans over seven weeks. Any changes there can result in undesired rotations of the pelvis and in the end the tumor position and shape can also change. In figure 13 a second custom-made vacuum cushion can be seen. The only purpose of this vacuum cushion is to enable a comfortable position of the patient during scan and later during the treatment (Fig. 14). The more comfortably the patient lies on the table the more robust and reproducible is the positioning. Fortunately MAGNETOM Aera has a bore diameter of 70 cm, hence there are almost no limitations concerning patient positioning. Now the accurate position of the patient should be checked with the moveable laser-system (Fig. 15). This is necessary to avoid rotations of the pelvis around the patients longitudinal and lateral axis. For the fixation of the flex-coil for the pelvic region a mounting-frame has to be attached to the overlay (Figs. 16, 17). This can be done with hook-and-loop tapes (Fig. 18). Now the patient set-up is completed and the MRI scan can be started (Fig. 19).

Results

Two examples are shown in the following pictures. In Fig. 20 you can see a brain tumor in two corresponding slices. The left picture shows the CT-slice and the right picture shows the corresponding MRI slice obtained with a T1-weighted sequence with contrast agent. It is clear to see that tumor boundary is much more pronounced in the MRI image. Figure 21 shows the same slices with structures created by the radiotherapists. It is also helpful to create some control structures, such as brain and ventricles, to check the accuracy of the registration. Figures 22 and 23 give an example of a patient with prostate cancer. In this case the MRI images on the right

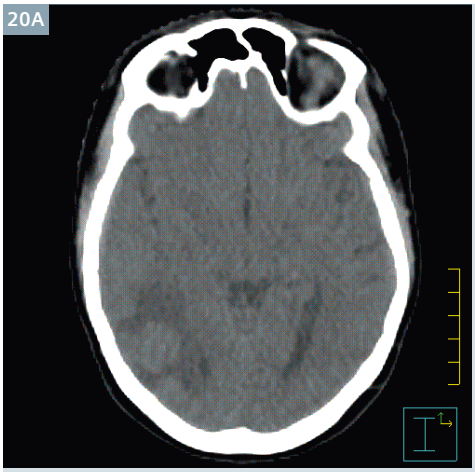

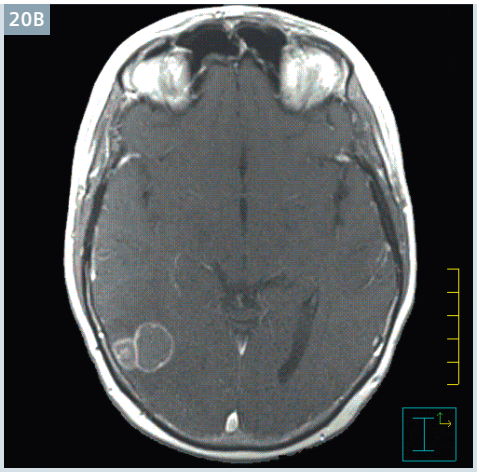

20

Two corresponding slices of a brain scan: **(20A)** CT slice and **(20B)** MRI slice obtained using a T1-weighted sequence with contrast agent.

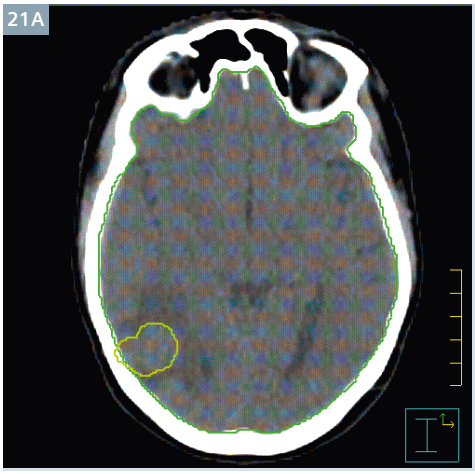

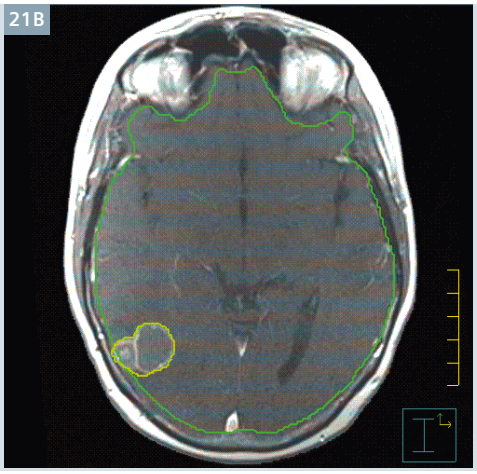

21

The same slices as in figure 20, but now with delineated tumor and help structures.

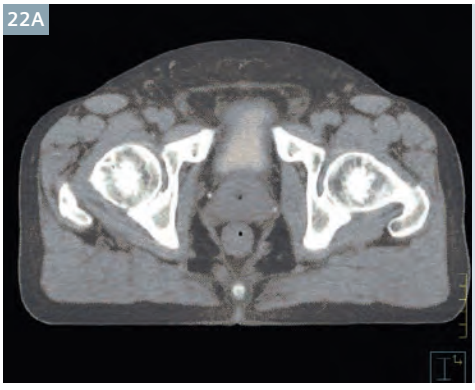

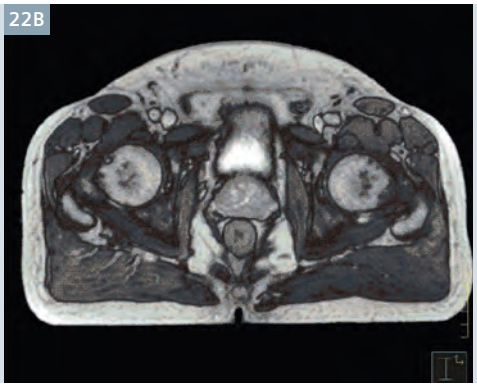

22

Two corresponding slices in the pelvic region of a patient with a prostate cancer: **(22A)** CT slice and **(22B)** MRI slice obtained with a T2-weighted TrueFISP sequence.

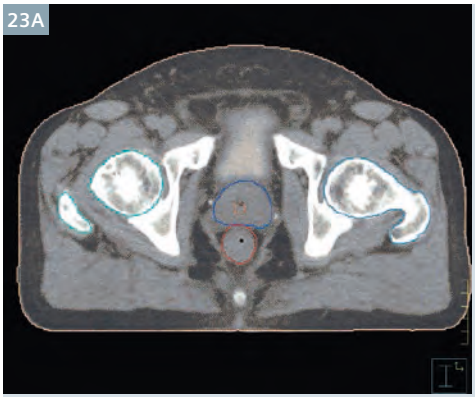

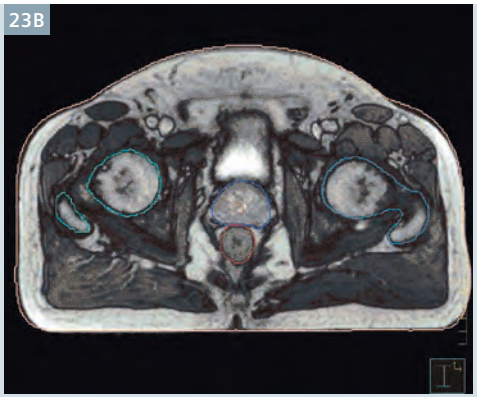

23

The important structures rectum and prostate as defined in the MRI slice are shown. The accuracy of the registration can be tested with the coincidence of help structures – like the femoral heads in this case – in both datasets.

are acquired using a T2-weighted TrueFISP sequence. The boundary of the prostate and the differentiation between prostate and rectum is much more easier to define in the MRI images. The control structures in this case are the femoral heads. For the head scans we normally use 3 sequences, a T1w SE with contrast agent, a T2w TSE and a FLAIR sequence. For the pelvis scans we normally use a T2w SPACE, a T2w TrueFISP and a T2w TSE sequence. The coordinate system should be the same for all sequences, that means same slices and same field-of-view. Hence one can use the same registration parameters for all sequences.

Conclusion and outlook

We can now look back over a period of two years working with the CIVKO IPPS MRI-Overlay. Our experience is very promising. The modifications on the table of the MRI scanner are very easy and can be executed and finished in only a couple of minutes. The procedure is well accepted by the radiologic technologists. To date, we have scanned more than 100 radiotherapy patients, mainly with diseases in the pelvis (rectum and prostate cancer) and in the head (brain tumors and metastasis). So far we have only used MRI dataset as a secondary image dataset. The co-registration with the CT datasets is now much easier because we have nearly identical transversal slices in both image datasets.

As a conclusion we can say that we are very happy with the options we have to create MRI scans in the treatment positions. It has been demonstrated that the MRI dataset is now much more helpful in the radiotherapy planning process. We should mention the need for a quality assurance program to take possible image distortions into consideration. Our next step is to install such a program, which involves the testing of suitable phantoms. A further step will be to assess whether we can use MRI datasets alone for RTP.

References

1 Njeh C. F. Tumor delineation: the weakest link in the search for accuracy in radiotherapy. J. Med. Phys. 2008 Oct-Dec; 33(4): 136-140.
2 Dean C.J. et al. An evaluation of four CT-MRI co-registration techniques for radiotherapy treatment planning of prone rectal cancer patients. Br. J. Radiol. 2012 Jan; 85: 61-68.
3 Hanvey S. et al. The influence of MRI scan position on image registration accuracy, target delineation and calculated dose in prostatic radiotherapy. Br. J. Radiol. 2012 Dec; 85: 1256-1262.
4 Brunt J.N.H. Computed Tomography – Magnetic Resonance Imaging Registration in Radiotherapy Treatment Planning. Clin. Oncol. 2010 Oct; 22: 688-697.
5 Beavis A.W. et al. Radiotherapy treatment planning of brain tumours using MRI alone. Br. J. Radiol. 1998 May; 71: 544-548.
6 Prabhakar R. et al. Feasibility of using MRI alone for Radiation Treatment Planning in Brain Tumors. Jpn. J. Clin. Oncol. 2007 Jul; 37(6): 405-411.
7 Lambert J. et al. MRI-guided prostate radiation therapy planning: Investigation of dosimetric accuracy of MRI-based dose planning. Radiother. Oncol. 2011 Mar 98: 330-334.
8 Raymakers B.W. et al. Integrating a 1.5 T MRI scanner with a 6 MV accelerator: proof of concept. Phys. Med. Biol. 2009 May; 54: 229-237.
9 Hu Y. et al. Initial Experience with the ViewRay System – Quality Assurance Testing of the Imaging Component. Med. Phys. 2012 Jun; 39:4013.
10 ViewRay. Available at: http://www.viewray.com

Contact

Thomas Koch, Ph.D.
Sozialstiftung Bamberg – Medizinisches Versorgungszentrum am Bruderwald
Praxis für Radioonkologie und Strahlentherapie
Head Medical Physics
Buger Straße 80
96049 Bamberg
Germany
Phone: +49 951 503 12931
thomas.koch@sozialstiftung-bamberg.de

Making MRI Scanning Quieter: Optimized TSE Sequences with Parallel Imaging

Eric Y. Pierre[1]; David Grodzki[2]; Bjoern Heismann[2]; Gunhild Aandal[3, 5]; Vikas Gulani[1, 3]; Jeffrey Sunshine[3]; Mark Schluchter[4]; Kecheng Liu[6]; Mark A. Griswold[1, 3]

[1]Biomedical Engineering, Case Western Reserve University, Cleveland, Ohio, USA
[2]Siemens Healthcare, Erlangen, Germany
[3]Radiology, Case Western Reserve University, Cleveland, Ohio, USA
[4]Division of Biostatistics, Case Western Reserve Univeristy, Cleveland, Ohio, USA
[5]Haraldsplass Deaconess Hospital, Bergen, Norway
[6]Siemens Medical Solutions, USA Inc., Malvern, Pennsylvania, USA

Introduction

Turbo Spin-Echo sequences at 1.5T can generate noise at over 100dB$_A$ inside the bore [1–3]. This noise is equivalent to standing 5 meters away from a jackhammer [3], and would be even louder on higher field systems. Despite the use of ear-protective equipment, reducing the Sound Pressure Level (SPL) generated by these standard clinical sequences could noticeably improve patient comfort [4]. MRI pulse sequences mostly generate acoustic noise because of rapidly varying gradient waveforms: The resulting Lorentz forces applied on the gradient coils make the entire scanner structure vibrate [5]. To circumvent this issue, several hardware solutions have been proposed. For example, the whole gradient coil can be enclosed in a vacuum chamber [6–8], or gradient field rotation can be performed mechanically [9]. While these solutions achieve significant noise reduction for all types of sequences, they can noticeably increase manufacturing cost, and can even decrease gradient efficiency. Mechanical and acoustic balanced designs of gradient coil systems including windings performing active acoustic control have also been considered and investigated [10, 11].

Modifying and/or optimizing pulse sequences can also reduce acoustic noise effectively. One such solution is to time the ramping up and ramping down of the gradient waveforms so that the induced scanner vibrations cancel each other out [12]. Another approach is to use lower gradient amplitude and slew rates of the gradient waveforms [13]. By low-pass filtering the gradient, vibration frequencies for which the acoustic response of the gradient coil is high can be avoided.

Elaborate redesigns of gradient waveforms coupled with parallel imaging have demonstrated further reduction

1

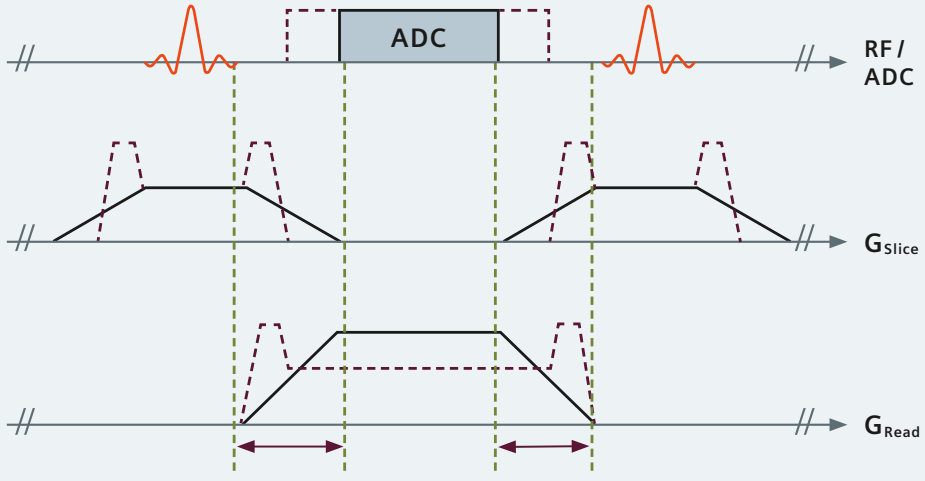

1 Comparison of conventional sequence (dashed lines) with quiet sequence (solid lines). The reduction of ADC represents a BW increase.

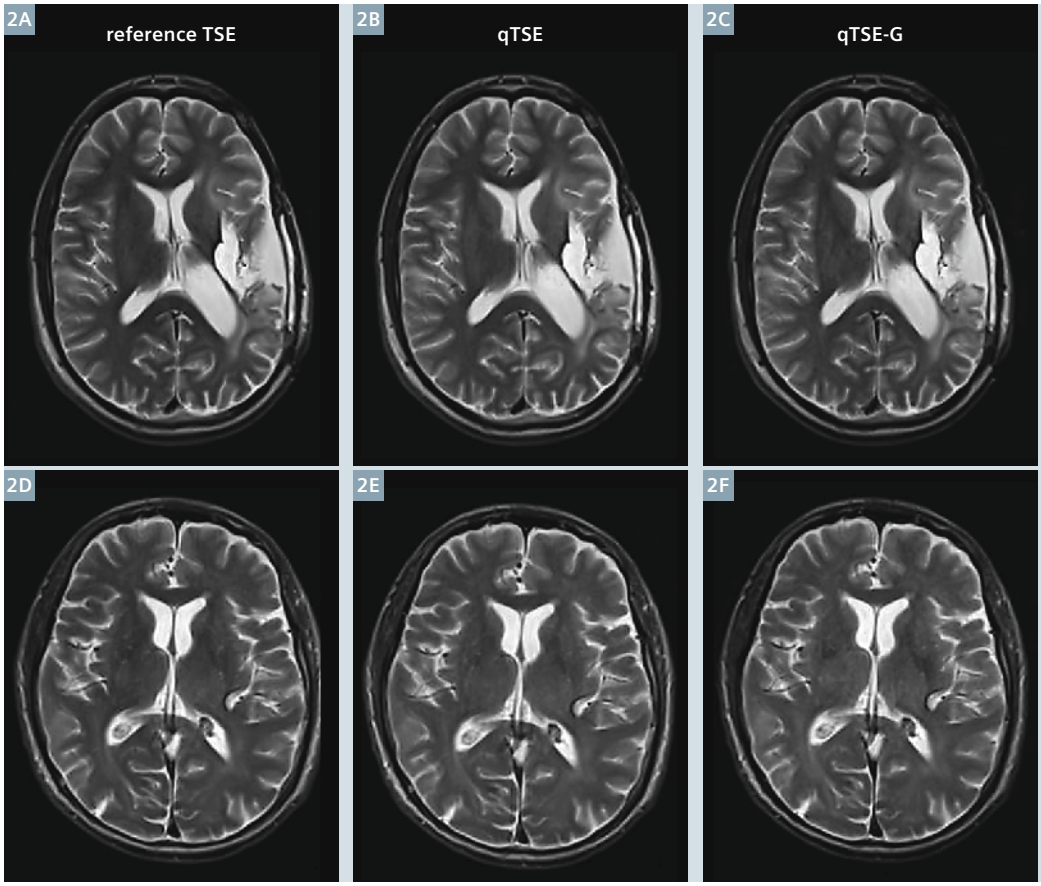

2

Representative slices from 2 patients acquired with the reference TSE sequence (left column), the qTSE sequence (center column) and the qTSE-G sequence (right column).

of acoustic noise in Echo Planar Imaging (EPI) [14, 15]. The reduction was achieved by counterbalancing lengthened gradient waveforms with increased acquisition speed, thereby reducing acoustic noise without increasing acquisition time while maintaining inter-echo spacing, only at cost of signal-to-noise ratio (SNR). By extending such principles to other generally-used standard clinical MR sequences, this article demonstrates that with minor SNR reductions (≤ 10%), effective reduction in acoustic noise can be further achieved without noticeable degrade of diagnostic information or imaging time, as well as without sacrificing gradient efficiency.

Two types of modifications in a T2-weighted Turbo Spin-Echo (TSE) sequence were investigated for acoustic noise reduction: First by solely modifying the gradient waveforms and second by additionally using GRAPPA at a reduction factor of two (R=2)*. Comparative SPL measurements at the bore were performed between standard TSE, quiet TSE (qTSE)* and quiet TSE with GRAPPA (qTSE-G)*. A statistical analysis of comparative scores from a reader's study was conducted.

Methods

The gradient waveforms of the TSE sequence were optimized with an automatic gradient optimization algorithm that extends any slope duration to its maximum and reduces the number of slopes to their minimum. For instance, with minor changes in protocols, spoiling and crusher gradient lobes are replaced by long rising or descending slopes, while maintaining the crusher moment unchanged. To keep the same total acquisition time, the reduction of the gradient slew rate is constrained by the fixed inter-echo spacing. The decreased slew rate of readout gradient will slightly reduce readout sampling time (Fig. 1). In consequence, the readout bandwidth (BW) increases slightly, with a tradeoff between reduction of SPL and SNR loss.

* WIP, the product is currently under development and is not for sale in the US and other countries. Its future availability cannot be ensured.

In addition, parallel acquisition could be further employed to reduce the echo-train length, i.e. number of echoes per train, by a factor of R. Keeping the acquisition time constant, the inter-echo spacing can be extended by R, allowing further stretching of the gradient moments. This effectively represents a benefit of parallel imaging acceleration in acoustic noise reduction rather than imaging time reduction.

The acquisition protocols changes are as follows: The readout BW was increased by about 10%, from 107 Hz/pixel in the standard protocol to 125 Hz/pixel. The effective TR/TE were increased from 5000/93 ms to 5180/85 ms, which resulted in only a 3 second increase in acquisition time, from 1:37 min to 1:40 min. The qTSE-G parameters were identical to the qTSE protocol, but with use of GRAPPA with R=2. For both qTSE and qTSE-G protocols, and the gradient slopes were maximally stretched as illustrated in figure 1.

Table 1: Comparison of dB_A values

Sequence type	Standard TSE	qTSE	qTSE-G	Background
LAEQ (30 sec average)	92.5	81.3	72.7	53.0
Max Peak	102.8	95.8	92.0	77.7

Comparison of dB_A values for standard TSE, qTSE, qTSE-G sequences, and measured background noise. Measurements were performed inside the bore at patient head position using a 2238 Mediator sound level meter (Brueel & Kjaer GmbH, Bremen, Germany).

Table 2: Ratings by readers

Sequence type	All techniques compared to themselves	qTSE : TSE	qTSE-G : TSE
Reader #1	0.35 ± 0.40 (0.06, 0.64) p = 0.02	-0.20 ± 0.26 (-0.38, -0.02) p = 0.04	0.20 ± 0.59 (-0.22, 0.62) p = 0.31
Reader #2	-0.03 ± 0.11 (-0.11, 0.04) p = 0.34	1.30 ± 1.96 (-0.10, 2.70) p = 0.07	3.95 ± 0.86 (3.33, 4.57) p < 0.0001
Reader #3	0 ± 0 –	0.73 ± 1.59 (-0.41, 1.86) p = 0.18	3.08 ± 1.25 (2.18, 3.97) p < 0.0001
Average	0.11 ± 0.14 (0.01, 0.21) p = 0.04	0.61 ± 1.17 (-0.23, 1.45) p = 0.13	2.41 ± 0.80 (1.83, 2.98) p < 0.0001

Mean and standard deviation, 95% confidence interval, and p-value of the scores given by each radiologist to the different types of image volume pairs after self-bias correction. Positive score show preference of the right volume over the left volume, on a -10 to +10 scale.

In-vivo studies were performed on a 3T MAGNETOM Verio MRI scanner (Siemens Healthcare, Erlangen, Germany) with a 12-channel head coil with patients admitted for head examination. Informed consent was obtained from the volunteer before the start of the study in accordance with IRB protocol. A total of 10 different patient scannings were performed, each comparing standard TSE images with qTSE and qTSE-G images. The image resolution (192 × 256 matrix), number of slices (26), slice thickness (5 mm) and slice orientation were kept identical throughout the 3 different acquisitions.

To measure acoustic noise level LAEQ (Equivalent Continuous Sound Level in A-weighting) with 30 seconds average and peak values, a professional device, 2238 Mediator sound level meter (Brueel & Kjaer GmbH, Bremen, Germany), was used, which was placed inside the bore at patient head position. The background noise is mainly generated by the cold-head pump and the ventilation among other sources.

To evaluate the image quality, a total of 7 image-volume-pairs were assembled from each of the 10 patient datasets. The first 2 pairs compared qTSE with TSE volumes, alternatively with qTSE on the left and TSE on the right. Similarly, another 2 pairs compared qTSE-G with TSE volumes in both left-right orders randomly. Finally, 3 pairs were assembled with the same volume on the left and right, which consist of TSE vs. TSE, qTSE vs. TSE, and qTSE-G vs. qTSE-G volumes, respectively.

All 70 volume pairs were presented in the same random order to 3 trained radiologists blinded to the acquisition technique, who were asked the following question: "On a scale from -10 to +10, how much better is the image quality of the volume on the right compared to the volume on the left, with a positive score indicating superiority of the right volume, and 0 representing no difference in quality between left and right?". The graphical user interface used for the reading allowed user-navigation through the paired-volume slices, and simultaneous image windowing of the 2 displayed images.

To avoid possible left-right bias, the average of the qTSE vs. TSE score and the TSE vs. qTSE score multiplied by -1 was then calculated for each reader's reading on each patient. The average of the corrected scores across readers was then computed for each patient. Corrected scores were calculated in the same way for the qTSE-G vs. TSE comparison. One-sample t-tests were used to test whether the mean average reader scores differed from zero, and 95% confidence intervals (CI) for the mean scores were also calculated. One-sample t-tests and CI were also carried out using each reader's scores

3

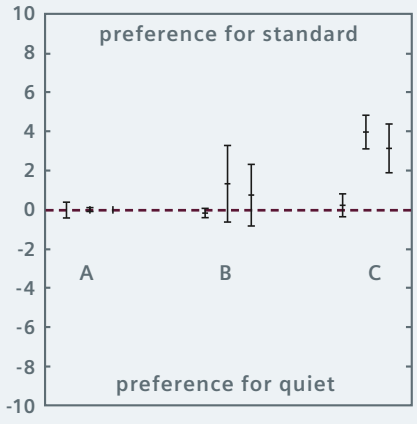

A. self image comparison (all methods)
($p < 0.05$)

B. qTSE vs. standard TSE
Non significant difference for all 3 readers
($p = 0.20$, $p = 0.06$, $p = 0.18$)

C. qTSE+GRAPPA vs. standard TSE
($p < 0.0001$)

3

(A) 95% confidence intervals for averages scores by readers for volumes compared to themselves; (B) qTSE vs. standard TSE; and (C) qTSE-G vs. standard TSE. Positive scores show preference for standard TSE in the last two cases.

separately. A reader's average rating of these three self-comparisons using images from each patient were averaged, and then the three reader averages were averaged for each patient. A t-test was used to test whether the average of the reader ratings across patients differed from zero. One-sample t-tests and CI were also carried out for each reader separately.

Results

The respective average and peak SPL in [dB_A] measurements for standard TSE, qTSE and qTSE-G protocols are listed in table 1. The achieved reduction of average SPL for qTSE and qTSE-G were 10 dB_A and near 20 dB_A (30 seconds average), respectively.

Discussion

Optimizing the gradient waveforms alone with a 10% increase in bandwidth achieves an 11 dB_A SPL reduction (Table 1), with little cost to image quality (Fig. 3). These results are in accordance with [16] though here the measurements were made directly at the bore. This cost might be more noticeable with lower SNR systems, however in this configuration, no statistically significant difference in image quality was observed (Table 2), making gradient redesign a viable solution to make TSE sequences quieter.

With additional use of Parallel Imaging, the modified quiet TSE sequence allows on average a 20 dB_A reduction in SPL (Table 1). The modified sequence had an effect on in image quality (Fig. 3): The average preference score across readers for standard TSE images over qTSE-G images was +2.41 ($p<0.0001$, Table 2), and the 95% confidence interval places its true value between +1.8 and +3. However it should be noted that this change in image quality is to be expected as Parallel Imaging was used. In compensation, the reduction of acoustic noise was highly effective: the SPL at the bore of the standard TSE sequence was 39.5 dB_A higher than the background noise, compared to 19.7 dB_A for the modified sequence.

Conclusion

In comparison with standard MR sequences, gradient wave modifications in TSE sequence coupled with Parallel Imaging can achieve over a factor 10 of acoustic noise reduction, yielding an improved patient comfort with nearly identical diagnostic information and imaging time. Without any hardware modifications or upgrade, both proposals described in this article, qTSE and qTSE-G, can be easily implemented on a conventional MRI system for routine clinical applications. In addition, scanning on a high field system with multiple channel coils, such as the 32-channel head coil, provides more flexibility to make MRI scanning quieter.

* Work in progress: The product is still under development and not commercially available yet. Its future availability cannot be ensured.

References

1 Shellock FG, Morisoli SM, Ziarati M. Measurement of acoustic noise during MR imaging: evaluation of six "worst-case" pulse sequences. Radiology 1994;191:91–93.
2 McJury M, Blug A, Joerger C, Condon B, Wyper D. Acoustic noise levels during magnetic resonance imaging scanning at 1.5 T. Br J Radiol 1994;67:413–415.
3 McJury M. Acoustic noise levels generated during high field MR imaging. Clin Radiol 1995;50:331–334.
4 Quirk ME, Letendre AJ, Ciottone RA, Lingley JF. Anxiety in patients undergoing MR imaging. Radiology 1989;170:463–466.
5 Hedeen R, Edelstein W. Characterization and prediction of gradient acoustic noise in MR imagers. Magn Reson Med 2005;37:7–10.
6 Katsunuma A, Takamori H, Sakakura Y, Hamamura Y, Ogo Y, Katayama R. Quiet MRI with novel acoustic noise reduction. MAGMA 2002;13:139–44.
7 Edelstein WA, Hedeen RA, Mallozzi RP, El-Hamamsy SA, Ackermann RA, Havens TJ. Making MRI quieter. Magn Reson Imaging 2002;20:155–63.
8 Edelstein WA, Kidane TK, Taracila V, Baig TN, Eagan TP, Cheng Y-CN, Brown RW, Mallick J a. Active-passive gradient shielding for MRI acoustic noise reduction. Magn Reson Med 2005;53:1013–7.
9 Cho ZH, Chung ST, Chung JY, Park SH, Kim JS, Moon CH, Hong IK. A new silent magnetic resonance imaging using a rotating DC gradient. Magn Reson Med 1998;39:317–21.
10 Mansfield P, Haywood B. Principles of active acoustic control in gradient coil design. MAGMA 2000;10:147–51.
11 Haywood B, Chapman B, Mansfield P. Model gradient coil employing active acoustic control for MRI. MAGMA 2007;20:223–31.

12 Shou X, Chen X, Derakhshan J, Eagan T, Baig T, Shvartsman S, Duerk J, Brown R. The suppression of selected acoustic frequencies in MRI. Appl Acoust 2010;71:191–200.
13 Hennel F, Girard F, Loenneker T. "Silent" MRI with soft gradient pulses. Magn Reson Med 1999;42:6–10.
14 De Zwart J, Vangelderen P, Kellman P, Duyn J. Reduction of Gradient Acoustic Noise in MRI Using SENSE-EPI. Neuroimage 2002;16:1151–1155.
15 Witzel T, Wald LL. Methods for Functional Brain Imaging. Massachusetts Institute of Technology; 2011.
16 Pierre EY, Grodzki D, Heismann B, Liu K, Griswold MA. Reduction of Acoustic Noise to Improve Patient Comfort Through Optimized Sequence Design. In: Proceedings of the 21st Annual Meeting of ISRMRM. Vol. 42. Salt Lake City, USA; 2013. p. 256.

Contact

Eric Y. Pierre, Ph.D.
Department of Biomedical Engineering
Case Western Reserve University
319 Wickenden Building
10900 Euclid Avenue
Cleveland, OH 44106-7207
USA
Phone: +1 (216)-368-4063
pierre@case.edu

Eric Pierre

Gunhild Aandal

Vikas Gulani

Jeffrey Sunshine

Mark Schluchter

Kecheng Liu

Mark Griswold

Quiet Suite

Imaging is to be seen, not heard.

Answers for life.

Quiet T1-weighted 3D Imaging of the Central Nervous System Using PETRA

Masahiro Ida, M.D.[1]; Matthew Nielsen, M.A.[2]

[1]Dept. of Radiology, Tokyo Metropolitan Ebara Hospital, Tokyo, Japan
[2]Research & Collaboration Dept., Healthcare Sector, Siemens Japan K.K., Tokyo, Japan

Introduction

Nearly all MRI sequences in routine clinical use employ rapidly varying magnetic field gradients that generate considerable acoustic noise, one of the primary causes of patient discomfort and restlessness [1]. Eliminating such noise would provide additional comfort for all patients, and may provide particular advantages for patients with pediatric*, dementia and certain psychiatric diseases who tend to have difficulty relaxing or remaining still during MR examinations.

Ultra-short echo time sequences such as zero-TE [2], SWIFT [3] and PETRA [4] require only limited gradient activity and allow for inaudible 3D scanning. However, due to ultra-short TEs, the image contrast is given by the steady state and is limited to the range of PD- to T1-weighting unless pre-pulses are used [5]. Similar to the MPRAGE sequence [6-8], stronger T1-weighting can be generated by applying an inversion pre-pulse before every n^{th} repetition in the PETRA* sequence. A study has shown that this quiet inversion-prepared PETRA sequence is capable of T1-weighting comparable to that of MPRAGE when measured in the same time and with the same spatial resolution [1].

In this article, examples of quiet inversion-prepared PETRA images are compared with conventional 3D T1-weighted images (MPRAGE or 3D-FLASH) from the same patients. All of the examples were obtained during brain examinations, and all but one of the examples employed contrast enhancement.

* WIP, the product is currently under development and is not for sale in the US and other countries. Its future availability cannot be ensured.

PETRA sequence principles and noise reduction

In the PETRA sequence, gradients are already on and stable at a certain amplitude before the excitation pulse, as shown in figure 1. At the end of each repetition, the gradient strength on each axis is altered only slightly meaning that the required slew rate is extremely low (e.g., < 5 T/m/s with

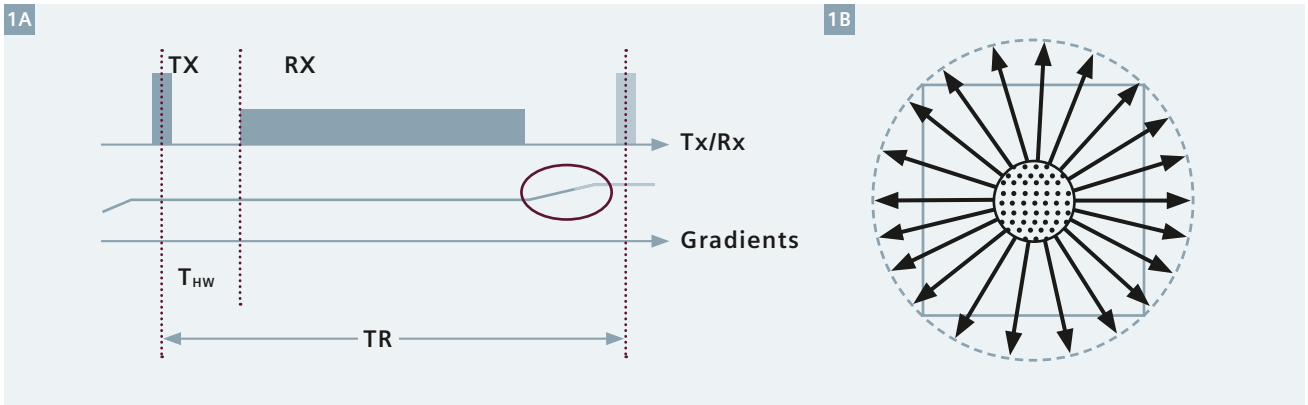

1 PETRA combines two different sequences, acquiring central *k*-space in a 'point-wise' fashion (one *k*-space point per repetition), and the rest of *k*-space with radial trajectories. PETRA stands for Pointwise Encoding Time reduction with Radial Acquisition. No hardware modifications or dedicated coils are needed [1].
(1A) Pulse sequence diagram for one repetition of the radial part of the PETRA sequence. Gradients are held constant during almost an entire repetition and altered only slightly at the end of each repetition without being ramped down. This leads to negligible deformation and vibration of the gradient coil. Thus, no acoustic noise is generated by the gradient coil. T_{HW} is the time required to switch from transmission mode to receive mode (in the range of 10 to 100 μs on clinical scanners) [1].
(1B) During T_{HW}, a spherical volume (dots) at the center of *k*-space is missed by the radial part of the sequence. Each *k*-space point inside that spherical volume is acquired separately in the Pointwise Encoding (PE) part of the sequence. The acquisition time of the PE part is approximately 3 to 5% of the total measurement time [1].

PETRA) [1]. The resulting deformation and vibration of the gradient coil is negligible and produces almost no audible sound. Completely unrelated to the gradients however, transmit-mode-to-receive-mode switching (and vice versa) in receive-only RF coils produces some noise [1], while PETRA is essentially inaudible when used with transmit-and-receive RF coils.

The acoustic noise levels generated by PETRA and MPRAGE on a MAGNETOM Trio A Tim System (3T) were measured using a sound-pressure meter with A-weighting. PETRA afforded a reduction in acoustic noise of more than 25 dB_A with both the 12-channel head matrix coil and the 32-channel head coil. Since both coils were receive-only, an even greater reduction can be expected with transmit-and-receive coils.

PETRA versus routine sequence image comparisons

While MR angiography (MRA) is undoubtedly the most commonly-used 3D sequence in brain MRI exams, other 3D sequences are used in certain circumstances at Tokyo Metropolitan Ebara Hospital. The most common one is contrast-enhanced (CE) 3D-FLASH which is employed for the following indications because of its high spatial resolution and short echo time:

(1) To precisely diagnose head & neck tumors, pre- & post-operatively (with Quick FatSat),
(2) to inspect blood pools (AVM, thrombosis, aneurysm, dissection), and
(3) to detect cranial nerve inflammation.

The second most common 3D scan other than MRA is CE MPRAGE which is employed to diagnose intracranial brain tumors. Among those, the most common indication is screening for intracranial metastases.

MR imaging was performed on a 3 Tesla MAGNETOM Trio A Tim System. PETRA was added to routine patient exams that included either MPRAGE or 3D-FLASH. The parameters of the three sequences are shown in table 1.

The center of *k*-space for MPRAGE (scan time: 5 min 56 sec) was acquired approximately 6 to 11 minutes after contrast media administration, while the center of *k*-space for PETRA was acquired approximately 3 minutes later than that of MPRAGE, 9 to 14 minutes after contrast media administration. PETRA acquires the central portion of *k*-space first (in a pointwise fashion as shown in figure 1) before acquiring the rest of 3D *k*-space with radial trajectories. A previous study showed that for enhancing intracranial lesions with a diameter of 5 mm or larger, enhancement reached a plateau in less than 10 minutes and lasted until at least 20 minutes after contrast media injection [9]. Thus, the 3 minute difference in the acquisition of $k = 0$ between MPRAGE and PETRA would not result in differing lesion enhancement, and any difference in lesion enhancement can be taken as primarily due to sequence characteristics.

Protocols provided with the PETRA sequence were designed to parallel the contrast and spatial resolution (0.9 to 1.0 mm cubic voxels) typically available with MPRAGE. Therefore, initial work with PETRA at our hospital focused on comparisons with MPRAGE. One of the protocols placed the priority on signal-to-noise ratio (SNR) (TI 900 ms), and one placed the priority on contrast-to-noise ratio (CNR) (TI 500 ms, for higher contrast between gray matter (GM) and white matter (WM)).

The scan times of both PETRA protocols were adjusted such that they were similar to that of the MPRAGE protocol used in patient exams. In a pilot study, volunteers and patients were scanned with both PETRA protocols and with

Table 1: Sequence parameters

	PETRA Figs. 2, 3, 11, 12	PETRA Figs. 4–10	MPRAGE Figs. 2–8	3D-FLASH Figs. 9–12
Voxel size / mm	$(0.99\ mm)^3$ for Figs. 2,3 $(0.80\ mm)^3$ for Figs. 11, 12	$(0.99\ mm)^3$	$(0.94\ mm)^3$	$0.6 \times 0.6 \times 1.0\ mm^3$
Matrix	288 × 288	288 × 288	256 × 256	346 × 384
Slices	288	288	176	144
TI / ms	500 for Figs. 2, 3 900 for Figs. 11, 12	700	900	n.a.
TR / ms	2.79	2.79	5.6[1]	11
TE / ms	0.07	0.07	2.4	6.2
FA / deg	6	6	10	20
FatSat	No	Yes	No	Yes
Scan time	05:59	06:20	5:56 (3:54 for Fig. 2)	02:52

[1]Repetition time of RF excitation pulses, which for MPRAGE is displayed on the MR console as 'Echo spacing'.

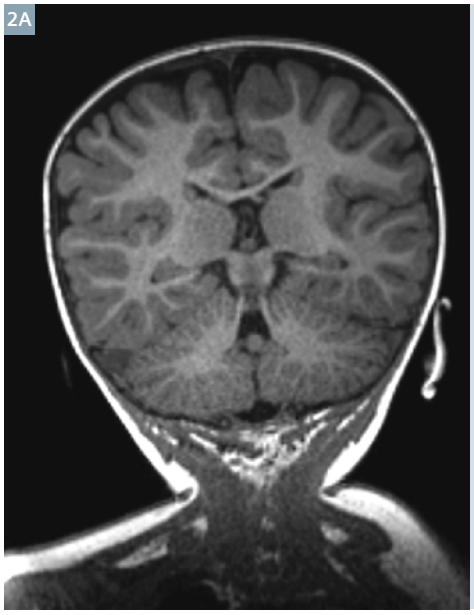

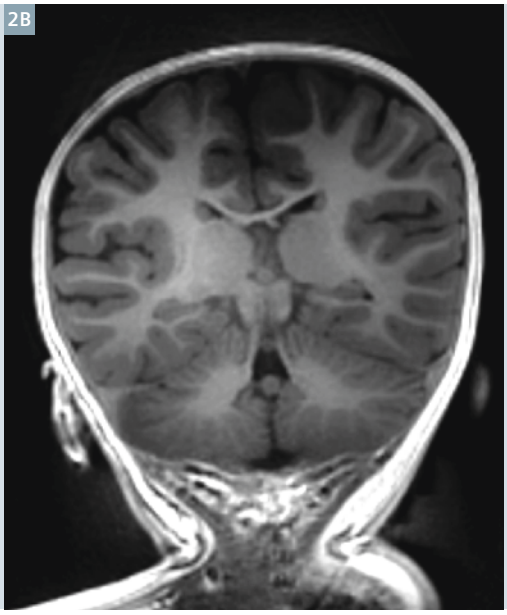

2

MR imaging was indicated for a 19-month-old* female experiencing seizures with no associated fever. Neither sequence revealed any brain abnormality. **(2A)** MPRAGE, **(2B)** CE PETRA with a TI of 500 ms demonstrated excellent gray-to-white-matter contrast comparable with that of MPRAGE.

* MR scanning has not been established as safe for imaging fetuses and infants less than two years of age. The responsible physician must evaluate the benefits of the MR examination compared to those of other imaging procedures.

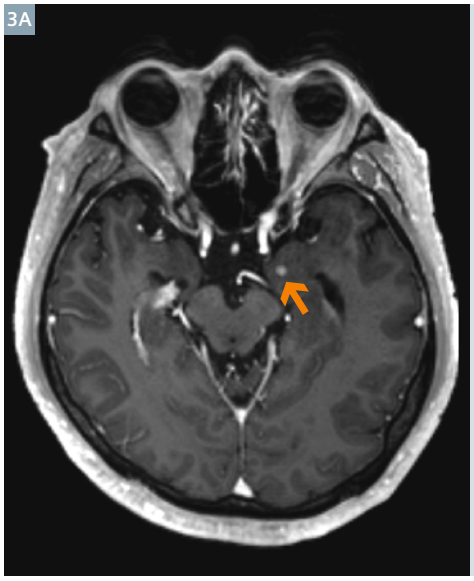

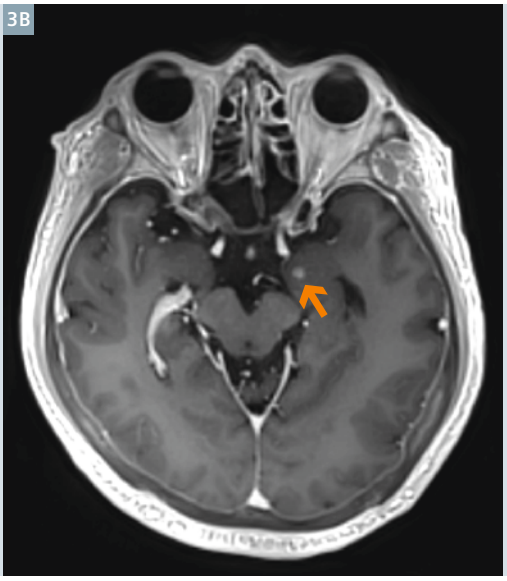

3

Contrast-enhanced screening for brain metastases was indicated for a 57-year-old male who had lung cancer. A tiny metastasis (diameter 3.5 mm) was detected in the medial portion of the left temporal lobe (arrows) on both sequences.
(3A) CE MPRAGE,
(3B) CE PETRA with an inversion time of 500 ms.

MPRAGE. The SNR on PETRA images with TI 900 ms was visibly higher than on MPRAGE images, while PETRA images with TI 500 ms provided more GM-to-WM contrast than necessary for CE studies in the opinion of one radiologist (MI). A decision was made that some of the SNR could be 'traded for' tissue CNR, and an intermediate TI of 700 ms was chosen for further CE studies. Statistical comparisons of contrast enhancement and SNR between PETRA and MPRAGE were performed (that study is under review for publication in a peer-reviewed journal).

PETRA was also compared with 3D-FLASH while remaining conscious of the fact that, compared to the PETRA implementation discussed in this article, 3D-FLASH was capable of higher spatial resolution.

Clinical observations

Comparisons of PETRA and MPRAGE

Comparisons between PETRA and MPRAGE with similar spatial resolution and without fat suppression are shown in figures 2 and 3. GM-to-WM contrast is seen to be similar, both without (Fig. 2) and with (Fig. 3) contrast enhancement (CE). In the latter CE case, a small enhancing lesion appears to have the same size and enhancement on the PETRA image as on the MPRAGE image.

The remaining comparisons between PETRA and MPRAGE, figures 4 through 8, were contrast-enhanced studies of intracranial primary or metastatic tumors with the same resolution parameters as above. However, two PETRA parameters were modified: TI was changed to 700 ms, sacrificing some GM-to-WM contrast for a gain in SNR, and fat-suppression was added (to PETRA only, avoiding a change to the hospital's routine MPRAGE protocol).

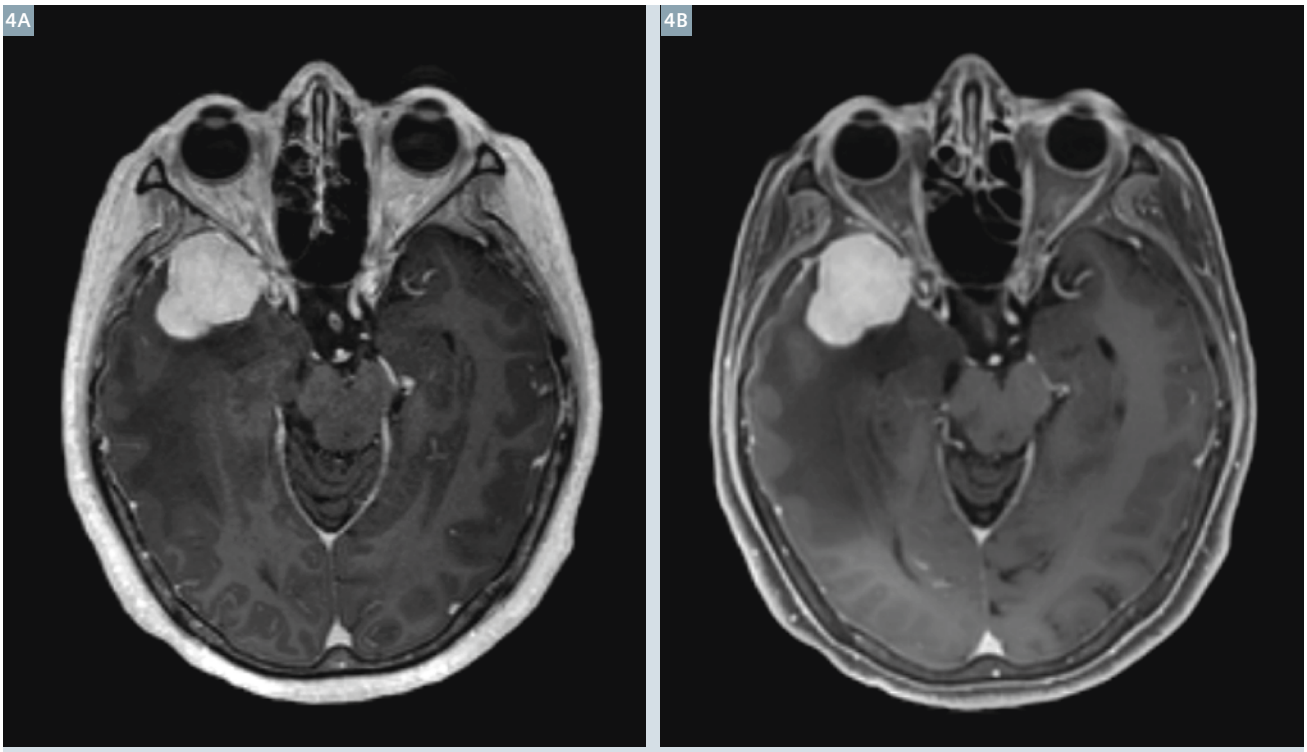

4 Contrast-enhanced images of gliobastoma in a 56-year-old female patient (not proven histologically).
(4A) CE MPRAGE, **(4B)** fat-suppressed CE PETRA.

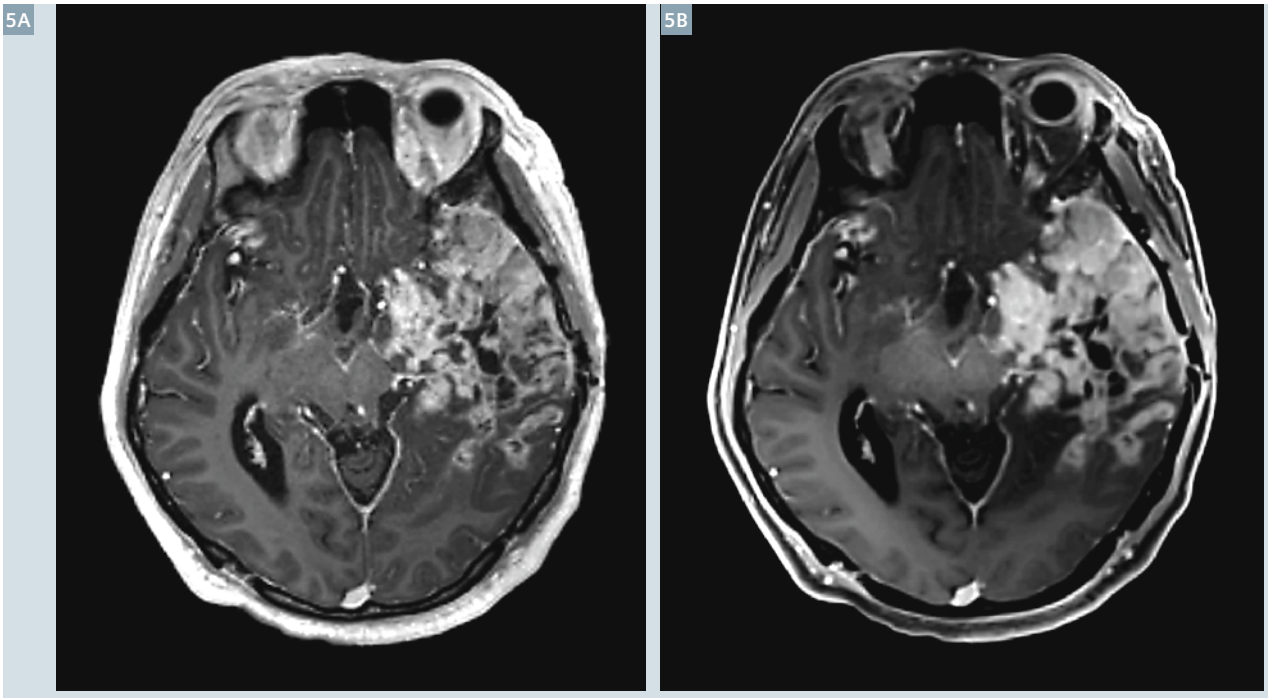

5 Contrast-enhanced images of glioblastoma in a 33-year-old male patient.
(5A) CE MPRAGE, **(5B)** fat-suppressed CE PETRA.

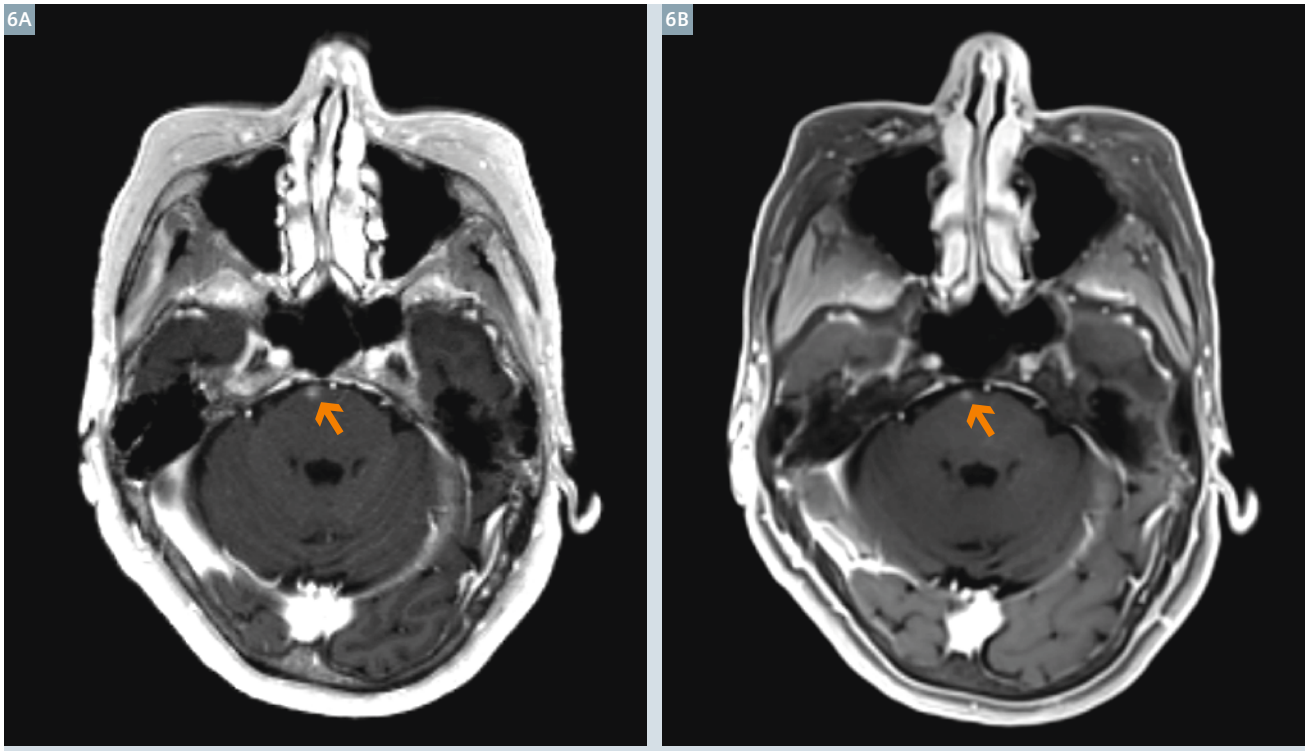

6 Contrast-enhanced screening for brain metastases was indicated for a 70-year-old female who had lung cancer. A small metastasis was detected in the supependymal zone of the pons (arrows) on both sequences. **(6A)** CE MPRAGE, **(6B)** fat-suppressed CE PETRA.

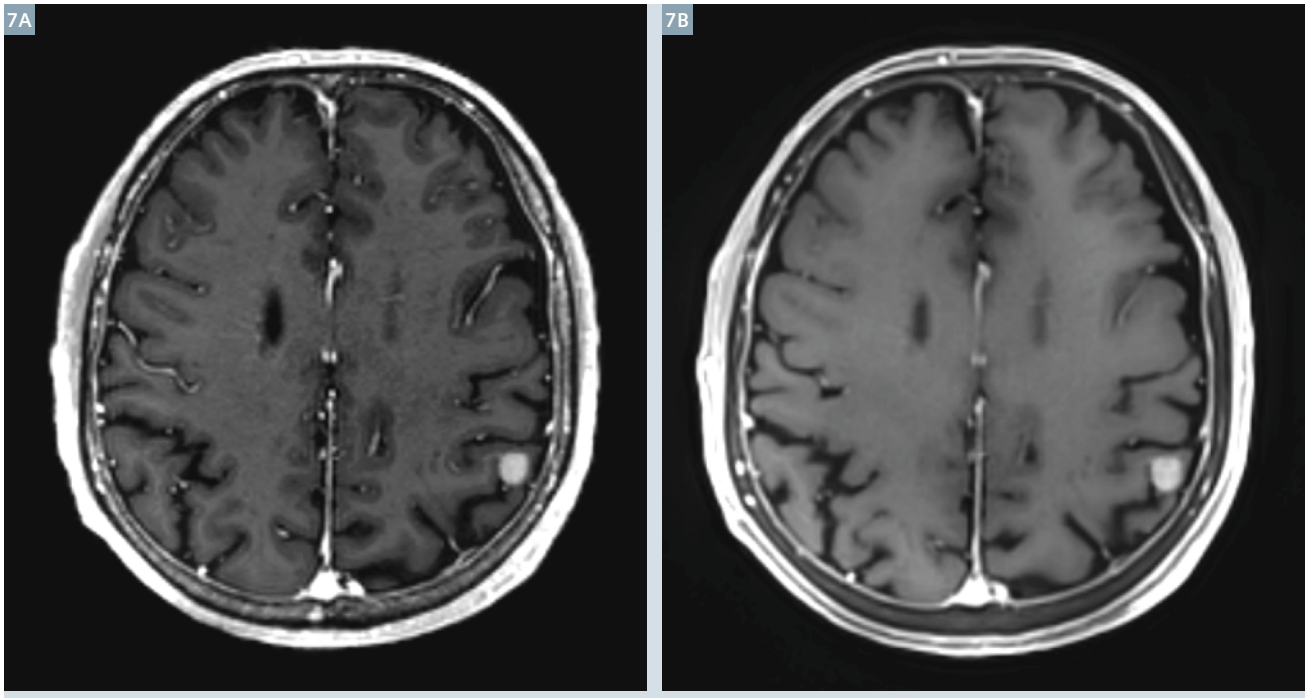

7 Contrast-enhanced screening for brain metastases was indicated for a 69-year-old male who had lung cancer. A small metastasis was detected in the corticomedullary junction of the left parietal lobe on both sequences. **(7A)** CE MPRAGE, **(7B)** fat-suppressed CE PETRA.

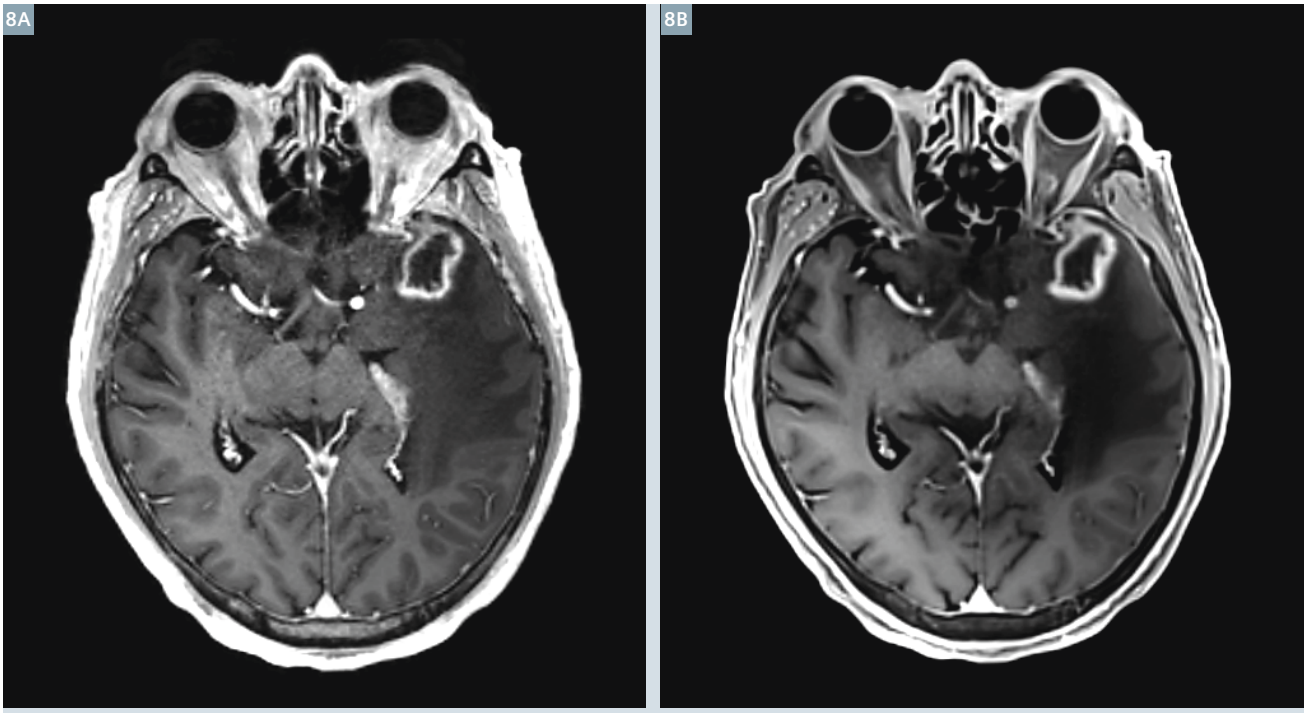

8 Contrast-enhanced screening for brain metastases was indicated for a 63-year-old male. A ring-enhancing lesion was detected in the left temporal lobe on both sequences. **(8A)** CE MPRAGE, **(8B)** fat-suppressed CE PETRA.

Comparisons of PETRA and 3D-FLASH

Comparisons between PETRA and 3D-FLASH are shown in figures 9 through 12. While the acquired spatial resolution was higher for 3D-FLASH ($0.6 \times 0.6 \times 1.0$ mm^3) than for PETRA, the clinical findings were not affected in these cases. PETRA had a voxel size of 0.993 mm^3 (Figs. 9, 10) or 0.803 mm^3 (Figs. 11, 12).

General clinical observations

Susceptibility-related artifacts and flow voids were absent on PETRA images, while signal from cortical bone was observed. All three observations can be attributed to the ultra-short TE. The absence of susceptibility-related artifacts should allow PETRA to detect sinusitis or tumors within the paranasal sinsuses which tend to be highly distorted on 3D gradient-echo-based sequences such as MPRAGE and 3D-FLASH. Positive signal from bone may be useful in cases of head trauma for detecting fractures and in surgical planning and follow-up. While CT is normally used for this purpose in adults, its use is highly restricted in children. PETRA may be able to readily provide 3D bone images even for children, or to provide more frequent follow-ups after surgery in adults.

The masticator space and the paranasal space at the skull base tended to appear 'dirty' or 'messy' on PETRA images, but this was not the result of an artifact or distortion. Rather, this appearance was caused by strong venous enhancement due to the absence of flow voids. Also on PETRA, the dura mater as well as the mucosa in the paranasal sinuses exhibited contrast enhancement, and the enhancement of the dura was uniform in most cases. This was likely due to blood pool enhancement in capillary arteries which are dense in those tissues, in combination with the absence of flow voids as a result the ultra-short TE. Such enhancement did not appear on MPRAGE and 3D-FLASH images. The uniform enhancement of the dura would prevent the use of PETRA for the detection of dural inflammation, dural metastasis, intracranial hypotension or other causes of local dural enhancement. Nevertheless, many other applications of 3D T1-weighted imaging exist such as those presented in the current article.

Finally, PETRA demonstrated excellent fat suppression which would allow the sequence to be employed, not only for the diagnosis of intracranial tumors, but also for the diagnosis of extracranial, orbital and paranasal tumors including bone-marrow metastases of the calvaria and cranial base.

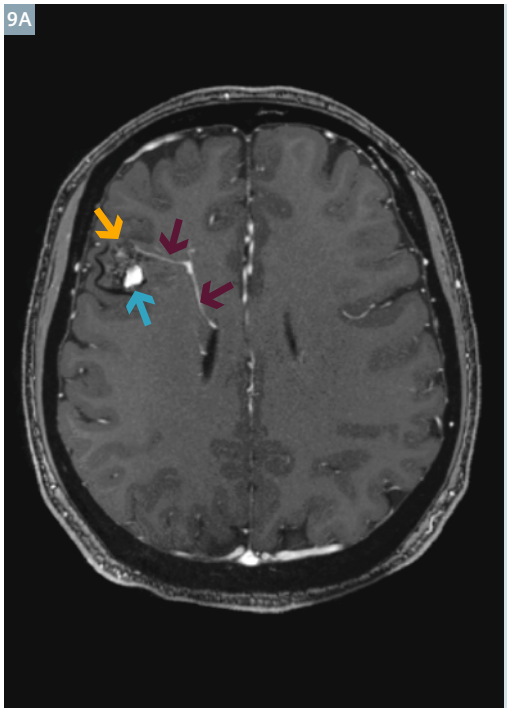

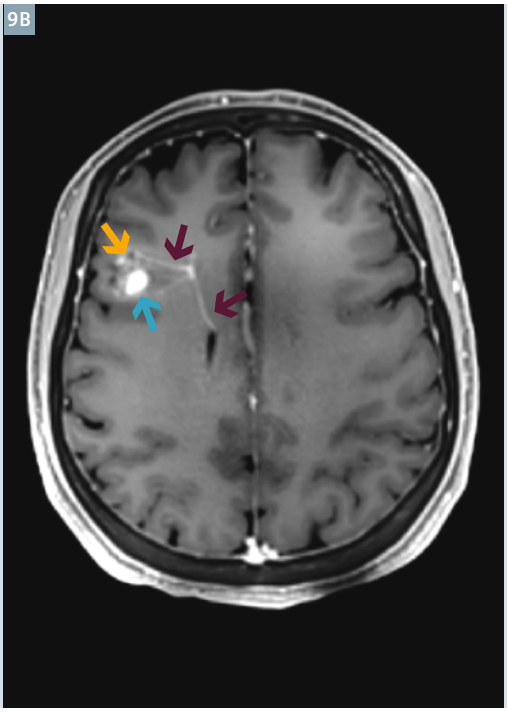

9

Contrast-enhanced images of dilated, abnormal medullary veins representing developmental venous anomaly **(red arrows)** in a 47-year-old female patient. **Yellow arrows:** Small blood pool enhancement in the combined cavernous malformation.
Blue arrows: T1 shortening caused by methemoglobin.
(9A) CE 3D-FLASH with a voxel size of 0.6 × 0.6 × 1.0 mm^3.
(9B) CE PETRA (TI 700 ms) with a voxel size of (0.99 $mm)^3$.

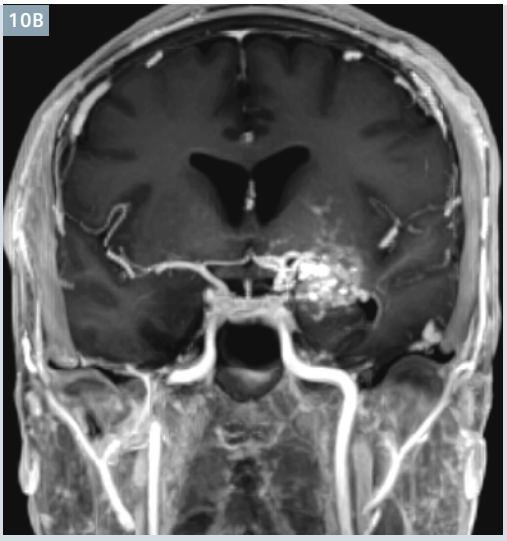

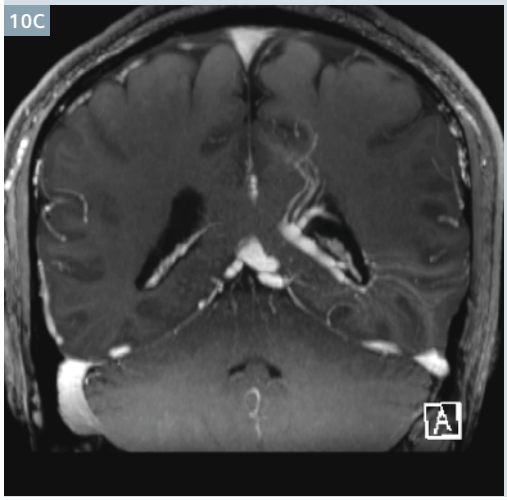

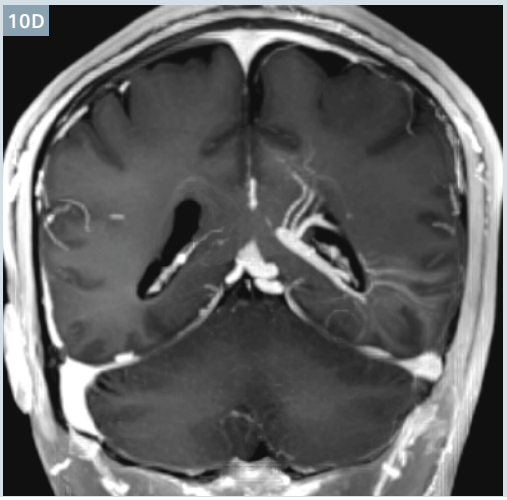

10

Contrast-enhanced images of combined cavernous malformation and developmental venous anomaly in a 47-year-old female patient.
(10A) CE 3D-FLASH with a voxel size of 0.6 × 0.6 × 1.0 mm^3.
(10B) CE PETRA (TI 700 ms) with a voxel size of (0.99 $mm)^3$.
Flow voids are absent due to the ultra-short TE causing the venous malformation to appear more prominently.
Developmental venous malformation was apparent in the same patient, again appearing more prominently on PETRA due to the ultra-short TE and lack of flow voids.
(10C) CE 3D-FLASH.
(10D) CE PETRA.

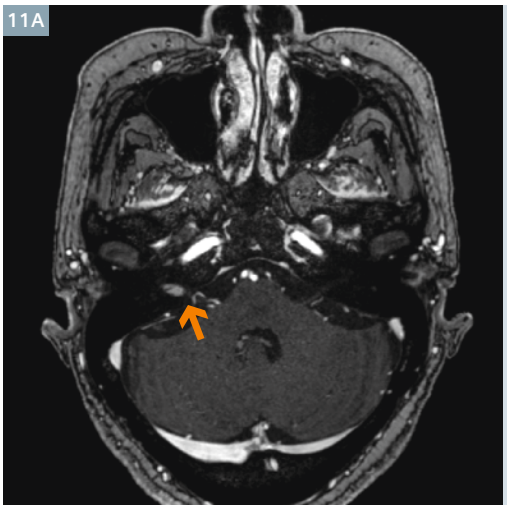

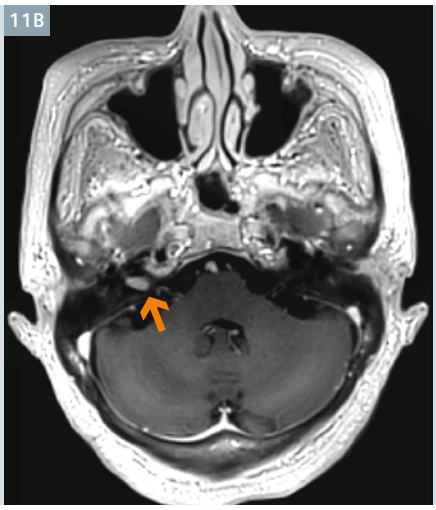

11

Contrast-enhanced images of small vestibular schwannoma (arrows) localized in the right acoustic canal of a 67-year-old female patient.
(11A) CE 3D-FLASH with a voxel size of 0.6 × 0.6 × 1.0 mm^3.
(11B) CE PETRA (TI 900 ms) with a voxel size of (0.80 $mm)^3$.

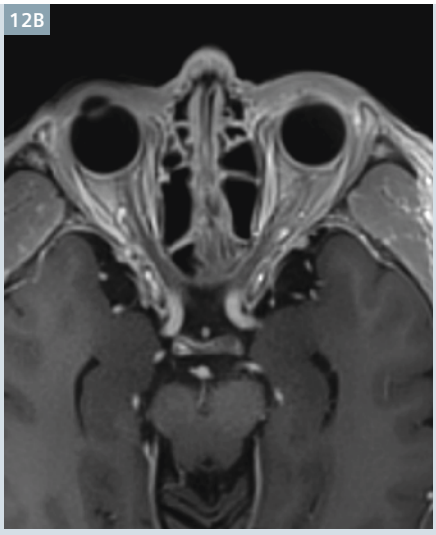

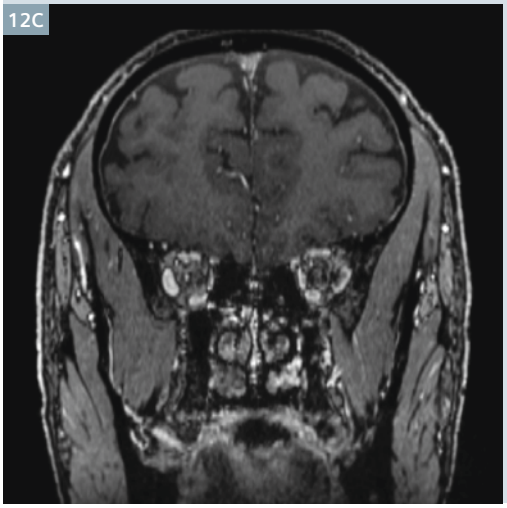

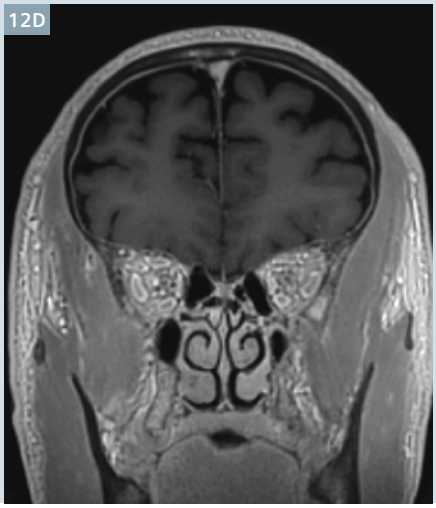

12

Normal optic nerves and paranasal sinuses in a 74-year-old male patient.
(12A) 3D-FLASH with a voxel size of 0.6 × 0.6 × 1.0 mm^3.
(12B) PETRA (TI 900 ms) with a voxel size of (0.80 $mm)^3$.
The septi of the paranasal sinuses are depicted clearly in the ethmoid sinuses due to the absence of susceptibility-induced artifacts.

Normal paranasal sinuses in the same patient.
(12C) 3D-FLASH.
(12D) PETRA. Notice the absence of susceptibility-induced artifacts in the paranasal sinus.

Conclusion

The acoustic noise (A-weighted) generated by PETRA was drastically lower than that of MPRAGE, while contrast-enhancement and image quality were similar between the two sequences, and clinical findings did not differ, as shown in several examples. In comparisons of PETRA with 3D-FLASH, although the latter provided a higher spatial resolution, again clinical findings did not differ. Quieter MRI examinations will be more comfortable for all patients, and may have particular advantages for pediatric, dementia and certain psychiatric patients.

References

1 Grodzki DM, Heismann B. Quiet T1-weighted head scanning using PETRA. Proc ISMRM 2013; 21:0456.
2 Weiger M, Pruessmann KP, Hennel F. MRI with zero echo time: hard versus sweep pulse excitation. Magn Reson Med 2011; 66(2):379-89.
3 Idiyatullin D, Corum C, Park JY, Garwood M. Fast and quiet MRI using a swept radio-frequency. J Magn Reson 2006; 181(2): 342-349.
4 Grodzki DM, Jakob PM, Heismann B. Ultrashort echo time imaging using pointwise encoding time reduction with radial acquisition (PETRA). Magn Reson Med 2012; 67(2):510-508.
5 Chamberlain R, Moeller S, Corum C, Idiyatullin C, Garwood M. Quiet T1- and T2-weighted brain imaging using SWIFT. Proc ISMRM 2011; 19:2723.
6 Mugler JP, Brookeman JR. Three-dimensional magnetization-prepared rapid gradient-echo imaging (3D MP RAGE). Magn Reson Med 1990; 15:152-157.
7 Brant-Zawadzki M, Gillan GD, Nitz WR. MP RAGE: a three-dimensional, T1-weighted, gradient-echo sequence-initial experience in the brain. Radiology 1992; 182:769-75.
8 Brant-Zawadzki MN, Gillan GD, Atkinson DJ, Edalatpour N, Jensen M. Three-dimensional MR imaging and display of intracranial disease: improvements with the MP-RAGE sequence and gadolinium. J Magn Reson Imaging. 1993; 3(4): 656-62.
9 Yuh WT, Tali ET, Nguyen HD, Simonson TM, Mayr NA, Fisher DJ. The effect of contrast dose, imaging time, and lesion size in the MR detection of intracerebral metastasis. AJNR 1995; 16:373-380.

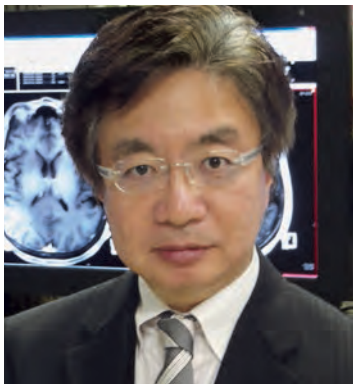

Contact

Masahiro Ida, M.D.
Chief Radiologist
Dept. of Radiology
Tokyo Metropolitan Ebara Hospital
4-5-10 Higashi-yukigaya, Ota-ku
Tokyo 145-0065
Japan
Phone: +81 3-5734-8000
rxb00500@nifty.com

Quiet Suite

Imaging is to be seen, not heard.

Answers for life.

Acute MR Stroke Protocol in Six Minutes

Kambiz Nael; Rihan Khan; Kevin Johnson; Diego Martin

University of Arizona, Department of Medical Imaging, Tucson, AZ, USA

Background

Stroke is a common and serious disorder, with an annual incidence of approximately 795,000. Based on American Heart Association statistics update in 2010, approximately 610,000 of these are first attacks, and 185,000 are recurrent attacks. On average, every 40 seconds, someone in the United States has a stroke with an estimated mortality rate of 5.5%, claiming approximately 1 of every 18 deaths in the United States [1].

Neuroimaging plays a central role in the evaluation of patients with acute ischemic stroke (AIS). With improved technology over the last decade, imaging now provides information beyond the mere presence or absence of intra-

92-year-old man with sudden onset of right-sided weakness and aphasia presented to our emergency department after receiving IV-tPA at an outside institution. The acute stroke protocol was performed after 9 hours from the onset in our institution and selective images are shown.

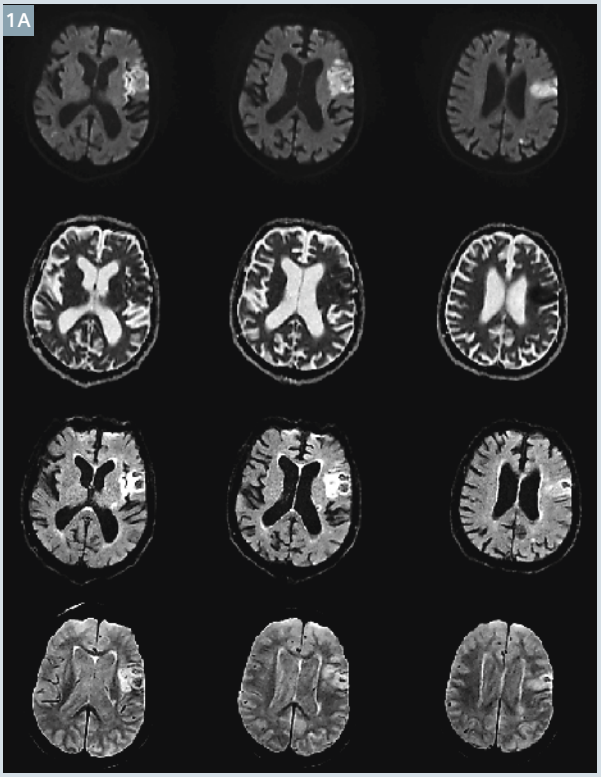

1A Serial aligned DWI, ADC, EPI-FLAIR and EPI-GRE images are shown. There is acute infarction of the left MCA distribution involving the left operculum and insula. Small focus of hemorrhagic conversion is present within the area of infarction seen on both EPI-FLAIR and EPI-GRE images.

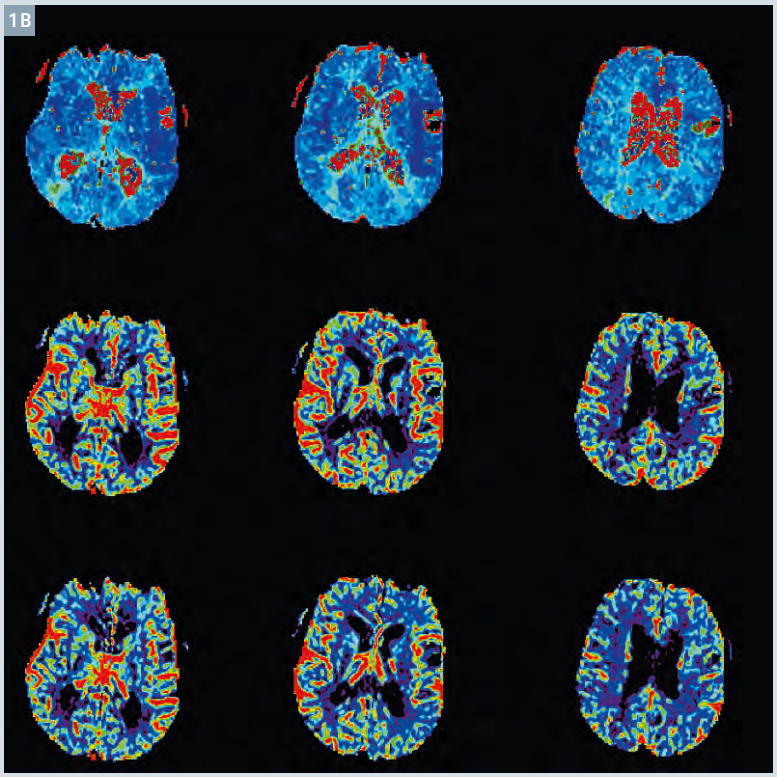

1B Aligned DSC-Tmax, DSC-CBF and DSC-CBV images are shown. DSC maps show a heterogeneous pattern of perfusion deficit containing a small perfusion defect in the region of hemorrhage and predominant luxury perfusion along the left MCA territory seen on Tmax and CBF maps.

cranial hemorrhage including tissue viability, site of occlusion, and collateral status. While computed tomography (CT) is the most widely available and faster imaging modality, some comprehensive stroke centers favor streamlined MR protocols over CT in the acute stroke setting due to the higher specificity and superior tissue characterization afforded by MRI. The success of CT in initial evaluation of AIS is due, in part, to fast acquisition time, widespread availability and ease of interpretation in the emergency setting. The introduction of multi-slice technology has dramatically increased the speed and simplicity of CT techniques and has set a high standard for alternative imaging techniques. A comprehensive CT stroke algorithm including parenchymal imaging (non-contrast head CT), CT angiography (CTA), and perfusion/penumbral imaging by CT perfusion can now be acquired and processed in less than 10 minutes [5, 6].

MRI has been demonstrated to be more sensitive for the detection of acute ischemia and more specific for delineation of infarction core volume when compared to CT [7, 8]. However, due to longer acquisition time and limited availability; it has been mainly used in large institutions and comprehensive stroke centers. A comprehensive MR protocol including parenchymal imaging, MRA and MR perfusion can now be obtained in the order of 20 minutes as demonstrated in several clinical trials [9–13]. If MRI is to compete with CT for evaluation of acute stroke, there is need for further improvements in acquisition speed.

In this article we describe our modified acute stroke MRI protocol that can be obtained in approximately 6 minutes rivaling that of any comprehensive acute stroke CT protocol. We describe the technical aspects and review a few clinical examples based on our preliminary results.

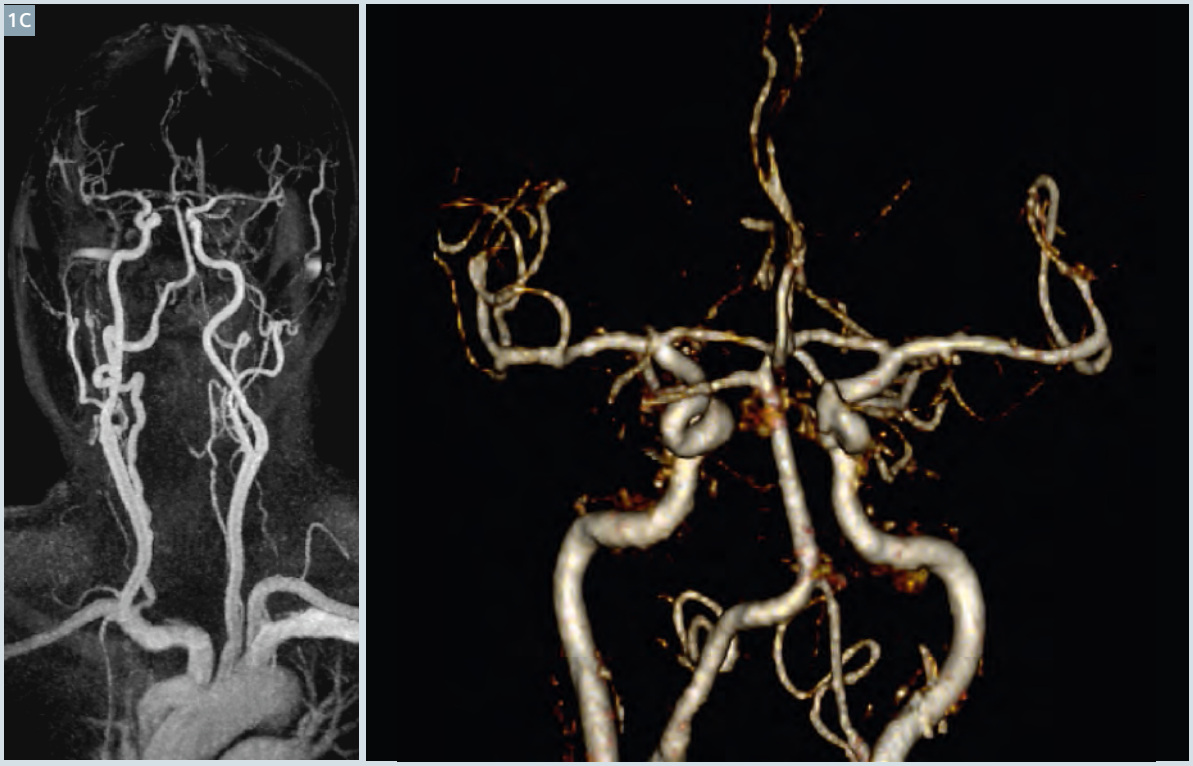

1C Coronal MIP from CE-MRA of the entire supra-aortic arteries and cropped volume-rendered reconstruction of the intracranial arteries show no evidence of hemodynamic significant arterial stenosis nor occlusion involving the proximal arteries. Note the high diagnostic image quality of the CE-MRA images which are obtained after administration of 8 ml of contrast.

Technical consideration

A comprehensive MR stroke protocol has three essential components:

1) Parenchymal imaging that identifies the presence and size of an irreversible infarcted core and determines the presence of hemorrhage;
2) MR angiogram to determine the presence of proximal arterial occlusion and/or intravascular thrombus that can be treated with thrombolysis or thrombectomy;
3) Pwerfusion imaging to determine the presence of hypoperfused tissue at risk for subsequent infarction if adequate perfusion is not restored.

Below we describe each of these components in detail and explain how recent technical advances can be used to enhance the performance of the different aspects of acute stroke imaging.

1. Parenchymal imaging
This encompasses three parts:

1) DWI (diffusion-weighted imaging) that can detect ischemic tissue within minutes of its occurrence and has emerged as the most sensitive and specific imaging technique for acute ischemia, far beyond NECT or any other type of MRI sequences [14].
2) FLAIR that helps to age the infarction and permits the detection of subtle subarachnoid hemorrhage;
3) GRE to detect parenchymal hemorrhage with comparable accuracy for the acute intraparenchymal hemorrhage to CT [15].

Both FLAIR and GRE images have been used to detect intraarterial clot with variable sensitivity and specificity [16, 17].

Introduction of fast imaging techniques such as parallel acquisition [18] and EPI [19, 20] has significantly enhanced the performance of MR imaging in terms of acquisition speed. The main advantage of EPI, as in the case of DWI imaging, is rapid acquisition time, which is made possible by rapid gradient switching which permits the acquisition of all frequency and phase encoding steps during a single pulse cycle. The addition of parallel imaging can further enhance the acquisition speed and may also serve to mitigate the geometric distortion and susceptibility artifacts commonly

68-year-old man with left sided weakness and altered level of consciousness of unknown onset.

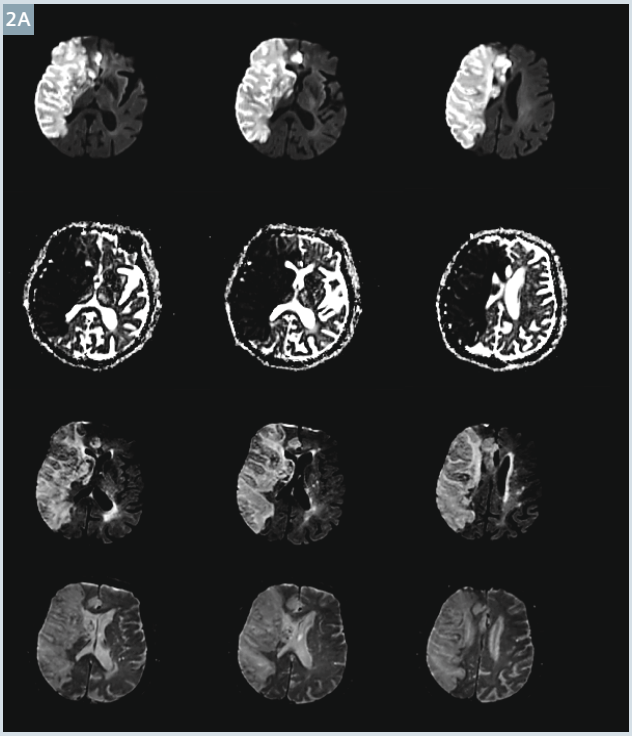

2A Serial aligned DWI, ADC, EPI-FLAIR and EPI-GRE images are shown. There is acute right hemispheric infarction involving both the ACA and MCA territories. The EPI-FLAIR images demonstrate corresponding hyperintensity suggestive of completed infarction. There is associated mass effect. No hemorrhage is identified on corresponding EPI-GRE images.

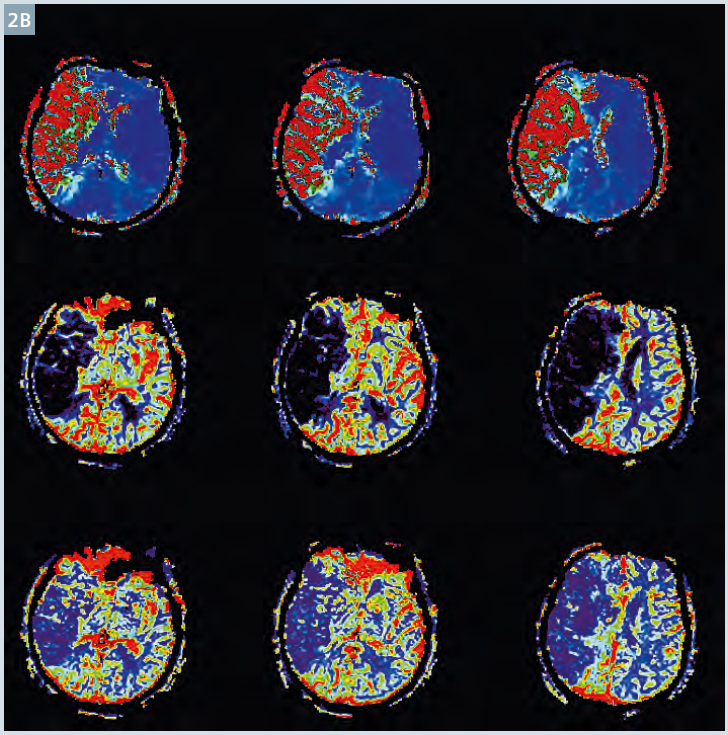

2B Aligned DSC-Tmax, DSC-CBF and DSC-CBV images are shown. There is a matched perfusion defect with the region of infarction.

associated with long echo-train sequences such as EPI [21, 22]. If their potential is realized, the application of EPI and parallel imaging techniques to the FLAIR and GRE sequences can result in reduction of image acquisition time of the entire brain to less than a minute, a three-fold reduction in scan time over conventional imaging [23, 24].

2. MR Angiogram

An important aspect of the workup of patients with AIS is the imaging of both the intracranial and extracranial vasculature. Precise imaging of the vascular tree is required during the initial assessment of patients with acute stroke to accurately detect the site of arterial disease, which in turn can be crucial in determining the type of acute therapy they are given. Intravenous thrombolysis has been shown to be more effective in small distal vessels than in the large vessels [25]. Larger vessel occlusion may be more effectively treated with intra-arterial thrombolysis or clot retrieval devices while associated with fewer complications [26, 27]. In addition, MRA of the extracranial circulation (neck arteries) is essential to establish the mechanism of ischemia and to prevent subsequent episodes. Extracranial tandem stenoses with plaque involving the carotid or vertebral arteries can be the source of disease that triggers an acute stroke.

Time-of-flight MRA (TOF-MRA) has been traditionally used in routine stroke protocols to evaluate the status of neck and brain arteries. Despite its promising results [28], TOF-MRA has significant disadvantages including spin saturation and phase dispersion due to slow or turbulent flow [29, 30]. This can result in overestimation of arterial stenosis and increase false positive rates, usually due to slow flow distal to a subocclusive thrombus or clot. Most importantly the acquisition time usually is long, typically lasting 5–7 minutes.

The general consensus is that contrast-enhanced MR angiography (CE-MRA) provides more accurate imaging of extracranial vessel morphology and of the degree of stenosis than TOF-MRA techniques [31–33]. However, CE-MRA has not been widely incorporated into acute stroke protocols for several reasons. First, CE-MRA has lower spatial resolution relative to TOF-MRA, since the competing requirements of coverage and acquisition speed generally force a compromise in spatial resolution for CE-MRA [34]. A second potential limitation to incorporation of CE-MRA into clinical stroke protocols is related to the requirement of an extra contrast dose, which would be in addition to the intravenous contrast bolus normally utilized for perfusion imaging. With introduction of high performance MR scanners and recent advances in fast imaging tools such as parallel acquisition (GRAPPA) [18], high matrices can now be spread out over a large field-of-view encompassing the entire head and neck, resulting in acquisitions with submillimeter voxel sizes and acquisition times on the order of 20 seconds [35, 36].

3. MR Perfusion

MR perfusion imaging has been used broadly in the identification of potentially salvageable tissue to determine the best treatment strategy in patients with acute ischemic stroke. Although the concept of perfusion-diffusion mismatch remains controversial [37, 38], it has been used with some success to identify patients who may respond favorably to revascularization therapies in several clinical trials [12, 13, 39].

Faster image acquisition combined with higher signal-to-noise ratio (SNR) resulting from the use of gadolinium contrast agents has helped dynamic susceptibility contrast (DSC) perfusion become a more robust and widely accepted technique in comparison to arterial spin labeling (ASL) to identify the presence of perfusion abnormalities in patients with AIS.

A refined MR stroke protocol that can combine both CE-MRA and DSC-perfusion with improved acquisition time and diagnostic image quality as previously suggested [47, 48] may have important therapeutic and prognostic implications in the management of patients with acute stroke. Higher inherent SNR of higher magnetic fields such as 3T with improved multi-coil technology has resulted in acquisition of low dose CE-MRA of the supra-aortic arteries with contrast dose as low as 8 ml [40, 41]. A modified 2-phase contrast injection scheme [46] can be used to perform both CE-MRA and DSC perfusion imaging, without the need for additional contrast. The influence of contrast dose reduction on DSC perfusion has been evaluated by several investigators [42, 43] and contrast dose as low as 0.05 mmol/kg has been used to perform DSC perfusion with promising results [44, 45].

Advances in MR technology including hardware and software, faster gradient performance of MR scanners, improved sequence design and fast imaging tools such as EPI and parallel

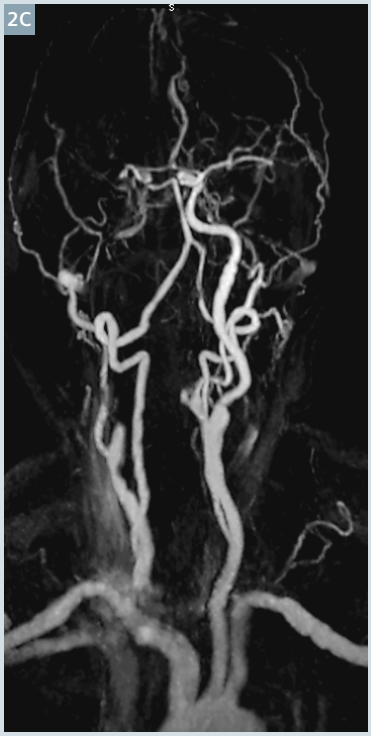

2C Coronal MIP from CE-MRA of the entire supra-aortic arteries shows complete occlusion of the right cervical ICA shortly after the origin. There is some reconstitution of flow signal at the supracliniod ICA likely via collaterals.

acquisition have promised the potential for a fast but comprehensive MR stroke protocol that can be performed in approximately 6 minutes rivaling those of CT protocols. Next we review our stroke protocol in terms of image acquisition and sequence parameters and show some of the clinical examples that were performed at our institution.

How we do it

At our institution, absent contraindication, MR is the default imaging modality for AIS. An MR safety questionnaire is administered, and MR compatible ECG leads are placed in the emergency department as patients are being evaluated by the neurology team. Patients are then placed onto an MR compatible table and wheeled to the MR magnet for rapid imaging.

We use both 3T and 1.5T MR scanners (MAGNETOM Skyra and MAGNETOM Aera, Siemens Healthcare, Erlangen, Germany), with 3T the default scanner for acute stroke imaging when available. For signal reception, a combination of a 16-element array coil [head (n = 12), neck (n = 4)] will be used. The coil design allows for application of parallel acquisition in both the phase and slice encoding directions. Our 6-minute MR imaging protocol consist of DWI, EPI-FLAIR, EPI-GRE, CE-MRA and DSC perfusion. The clinical indications for using this acute MR stroke protocol are patients with acute (< 9 hours) presentation from the onset of symptoms, unknown onset of symptoms, NIHSS > 4, or aphasia. Table 1 shows the sequence parameters of our acquisition protocol.

A modified 2-phase contrast injection scheme [46] is used to perform both CE-MRA and DSC perfusion imaging, without the need for additional contrast. To accomplish this, the total volume of 20 ml of gadolinium (Multihance, Bracco Diagnostics Inc., Princeton, NJ, USA) that is used routinely for MR perfusion is diluted with normal saline to a total 50 ml volume. Using a timing bolus, a total of 3 ml of contrast solution (1.2 ml of gadolinium) is injected at 1.5 ml/s to determine the transit time from the arm vein to the cervical carotid arteries. Then, a total of 22 ml contrast solution (8.8 ml of gadolinium) is injected at the same flow rate as the timing injection for the CE-MRA acquisition. A centric ordering *k*-space is used for CE-MRA to minimize intracranial venous contamination. Subsequently, the remaining 25 ml of contrast solution (10 ml of gadolinium) is injected at 5 ml/s for the MR perfusion scan which is performed at the end.

Image analysis

Following data acquisition, CE-MRA image processing is performed on the scanner console with standard commercial software using a maximum intensity projection (MIP) algorithm. All of the reconstructed data, as well as the source images are available on the workstation for image analysis. Perfusion analysis will be performed off-line on a dedicated FDA-approved workstation (Olea-sphere, Olea Medical SA, France). The arterial input function is selected automatically and multiparametric perfusion maps including time-to-peak (TTP), time-to-maximum (Tmax) cerebral blood flow (CBF) and cerebral blood volume (CBV) are then calculated using a block-circulant singular value decomposition technique [49].

Our initial results using the described stroke MR protocol have been promising. We have scanned more than 600 patients with ASI since January 2013. More than 97% of our studies have been rated with diagnostic image quality. The EPI-FLAIR sequence has been used in parallel to conventional FLAIR in a subset of patients with comparable qualitative and quantitative results [24]. In a study of 52 patients with AIS, the mean ± SD of the signal intensity ratios on EPI-FLAIR and FLAIR for DWI positive lesions were 1.28 ± 0.16 and 1.25 ± 0.17 respectively with sig-

Table 1: Imaging protocol

	DWI	EPI-FLAIR	EPI-GRE	CE-MRA	DSC
TR (ms)	4600	10000 (TI:2500)	1860	3.36	1450
TE	65	88	48	1.24	22
FA (degrees)	–	90	90	25	90
Matrix	160	192	192	448	128
FOV	220	220	220	340	220
Slices (n × thickness)	30 × 4	30 × 4	40 × 3	120 × 0.8	30 × 4
Bandwidth (Hz/pixel)	1250	1488	964	590	1502
Parallel acquisition (GRAPPA)	3	3	–	3	3
Acquisition time	58 sec	52 sec	56 sec	20 sec	1 min and 30 sec

nificant correlation (r = 0.899, z value = 8.677, p < 0.0001). The EPI-GRE sequence has been also used in parallel to conventional GRE in a subset of patients with comparable results in terms of detection of hemorrhage (Fig. 1) and blood clot in proximal arteries.

The combination of CE-MRA and DSC has been successfully tested in our institution [48] with diagnostic image quality. In a cohort of 30 patients with acute stroke, the specificity of CE-MRA for detection of arterial stenosis > 50% was 97% compared to 89% for TOF-MRA when compared to DSA as the standard of reference [48]. DSC perfusion imaging with reduced contrast dose is feasible with comparable quantitative and qualitative results to a full-dose control group [48]. Importantly, the presence of contrast in the circulating blood of the CE-MRA half-dose group does not negatively impact the image quality nor the quantitative analysis of perfusion data when compared to the control full-dose group.

Conclusion

Described multimodal MR protocol is feasible for evaluation of patients with acute ischemic stroke with total acquisition time of 6 minutes rivaling that of the multimodal CT protocol.

References

1 Lloyd-Jones D, Adams RJ, Brown TM, et al. Heart disease and stroke statistics – 2010 update: a report from the American Heart Association. *Circulation*. Feb 23 2010;121(7):e46-e215.

2 Saver JL. Time is brain-quantified. *Stroke*. Jan 2006;37(1):263-266.

3 Michel P, Bogousslavsky J. Penumbra is brain: no excuse not to perfuse. *Ann Neurol*. Nov 2005;58(5):661-663.

4 Gonzalez RG. Imaging-guided acute ischemic stroke therapy: From "time is brain" to "physiology is brain". *AJNR. American journal of neuroradiology*. Apr 2006;27(4):728-735.

5 Zhu G, Michel P, Aghaebrahim A, et al. Computed tomography workup of patients suspected of acute ischemic stroke: perfusion computed tomography adds value compared with clinical evaluation, noncontrast computed tomography, and computed tomography angiogram in terms of predicting outcome. *Stroke; a journal of cerebral circulation*. Apr 2013;44(4):1049-1055.

6 Schaefer PW, Roccatagliata L, Ledezma C, et al. First-pass quantitative CT perfusion identifies thresholds for salvageable penumbra in acute stroke patients treated with intra-arterial therapy. *AJNR. American journal of neuroradiology*. Jan 2006;27(1):20-25.

7 Jauch EC, Saver JL, Adams HP, Jr., et al. Guidelines for the early management of patients with acute ischemic stroke: a guideline for healthcare professionals from the American Heart Association/ American Stroke Association. *Stroke*. Mar 2013;44(3):870-947.

8 Chalela JA, Kidwell CS, Nentwich LM, et al. Magnetic resonance imaging and computed tomography in emergency assessment of patients with suspected acute stroke: a prospective comparison. *Lancet*. Jan 27 2007;369(9558):293-298.

9 Kang DW, Chalela JA, Dunn W, Warach S, Investigators NI-SSC. MRI screening before standard tissue plasminogen activator therapy is feasible and safe. *Stroke*. Sep 2005;36(9):1939-1943.

10 Hjort N, Butcher K, Davis SM, et al. Magnetic resonance imaging criteria for thrombolysis in acute cerebral infarct. *Stroke*. Feb 2005;36(2):388-397.

11 Schellinger PD, Jansen O, Fiebach JB, Hacke W, Sartor K. A standardized MRI stroke protocol: comparison with CT in hyperacute intracerebral hemorrhage. *Stroke; a journal of cerebral circulation*. Apr 1999;30(4):765-768.

12 Albers GW, Thijs VN, Wechsler L, et al. Magnetic resonance imaging profiles predict clinical response to early reperfusion: the diffusion and perfusion imaging evaluation for understanding stroke evolution (DEFUSE) study. *Ann Neurol*. Nov 2006;60(5):508-517.

13 Davis SM, Donnan GA, Parsons MW, et al. Effects of alteplase beyond 3 h after stroke in the Echoplanar Imaging Thrombolytic Evaluation Trial (EPITHET): a placebo-controlled randomised trial. *Lancet neurology*. Apr 2008;7(4): 299-309.

14 Fiebach JB, Schellinger PD, Jansen O, et al. CT and diffusion-weighted MR imaging in randomized order: diffusion-weighted imaging results in higher accuracy and lower interrater variability in the diagnosis of hyperacute ischemic stroke. *Stroke; a journal of cerebral circulation*. Sep 2002;33(9):2206-2210.

15 Kidwell CS, Chalela JA, Saver JL, et al. Comparison of MRI and CT for detection of acute intracerebral hemorrhage. *JAMA : the journal of the American Medical Association*. Oct 20 2004;292(15):1823-1830.

16 Flacke S, Urbach H, Keller E, et al. Middle cerebral artery (MCA) susceptibility sign at susceptibility-based perfusion MR imaging: clinical importance and comparison with hyperdense MCA sign at CT. *Radiology*. May 2000;215(2):476-482.

17 Assouline E, Benziane K, Reizine D, et al. Intra-arterial thrombus visualized on T2* gradient echo imaging in acute ischemic stroke. *Cerebrovasc Dis*. 2005;20(1):6-11.

18 Griswold MA, Jakob PM, Heidemann RM, et al. Generalized autocalibrating partially parallel acquisitions (GRAPPA). *Magnetic resonance in medicine : official journal of the Society of Magnetic Resonance in Medicine / Society of Magnetic Resonance in Medicine*. Jun 2002;47(6):1202-1210.

19 Mansfield P. Real-time echo-planar imaging by NMR. *Br Med Bull*. Apr 1984;40(2): 187-190.

20 DeLaPaz RL. Echo-planar imaging. *Radiographics*. Sep 1994;14(5):1045-1058.

21 Pruessmann KP. Parallel imaging at high field strength: synergies and joint potential. T*opics in magnetic resonance imaging : TMRI*. Aug 2004;15(4):237-244.

22 Wiesinger F, Van de Moortele PF, Adriany G, De Zanche N, Ugurbil K, Pruessmann KP. Potential and feasibility of parallel MRI at high field. *NMR in biomedicine*. May 2006;19(3):368-378.

23 Kinoshita T, Okudera T, Tamura H, Ogawa T, Hatazawa J. Assessment of lacunar hemorrhage associated with hypertensive stroke by echo-planar gradient-echo T2*-weighted MRI. *Stroke*. Jul 2000;31(7): 1646-1650.

24 Meshksar A, Khan R, Carmody R, Nael K. The Role of Echo-planar Fluid-Attenuated Inversion Recovery (EPI-FLAIR) in Acute Stroke Setting: A Feasibility Study. Paper presented at: ASNR; May 22, 2013, 2013; San Diego, CA.

25 del Zoppo GJ, Poeck K, Pessin MS, et al. Recombinant tissue plasminogen activator in acute thrombotic and embolic stroke. *Ann Neurol*. Jul 1992;32(1):78-86.

26 Furlan A, Higashida R, Wechsler L, et al. Intra-arterial prourokinase for acute ischemic stroke. The PROACT II study: a randomized controlled trial. Prolyse in Acute Cerebral Thromboembolism. *JAMA : the journal of the American Medical Association*. Dec 1 1999;282(21): 2003-2011.

27 Becker KJ, Brott TG. Approval of the MERCI clot retriever: a critical view. *Stroke; a journal of cerebral circulation.* Feb 2005; 36(2):400-403.

28 Yucel EK, Anderson CM, Edelman RR, et al. AHA scientific statement. Magnetic resonance angiography : update on applications for extracranial arteries. *Circulation.* Nov 30 1999;100(22):2284-2301.

29 Isoda H, Takehara Y, Isogai S, et al. MRA of intracranial aneurysm models: a comparison of contrast-enhanced three-dimensional MRA with time-of-flight MRA. *J Comput Assist Tomogr.* Mar-Apr 2000; 24(2):308-315.

30 Lin W, Tkach JA, Haacke EM, Masaryk TJ. Intracranial MR angiography: application of magnetization transfer contrast and fat saturation to short gradient-echo, velocity-compensated sequences. *Radiology.* Mar 1993;186(3):753-761.

31 Somford DM, Nederkoorn PJ, Rutgers DR, Kappelle LJ, Mali WP, van der Grond J. Proximal and distal hyperattenuating middle cerebral artery signs at CT: different prognostic implications. *Radiology.* Jun 2002;223(3):667-671.

32 Cosottini M, Pingitore A, Puglioli M, et al. Contrast-enhanced three-dimensional magnetic resonance angiography of atherosclerotic internal carotid stenosis as the noninvasive imaging modality in revascularization decision making. *Stroke; a journal of cerebral circulation.* Mar 2003; 34(3):660-664.

33 Huston J, 3rd, Fain SB, Wald JT, et al. Carotid artery: elliptic centric contrast-enhanced MR angiography compared with conventional angiography. *Radiology.* Jan 2001;218(1):138-143.

34 Fellner C, Lang W, Janka R, Wutke R, Bautz W, Fellner FA. Magnetic resonance angiography of the carotid arteries using three different techniques: accuracy compared with intraarterial x-ray angiography and endarterectomy specimens. *Journal of magnetic resonance imaging : JMRI.* Apr 2005;21(4):424-431.

35 Nael K, Villablanca JP, Pope WB, McNamara TO, Laub G, Finn JP. Supraaortic arteries: contrast-enhanced MR angiography at 3.0 T-highly accelerated parallel acquisition for improved spatial resolution over an extended field of view. *Radiology.* Feb 2007;242(2):600-609.

36 Phan T, Huston J, 3rd, Bernstein MA, Riederer SJ, Brown RD, Jr. Contrast-enhanced magnetic resonance angiography of the cervical vessels: experience with 422 patients. *Stroke; a journal of cerebral circulation.* Oct 2001;32(10): 2282-2286.

37 Hacke W, Furlan AJ, Al-Rawi Y, et al. Intravenous desmoteplase in patients with acute ischaemic stroke selected by MRI perfusion-diffusion weighted imaging or perfusion CT (DIAS-2): a prospective, randomised, double-blind, placebo-controlled study. *Lancet neurology.* Feb 2009;8(2):141-150.

38 Kidwell CS, Jahan R, Gornbein J, et al. A trial of imaging selection and endovascular treatment for ischemic stroke. *The New England journal of medicine.* Mar 7 2013;368(10):914-923.

39 Lansberg MG, Straka M, Kemp S, et al. MRI profile and response to endovascular reperfusion after stroke (DEFUSE 2): a prospective cohort study. *Lancet neurology.* Oct 2012;11(10):860-867.

40 Tomasian A, Salamon N, Lohan DG, Jalili M, Villablanca JP, Finn JP. Supra-aortic arteries: contrast material dose reduction at 3.0-T high-spatial-resolution MR angiography--feasibility study. *Radiology.* Dec 2008;249(3):980-990.

41 Nael K, Moriarty JM, Finn JP. Low dose CE-MRA. *Eur J Radiol.* Oct 2011;80(1): 2-8.

42 Heiland S, Reith W, Forsting M, Sartor K. How do concentration and dosage of the contrast agent affect the signal change in perfusion-weighted magnetic resonance imaging? A computer simulation. *Magnetic resonance imaging.* Jul 2001;19(6):813-820.

43 Alger JR, Schaewe TJ, Lai TC, et al. Contrast agent dose effects in cerebral dynamic susceptibility contrast magnetic resonance perfusion imaging. *Journal of magnetic resonance imaging: JMRI.* Jan 2009;29(1):52-64.

44 Manka C, Traber F, Gieseke J, Schild HH, Kuhl CK. Three-dimensional dynamic susceptibility-weighted perfusion MR imaging at 3.0 T: feasibility and contrast agent dose. *Radiology.* Mar 2005; 234(3):869-877.

45 Alger JR, Schaewe TJ, Liebeskind DS, Saver JL, Kidwell CS. On the feasibility of reduced dose Dynamic Susceptibility Contrast perfusion MRI for stroke. Paper presented at: Intl. Soc. Mag. Reson. Med; 7-13 May 2011, 2011; Montréal, Québec, Canada.

46 Habibi R, Krishnam MS, Lohan DG, et al. High-spatial-resolution lower extremity MR angiography at 3.0 T: contrast agent dose comparison study. *Radiology.* Aug 2008;248(2):680-692.

47 Ryu CW, Lee DH, Kim HS, et al. Acquisition of MR perfusion images and contrast-enhanced MR angiography in acute ischaemic stroke patients: which procedure should be done first? *The British journal of radiology.* Dec 2006; 79(948):962-967.

48 Nael K, Pirastehfar M, Villablanca JP, Salamon N. Addition of a Low-dose Contrast Enhanced MRA at 3.0T in the Assessment of Acute Stroke: A More Efficient and Accurate Stroke Protocol. Paper presented at: ASNR 50th Annual Meeting; April, 2012; New York, NY.

49 Wu O, Ostergaard L, Weisskoff RM, Benner T, Rosen BR, Sorensen AG. Tracer arrival timing-insensitive technique for estimating flow in MR perfusion-weighted imaging using singular value decomposition with a block-circulant deconvolution matrix. *Magnetic resonance in medicine : official journal of the Society of Magnetic Resonance in Medicine / Society of Magnetic Resonance in Medicine.* Jul 2003;50(1):164-174.

Contact

Kambiz Nael, M.D.
Assistant Professor of Radiology
Director of Neuroradiology MRI
University of Arizona
Medical Center
Department of Medical Imaging,
Neuroradiology Section
1501 N. Campbell,
PO Box 245067
Tucson, AZ 85724-5067
USA
Phone: +1 520-626-2138
Fax: +1 520-626-7093
kambiz@radiology.arizona.edu

TOGETHER WE MOVE FORWARD IN THE FIGHT AGAINST CANCER

When two leading companies join forces in the fight against cancer, it broadens the realm of what's possible. That's why Varian and Siemens have partnered. Siemens' advanced diagnostic imaging capabilities coupled with Varian's powerful delivery systems and treatment planning tools give even more of an edge in the pursuit of our common goal: to **EnVision better cancer care**. Together we offer more personalized treatment and expanded care options that aid you in making the best possible decisions for your patients—with confidence. By gathering our strengths, we have the energy and vision to better help healthcare professionals detect, diagnose and treat cancer while paving the way for the future of cancer care.

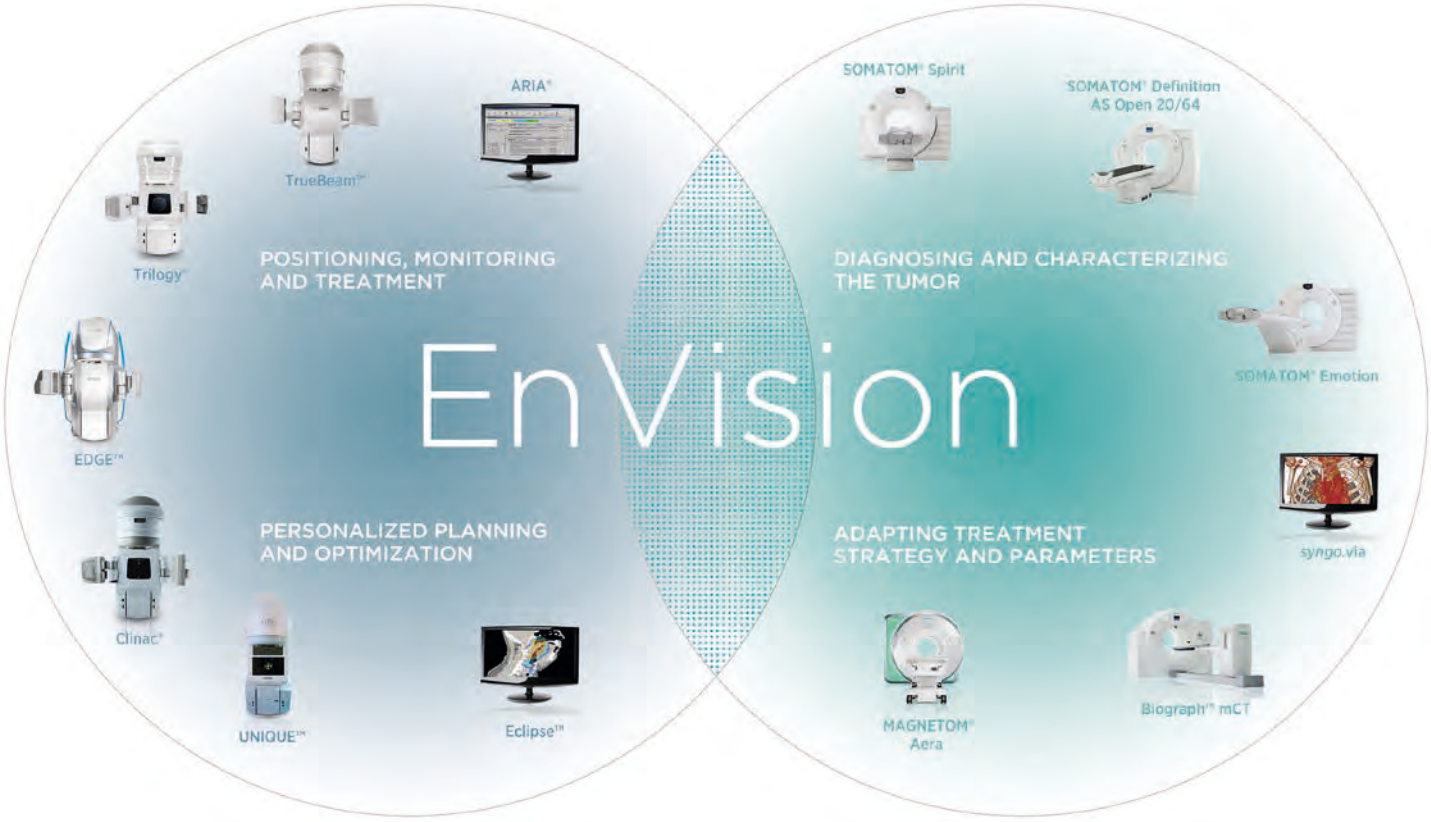

VARIAN
medical systems

SIEMENS
Strategic Partner of Varian for Radiation Therapy

© 2013 Varian, Varian Medical Systems, Trilogy, and ARIA are registered trademarks, and TrueBeam, Edge Radiosurgery and Eclipse are trademarks of Varian Medical Systems, Inc. All other trademarks are property of Siemens AG.

Varian Medical Systems
International AG
Zug, Switzerland
Tel: +41 - 41 749 88 44
Fax: +41 - 41 740 33 40
varian.com
info.europe@varian.com

Global Siemens Healthcare Headquarters
Siemens AG
Healthcare Sector
Henkestrasse 127
91052 Erlangen, Germany
Tel: +49 9131 84-0
siemens.com/healthcare

Find out more at **varian.com/envision**

Susceptibility-Weighted Imaging. Initial Experience

José Luis Ascencio L.[1]; Tania Isabel Ruiz Z.[2]

[1] Escanografia Neurologica, Medellin, Colombia
[2] Universidad CES, Radiology, Medellín, Antioquia, Colombia

Introduction

Susceptibility-weighted imaging (SWI) is a sequence that utilizes a phenomenon in which the phase and change in the local magnetic field of the tissues are proportional to one another, provided the echo time is constant [1]. It uses magnitude and phase images, as well as a summation of these in a three-dimensional gradient echo sequence with flow compensation [2]. It offers very high sensitivity for visualizing calcium, non-heme iron (ferritin) and hemoglobin degradation products (deoxyhemoglobin and hemosiderin) [3, 4].

Initial experience

By means of a series of cases we will illustrate the clinical usefulness of SWI with certain neurological conditions. The studies reviewed were performed in the Neurological Scanography Magnetic Resonance Imaging Service using a Siemens MAGNETOM ESSENZA 1.5 Tesla MRI unit with the following settings: TR 49 ms, TE 40 ms, FA 15°, number of slices 60, slice thickness 2 mm, acquisition matrix 256 ×157.

Susceptibility-weighted imaging takes advantage of the loss of signal intensity created by alterations in a homogenous magnetic field; these disturbances can be caused by several different paramagnetic or diamagnetic substances. The loss of signal intensity in the T2*-weighted sequence is a result of the difference in the precession rate of the spins [5].

The susceptibility image is obtained during the acquisition process by combining the magnitude and phase of the images. Routine MR images are magnitude images where the signal's intensity is converted to a gray scale. Phase information is obtained at the same time, but is generally ignored. A filter is applied to the phase image (High-pass Hamming Window Filter) on a 64 × 64 matrix to reduce aliasing artifacts. A new phase mask is created which, when added to the magnitude image, creates the susceptibility image. In order to obtain a better interpretation, minimum intensity projections (minIP) are used [6]. During post-processing the phase contrast image is filtered to reduce undesirable low spatial frequency components, leaving the high frequency field variations. The phase mask created can be 'positive' or 'negative'. The phase mask is multiplied using the original magnitude image to produce images that maximize the negative intensity of the mineralization of the parenchyma. Minimum intensity projection (usually from 2 to 4 slices) is used to display the processed data [1].

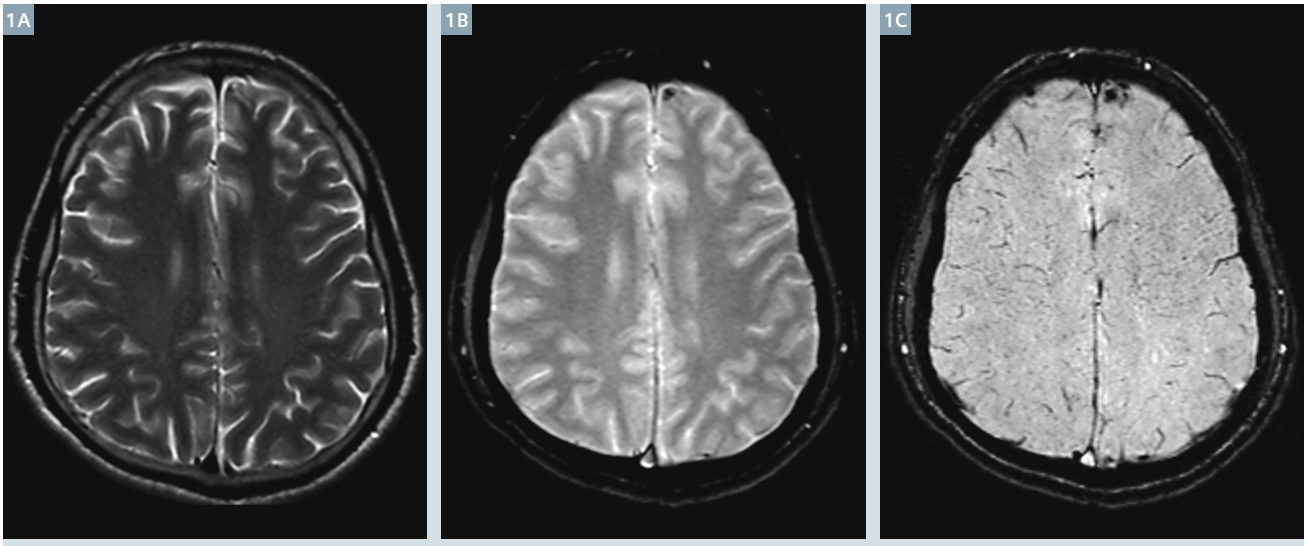

1 Patient with bilateral frontal hemorrhagic contusion. **(1A)** T2w axial; no lesions observed. **(1B)** Axial gradient echo shows a low-signal lesion in left frontal lobe with a slight blooming effect. **(1C)** SWI magnitude, two bilateral frontal hemorrhagic contusions are observed.

The method is highly sensitive for purposes of visualizing venous circulation, blood products and iron content, and is also useful for evaluating the vascularization of tumors and for identifying brain tissue that has been compromised by a stroke, vascular dementia or trauma, and can also be used in functional imaging [1, 4, 7-9] (Fig. 1).

Hemorrhage

Oxyhemoglobin, formed by the binding of an oxygen and an iron atom contained in the Hem group, is a diamagnetic substance. When the oxygen is released from the iron atom it forms deoxyhemoglobin, which is paramagnetic because of its unpaired electrons. Metahemoglobin is produced when deoxyhemoglobin oxidizes, making it less stable; in this state there is little susceptibility effect and thus it is more easily visualized in T1w images. Hemosiderin is the final product of the degradation of hemoglobin when it degrades within phagocytic cells, and is a highly paramagnetic [3, 4, 10] substance. Diamagnetic substances produce a weak local magnetic field, while paramagnetics generate a stronger magnetic field that leads to a signal de-phase and therefore a signal reduction in the T2*w sequence [4]. The ferritin produced by different metabolic processes also has paramagnetic characteristics and is associated with Parkinson's disease, Huntington's disease and Alzheimer's disease [9-11].

Trauma

In the detection of diffuse axonal damage, this approach is more sensitive than conventional imaging for detecting microhemorrhages in the deep and subcortical white matter, which can be obscured in computed tomography (CT) scans [12, 13]. It is three to six times more sensitive than gradient echo images for detecting the number, size, and location of the lesions associated with this clinical status of the patient [1, 13-16]. It is equally useful in detecting brainstem lesions, subarachnoid and intraventricular hemorrhage, as well as other types of hemorrhagic lesions of different origins [17] (Fig. 2).

Calcifications

Calcium is also diamagnetic and can lead to changes in the susceptibility image [12, 18]. SWI differentiates iron from calcium based on their diamagnetic or paramagnetic characteristics in the filtered-phase image. Calcium appears brilliant in this latter image, while the hemorrhage and its derivative products have low signal intensity. This differentiation is important when dealing with neurodegenerative and metabolic diseases, trauma, and tumors [12, 18].

Vascular malformations

Venous blood causes non-homogeneity in the magnetic field due to the paramagnetic effect of the deoxygenated blood due to T2* reduction, depending on the oxygen saturation, the hematocrit and the condition of the erythrocytes; thus, the deoxyhemoglobin present in venous blood allows for the visualization of the latter [4] as well as the phase difference between the vessels and surrounding structures [19]. The susceptibility image provides contrast similar to that of a functional image (BOLD blood oxygen level-dependent).

SWI is more sensitive in the detection of vascular structures that are hidden to T2* and low-flow malformations that are not detected by MR angiography, such as venous development malformations, telangiectasias and cavernomas, as well as vascular abnormalities and calcifications related to Sturge-Weber Syndrome, since it is not affected by flow velocity or direction [20-24]. In dural sinus thrombosis they show venous statis and collateral flow, as well as early detection of venous hypertension before infarcts or hemorrhages occur [7, 8, 19] (Figs. 3–5).

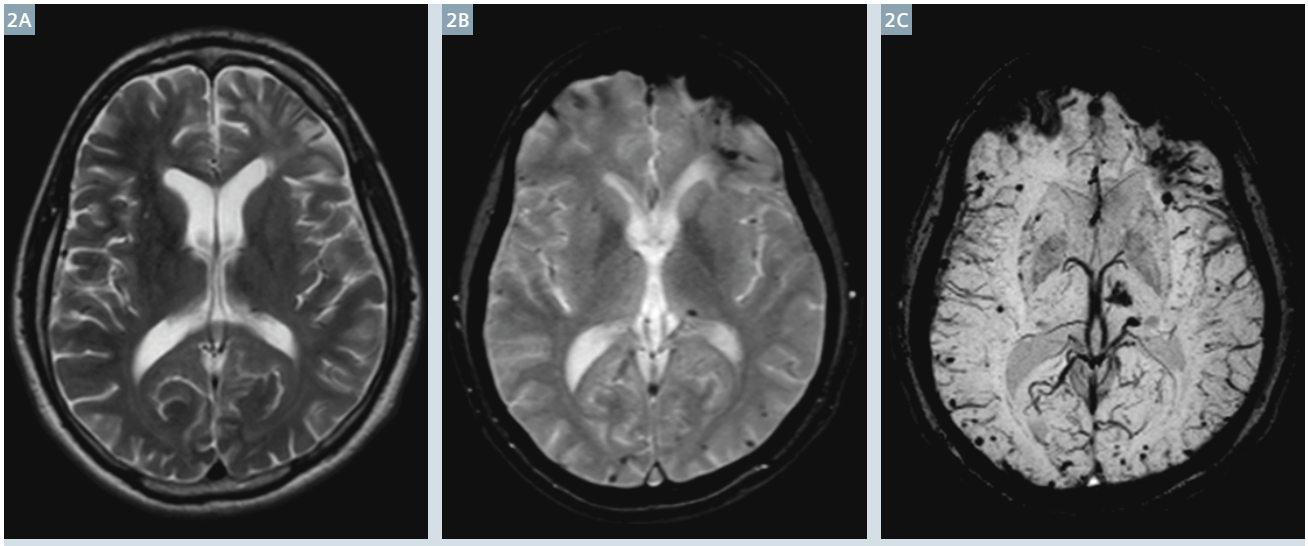

2 Patient with diffuse axonal lesion. **(2A)** T2w axial; no lesions observed. **(2B)** Low-signal, puntiform lesions. **(2C)** SWI minIP makes the multiple microhemorrhagic lesions more apparent.

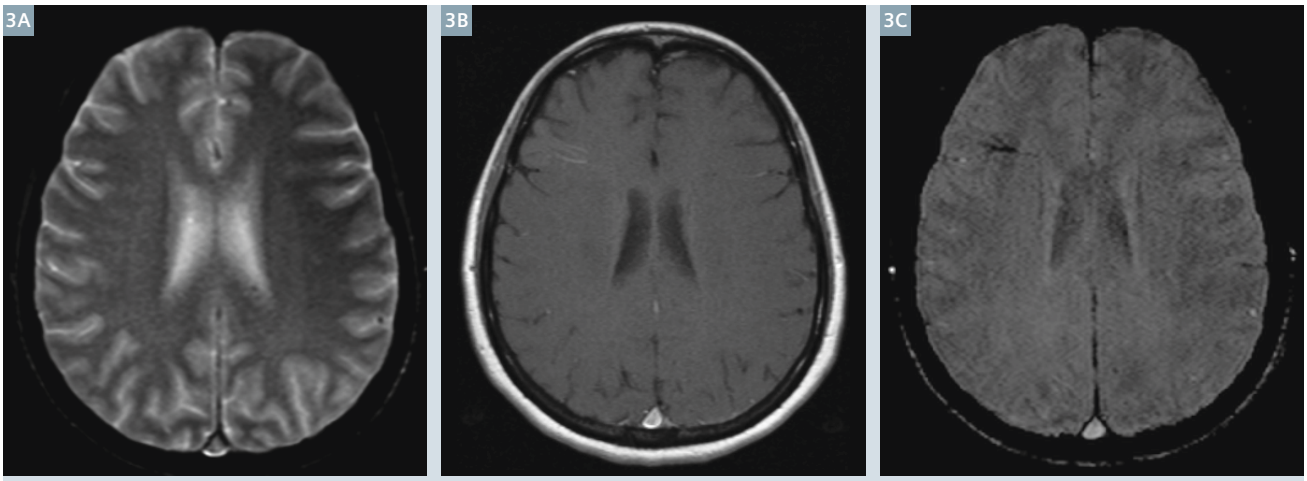

3 Venous development anomaly. **(3A)** Axial gradient echo; anomaly not visible. **(3B)** Axial contrast-enhanced image shows right frontal venous development anomaly that is more evident in the susceptibility image **(3C)**.

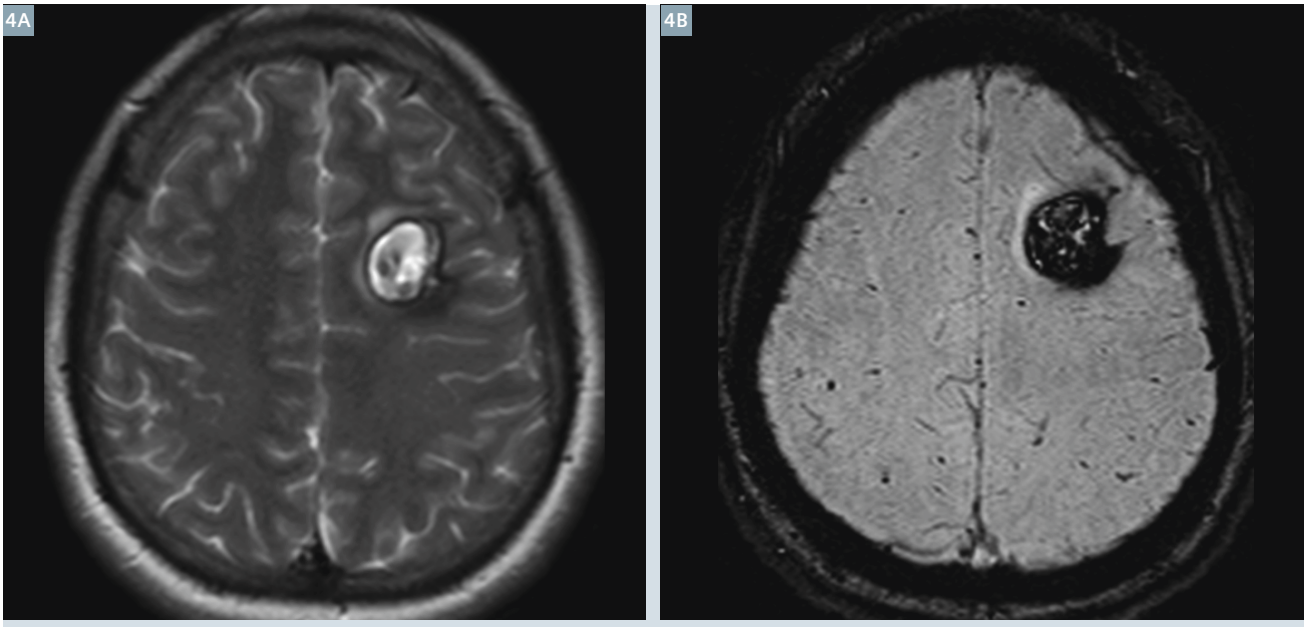

4 Left frontal cavernoma. **(4A)** Axial proton density-weighted image; **(4B)** minIP SWI.

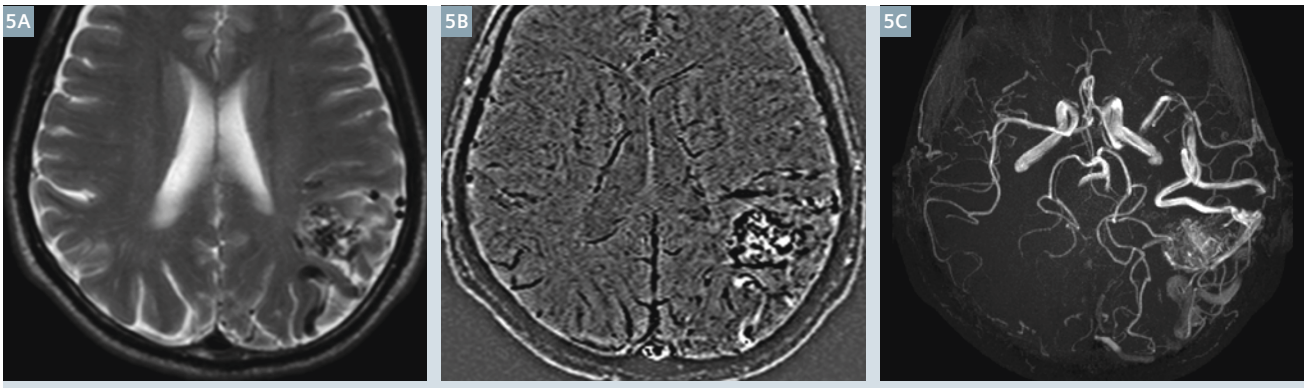

5 Left parietal arteriovenous malformation. **(5A)** Axial PDw show serpinginous images with absence of flow signal. **(5B)** mIP SWI. **(5C)** MIP TOF shows the AVM and the cortical drainage vein.

Brain tumors

This approach provides information that supplements T1 with contrast for detecting margins, internal architecture, hemorrhage and vascularization of a tumor that are not visible with conventional sequences. This aids in differentiating between a recurring tumor and post-operative changes. The use of susceptibility imaging before and after the administration of gadolinium can differentiate areas of enhancement of the vessels. Because of its suppression of cerebrospinal fluid, it enhances contrast between edema and normal tissue, similarly to what is provided by FLAIR, thus facilitating the detection of space-occupying lesions [4, 7, 25] (Figs. 6–8).

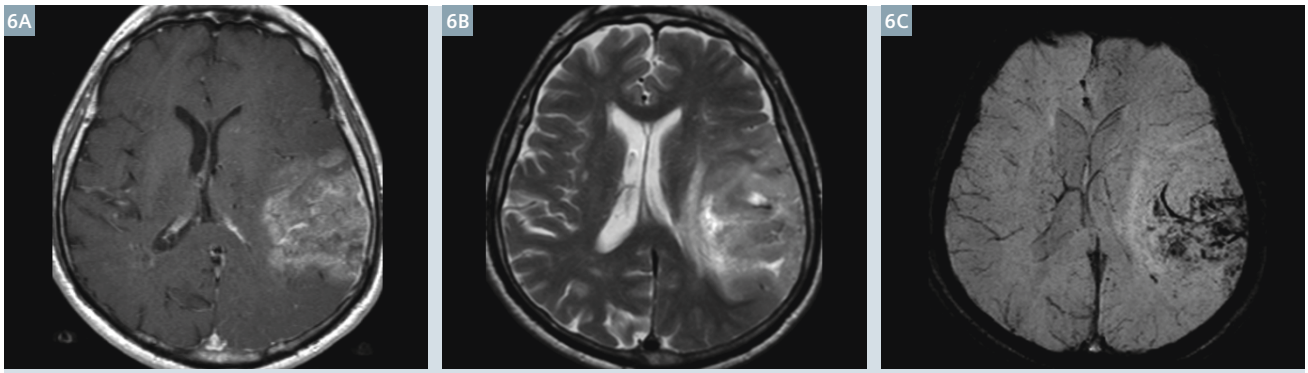

6 Hemorrhagic metathesis. **(6A)** T1w axial gadolinium-enhanced, **(6B)** T2w axial show a left parietal mass with heterogeneous enhancement, perilesional edema and mass effect on the lateral ventricles. **(6C)** MIP SWI shows hypervascularity and hemorrhage in the interior of the mass.

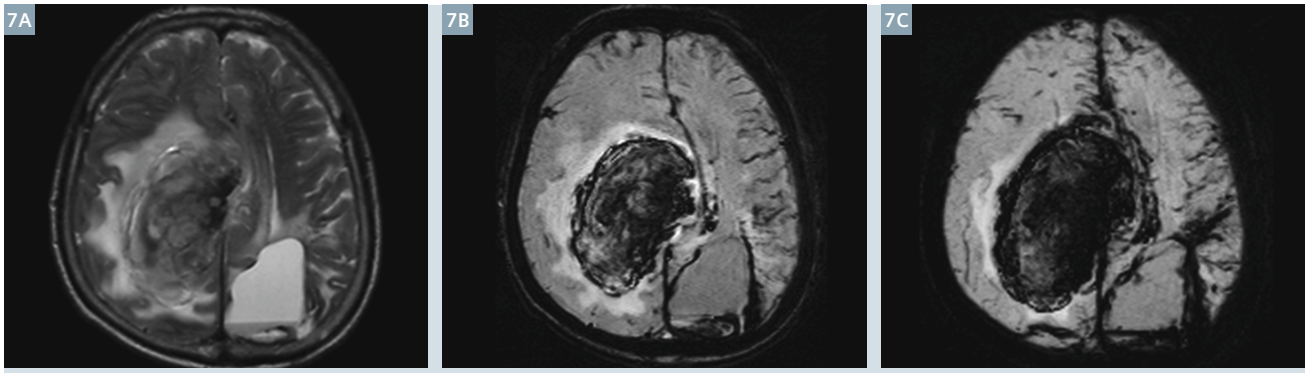

7 Metastatic melanoma. **(7A)** T2w axial; large mass displacing the midline, with major edema and hypointense zone due to hemorrhage in the medial portion. **(7B)** Magnitude image, **(7C)** MIP SWI shows a greater hemorrhagic component of the mass, on the contralateral side, as well as intraventricular hemorrhaging.

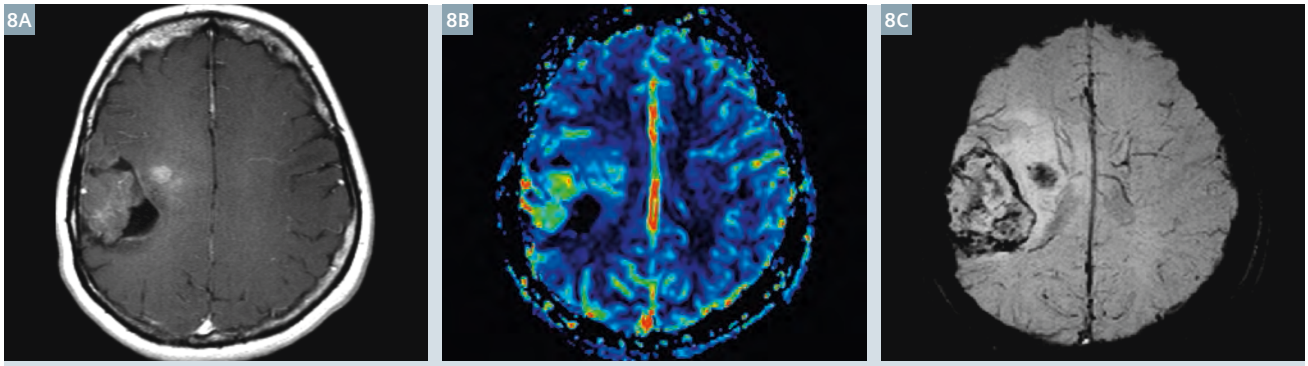

8 Oligodendroglioma. **(8A)** T1w axial gadolinium shows mass with enhanced foci and a cystic component, **(8B)** MIP SWI right parietal hypervascular mass with increased relative flow **(8C)**.

Cerebrovascular disease

The susceptibility image can be used together with diffusion images to detect the hypoperfused region, the presence of hemorrhaging within the infarct (which could affect the treatment), detect acute thrombus and predict the likelihood of hemorrhagic transformation and hemorrhagic complications during and after thrombolysis treatment, as well as microbleeding due to amyloid angiopathy and lacunar infarcts in patients with hypertensive encephalopathy [19, 26-28] (Figs. 9, 10).

Vascular occlusion can change the susceptibility of the tissue as a result of reduced arterial flow and an increase in the accumulation of deoxygenated blood, which increases the amount of deoxyhemoglobin that can be detected by SWI [27, 29].

Neurodegenerative illnesses

Certain disorders, such as Parkinson's Disease, Huntington's Disease, Alzheimer's, multiple sclerosis and amyotrophic lateral sclerosis (Lou Gherig's Disease) present with abnormal iron deposition, which can be detected and quantified using susceptibility imaging [11, 30-33]. SWI can show chronic demyelinating plaques with iron depositions that are hidden in conventional sequences, as the iron content makes the lesions more visible. It can also determine the iron content of the nucleii of deep gray matter that can also be observed in patients with multiple sclerosis, as well as the perivenular distribution of the demyelinating lesions [30].

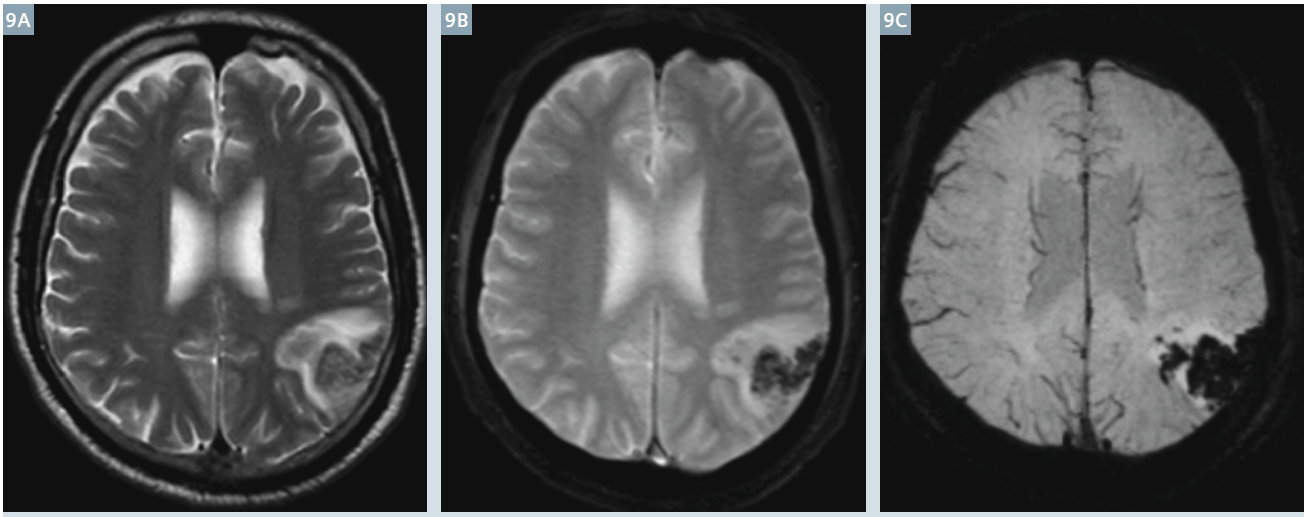

9 CVD with hemorrhagic transformation. **(9A)** Axial T2w, **(9B)** gradient echo in patient with left parietal hemorrhagic infarct with surrounding edema and hemorrhage. **(9C)** SWI makes the greater hemorrhagic component more obvious.

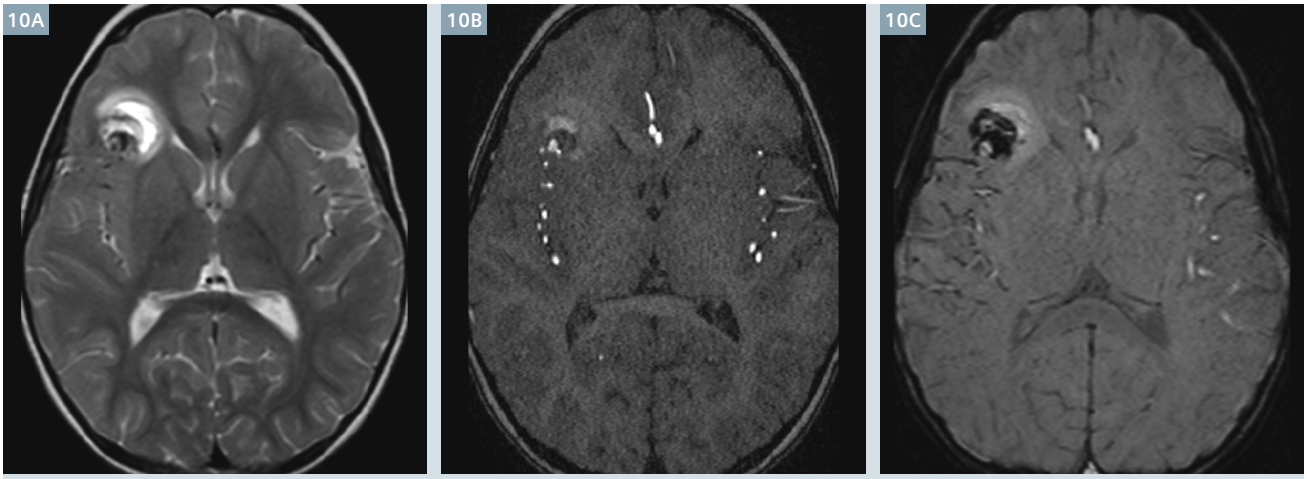

10 Right MCA aneurism with bleeding. **(10A)** Axial T2w, **(10B)** TOF demonstrating aneurysm with bleeding, **(10C)** SWI aneurism with greater bleeding than that shown in the T2w sequence.

References

1 Haacke EM, Xu Y, Cheng Y-CN, Reichenbach JR. Susceptibility weighted imaging (SWI). Magnetic Resonance in Medicine. 2004;52(3):612-8.
2 Haacke EM, Mittal S, Wu Z, Neelavalli J, Cheng Y-CN. Susceptibility-Weighted Imaging: Technical Aspects and Clinical Applications, Part 1. AJNR Am J Neuroradiol. 2009 January 1, 2009;30(1):19-30.
3 Mittal S, Wu Z, Neelavalli J, Haacke EM. Susceptibility-Weighted Imaging: Technical Aspects and Clinical Applications, Part 2. AJNR Am J Neuroradiol. 2009 February 1, 2009;30(2):232-52.
4 Sehgal V, Delproposto Z, Haacke EM, Tong KA, Wycliffe N, Kido DK, et al. Clinical applications of neuroimaging with susceptibility-weighted imaging. Journal of Magnetic Resonance Imaging. 2005;22(4):439-50.
5 Tong KA, Ashwal S, Obenaus A, Nickerson JP, Kido D, Haacke EM. Susceptibility-Weighted MR Imaging: A Review of Clinical Applications in Children. AJNR Am J Neuroradiol. 2008 January 1, 2008;29(1):9-17.
6 Matsushita T AD, Arioka T, Inoue S, Kariya Y, Fujimoto M, Ida K, Sasai N, Kaji M, Kanazawa S, Joja I. Basic study of susceptibility-weighted imaging at 1.5T. Acta medica Okayama. [Journal Article]. 2008 Jun;62(3):159-68.
7 Thomas B, Somasundaram S, Thamburaj K, Kesavadas C, Gupta A, Bodhey N, et al. Clinical applications of susceptibility weighted MR imaging of the brain – a pictorial review. Neuroradiology. 2008;50(2):105-16.
8 Ong BC, Stuckey SL. Susceptibility weighted imaging: A pictorial review. Journal of Medical Imaging and Radiation Oncology. 2010;54(5):435-49.
9 Robinson RJ, Bhuta S. Susceptibility-Weighted Imaging of the Brain: Current Utility and Potential Applications. Journal of Neuroimaging. 2011:no-no.
10 Goos JDC, van der Flier WM, Knol DL, Pouwels PJW, Scheltens P, Barkhof F, et al. Clinical Relevance of Improved Microbleed Detection by Susceptibility-Weighted Magnetic Resonance Imaging. Stroke. 2011 May 12, 2011:STROKEAHA. 110.599837.
11 Gupta D, Saini J, Kesavadas C, Sarma P, Kishore A. Utility of susceptibility-weighted MRI in differentiating Parkinson's disease and atypical parkinsonism. Neuroradiology. 2010;52(12):1087-94.
12 ZHU Wen-zhen QJ-p, ZHAN Chuan-jia, SHU Hong-ge, ZHANG Lin, WANG Cheng-yuan, XIA Li-ming, HU Jun-wu, FENG Ding-yi. Magnetic resonance susceptibility weighted imaging in detecting intracranial calcification and hemorrhage. Chinese Medical Journal. [Journal Article]. 2008 oct 20;121(20):2021-5.
13 Beauchamp MH, Ditchfield M, Babl FE, Kean M, Catroppa C, Yeates KO, et al. Detecting Traumatic Brain Lesions in Children: CT versus MRI versus Susceptibility Weighted Imaging (SWI). Journal of Neurotrauma. 2011;28(6):915-27.
14 Wang M, Dai Y, Han Y, Haacke EM, Dai J, Shi D. Susceptibility weighted imaging in detecting hemorrhage in acute cervical spinal cord injury. Magnetic resonance imaging. 2011;29(3):365-73.
15 Tong KA, Ashwal S, Holshouser BA, Shutter LA, Herigault G, Haacke EM, et al. Hemorrhagic Shearing Lesions in Children and Adolescents with Posttraumatic Diffuse Axonal Injury: Improved Detection and Initial Results1. Radiology. 2003 May 1, 2003;227(2):332-9.
16 Babikian T, Freier MC, Tong KA, Nickerson JP, Wall CJ, Holshouser BA, et al. Susceptibility weighted imaging: neuropsychologic outcome and pediatric head injury. Pediatr Neurol. 2005;33(3):184-94.
17 Wu Z, Li S, Lei J, An D, Haacke EM. Evaluation of Traumatic Subarachnoid Hemorrhage Using Susceptibility-Weighted Imaging. AJNR Am J Neuroradiol. 2010 August 1, 2010;31(7):1302-10.
18 Wu Z, Mittal S, Kish K, Yu Y, Hu J, Haacke EM. Identification of calcification with MRI using susceptibility-weighted imaging: A case study. Journal of Magnetic Resonance Imaging. 2009;29(1):177-82.
19 Tsui Y-K, Tsai FY, Hasso AN, Greensite F, Nguyen BV. Susceptibility-weighted imaging for differential diagnosis of cerebral vascular pathology: A pictorial review. Journal of the neurological sciences. 2009;287(1):7-16.
20 Hu J, Yu Y, Juhasz C, Kou Z, Xuan Y, Latif Z, et al. MR susceptibility weighted imaging (SWI) complements conventional contrast enhanced T1 weighted MRI in characterizing brain abnormalities of Sturge-Weber Syndrome. Journal of Magnetic Resonance Imaging. 2008;28(2):300-7.
21 Deistung A, Dittrich E, Sedlacik J, Rauscher A, Reichenbach JR. ToF-SWI: Simultaneous time of flight and fully flow compensated susceptibility weighted imaging. Journal of Magnetic Resonance Imaging. 2009;29(6):1478-84.
22 Koopmans P, Manniesing R, Niessen W, Viergever M, Barth M. MR venography of the human brain using susceptibility weighted imaging at very high field strength. Magnetic Resonance Materials in Physics, Biology and Medicine. 2008;21(1):149-58.
23 de Champfleur NM, Langlois C, Ankenbrandt WJ, Le Bars E, Leroy MA, Duffau H, et al. Magnetic Resonance Imaging Evaluation of Cerebral Cavernous Malformations With Susceptibility-Weighted Imaging. Neurosurgery. 2011;68(3):641-8 10.1227/NEU.0b013e31820773cf.
24 Jagadeesan BD, Delgado Almandoz JE, Moran CJ, Benzinger TLS. Accuracy of Susceptibility-Weighted Imaging for the Detection of Arteriovenous Shunting in Vascular Malformations of the Brain. Stroke. 2011 January 1, 2011;42(1):87-92.
25 Hori M, Ishigame K, Kabasawa H, Kumagai H, Ikenaga S, Shiraga N, et al. Precontrast and postcontrast susceptibility-weighted imaging in the assessment of intracranial brain neoplasms at 1.5 T. Japanese Journal of Radiology. 2010;28(4):299-304.
26 Cherian A, Thomas B, Kesavadas C, Baheti N, Wattamwar P. Ischemic hyperintensities on T1-weighted magnetic resonance imaging of patients with stroke: New insights from susceptibility weighted imaging2010 January 1, 2010 Contract No.: 1.
27 Mittal P, Dua S, Kalia V. Pictorial essay: Susceptibility-weighted imaging in cerebral ischemia2010.
28 Santhosh K, Kesavadas C, Thomas B, Gupta AK, Thamburaj K, Kapilamoorthy TR. Susceptibility weighted imaging: a new tool in magnetic resonance imaging of stroke. Clinical Radiology. 2009;64(1):74-83.
29 Hermier M, Nighoghossian N. Contribution of Susceptibility-Weighted Imaging to Acute Stroke Assessment. Stroke. 2004 August 1, 2004;35(8):1989-94.
30 Haacke EM, Makki M, Ge Y, Maheshwari M, Sehgal V, Hu J, et al. Characterizing iron deposition in multiple sclerosis lesions using susceptibility weighted imaging. Journal of Magnetic Resonance Imaging. 2009;29(3):537-44.
31 Niwa T, de Vries L, Benders M, Takahara T, Nikkels P, Groenendaal F. Punctate white matter lesions in infants: new insights using susceptibility-weighted imaging. Neuroradiology. 2011:1-11.
32 Vinod Desai S, Bindu PS, Ravishankar S, Jayakumar PN, Pal PK. Relaxation and susceptibility MRI characteristics in Hallervorden-Spatz syndrome. Journal of Magnetic Resonance Imaging. 2007;25(4):715-20.
33 Kirsch W, McAuley G, Holshouser B, Petersen F, Ayaz M, Vinters HV, et al. Serial susceptibility weighted MRI measures brain iron and microbleeds in dementia. Journal of Alzheimer's disease: JAD. 2009;17(3):599-609.

Contact

Jose Luis Ascencio L.
Escanografia Neurologica
Medellin
Colombia

jotaascencio@yahoo.com

Curve Fitting of the Lipid-Lactate Range in an MR Spectrum: Some Useful Tips

Jamie Ho Xiu Mei; Helmut Rumpel

Department of Diagnostic Radiology, Singapore General Hospital, Singapore

Purpose

In the course of a neurological spectroscopic application, questions about the lipid-lactate signals often occur: How can we accurately interpret an asymmetric pattern with 'humps' and partially inverted signals? How can we recognise some fundamental patterns in order to differentiate between, for example, an early membrane degradation and necrosis? In addition, questions always arise about the proportion of lipid and lactate in an overlapping pattern. This article offers some hints to curve fitting of the lipid-lactate range and to avoid incorrect or misleading labelling of the peaks of an MR spectrum.

Background

The lipids are a large and diverse group of naturally occurring molecules with various functions, from storing energy to being components of membranes. They include miscellaneous subgroups, such as triglycerides of subcutaneous fat or bone marrow and glycerophospholipids of membranes (Fig. 1). They have in common fatty acids comprising four different proton groups: olefinic protons at 5.3 ppm, allylic protons and protons adjacent to the carboxyl group at 2.0 ppm, aliphatic methylene groups (main peak) at 1.3 ppm, and the terminal methyl group at 0.9 ppm. However, their T2 values differ according to whether the fatty acids are part of triglycerides or cell membranes. Unlike glycerophospholipids, fatty acids in membranes are embedded in the interior of the membrane resulting in efficient spin-spin interactions, thus revealing short T2 values. As such, even in short TE spectra, signals from intact membranes are hardly visible, whereas the freely tumbling fatty acids in triglycerides and also the less restricted 'fragments' of fatty acids from membrane degradation produce strong signals due to a longer T2. In drawing a comparison with an iceberg, protons of membranes namely those of methyl-, methylene-groups, choline, and myo-inositol, are MR-invisible unless they 'surface' due to degradation processes (Fig. 2). For example, depending on the grade of degradation of membranes in brain tumours, the MR signals of the said membrane fragments are raised in a characteristic way [1].

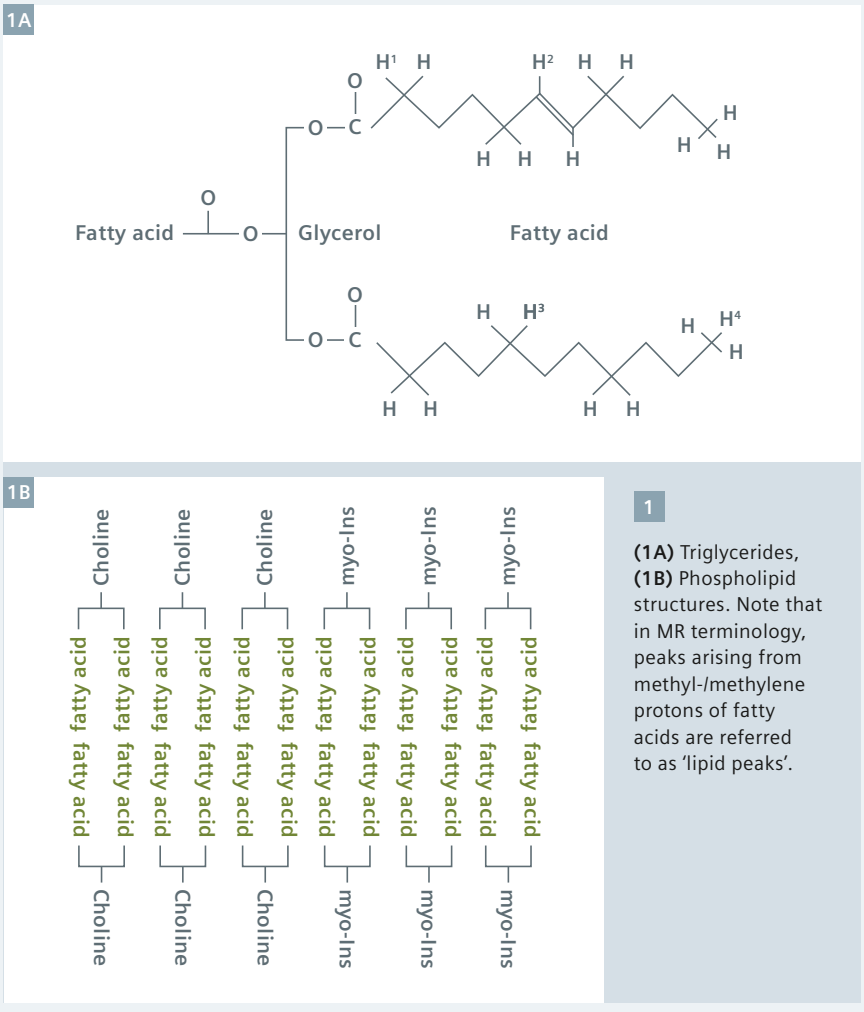

1

(1A) Triglycerides, **(1B)** Phospholipid structures. Note that in MR terminology, peaks arising from methyl-/methylene protons of fatty acids are referred to as 'lipid peaks'.

Line curve fitting in the NUMARIS software

Within the NUMARIS software, line curve fitting is done in the frequency domain [2]. It is the last of the post-processing steps. Provided that the phase correction is optimal, the adequate line curve fitting protocol has to be selected out of a set of three 'customised' protocols, namely:

1. lipid signal only, e.g. ***TE 30_lip***
2. lactate signal only, e.g. ***TE 30_lac***
3. lactate and lipid signals e.g. ***TE 30_lip_lac***

They are easily derived from the Siemens protocol (CSI or SVS) TE 30 using the interactive post-processing environment and adding new peak parameters and peak restrictions (see User Manual). The lipid-containing protocols fit both the lipid_1.3 and the lipid_0.9 peaks with parameters as shown in figure 3. An analogous set of protocols shall be customised for TE 135.

How do we identify lipids and lactate?

- **Lipid-only peak (Fig. 3A):** Here, the assignment method is straightforward. Firstly, we look at the line width of the peaks. Their full width at half maximum is reciprocally proportional to T2. As a rule of thumb, T2 of lipids is shorter than that of lactate, and thus the lipid peak is broader. Secondly, one can also look at the symmetry of the peak (whether it has a symmetrical Gaussian / Lorentzian shape). Thirdly, lipids should appear as two peaks. Their relative intensities may vary depending on the stage of degradation (Fig. 4).
- **Lactate-only peak (Fig. 3A):** The scalar coupling constant J_{IS} and phase dependency of the lactate signal, $S \sim [\cos (J_{IS} TE)]$ can be used as a kind of lactate editing: a doublet signal of 7 Hz and a 180 degree phase shift at TE 135 ms. In contrast to the lipid peak, the lactate peak reveals a sharp doublet pattern, or at least it appears foreshadowed.

2

2 Schematic MR spectrum of normal brain tissue. Myo-inositol, choline, and lipid signals are 'iceberg-like' as most signal is invisible due to short T2. In the event of hydrolysis of inositol phospholipids or high cellular membrane turnover, myo-inositol, choline, and lipids become more 'MR visible' due to change in T2 towards higher values.

3A 3B

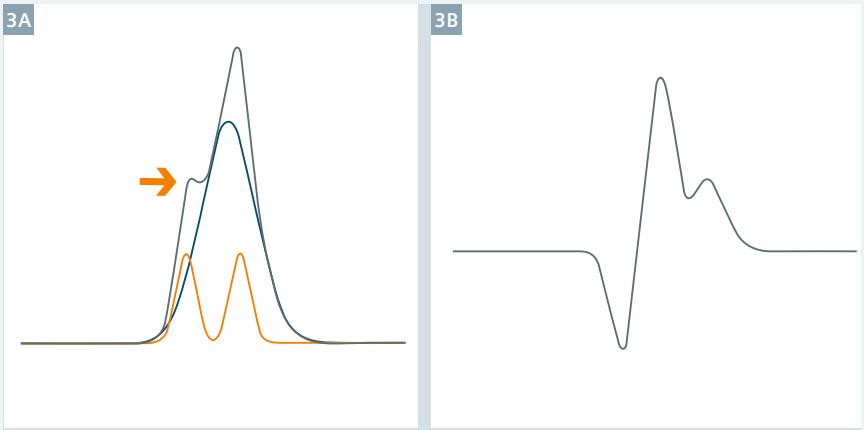

3 Schematic diagram of the peak pattern in the lipid-lactate range. **(3A)** Broad lipid peak due to short T2 *(blue)*, sharp lactate doublet due to J coupling and long T2 *(orange)*, superposition of the lipid and lactate peak *(black)* for short TE. Depending on slight resonance offsets and relative intensities, often a 'hump' is visible (arrow). **(3B)** Superposition of lipid and lactate peaks for long TE (135 ms).

- **Lipid-lactate peak (Fig. 3A):** In the case of lipid-lactate overlapping, this approach of Lorentzian-Gaussian curve fitting will be inaccurate in differentiating between lipid and lactate proportions, because the best fit is driven by the method of least squares rather than taking pre-knowledge of different shapes into account. In fact the operator will identify asymmetric patterns (showing a hump on one side) or if they partially invert on TE 135 spectra (Fig. 3B).

Representative cases are shown in figures 5 and 6.

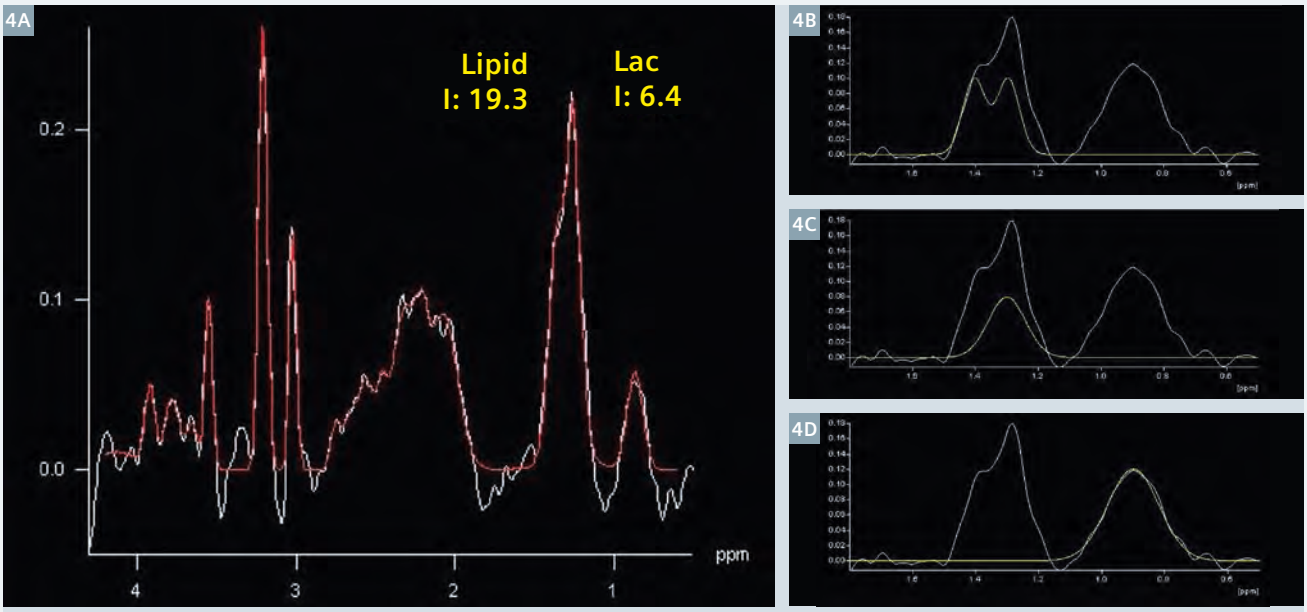

4 Line curve fitting in the NUMARIS software. **(4A)** Entire spectrum, **(4B)** lactate component, **(4C)** lipid _1.3 component, **(4D)** lipid_0.9 component. Note that the proportions of lipid and lactate should be regarded with caution.

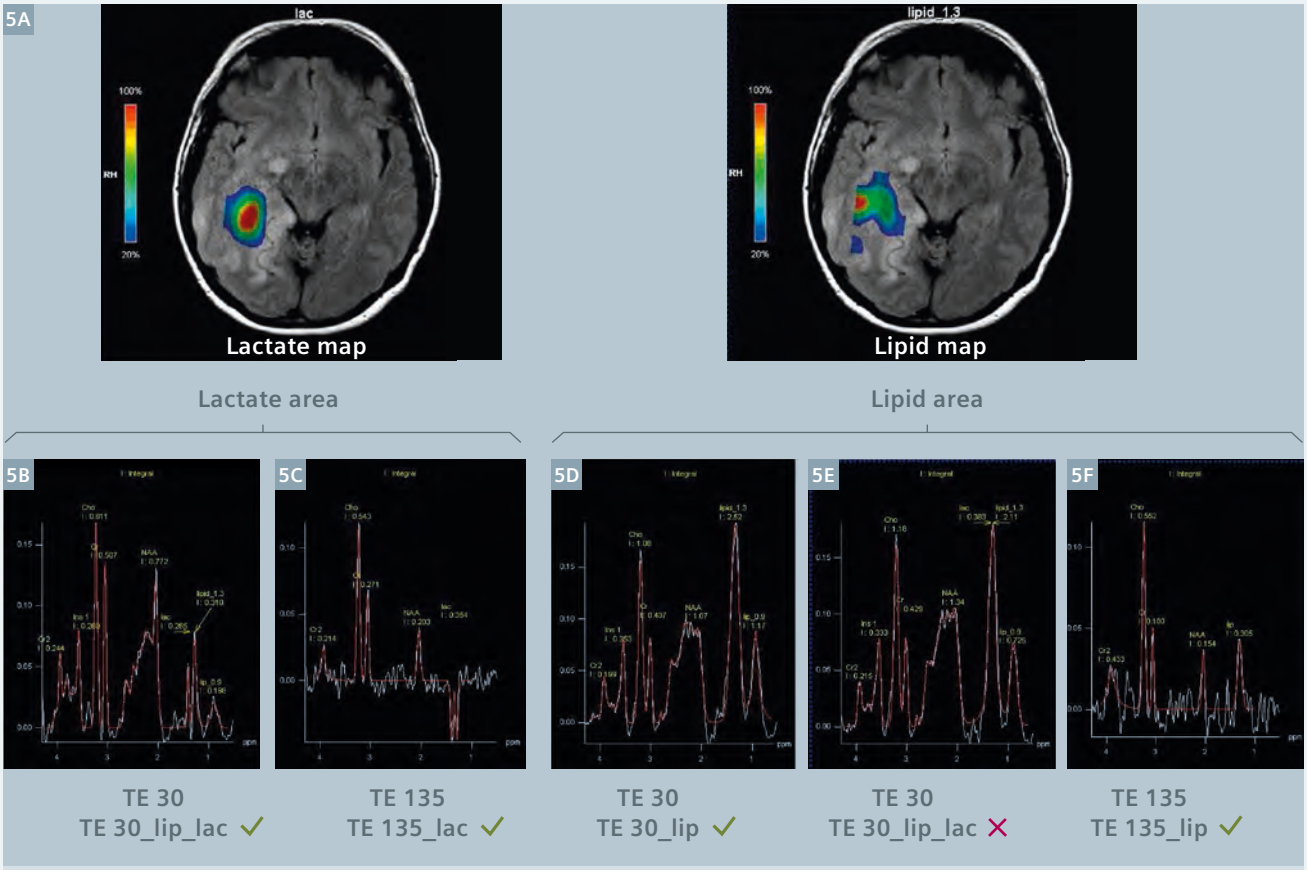

5 Illustration of a representative case of lipid-lactate overlap. **(5A)** Metabolite maps. In **(5B)**, the lactate doublet peak dominates the pattern which also shows an unequal doublet with higher signal and broadening of the right peak of the doublet. Therefore, the *TE_30_lip_lac* protocol has been used. Due to T2 relaxation, the lipid component became negligible at TE 135, and only the lactate has been labelled with the *TE_135_lac* protocol in **(5C)**. In **5D–F**, lipids overwhelm the pattern. Since lactate is neither detected on TE 135, nor a 'hump' is observable on TE 30, the protocol *TE_30_lip_lac* is inappropriate.

Line curve fitting in *syngo*.via

In ***syngo***.via the approach of curve fitting in the time domain has been chosen [3]. It is based on PRISMA [4] using the basis set of metabolic time signals of brain metabolites together with published values of chemical shifts and coupling constants.

The delineation of a lactate-lipid overlap is based on free induction decays (FIDs), in which the distinct T2 values make the segmentation more accurate. Figure 7 depicts two examples:

a) with a clearly visible hump at half maximum of the Lip_1.3 peak, and
b) with only an adumbrated hump (arrow).

It demonstrates that delineating highly non-uniform signal compositions is possible with only one protocol for all cases. The protocol can be easily linked together by selecting the appropriate lactate and lipid templates as shown in figure 8.

6A

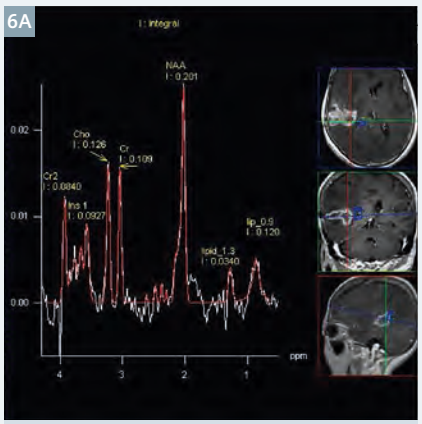

6B

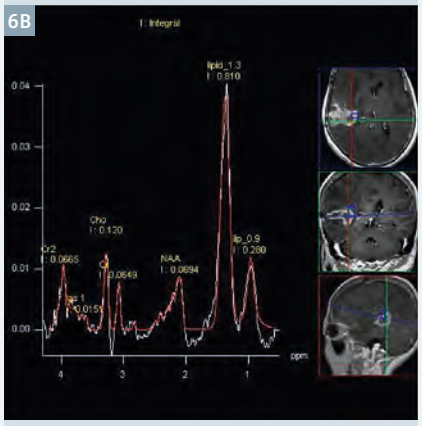

6C

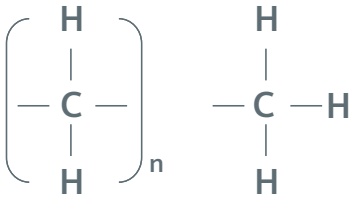

Methylene – Group @ 1.3ppm

Methyl – Group @ 0.9ppm

6 Spectra of a glioblastoma multiforme, **(6A)** from the perilesional area, **(6B)** from the solid enhancing area. Note the relative intensities of lipid at 1.3 ppm and 0.9 ppm as in an early stage of membrane degradation **(6A)** these signals do not reflect a proton density even at TE 30, rather they are T2-weighted, whilst in a more advanced stage **(6B)** T2 becomes long enough for both signals resulting in a proton density spectrum **(6C)**.

7A

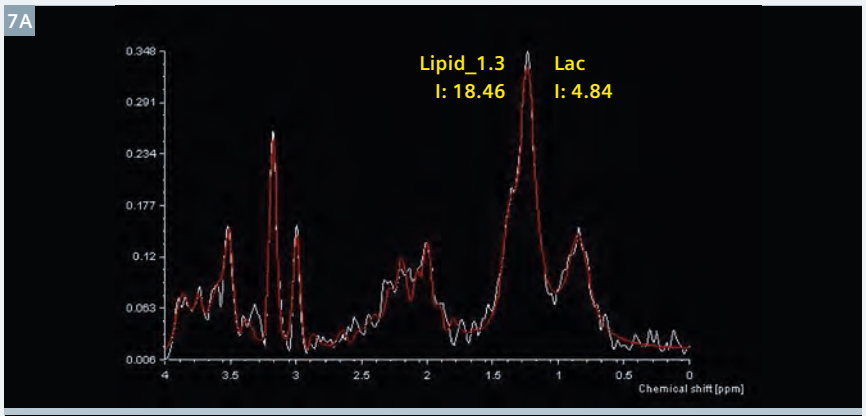

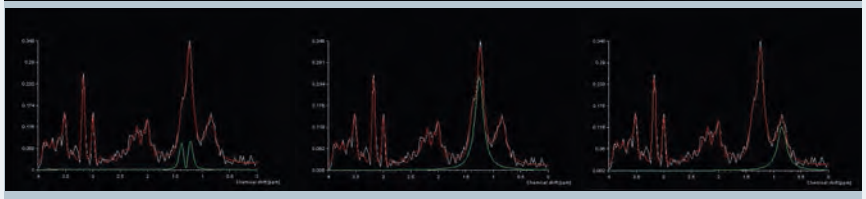

7B

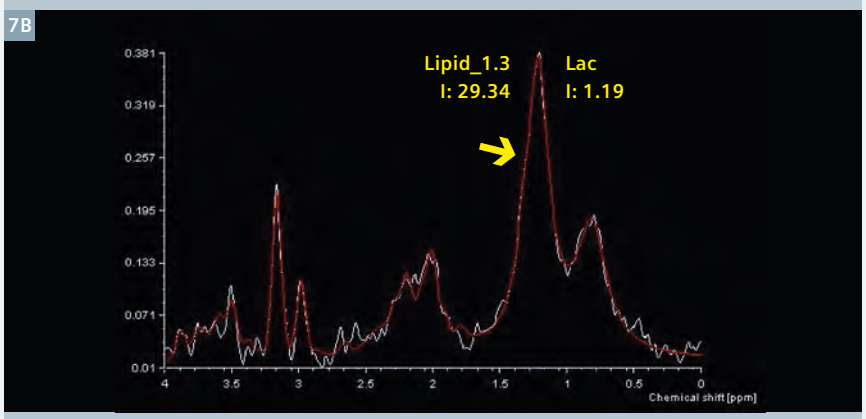

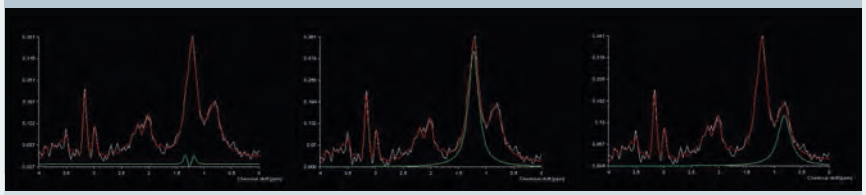

7 Line curve fitting in the *syngo*.via software. Lipid-lactate compositions are slightly different in **(7A)** and **(7B)**.

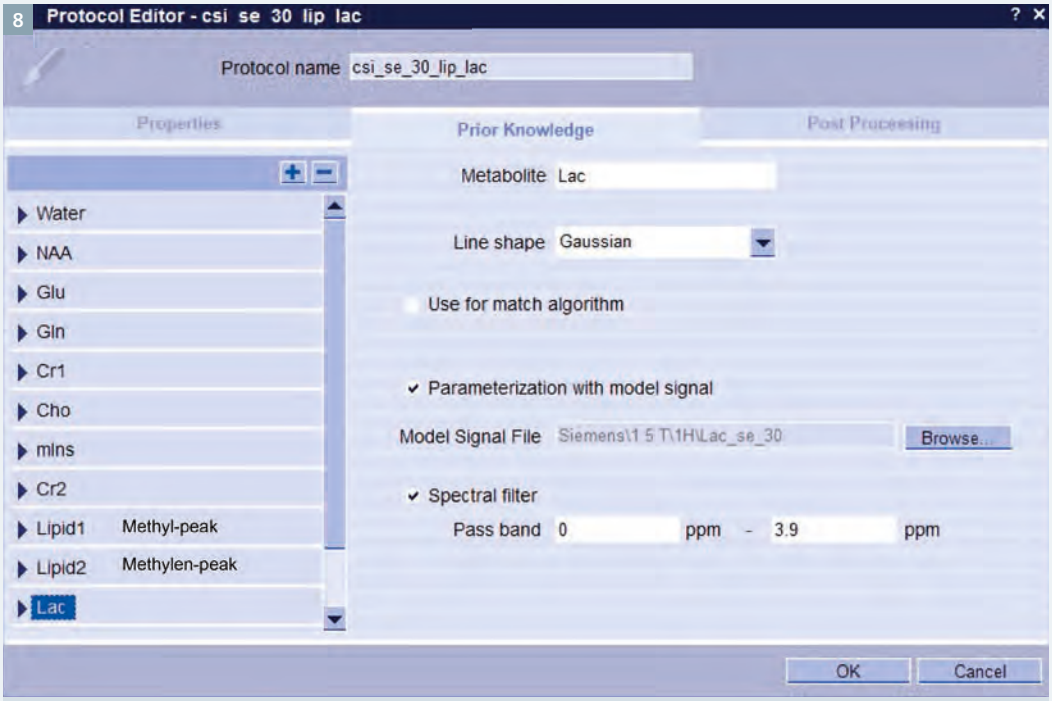

8 Lipid-lactate protocol in *syngo*.via.

Conclusion

- Carefully labelled spectra in the lactate–lipid region are a prerequisite to sending them to a PACS system as otherwise they can be misleading for further examinations and treatment planning by clinicians.
- Curve fitting based on chemical shift assignments should be made with caution. The technologist is required to identify 'what is what', as erroneous lipid-lactate discrimination is inherent to frequency domain curve fitting of overlapping peaks. By following basic steps, the lactate-lipid overlap within the region from 0.9 to 1.3 ppm can be reliably delineated. However, the proportions of lipid and lactate remain ambiguous as various sets of model peaks, i.e. half-width, signal intensity and chemical shift, may lead to the same result of curve fitting.
- Incorporation of prior knowledge such as supportive model spectra automates the curve fitting of a lactate-lipid overlap. The protocol ***TE_30_lip_lac*** can be made standard practice.

References
1 Li X, Vigneron DB, Cha S, Graves EE, Crawford F,Chang SM, Nelson SJ. 2005. Relationship of MR-Derived Lactate, Mobile Lipids, and Relative Blood Volume for Gliomas *in Vivo*. *AJNR Am J Neuroradiol* 26:760–769.
2 Mierisová Š, Ala-Korpela M.2001.MR spectroscopy quantitation: a review of frequency domain methods. NMR in Biomedicine;14, 247-259.
3 Vanhamme L, Sundin T, Van Hecke P, Van Huffel S. 2001. MR spectroscopy quantitation: a review of time-domain methods NMR in Biomedicine; 14,233–246.
4 http://elib.suub.uni-bremen.de/publications/diss/html/E-Diss1066_HTML.html

Contact

Helmut Rumpel, Ph.D.
Department of
Diagnostic Radiology
Singapore General Hospital
helmut.rumpel@sgh.com.sg

Relevant clinical information at your fingertips

From technology to clinical applications, you will find all the latest news on Siemens MR at

www.siemens.com/magnetom-world

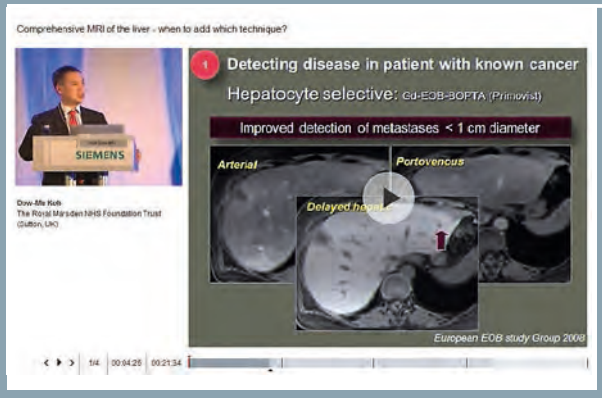

Don't miss the talks of international experts on all aspects of Magnetic Resonance Imaging.

Go to
Clinical Corner > Clinical Talks

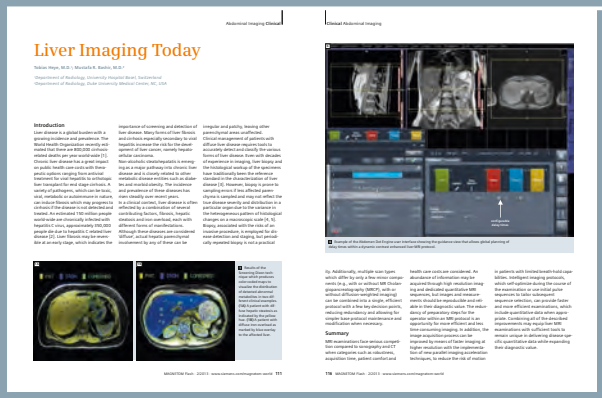

The centerpiece of the MAGNETOM World Internet platform consists of our users' clinical results. Here you will find case reports and clinical methods.

Go to
Clinical Corner > Case Studies

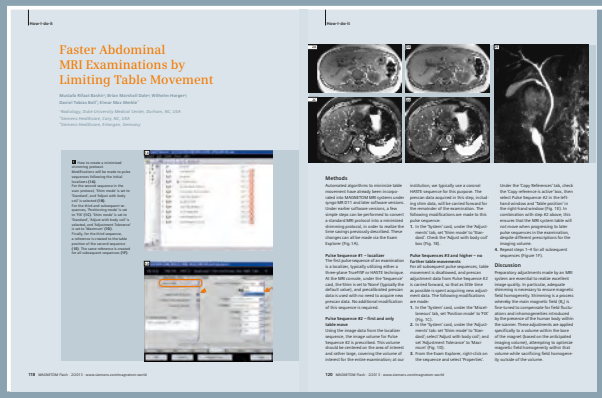

Just a mouse click away you will find application videos and useful tips allowing you to optimize your daily MR examinations.

Go to
Clinical Corner > Application Tips

For the whole range of clinical MR information visit us at

www.siemens.com/magnetom-world

T1-weighted Phase Sensitive Inversion Recovery for Imaging Multiple Sclerosis Lesions in the Cervical Spinal Cord

Bart Schraa, MSc., Senior MR Application Specialist

Siemens LTD Canada

Introduction

Multiple sclerosis (MS) is an inflammatory disease in which the insulating covers of nerve cells in the brain and spinal cord are damaged. Magnetic resonance imaging (MRI) was first used to visualize multiple sclerosis (MS) in the upper cervical spine in late 1980 [1]. Spinal MS is often associated with concomitant brain lesions; however, as many as 20% of patients with spinal lesions do not have intracranial plaques [2]. This article describes the experiences with a T1-weighted phase sensitive inversion recovery sequence for the detection of MS lesions in the cervical spinal cord using the MAGNETOM Skyra with *syngo* MR D13A software.

Inversion Recovery Sequences used for imaging Multiple Sclerosis

Several inversion recovery techniques are used for imaging lesions in MS. Among these are Fluid Attenuated Inversion Recovery (FLAIR), Sampling Perfection with Application optimized Contrasts using different flip-angle Evolutions Double Inversion Recovery (SPACE-DIR), and T1-weighted Phase Sensitive Inversion Recovery (PSIR).

Fluid Attenuated Inversion Recovery

FLAIR is commonly used to assess white matter lesions and in particular MS lesions in the brain. The FLAIR technique is a T2-weighted sequence with a long TR and TE and is used to demonstrate the changes in T2 relaxation times in lesions when compared to normal tissue. As the name indicates, the signal of cerebro-spinal fluid (CSF) is attenuated.

CSF has a long T1 relaxation times compared to the other tissues in both the brain and cervical spine. Therefore, a rather long inversion time is needed to null the signal of CSF (~ 2500 ms). Hence, the contrast in T2-weighted FLAIR images allows for easier assessment of (MS) lesions, especially when the lesions are close to CSF, as compared to normal T2-weighted images. However, while the FLAIR technique works well in the brain, it is hampered by flow and motion artifacts when used in the cervical spine.

Double Inversion recovery

The Double Inversion Recovery technique has been implemented in the SPACE-DIR sequence in the Siemens *syngo* MR D13 software. A protocol optimized for brain imaging is also provided. SPACE-DIR is a T2-weighted technique which uses two inversion pulses, combined with a fat saturation pulse, to null both the signal of CSF and normal white matter. Similar to the FLAIR technique, this sequence is used to exploit the changes in T2 relaxation times in lesions when compared to normal tissue. In the brain, SPACE-DIR improves visualization of

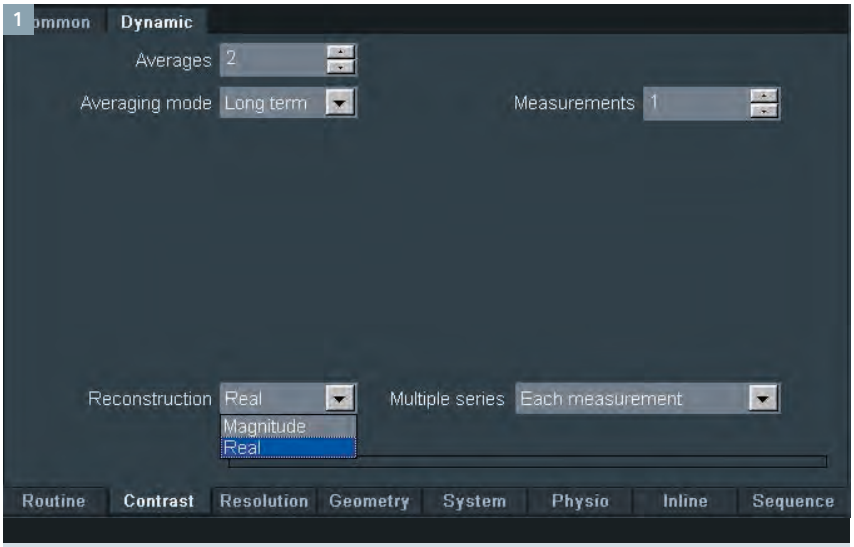

1 Parameter Card for choosing magnitude or phase sensitive (real) reconstruction method in an Inversion Recovery sequence.

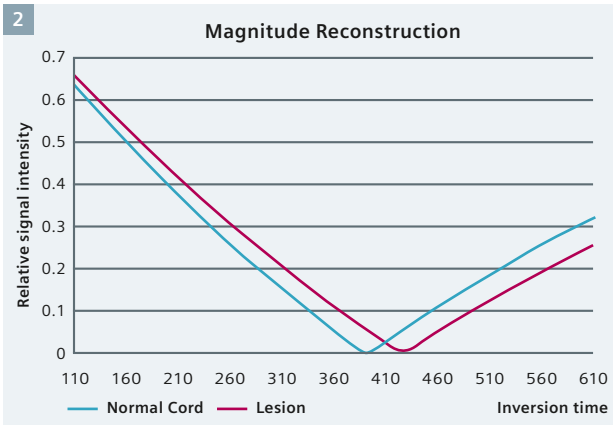

2 Signal behavior in an inversion recovery sequence using magnitude reconstruction.

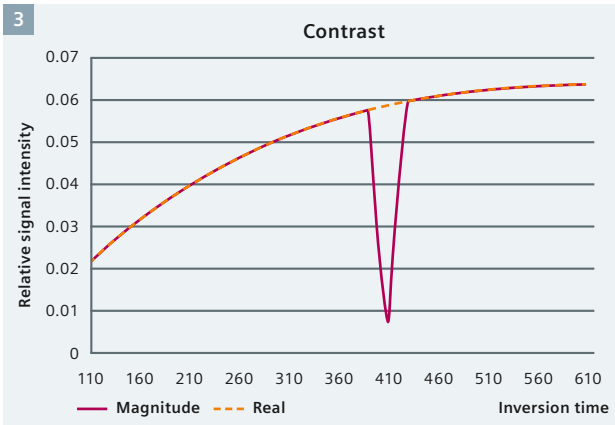

3 Contrast behavior in an inversion recovery sequence using magnitude or phase sensitive (real) reconstruction.

the cortex and reveals cortical lesions as hyperintense relative to normal surrounding gray matter. It also provides a high contrast between white matter lesions and the surrounding normal white matter. Initial studies have investigated the applicability of DIR for lesion imaging in the spinal cord with positive results [3]. Nevertheless, while SPACE-DIR provides a high contrast and isotropic voxels, its rather long acquisition time (~8 min) may prove challenging within a clinical setting.

T1-weighted phase sensitive inversion recovery

A promising potential alternative for imaging MS lesions in the cervical spinal cord [4], is the T1-weighted true or phase sensitive inversion recovery (PSIR) sequence. This technique has been used to detect MS lesions both in white and cortical gray matter in the brain [5, 6]. This sequence exploits the differences in T1 relaxation times of tissues rather than the differences in T2 relaxation times as for both FLAIR and SPACE-DIR.

Since the inversion time used is chosen such that it nulls the signal of normal white matter (~350–400 ms @ 3T), normal white matter is displayed as intermediate gray. All other tissues will have either lower or higher signal intensity than normal white matter depending on their T1 relaxation time relative to normal white matter. This provides a high contrast between MS lesions and surrounding tissue. Moreover, because PSIR uses a short TE, it is less sensitive to flow artifacts. High resolution imaging can also be achieved within reasonable scan times.

Based on these advantages, T1-weighted PSIR is now being explored for the detection of MS lesions in the cervical spinal cord.

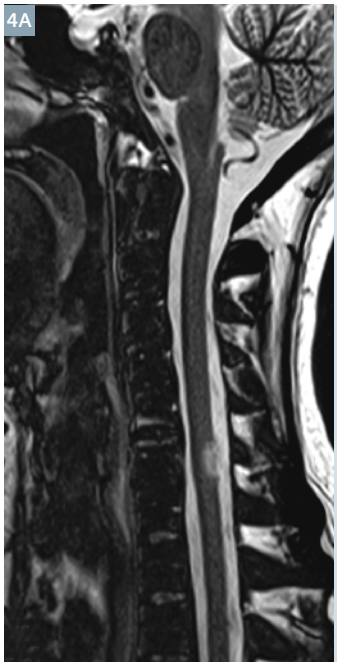

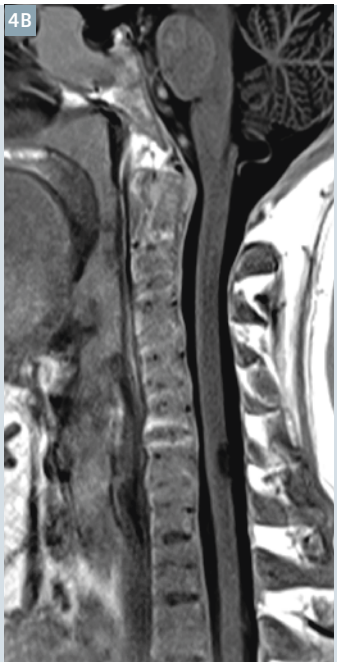

4 T1-weighted PSIR images using **(4A)** magnitude and **(4B)** phase sensitive (real) reconstructions.

Reconstruction methods

The T1-weighted PSIR images can be reconstructed as a magnitude or a phase sensitive (real) image (Fig. 1).

Magnitude reconstruction

The magnitude reconstruction does not consider the sign of the signal. Therefore, the tissue which is nulled by the inversion time will have a signal intensity of zero and all other tissues will have higher signal intensity (ranging from 0 to +4096), regardless of whether they have shorter or longer T1 relaxation time than the nulled tissue (Fig. 2). However, there is a range of inversion times where the contrast between two different

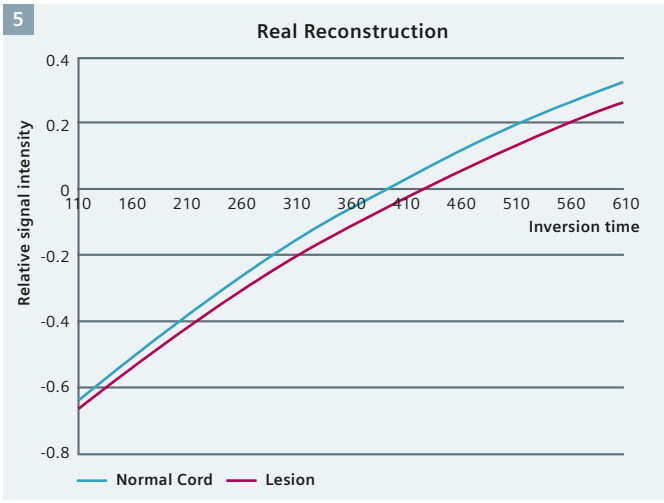

5 Signal behavior in an inversion recovery sequence using phase sensitive (real) reconstruction.

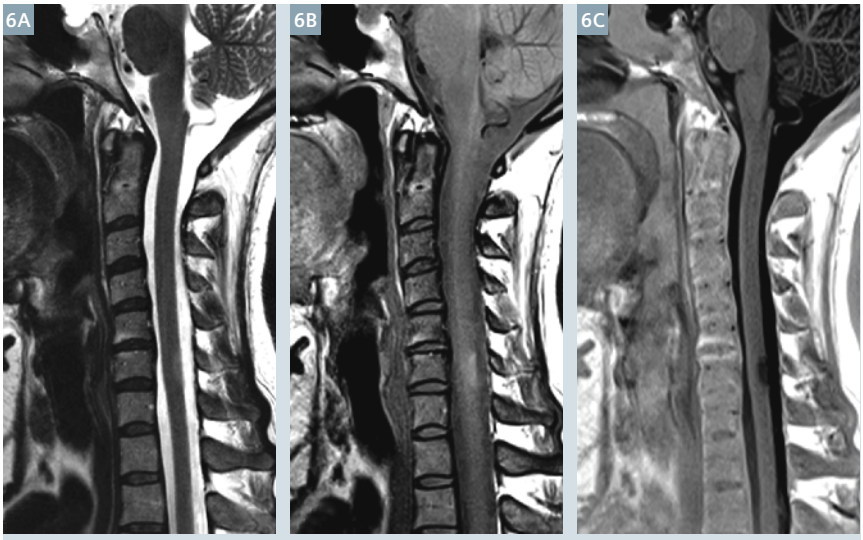

6 T2- **(6A)**, PD- **(6B)** and T1-weighted **(6C)** PSIR images of a patient with a known MS lesion at the level of C6 (Case 1).

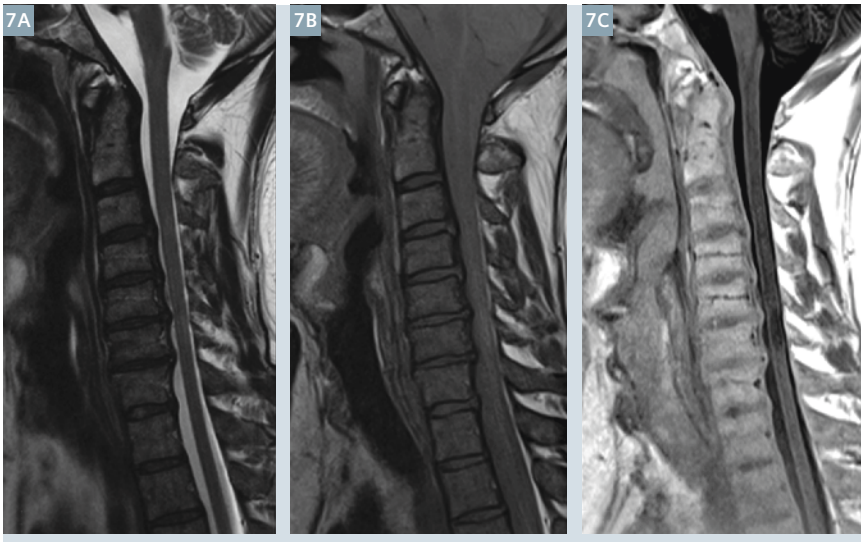

7 T2- **(7A)**, PD- **(7B)** and T1-weighted PSIR **(7C)** images of a patient with known diffuse MS lesions at the level of C3–C6 (Case 2).

tissues, e.g., lesion and normal tissue, can be decreased or even disappear. This range depends on T1 relaxation times of the two tissues and range between the two inversion times that would null one or the other tissue. In the example shown in figure 3, it ranges from approximately 390 to 430 ms. An example of the magnitude image is shown in figure 4A.

Phase sensitive reconstruction

In the phase sensitive reconstruction, the sign of the signal is taken in account for the reconstruction of the image (Fig. 5). As opposed to the magnitude reconstruction where the signal intensity in the image ranges from 0 to +4096, for the phase sensitive reconstruction it ranges from -4096 to +4096. This results in an image where the tissue which is nulled by the inversion time will be displayed as intermediate gray and all other tissues will have a lower or higher signal intensity depending on their T1 relaxation times relative to the T1 relaxation time of the nulled tissue. Tissues with a shorter T1 relaxation time will have a higher signal (e.g. fat), whereas tissues with a longer T1 relaxation time will have lower signal (e.g. CSF). Unlike the magnitude reconstruction, the contrast between tissues remains largely preserved independent of the chosen inversion time. Since the T1 relaxation time of lesions might vary from patient to patient and even from lesion to lesion, the phase sensitive reconstruction should be used to reconstruct the images. An example of the phase sensitive reconstruction is shown in figure 4B.

Clinical Cases

Case 1

Patient with a MS lesion at the level of C6 (Fig. 6). The lesion is difficult to see on the T2- and PD-weighted images. However, the MS lesion can be clearly seen in the T1-weighted PSIR image.

Case 2

Patient with diffuse MS lesions in the spinal cord from level C3 to C6 (Fig. 7). The lesions are hardly visible on the T2- and PD-weighted images, whereas the T1-weighted PSIR shows the lesions more clearly.

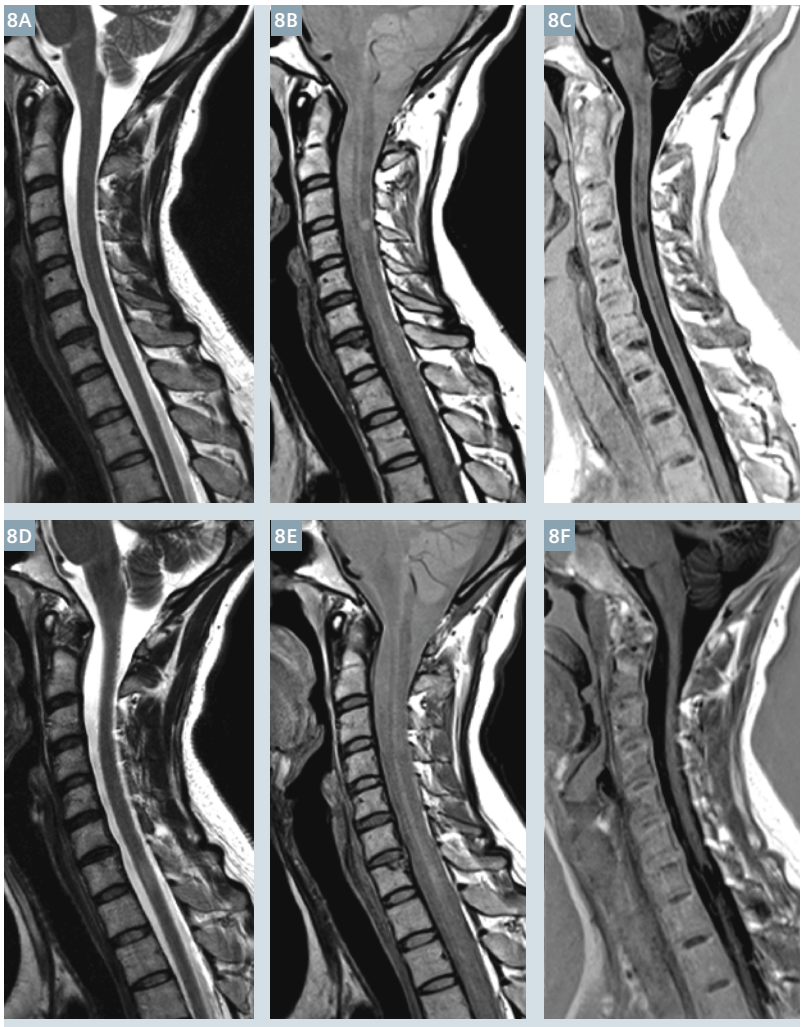

8 T2- **(8A, D)**, PD- **(8B, E)** and T1-weighted PSIR **(8C, F)** images of a patient with known MS lesions at the level of C3–C4 (top row) and C7-T1 (bottom row) (Case 3).

Table 1: Imaging parameters for the sequences used in the clinical cases.

	t2_tse_sag_384	pd_tse_sag_p2	t1_tir_sag_ms
TR	3500.0 ms	2500.0 ms	2400.0 ms
TE	106.0 ms	23 ms	9.4 ms
TI			400 ms
Slices	15	15	15
Slice thickness	3.0 mm	3.0 mm	3.0 mm
FOV Read	220 mm	220 mm	220 mm
FOV Phase	100.0%	100.0%	100.0%
Magn. preparation	None	None	Slice-sel. IR
Base resolution	384	320	320

Case 3
Patient with a known MS lesion at the level of C3-C4 (Figs. 8 A–C) and C7-T1 (Figs. 8 D–F). The lesion at the level of C3-C4 can hardly be seen on the T2-weighted image. Both the PD- and the T1-weighted PSIR show this lesion clearly. While the lesion at the level of C7-T1 is poorly visible on the T2- and PD-weighted images, the T1-weighted PSIR shows it very clearly.

Imaging Parameters
The parameters for the sequences used in the clinical cases are listed in table 1.

Conclusion

The T1-weighted PSIR shows great potential in revealing MS lesions in the cervical spinal cord. While using this technique it is important to use the phase sensitive reconstruction to preserve the contrast between MS lesions and normal appearing tissue. Due of the nature of the reconstruction, and because T1 values of lesions can vary from patient to patient, for reliable depiction of lesions, the phase sensitive reconstruction is recommended. This is as, unlike the magnitude reconstruction, the phase sensitive reconstruction provides a contrast between different tissues that is largely independent of the chosen inversion time.

Acknowledgements

We acknowledge the invaluable support of Dr. Montanera, Dr. Alcaide Leon and Mrs. Karima Murji of St. Michael's Hospital (Toronto, Canada) for providing the clinical cases and their feedback.

References

1 Honig LS, Sheremata WA. Magnetic resonance imaging of spinal cord lesions in multiple sclerosis. J Neurol Neurosurg Psychiatry. Apr 1989;52(4):459-466.
2 Noseworthy JH, Lucchinetti C, Rodriguez M, et al. Multiple sclerosis. N Engl J Med. Sep 28 2000;343(13):938-452.
3 Shipp D. Case Report: Cervical Spine 3D Double Inversion Recovery (DIR) in Demyelination. MAGNETOM FLASH magazine 1/2012 ISMRM Edition: 49-50
4 Poonawalla AH, Hou P, Nelson FA, Wolinsky JS, Narayana PA. Cervical Spinal Cord Lesions in Multiple Sclerosis: T1-weighted Inversion-Recovery MR Imaging with Phase-Sensitive Reconstruction. Radiology. 2008 Jan; 246(1): 258-264.
5 Hou P, Hasan KM, Sitton CW, Wolinsky JS, Narayana PA. Phase-sensitive T1 inversion recovery imaging: a time-efficient interleaved technique for improved tissue contrast in neuro-imaging. AJNR Am J Neuroradiol 2005;26:1432–1438.
6 Nelson F, Poonawalla AH, Hou P, Huang F, Wolinsky JS, Narayana P. Improved visualization of intracortical lesions in multiple sclerosis by phase-sensitive inversion recovery in combination with fast double inversion recovery MR imaging. Presented at the 22nd Congress of the European Committee for the Treatment and Research in Multiple Sclerosis, Madrid, September 27–30, 2006; 639.

Download

Visit us at
www.siemens.com/
MAGNETOM-world
to download the .edx file for
3T MAGNETOM Skyra

Contact

Bart Schraa, MSc.
Siemens Canada Ltd.
NAM RC-CA H CX-CS APP
1577 North Service
Road East
L6H 0H6 Oakville ON
Canada
Phone: +1 (416) 818 6795
bart.schraa@siemens.com

Expert Talks

Don’t miss the talks of experienced and renowned experts covering a broad range of MR imaging

Highest quality imaging in an optimized clinical workflow

Johan Dehem, M.D.
VZW Jan Yperman, Ieper, Belgium

MR/PET and radiology as information business

Dieter Enzman, M.D.
University of California Los Angeles, Los Angeles, CA, USA

Visit us at **www.siemens.com/magnetom-world**
Go to **Clinical Corner > Clinical Talks**

Save the Date

Heidelberg Summer School

Musculoskeletal Cross Sectional Imaging 2014

July 25th / 26th 2014
Heidelberg, Germany

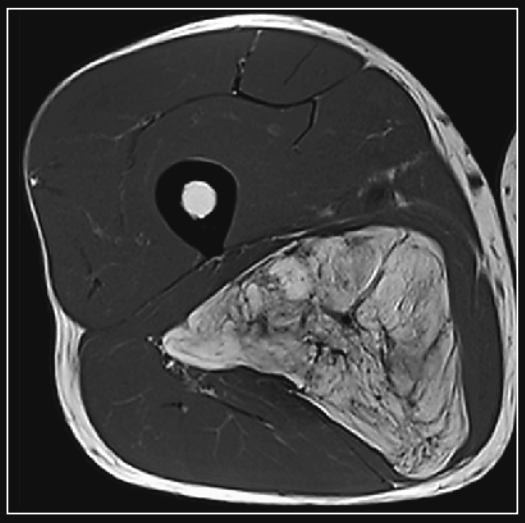

The Heidelberg Summer School offers advanced learning opportunities and promotes the academic exchange of knowledge, ideas, and experiences by bringing together physicians and professional staff from all over the world. Excellent speakers will cover a wide range of medical, physical, and technical topics in musculoskeletal imaging. All lectures are in English.

Course director

Marc-André Weber, M.D., M.Sc.

Professor of Radiology, Section Head Musculoskeletal Radiology at the University Hospital Heidelberg

CME Accreditation

The symposium will be accredited by the 'Landesärztekammer Baden-Württemberg' with CME credits (category A).
Also, the symposium is accredited for 1 category 3 credit point for the ESSR diploma by the European Society of Musculoskeletal Radiology.

Registration

Mrs. Marianne Krebs, Secretary of the Section Musculoskeletal Radiology

Marianne.Krebs@med.uni-heidelberg.de

For further information please visit:

www.heidelbergsummerschool.de

Pictorial Essay
Benign and Malignant Bone Tumors: Radiological Diagnosis and Imaging Features

Katharina Grünberg, M.D.; Christoph Rehnitz, M.D.; Marc-André Weber, M.D., M.Sc.

Section Musculoskeletal Radiology, Diagnostic and Interventional Radiology,
University Hospital Heidelberg, Germany

Topics

The learning objectives of this review article are to identify benign vs. malignant criteria in bone tumor diagnosis and also to differentiate the types of bone tumors and their characterization. Based on the Lodwick classification an overview of the three main types of bone destruction patterns visible on radiographs will be given with many examples. Typical examples of benign and malignant bone tumors will be demonstrated, the various imaging modalities will be compared, and their utility will be discussed. The image gallery comprises pearls and pitfalls. Presentation of standardized magnetic resonance imaging (MRI) protocols will be given. Of course, this pictorial essay does not have the focus of comprehensively presenting all bone tumor entities.

Introduction

Primary bone tumors are categorized according to their tissue of origin into cartilage, osteogenic, fibrogenic, fibrohistiocytic, haematopoietic, vascular, lipogenic tumors and several other tumors, like Ewing sarcoma and giant cell tumor [1]. Thy are also classified as either benign, malignant or semi-malignant, as well as tumor-like lesions [2]. They are rare, but found on radiographs during an investigation of a painful skeletal region or incidentally, e.g. when performing a joint or whole-body MRI. You will need four diagnostic columns to make a diagnosis of a bone tumor.

1

Four diagnostic columns

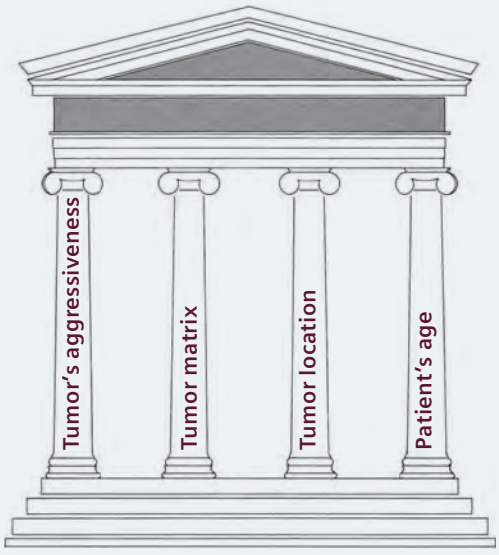

1. Malignant vs. benign?
   X-rays:
   Aggressiveness: Analysis of growth rate (Lodwick classification), periosteal reaction?
   Further imaging modality → CT, MRI?
   Make a specific diagnosis:
2. Analysis of tumor matrix: X-rays, CT: Osteolytic, osteoblastic, mixed
3. Location within the tumor-bearing bone: Epi-, meta-, diaphysis
4. Patient's age, (affected bone)

in 80% correct specific diagnosis [4]

1 The four diagnostic columns needed to achieve a correct, specific diagnosis in about 80% of cases [4].

Four diagnostic columns (Fig. 1)

Tumor's aggressiveness
The radiograph is the first method to distinguish benign from malignant lesions: at first by analysing the aggressiveness (analysis of growth rate) of a lesion according to the classification of Lodwick [3]. In radiographs there is a correlation between bone tumor's growth rate and dignity. If you identify an aggressive growth pattern and/or malignant periosteal reaction another imaging modality like computed tomography (CT) or magnetic resonance imaging (MRI) is needed. MRI is important for defining the extension of tumor before biopsy.

Tumor matrix
In a second step, it is essential to analyze the mineralisation of tumor matrix in radiographs or CT. The matrix may be osteolytic, osteoblastic, or mixed, i.e. osteolytic with matrix mineralisation.

Tumor location and patient age
To make a specific tumor diagnosis, the location within the tumor-bearing bone (epi-, meta- and diaphysis) and the patient's age are also important. With an optimized combination of the different parameters, the expert achieves a correct, specific diagnosis in about 80% of cases [4, 5]. In other words, even a dedicated musculoskeletal radiologist fails to predict the correct histological diagnosis in one fifth of all cases.

Lodwick classification (Fig. 2)

Based on the Lodwick classification, an overview of the three main types of bone destruction patterns visible on radiographs are given with a representative example:

Type 1: geographic (with a: well-defined border with sclerotic rim, b: well-defined and sharp border but without sclerotic rim, c: ill-defined and blurred border);

Type 2: geographic with moth-eaten or permeated pattern (patchy lysis);

Type 3: small, patchy, ill-defined areas of lytic bone destruction with moth-eaten or permeated pattern (patchy lucencies) [3, 6].

2

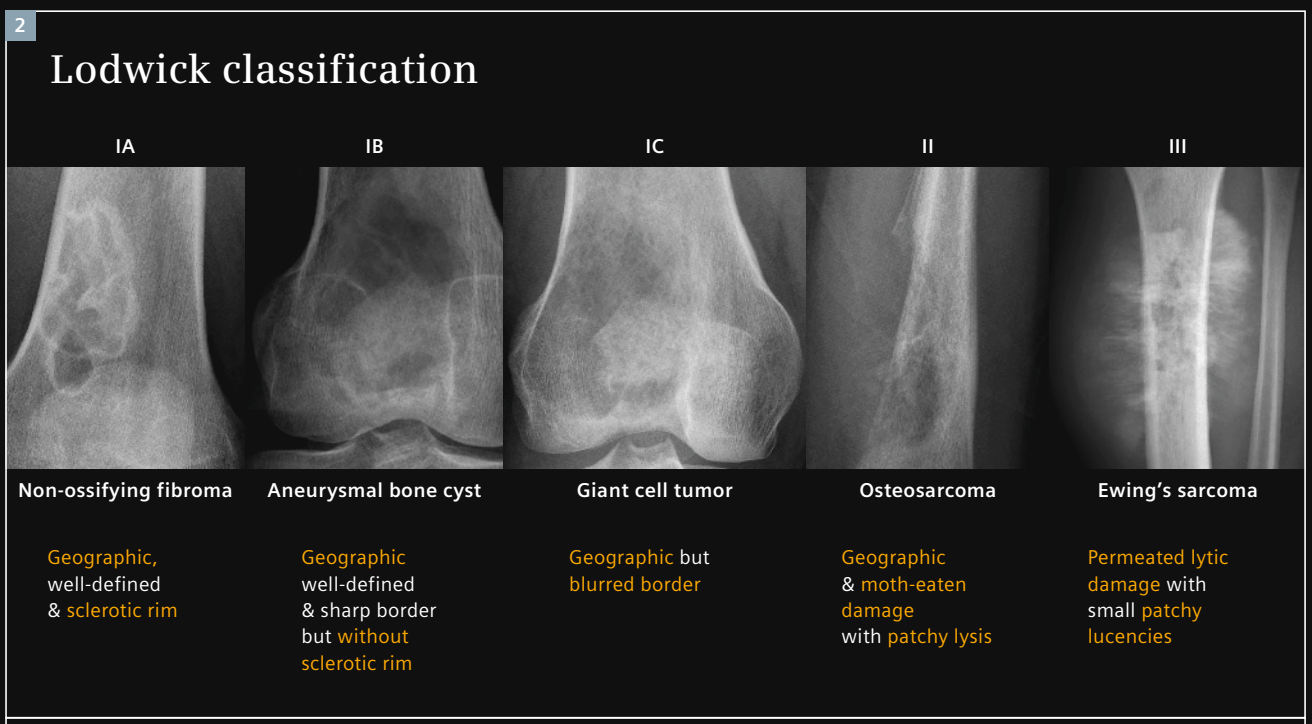

2 Lodwick classification: An overview of the three main types of bone destruction patterns with representative image examples.

Criteria of malignancy (Fig. 3)

Periosteal reactions are also indicators of lesion aggressiveness and can be differentiated according to a benign (thick, dense, wavy) type or an aggressive (lamellated, amorphous, sunburst) type. Figures 3A–D show an example of an 80-year-old man with a cloudy inhomogeneous tumor of the distal humerus with perpendicular periosteal reaction of a malignant sunburst type, partial cortical destruction and a big soft tissue component, best seen in MRI. All these criteria suggest a malignant process. Differential diagnoses are osteosarcoma or bone metastasis. Biopsy results in the diagnosis of metastasis of rectal cancer (adenocarcinoma).

Types of bone tumors

According to their type of matrix (osteolytic, osteoblastic, or osteolytic with matrix mineralization) and to their tissue of origin, bone tumors are categorized into different types: osteoid, chondroid, fibrous, lipoid/fatty, other, cystic (solitary bone cyst, aneurysmal bone cyst), vascular (hemangioma), special cell type: Giant cell (osteoclastoma), small cell (Ewing's sarcoma), histiocytes (eosinophilic granuloma), plasma cells (multiple myeloma), notochordal cells (chordoma) and metastases.

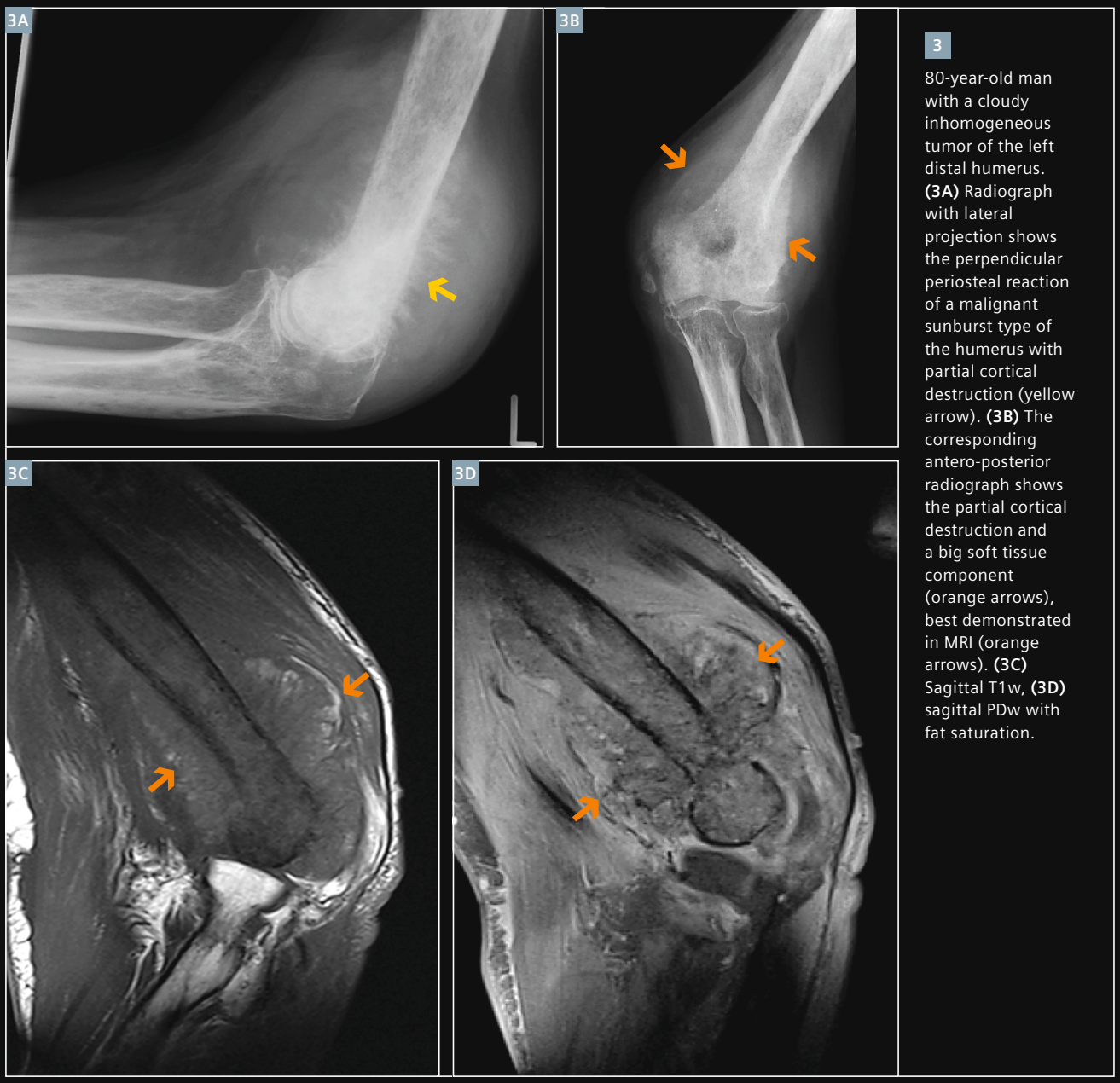

3

80-year-old man with a cloudy inhomogeneous tumor of the left distal humerus. **(3A)** Radiograph with lateral projection shows the perpendicular periosteal reaction of a malignant sunburst type of the humerus with partial cortical destruction (yellow arrow). **(3B)** The corresponding antero-posterior radiograph shows the partial cortical destruction and a big soft tissue component (orange arrows), best demonstrated in MRI (orange arrows). **(3C)** Sagittal T1w, **(3D)** sagittal PDw with fat saturation.

Osteoid type

Osteoid osteoma and Osteoblastoma (Fig. 4)
This entity is frequent: around 13.5% of all benign bone tumors are osteoid osteomas. The patients are usually younger than 30 years and suffer „night pain relieved by aspirin" and other platelet aggregation inhibitors. The main location is in more than 50% within diaphysis of long bones and in 10% within the vertebral column with painful scoliosis. Osteoid osteomas show in CT and X-ray a perifocal sclerotic lesion with a central lucency (nidus) that is cortically based in 80%. Medullary, subperiosteal and articular locations also occur. Calcification of the nidus is possible. The nidus is extremely vascular in contrast-enhanced MRI and it is important to identify the nidus as the tumor itself; surrounding sclerosis and bone marrow edema pattern is just reactive. It should be noted that lesions may have less or no sclerosis if the nidus is located in the marrow or in/adjacent to a joint (Fig. 5). Osteoid osteoma resembles osteomyelitis: For example if a Brodie's abscess is in an eccentric position, e.g. cortically located, it is difficult to differ Brodie's abscess from osteoid osteoma. The differentiation can then only be done by biopsy or radionuclide bone scan:

Osteoid osteoma shows – in contrast to osteomyelitis – the 'double density sign' (i.e. a high intense central activity surrounded by an area of medium activity). A lesion larger than 1.5 cm is called osteoblastoma [7, 11]. Radiofrequency ablation (RFA) is a successful treatment [8, 9, 10].

Keys to diagnosis: Sclerotic lesion with a small lucency in X-ray.
The nidus shows a high signal on T2-weighted MR images and has a strong contrast-enhancement.

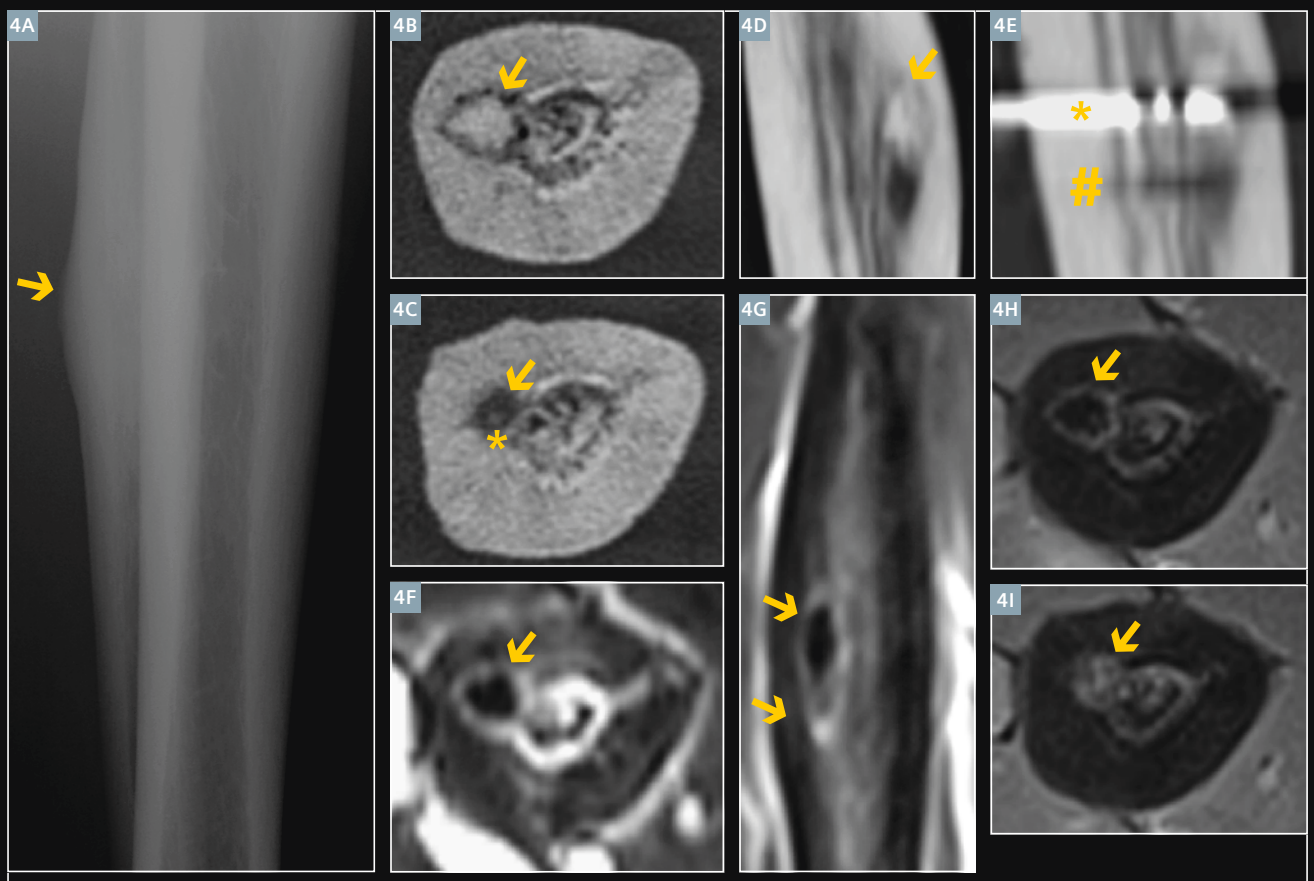

4 16-year-old male patient with osteoidblastoma (OB) of the right fibula. **(4A)** lateral radiograph shows well the cortical swelling of the fibula in the patient with OB but without lucency. The reason for that is best seen in **4B**, **C** (axial CT in different positions) and **4D** (coronal CT), where the upper part of the nidus is completely calcified whereas the smaller lower part shows only little calcification (*). **(4E)** shows a coronal CT with the ablation cannula (*) in the upper calcified part of the nidus during CT-guided radiofrequency ablation and the second ablation channel thereunder (#). T2w STIR images (**4F** axial and **4G** coronal) as well as T1w axial images **(4H, I)** demonstrate the vascularisation of the lower and the calcification of the upper nidus part with low T2w signal.

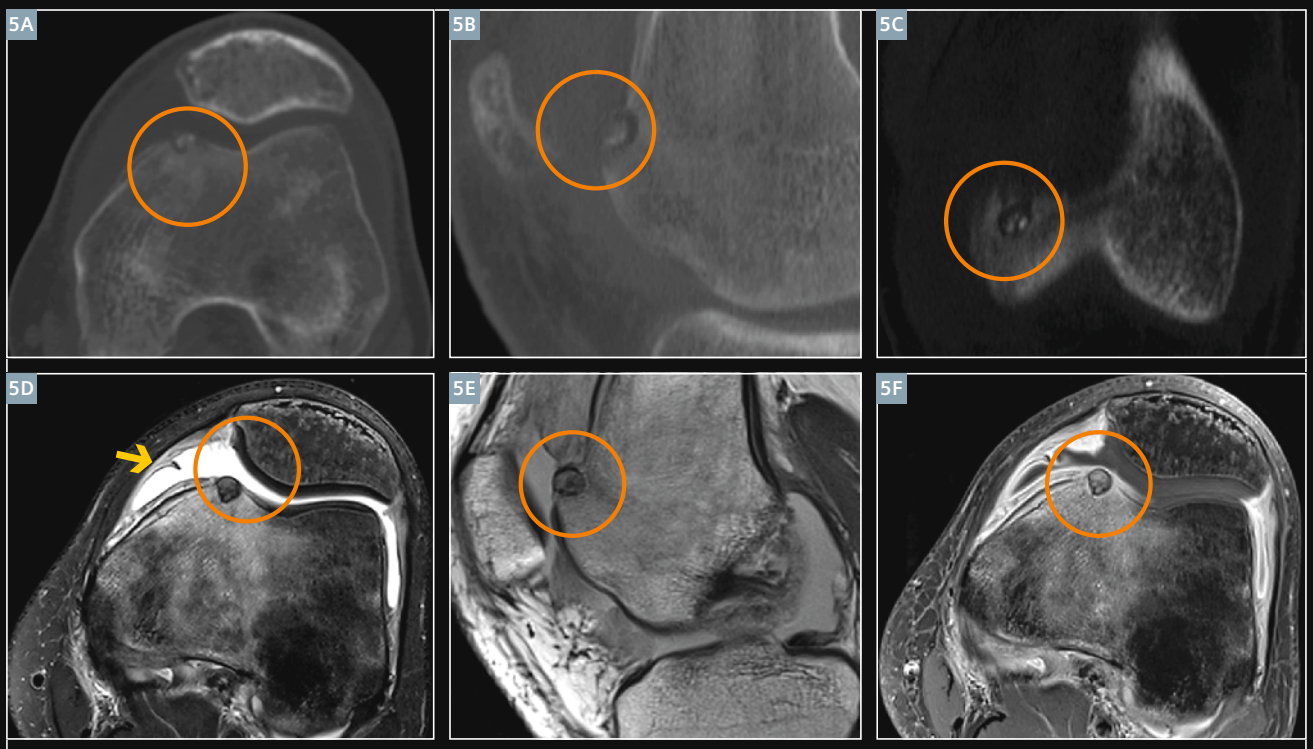

5 17-year-old male patient with articular osteoid osteoma (OO) of the left knee joint. **(5A–C)** Axial, sagittal and coronal CT with the articular position of the OO show no sclerosis of the nidus-margin (orange circle). In CT you see well that the nidus shows some central ossifications. The axial T2w MRI with fat saturation **(5D)** demonstrates the joint effusion and synovitis (yellow arrow). You can also see well that because of the central nidus calcifications the OO has only isointense to less hyperintense signal in T2w (orange circle) instead of the typical strong hyperintense signal. **(5E)** Sagittal PDw MRI also shows the calcification. **(5F)** Axial contrast-enhanced T1w MRI with fat saturation demonstrates the enhancing nidus (orange circle).

Osteosarcoma

The patients are usually younger than 20 years. A 2nd peak exists in the 5th decade and these cases are mostly secondary in Paget's disease and after irradiation. Osteosarcoma has a predilection for sites of rapid bone growth, usually the metaphyseal region. Typical symptoms are pain and local swelling. This entity shows typically destructive periosteal reactions as mentioned above (Fig. 6). Their X-ray morphology is very variable: Osteosarcomas may be osteogenic (i.e. the tumor induces new bone formation), lytic or mixed, which is the common manifestation form (Fig. 7) [12]. If such a lesion is lytic, consider also teleangiectatic osteosarcoma! From origin, sclerosis grade and soft tissue component, osteosarcomas are separated into a central, parosteal (originates from the periosteum) and a periosteal variant, which is very rare (1% of osteosarcomas). In periosteal osteosarcomas the process starts either in the periosteum or adjacent soft tissue. Typical – in contrast to parosteal osteosarcoma – the periosteal osteogenic sarcoma does not have large amounts of calcification in the soft tissue (Fig. 8) [11]. Osteosarcomas may produce osteoblastic lung metastases (Fig. 9).

Keys to diagnosis are to detect criteria of malignancy in X-ray and further imaging modalities: CT is the best for identifying periosteal reaction versus tumor matrix because you can already see faint mineralization in CT. In MRI the signal depends on the degree of matrix mineralization. But MRI is important for assessing the tumor extent and for staging purposes, i.e. to identify skip-lesions, to assess the soft tissue, nerve and vessel involvement, and a potential joint infiltration.

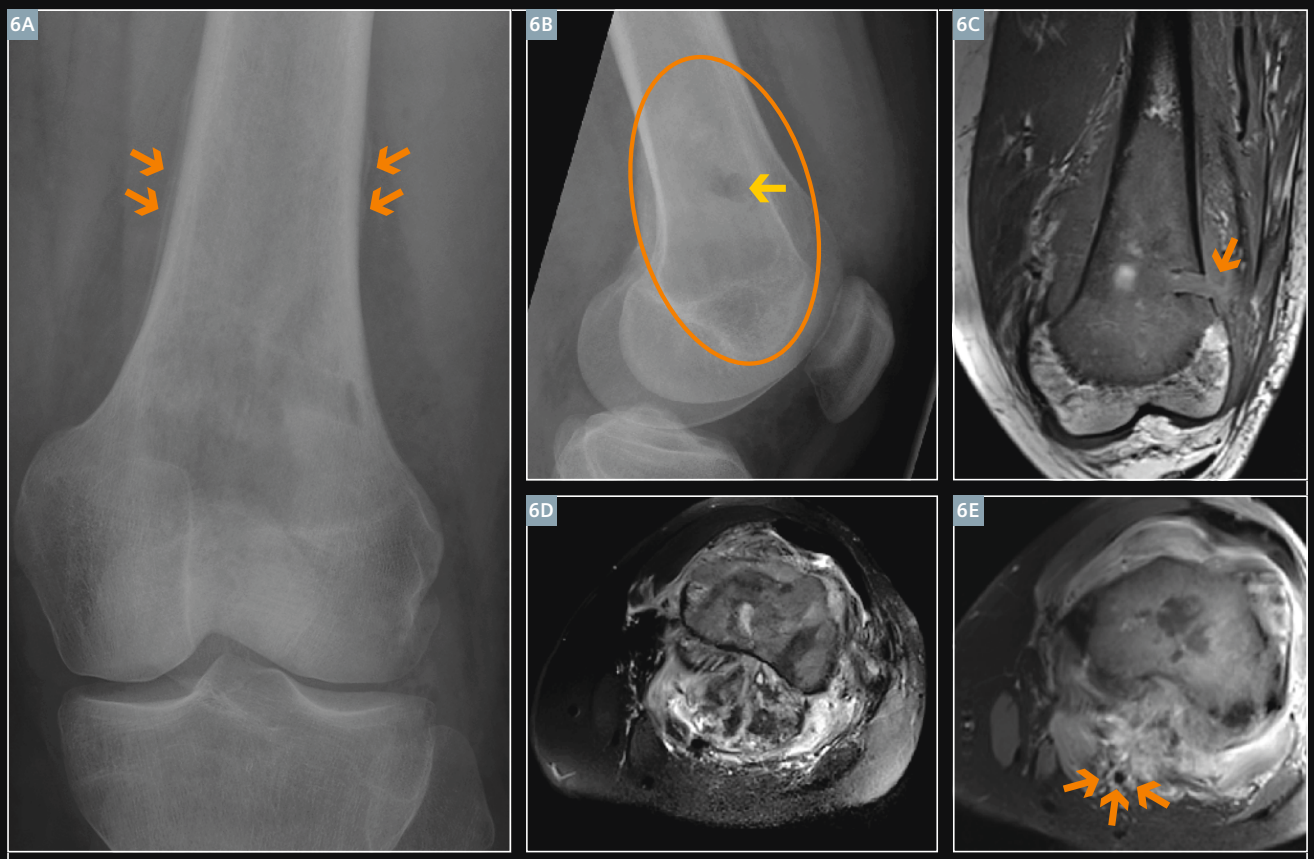

6 21-year-old man with a central high-grade osteosarcoma in the distal left femur. Conventional osteosarcomas are the central osteosarcomas placed in the center of the metaphysis. Figure **(6A)** shows the antero-posterior and **(6B)** the lateral radiograph. In this case you can see in addition to periosteal reactions (orange arrows in 6A) the channel-shaped lucency in the radiograph correlating with the biopsy channel (yellow arrow in 6B) within a disorganization of the bone pattern and osteoid formation (orange circle in 6B). You also see the biopsy channel in the coronal T1-weighted MRI (orange arrow in **6C**). Figure **6D** demonstrates the heterogeneity of the tumor mass (axial T2w MRI with fat saturation). Performing MRI is important for preoperative local staging, e.g. in this case the vessel infiltration (orange arrows in **6E**) is visible in the axial post-contrast T1-weighted MRI.

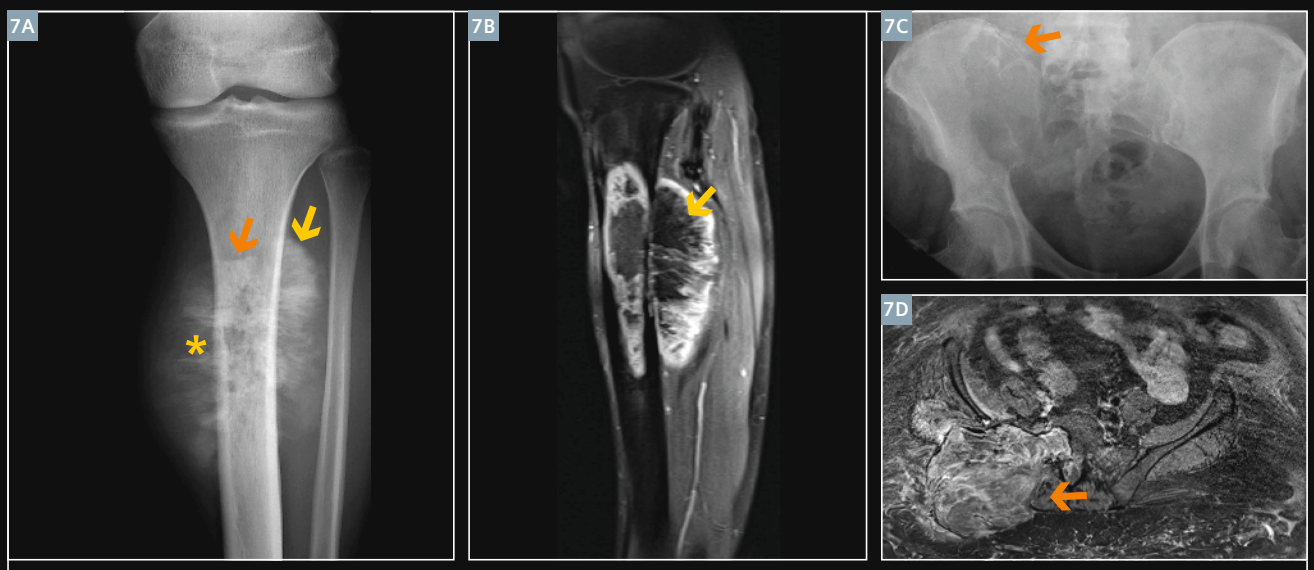

7 These images demonstrate well the difference between osteogenic versus lytic osteosarcoma. Figures **7A** (antero-posterior radiograph of the lower leg) and **7B** (sagittal contrast-enhanced T1w MRI with fat saturation of the lower leg) show an osteogenic parosteal osteosarcoma of the left tibia, a bone forming tumor with fluffy, amorphous, cloudlike mineralization (orange arrow in 7A) beside sunburst periosteal reaction as a criterion of malignancy (* in 7A). This tumor has a big soft tissue component (yellow arrow in 7B) with large amounts of calcification (yellow arrow in 7A). Figures **7C** (antero-posterior radiograph of the pelvis) and **7D** (axial contrast-enhanced T1w MRI with fat saturation) show a more lytic osteosarcoma of a 61-year-old female patient in the right os ileum with no mineralization (orange arrow).

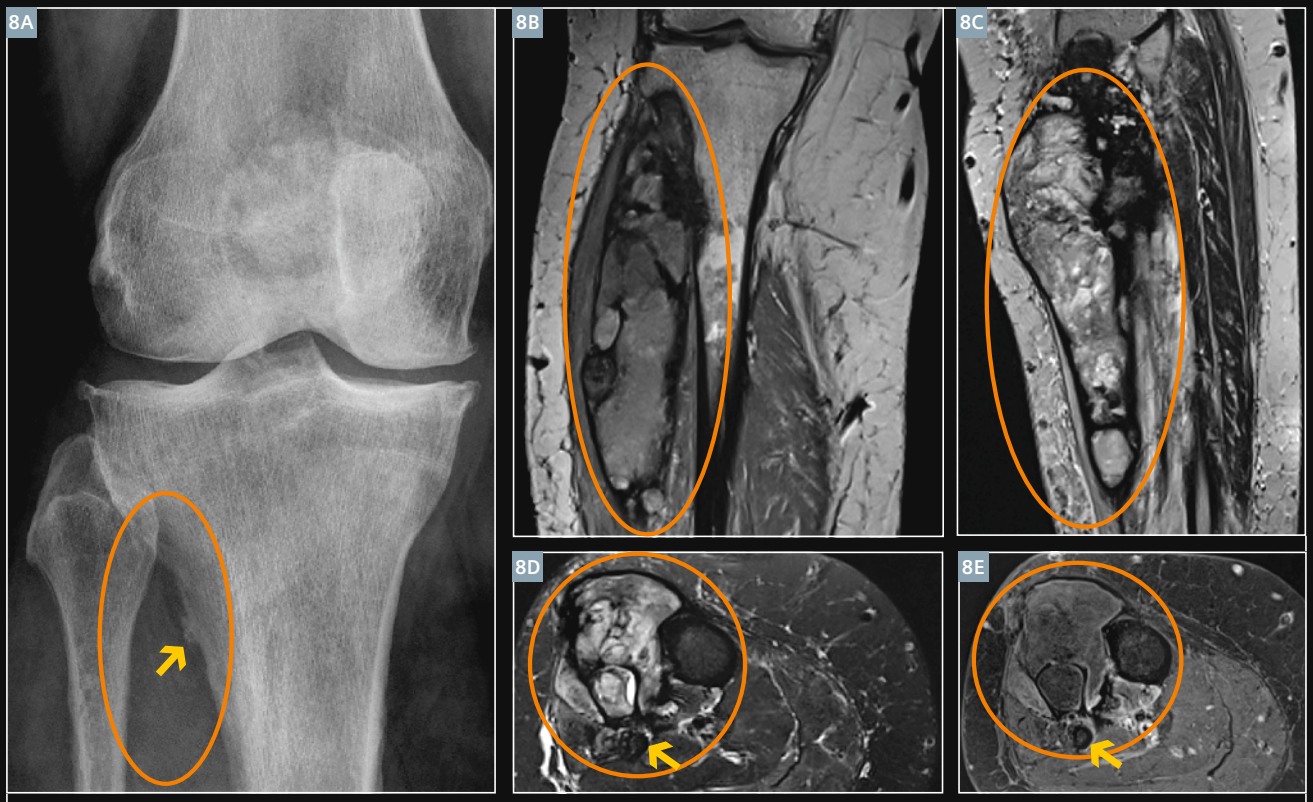

8 57-year-old female patient with a periosteal osteosarcoma (G3) of the right lower leg. Figure **8A**, antero-posterior radiograph of the right knee shows saucerization of the tibial metaphysic (orange circle) and also a bone prominence (yellow arrow). **8B** (coronal T1w MRI of the lower right leg) and **8C** (sagittal T1w MRI of the lower right leg) show the big inhomogeneous tumor with a large soft tissue component. Keep in mind that the periosteal osteogenic sarcoma does not have large amounts of calcification in soft tissue as shown in 8A–C (orange circle). Figures **8D** (axial T2w MRI with fat saturation) and **8E** (axial contrast-enhanced T1w MRI with fat saturation) clearly demonstrate that the tumor inexplicably will not invade the medullary space of the tibia (orange circle) and that the fibula is not involved (yellow arrow).

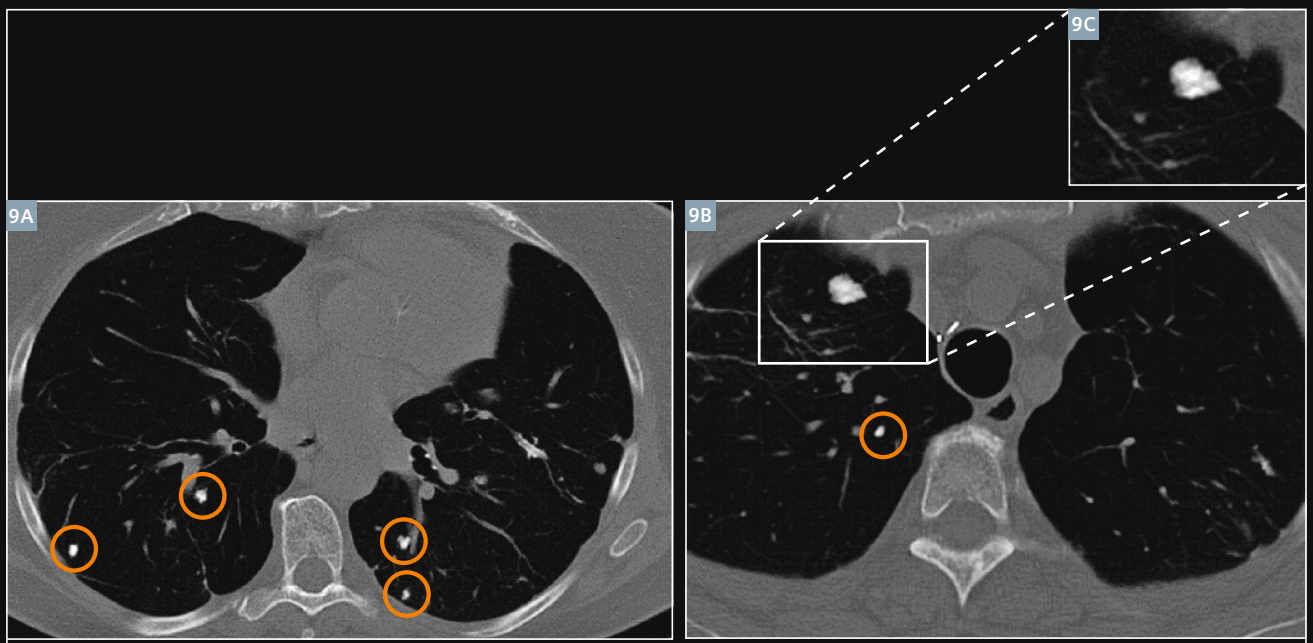

9 63-year-old female with osteoblastic lung metastases one year after resection of an osteosarcoma of the left thigh. Axial CT images **(9A–C)** show several osteoblastic lung metastases of a bone producing primary tumor: an osteosarcoma. Therefore the lung metastases may be also sclerotic.

Chondroid type

Enchondroma

Enchondroma is a benign lytic lesion typically placed in the hand and chiefly centrally located, often with endosteal scalloping. It must have calcification except in the phalanges (Fig. 10). A typical size of enchondroma is around 1–2 cm; low grade chondrosarcoma is larger than 4–5 cm. The enchondroma shows no periosteal reaction. An important differential diagnosis is the bone infarction (Fig. 12).

Keys to diagnosis are: In T1-weighted MR imaging the lesion has a low signal. The T2-weighted signal depends on the degree of calcification. After contrast-enhancement the tumor shows in T1-weighting MR imaging a lobulated appearance with septa (Figs. 10 and 11).

Suspicious of malignancy in chondroid tumors are pain, a size larger than 5 cm, the presence of a soft tissue mass and a growing surrounding edema on T2-weighted images.

Multiple enchondromas occur on occasion, a condition called Ollier's disease. This is not hereditary and with no increased rate of malignant degeneration.

By contrast, Maffucci's syndrome is a condition with multiple enchondromas associated with soft tissue hemangiomas. Maffucci's syndrome is likewise not hereditary, but is characterized by an increased incidence of malignant degeneration of the enchondromas [11].

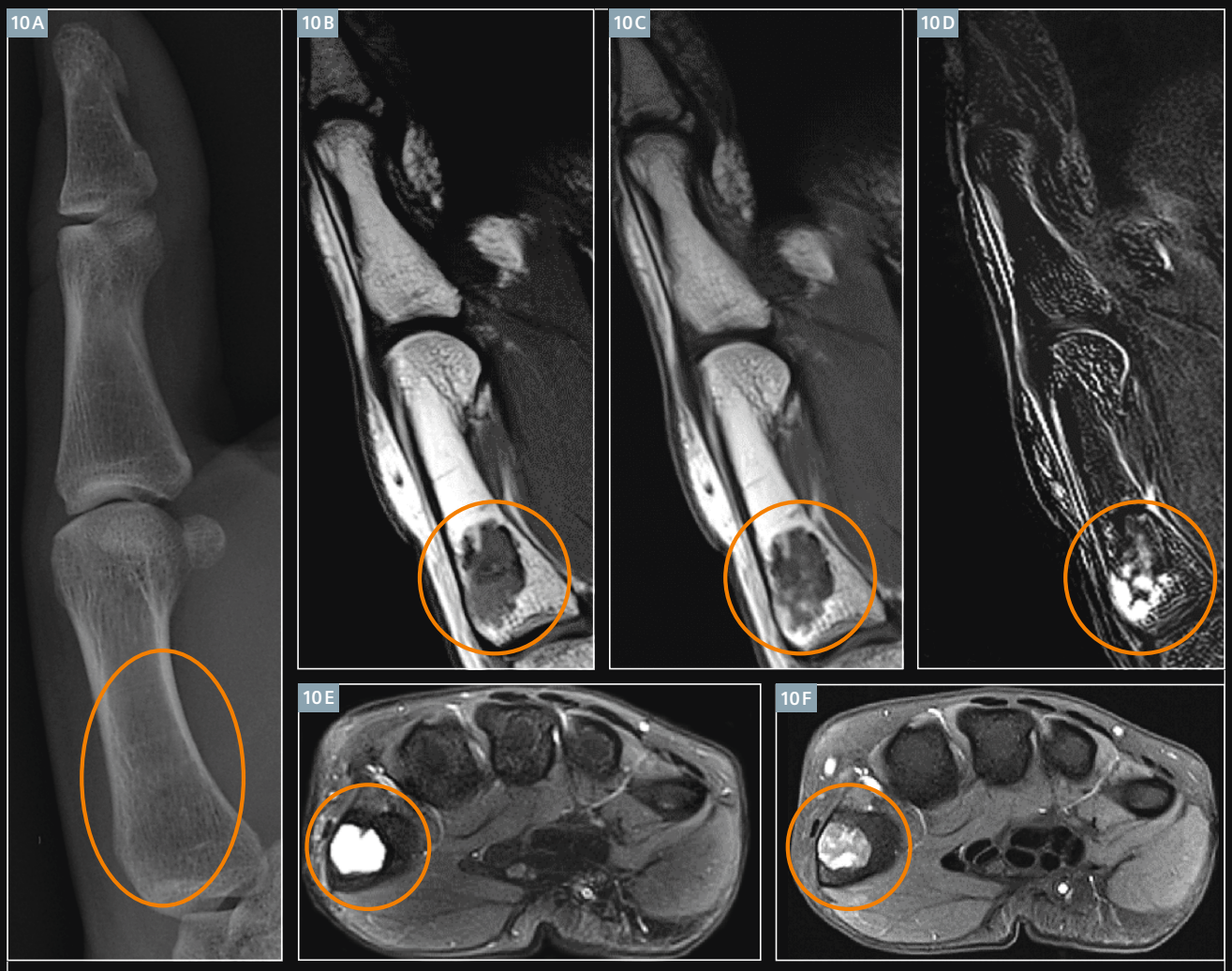

10 29-year-old female with an enchondroma of the phalanx D1. **(10A)** Lateral radiograph of the right D1 shows the lytic lesion in the proximal metacarpus of D1 which is hardly to identify and without sclerotic rim, according to a Lodwick IB lesion (orange circle) and without calcifications. (10B-F) show the typical signal characteristics of an enchondroma in MRI (orange circles) and that the lesion is smaller than 2 cm: low signal in T1-weighted imaging (**10B**, coronal), high signal in T2-weighted imaging because of absent calcification as shown in 10A (**10E**, axial T2w MRI with fat saturation). Coronal contrast-enhanced T1w MRI **(10C)**, coronal T1w MRI subtraction **(10D)**, and axial contrast-enhanced T1w MRI with fat saturation **(10F)**, show that the tumor has a lobulated appearance with septa.

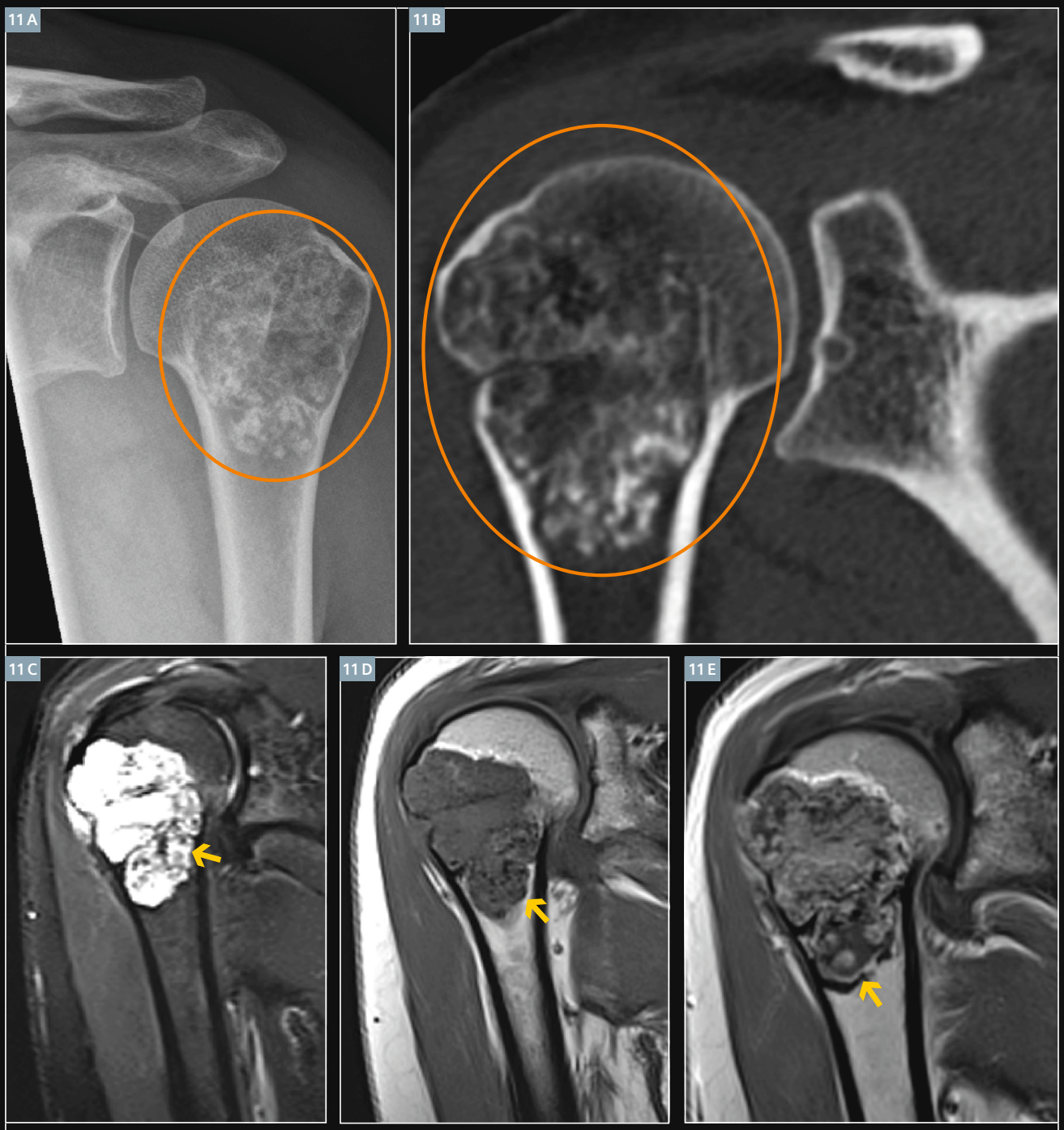

11 44-year-old female with an enchondroma within the humeral head. **(11A)** Antero-posterior radiograph of the shoulder, **(11B)** coronal CT of the shoulder, **(11C)** coronal T2w MRI with fat saturation, **(11D)** coronal T1w MRI, **(11E)** coronal contrast-enhanced T1w MRI. 11A and B show a lesion bigger than 2 cm with a sharp border (Lodwick IB) in the humerus head with the following different forms of calcification of the chondral tissue: Punctate, comma-shaped, arc like, ring like mineralization (orange circle). In T1w the tumor shows low signal **(11D)**, in T2w with fat saturation high signal with some low signals according to the calcifications, thus containing no fat **(11C)** and post-contrast a homogenous contrast-enhancement with a rough lobulated pattern **(11E)** (yellow arrows).

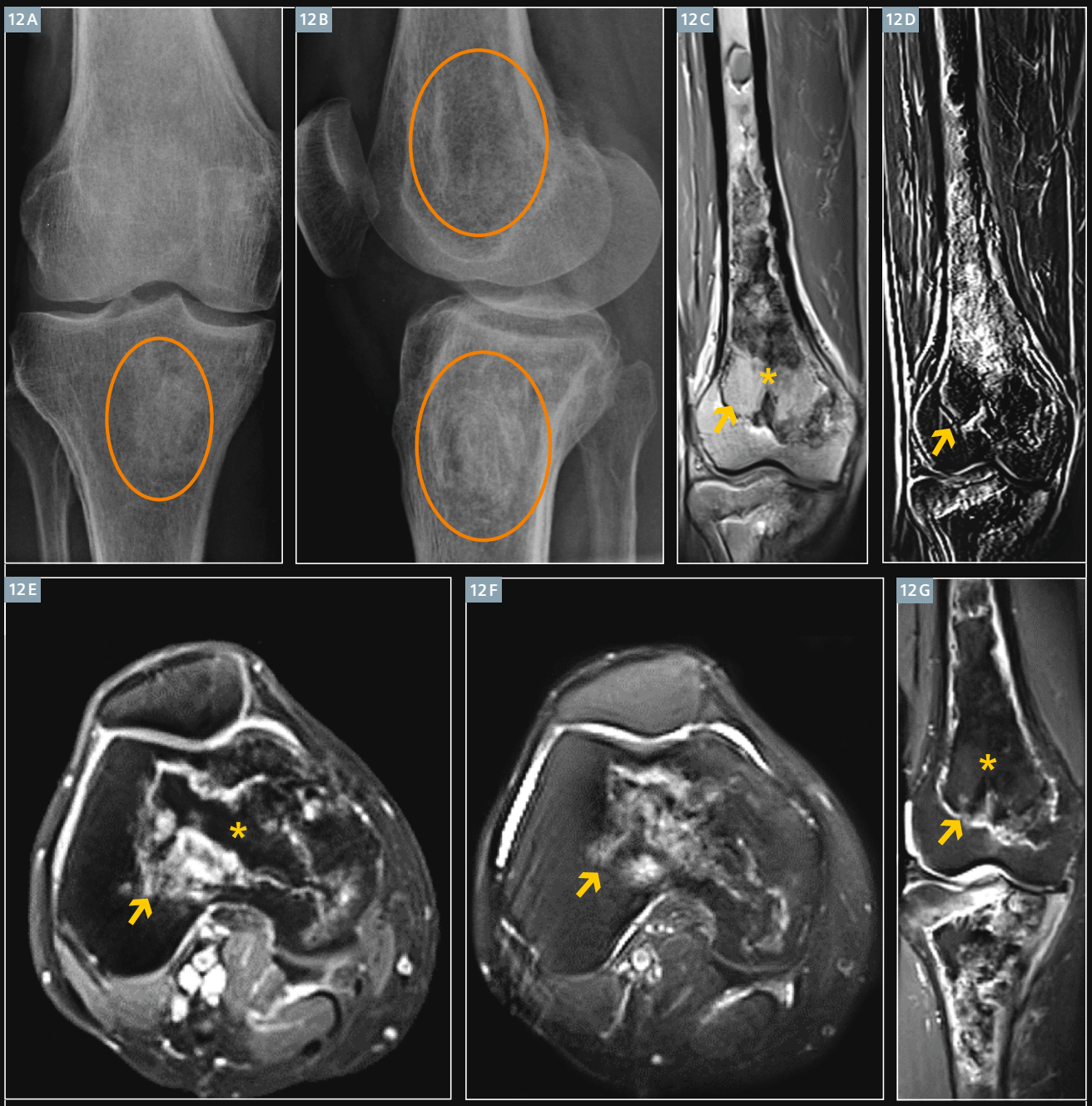

12 40-year-old female with bone infarction in the right tibia and femur. **(12A)** Antero-posterior, **(12B)** lateral radiograph of the knee, **(12C)** coronal contrast-enhanced T1w MRI, **(12D)** coronal T1w subtraction MRI, **(12E)** axial contrast-enhanced T1w MRI with fat saturation, **(12F)** axial T2w MRI with fat saturation, **(12G)** coronal STIR MRI. An infarct usually has a well-defined, densely sclerotic, serpiginous border as well shown in 12A and B (orange circles) and in MRI in 12C-G (yellow arrow), whereas an enchondroma does not. Fat in the lesion as seen in 12C, E and G (yellow star) is a hint of bone infarction and speaks against an enchondroma.

Chondroid type

Osteochondroma (Fig. 13)

A synonym for osteochondroma is cartilaginous exostosis. It is a common benign tumor of the extremities (10%–15% of all bone tumors) and is located in 50% of cases in the lower extremities, in 10–20% in the humerus, but rarely in the spine. For the diagnosis it is important to identify the continuation of bone marrow and trabecular bone structures into the exostosis as well as the cartilage cap. The malignant degeneration occurs mainly in tumors near the trunk.

Key to diagnosis is a mushroom-like tumor. The thickness of the cartilage cap is 8 mm or more (threshold in our institution, see also explanation in the next chapter) (Fig. 13) [13]. Contrast media is not needed to determine the thickness of the cartilage cap, because it is clearly visible on T2-weighted images.

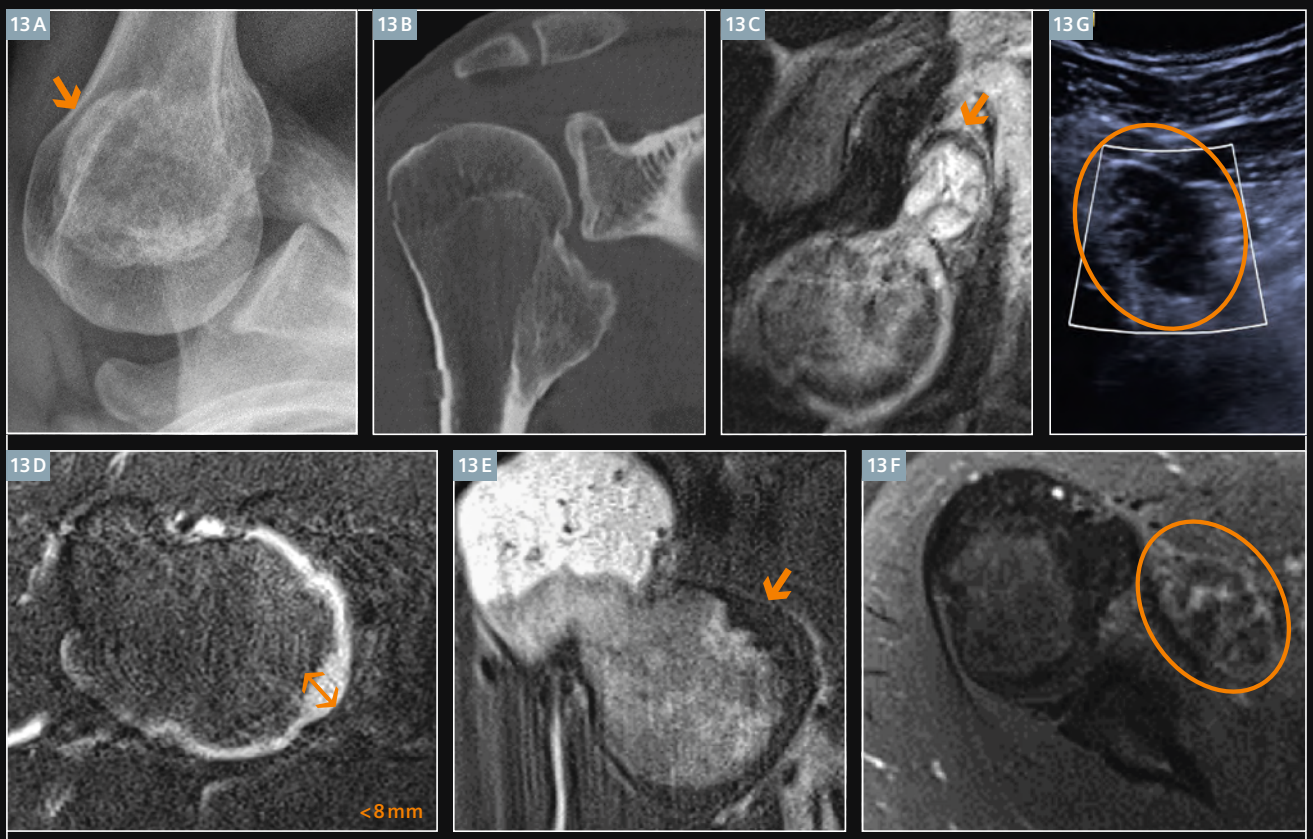

13 20-year-old male patient with an osteochondroma of the proximal right humerus and a loose body within joint space. **(13A)** Axial radiograph of the right shoulder shows the sharp-bordered tumor of the humerus, **(13B)** coronal CT shows the osteochondroma of the right shoulder, **(13C)** sagittal T2w MRI shows another part of the osteochondroma with its cartilage cap, where the cap seems to be much larger than 8 mm, see also 13F, **(13D)** axial T2w MRI with fat saturation shows the measurement of the T2w hyperintense cartilage cap with a distance of 8 mm, **(13E)** coronal T1w MRI shows the cartilage cap that is hypointense in T1w, **(13F)** axial contrast-enhanced T1w MRI with fat saturation show the same part of figure 13C with a chondroid lobated pattern after contrast-enhancement, **(13G)** 9 MHz ultrasound shows the structure seen in 13C and G as a round non-cystic structure. This lesion is with all imaging modalities suspicious of a low grade chondrosarcoma. After surgery and histologic examination revealed it to be no more than an osteochondroma and a neighboring loose body within joint space with caplike borders and nodose lobulated chondroid tissue with kept structure of the lobules.

Osteochondroma vs. chondrosarcoma

A malignant transformation is more likely if the cartilage cap thickness is 8 mm or more, which is the threshold of our clinic. Further publicized threshold values are 1.5 cm according to Murphey et al. [14] and 2.0 cm according to Bernard et al. [15]. Proximity to trunk (location in the pelvis with highest malignant transformation rate!) and hereditary multiple exostoses (autosomal dominant inheritance) (Fig. 14) are correlated with a higher risk of malignant transformation (3–5% of tumors develop into chondrosarcomas). A further criterion is a cartilage cap growth, especially beyond age 20. Note: It is extremely difficult for either a radiologist or a pathologist to differentiate a low-grade chondrosarcoma from enchondroma (Fig. 15).

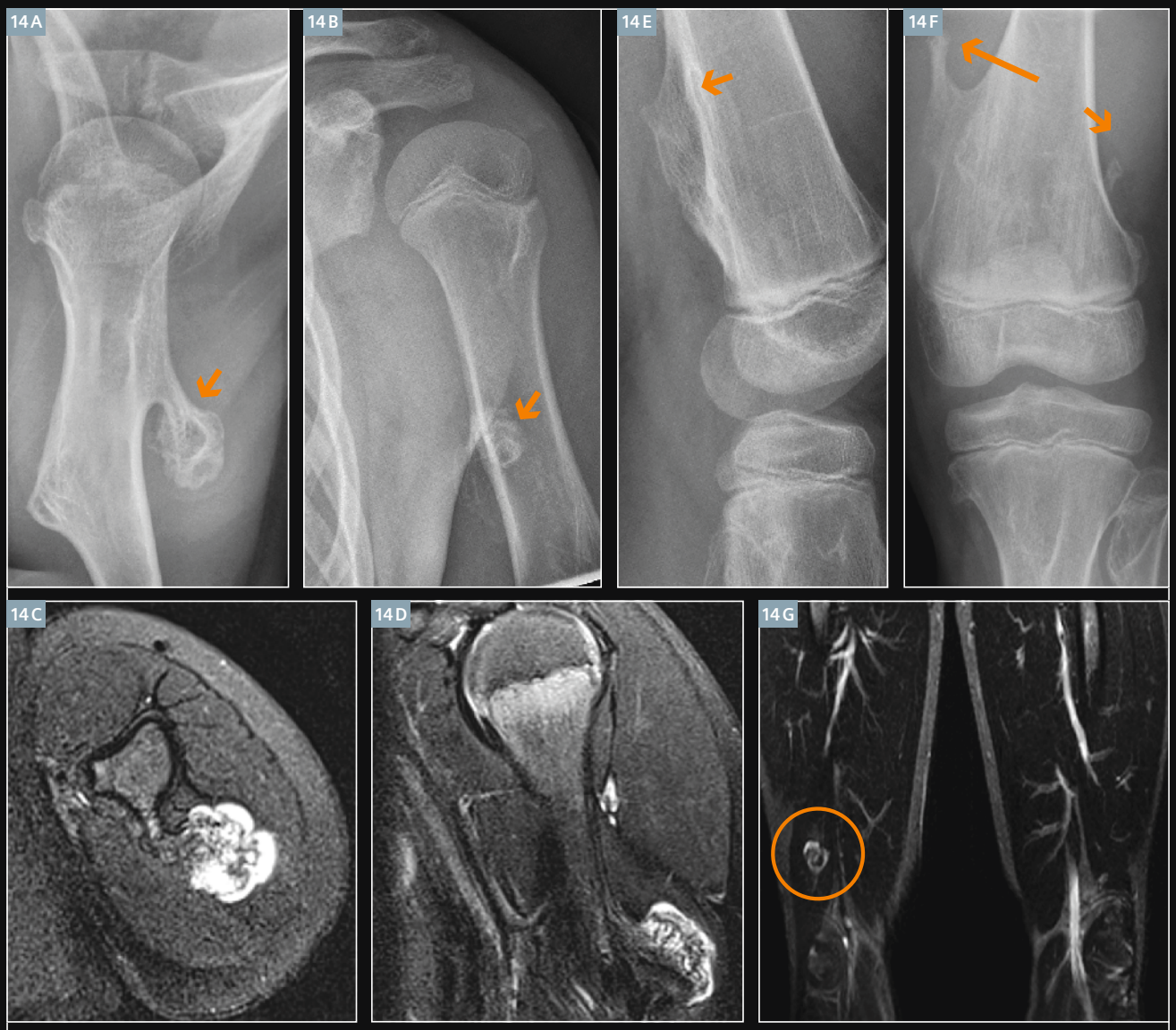

14 12-year-old male patient with hereditary multiple exostoses. **(14A)** Axial radiograph of the left shoulder, **(14B)** antero-posterior radiograph of the left shoulder, **(14C)** axial T2w MRI with fat saturation of the left humerus, **(14D)** sagittal T2w MRI with fat saturation of the left humerus, **(14E)** lateral radiograph of the left knee, **(14F)** antero-posterior radiograph of the left knee, **(14G)** coronal STIR MRI of the upper extremities. In 14A, B, E and F the continuation of bone marrow and trabecular bone structures into the exostosis are clearly depicted. The cartilage cap can be well evaluated in T2-weighted images as seen in 14C, D and also in 14G.

Chondrosarcoma (Figs. 15–17)
Patients are mostly older than 40 years and experience pain. Tumors are near the trunk and have a chondroid matrix. Chondrosarcomas are characterized by slow growth. Primary chondrosarcomas are lytic, permeative and destructive lesions with calcification in 50%. Secondary chondrosarcomas have a cartilage cap's thickness larger than 8 mm as a sign of malignant transformation of an osteochondroma (see also the comments to threshold value in the last chapter) [13-15].

Keys to diagnosis are lytic, destructive lesion with flocculent, snowflake or popcorn calcification in patients older than 40 years. MRI: soft tissue mass or edema. The following criteria are in favor of a chondrosarcoma as opposed to an enchondroma: Pain, tracer uptake in bone scan, growth, cortical bone penetration.

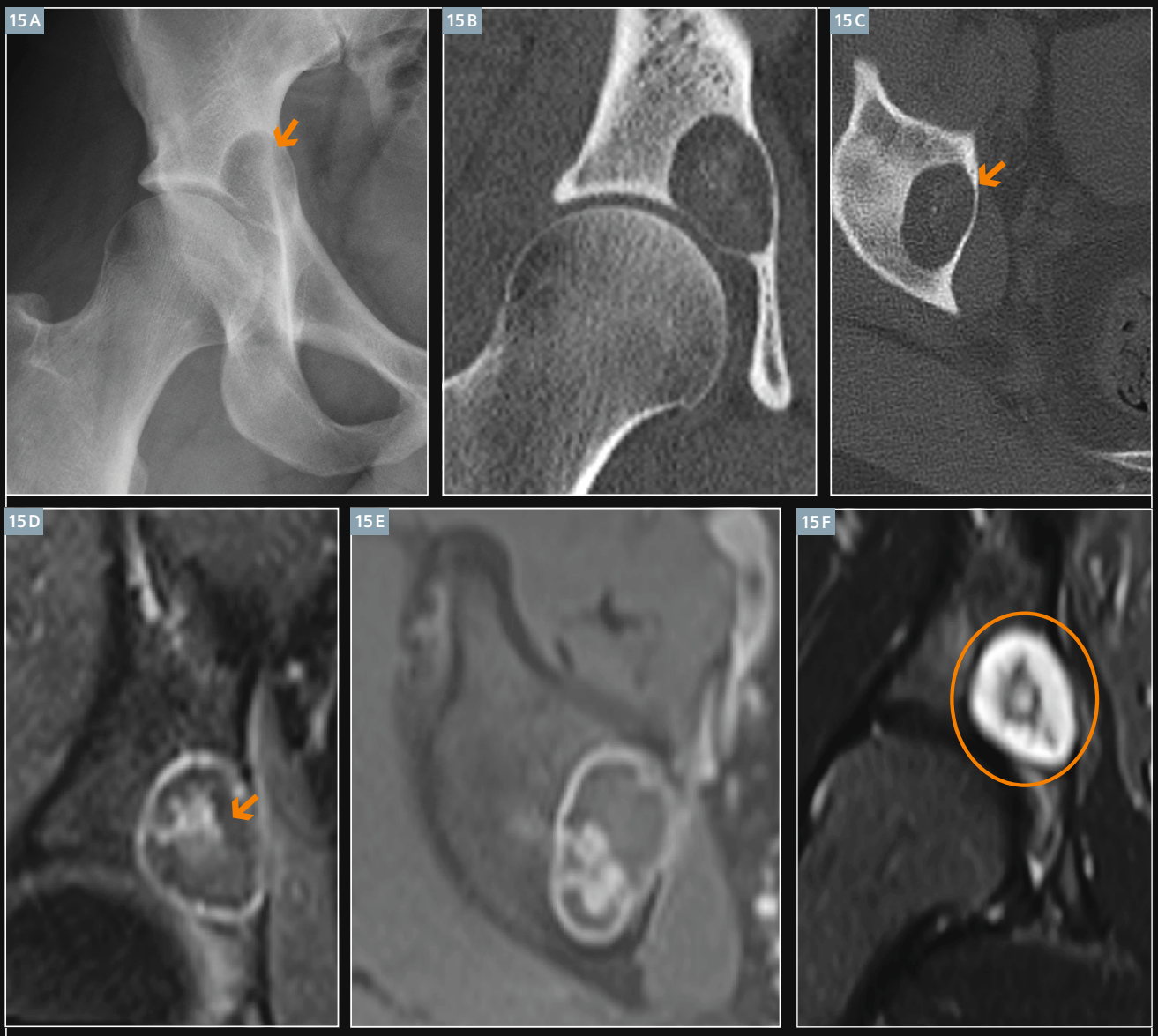

15 31-year-old male patient with grade 1 chondrosarcoma of the right os ilium. **(15A)** The antero- posterior radiograph of the right hip joint shows a geographic well-defined lytic lesion in the right acetabulum with a sharp border but without sclerotic rim according to a Lodwick IB lesion (orange arrow), in the center there is some flocculent calcification. **(15B)** Coronal CT and **(15C)** axial CT of the right hip show the lytic lesion with sharp border, thinned cortex and central punctuate calcification without cortical destruction. **(15D, E)** Contrast-enhanced T1w MRI with fat saturation (coronal in 15D and axial in 15E) show a central contrast-enhancement. Figure 15F shows a coronal STIR MRI with a high signal in the border area of the tumor.

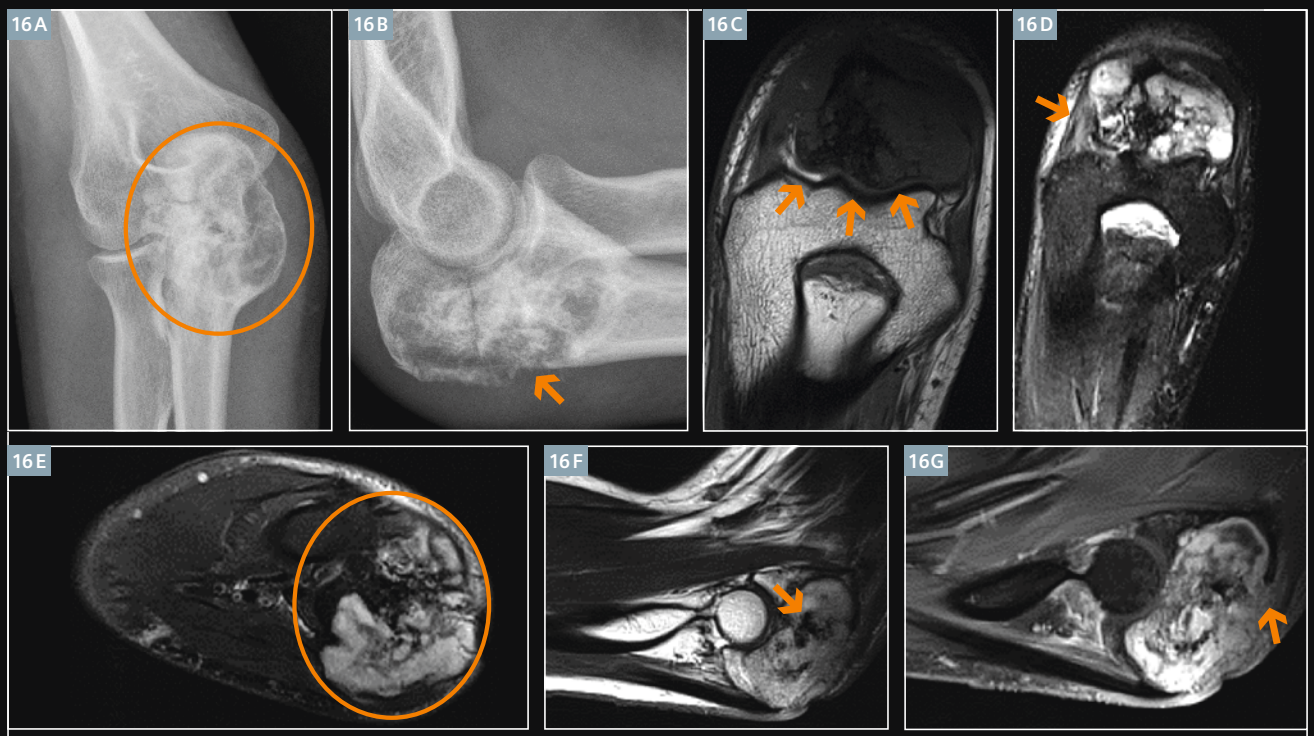

16 33-year-old female with grade 2 chondrosarcoma of the left olecranon. **16A** shows an antero-posterior radiograph of the left olecranon with a Lodwick type IC lesion: geographic but blurred border (orange circle). Figure **16B** shows the lateral radiograph of the left olecranon and reveals a cortical destruction (orange arrow). **(16C)** Coronal T1-weighted MR image of the olecranon clearly shows the intraosseous borders of the tumor (orange arrows). **(16D)** Coronal STIR MR image clearly shows the muscle edema (orange arrow). **(16E)** Axial T2w MRI with fat saturation shows the chondroid matrix of the tumor (orange circle). **(16F)** Sagittal T2w MRI shows the hypointense calcification (orange arrow) in the center of the chondroid tumor. **(16G)** Sagittal contrast-enhanced T1w MRI with fat saturation shows the infiltration of the surrounding soft tissue (orange arrow).

17 58-year-old male patient with grade 3 chondrosarcoma of the right humerus. **(17A)** The antero-posterior radiograph of the right humerus shows in addition to a patchy lysis pattern (Lodwick II) the cortex destruction (orange circle). **(17B)** Coronal STIR MRI clearly shows the extension of this large amorphous lesion (size of 10 cm, long yellow arrow) and the soft tissue infiltration (small yellow arrow). The tumor has a predominant chondroid matrix with low signal in T1w (**17C** coronal T1w MRI) and an inhomogeneous high signal in T2w (**17D** sagittal T2w MRI) as a further hint of a high-grade chondrosarcoma. (17D) Also shows well the cortex destruction and soft tissue infiltration (orange circle). **(17E)** Coronal contrast-enhanced MRI shows necrotic tumor areas within the tumor (yellow arrows). Also areas without chondroid matrix are a hint of a high-grade chondrosarcoma.

Chondroblastoma (Fig. 18)
Patients are usually younger than 20 years (i. e. skeletally immature patients). The lesion must be located epiphyseally and is rare in metaphysis. This entity also occurs in carpal and tarsal bones and rarely in the patella (which with regard to the differential diagnosis of lytic lesions behaves like an epiphysis) [11]. Usually it appears in long bones and shows in 40–60% calcification. Differential diagnoses are the sequestrum (osteomyelitis) and the eosinophilic granuloma.

Key to diagnosis: Chondroblastomas are lytic epiphyseal lesions with sclerotic rim. In MRI it shows a chondroid component with high signal in T2-weighted imaging and calcification with low signal in T2-weighted imaging [4].

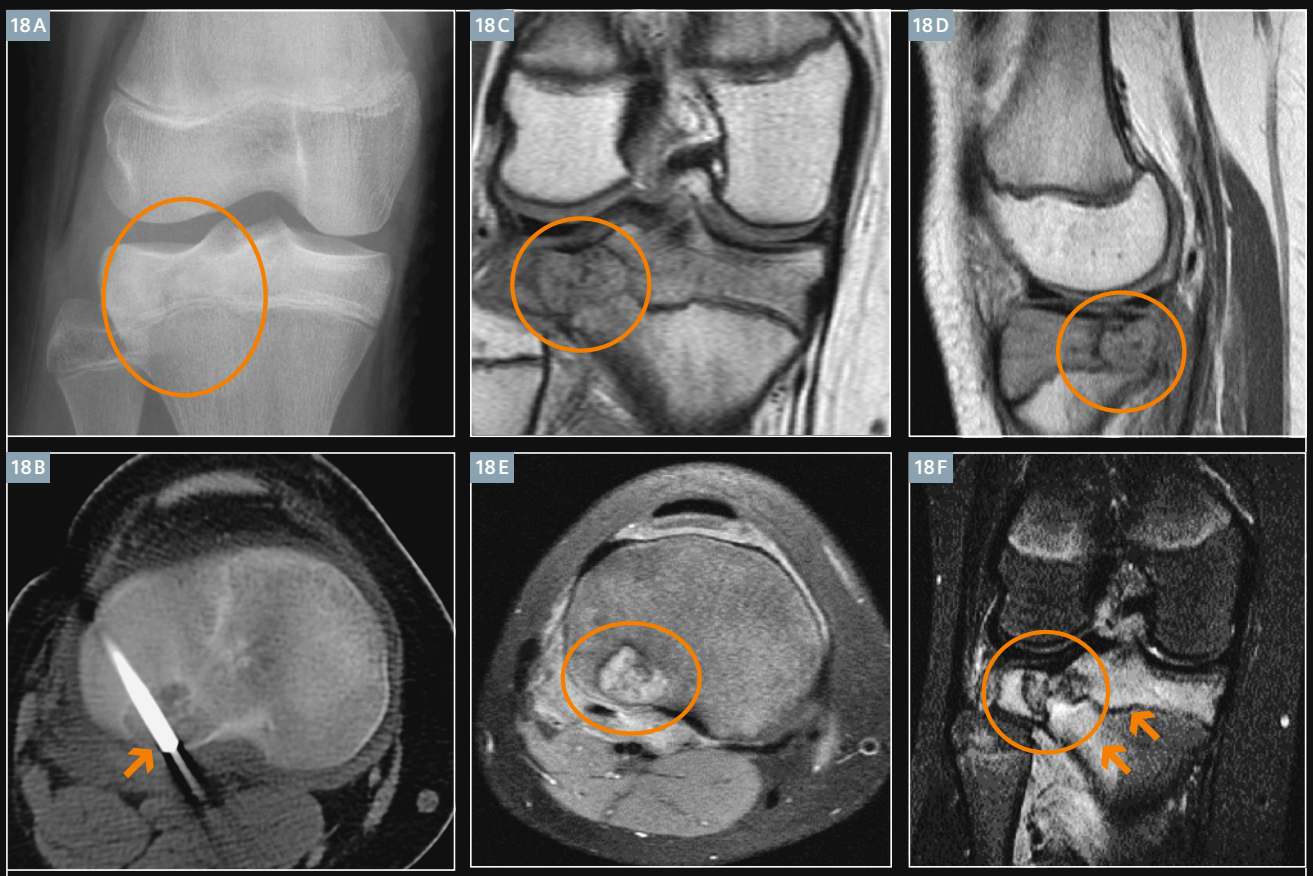

18 12-year-old female patient with a chondroblastoma of the right lateral tibia epiphysis. **(18A)** Antero-posterior radiograph of the right knee shows the epiphyseal located lytic lesion of the tibia with discreet sclerotic rim and some central located calcification (orange circle). **(18B)** Axial CT shows the puncture needle in that lytic lesion having a sharp border (orange arrow). **(18C)** Coronal and **(18D)** sagittal T1-weighted MR images show the bordered lesion having a discreet hypointense sclerotic rim and a central hypointense punctual calcification (orange circle). **(18E)** Axial PD-weighted MR image shows a chondroid component with high signal and central calcification with low signal (orange circle). **(18F)** Coronal STIR MR image also shows a chondroid component with high signal and central calcification with low signal (orange circle) and a bone marrow edema in the circumference (orange arrows). Therefore biopsy was performed.

Fibrous type

Non-ossifying fibroma – NOF (Figs. 19 and 20)

Patients are usually younger than 20 years and have no pain or periosteal reaction. This lesion is located in the metaphysis of long bone in eccentric position and emanates from the cortex, so that the cortex will be replaced with benign fibrous tissue. Non-ossifying fibromas 'heal' with sclerosis and disappear in the following years. Lesions smaller than 3 cm in length are called fibrous cortical defect and lesions larger than 3 cm in length are called non-ossifying fibroma.

Key to diagnosis: A lytic lesion with expansive growth and scalloped, well-defined sclerotic border. The MRI appearance of an NOF is somewhat variable. Although they are essentially always low signal on T1-weighted MR imaging, they can have high or low signal on T2-weighted imaging. NOF has partly homogeneous or partly non-homogeneous contrast-media enhancement. During the 'healing period' the non-ossifying fibroma can be hot on radionuclide bone scans indicating the osteoblastic activity.

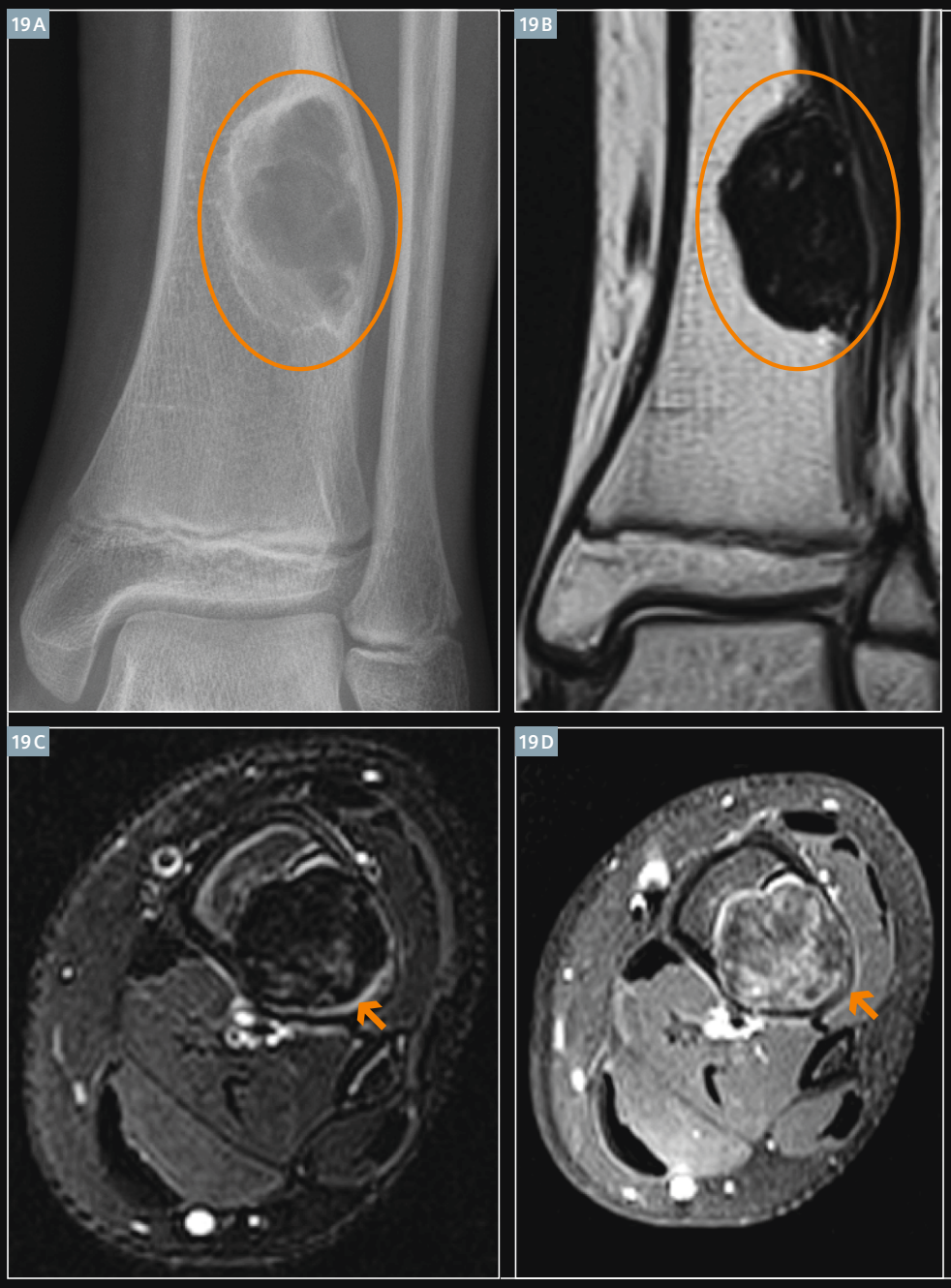

19

14-year-old male patient with a non-ossifying fibroma of the left distal tibia. **(19A)** Antero-posterior radiograph shows a classic example of a non-ossifying fibroma that is slightly expansile and lytic and has a scalloped, well-defined sclerotic border (Lodwick IA, orange circle). **(19B)** Coronal T1-weighted MR image shows the typical low signal of the lesion (orange circle). **(19C)** Axial T2-weighted MR image shows in this case a low signal in T2-weighting what is variable (orange arrow). **(19D)** Axial contrast-enhanced T1-weighted MR image with fat saturation shows that in this case the NOF has a partly inhomogeneous contrast-media enhancement (orange arrow).

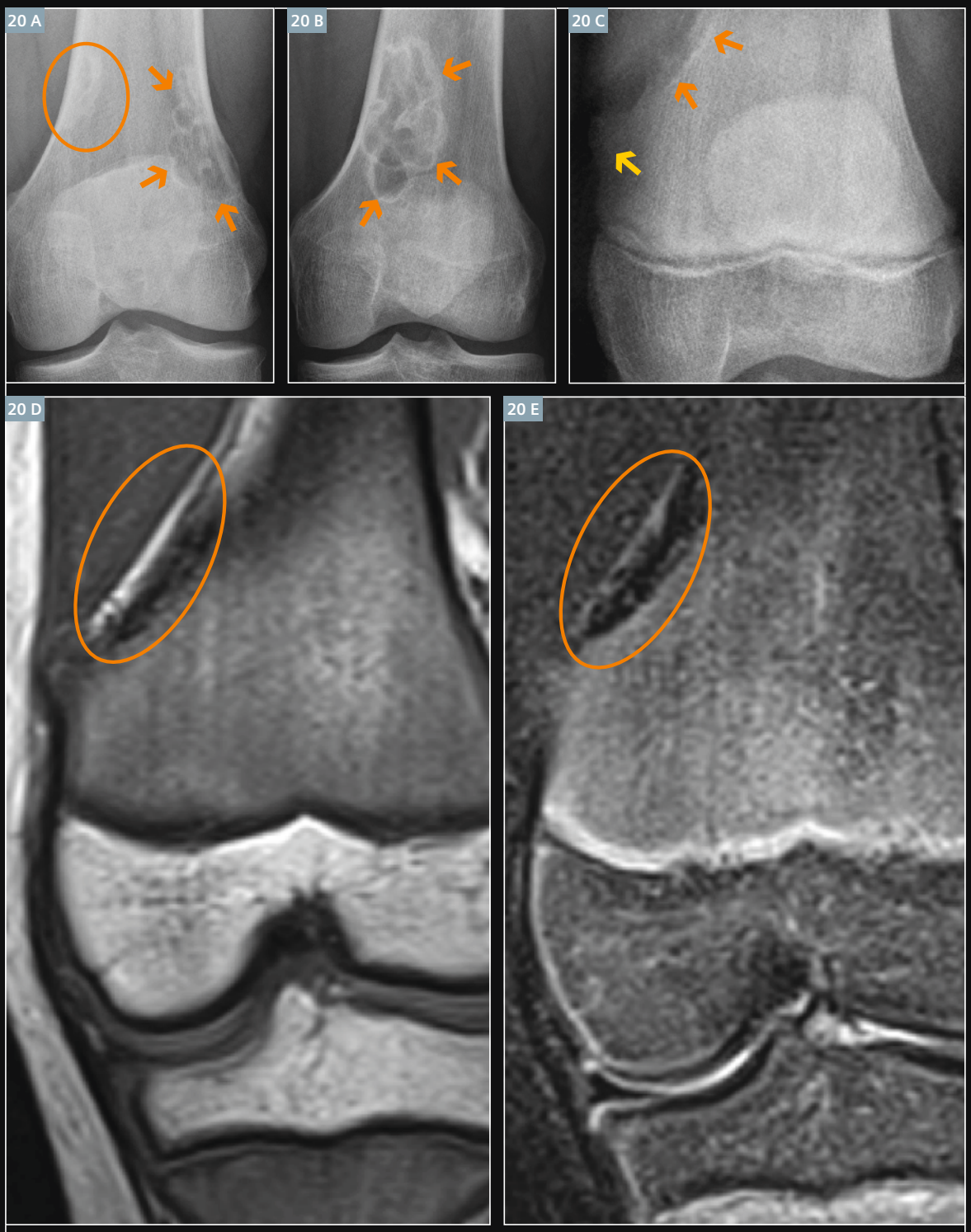

20 Image gallery of the non-ossifying fibroma.
(20A) Antero-posterior radiograph of the right knee of a 17-year-old male patient clearly shows the various appearance of a NOF. Two healing periods can be seen: Lateral, a lesion with proceeding sclerosis indicating that the lesion is in a progressed healing stadium (orange circle) and medial, a classical scalloped lesion with well-defined sclerotic border (orange arrows).
(20B) Antero-posterior radiograph of the left knee of an 18-year-old male patient shows the typical appearance of a NOF: Scalloped lesion with well-defined sclerotic border.
(20C) Antero-posterior radiograph of the knee of a 12-year-old male patient shows a lytic lesion with sclerotic rim (orange arrow) and below an exostosis (yellow arrow). **(20D)** Coronal T1-weighted MR image shows the typical low signal of a NOF (orange circle) and **(20E)** a coronal STIR MR image shows in this case also a low signal compatible to the diagnosis of a NOF.

Fibrous dysplasia (Figs. 21–23)
Patients have usually no pain or periosteal reaction. Fibrous dysplasia can be either monostotic (most commonly) or polyostotic (McCune-Albright syndrome) and has a predilection for the pelvis, the proximal femur, the ribs and skull. In its classic description, fibrous dysplasia has a, 'ground-glass appearance' or 'smoky appearing' in X-ray and/or CT (Fig. 21), but the ground glass appearance is not always present. Lesions may be mixed lytic and sclerotic [11] and bone may be deformed.

Keys to diagnosis are: No periosteal reaction. Fibrous dysplasia shows lytic lesions, as the matrix calcifies it has a hazy, smoky and ground-glass look to the point of sclerotic lesion. The signal alterations of fibrous dysplasia in MRI follow the uniform pattern of all tumors (low signal in T1-weighted and intermediate to high signal in T2-weighted images). The fibrous tissue enhances contrast media. If the lesion is located in the tibia, consider also adamantinoma, which has malignant potential, i.e. a mixed lytic and sclerotic lesion in anterior cortex of tibia that resembles the fibrous dysplasia.

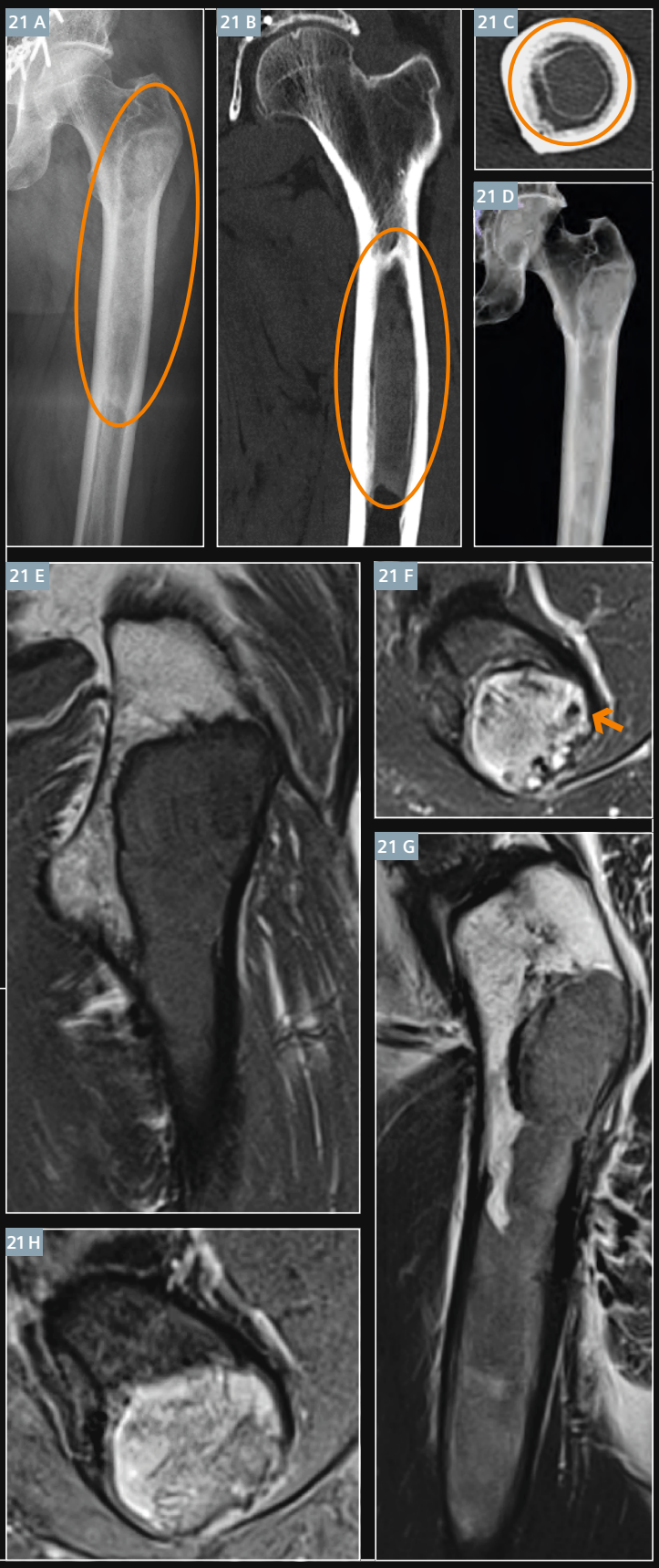

21

44-year-old male patient with fibrous dysplasia of the left femur.
(21A) Antero-posterior radiograph of the left femur shows well the ground glass appearance of a sclerotic lesion in the proximal diaphysis (orange circle). **(21B)** Coronal CT, **(21C)** axial CT and **(21D)** 3D figure also clearly show the ground glass appearance of that lesion (orange circle). **(21E)** Coronal T1-weighted MR image shows low signal of the lesion. **(21F)** Axial T2-weighted MR image with fat saturation shows that the lesion contains only point-shaped lipoid and calcified parts (orange arrow). **(21G)** Sagittal T2-weighted MR image shows in this case a homogenous low signal, **(21H)** axial contrast-enhanced T1-weighted MR image with fat saturation shows a relatively homogenous contrast enhancing of the lesion. An inhomogeneous contrast-enhancement occurs in lesions with bigger parts of blood, fat and calcifications leading to signal alterations.

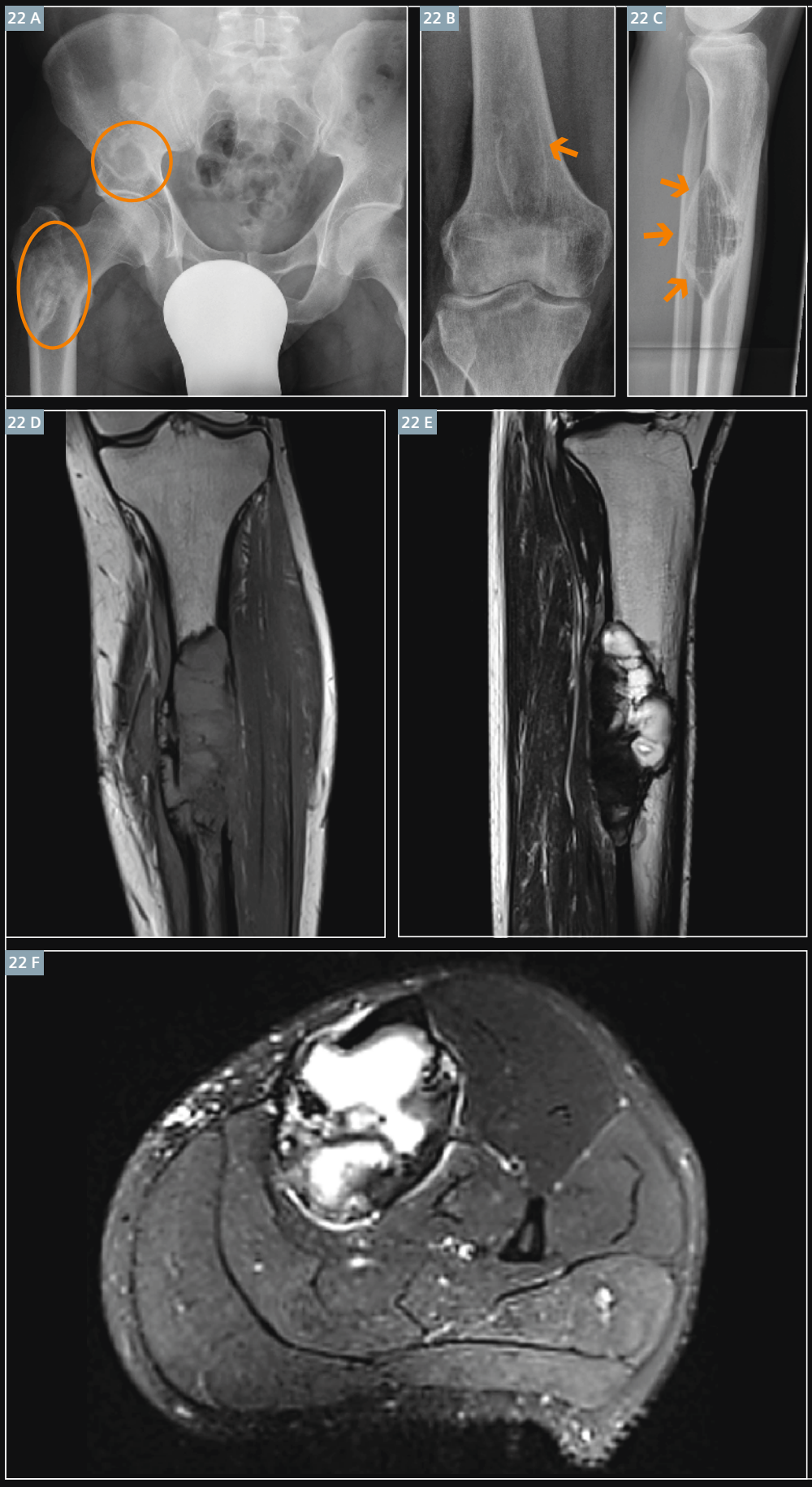

22

Image gallery of fibrous dysplasia: "Fibrous dysplasia...can look like almost anything!" [11], as is clearly visible when you compare the following three cases. **(22A)** Antero-posterior radiograph of the pelvis of a 36-year-old male patient clearly shows that the ipsilateral proximal femur is always affected when the pelvis is involved with fibrous dysplasia (orange circles). The lesion in the pelvis is more lytic than the lesion in the femur which is more sclerotic. **(22B)** Antero-posterior radiograph of the right knee of a 33-year-old female patient shows a circumscripted lytic lesion of the distal femur with smoky parts (orange arrow). **(22C)** Lateral radiograph of the left lower leg of a 22-year-old male patient with a fibrous dysplasia of the tibia shows a lytic lesion in the tibia with cortical destruction (orange arrows). MRI and biopsy were needed to confirm the diagnosis. Figures 22D–F show the corresponding MRI images to this case: **(22D)** Coronal T1-weighted MR image shows the classically low signal of lesion. **(22E)** Sagittal T2-weighted MR image and **(22F)** axial T2-weighted MR image with fat saturation show that the lesion is inhomogeneous.

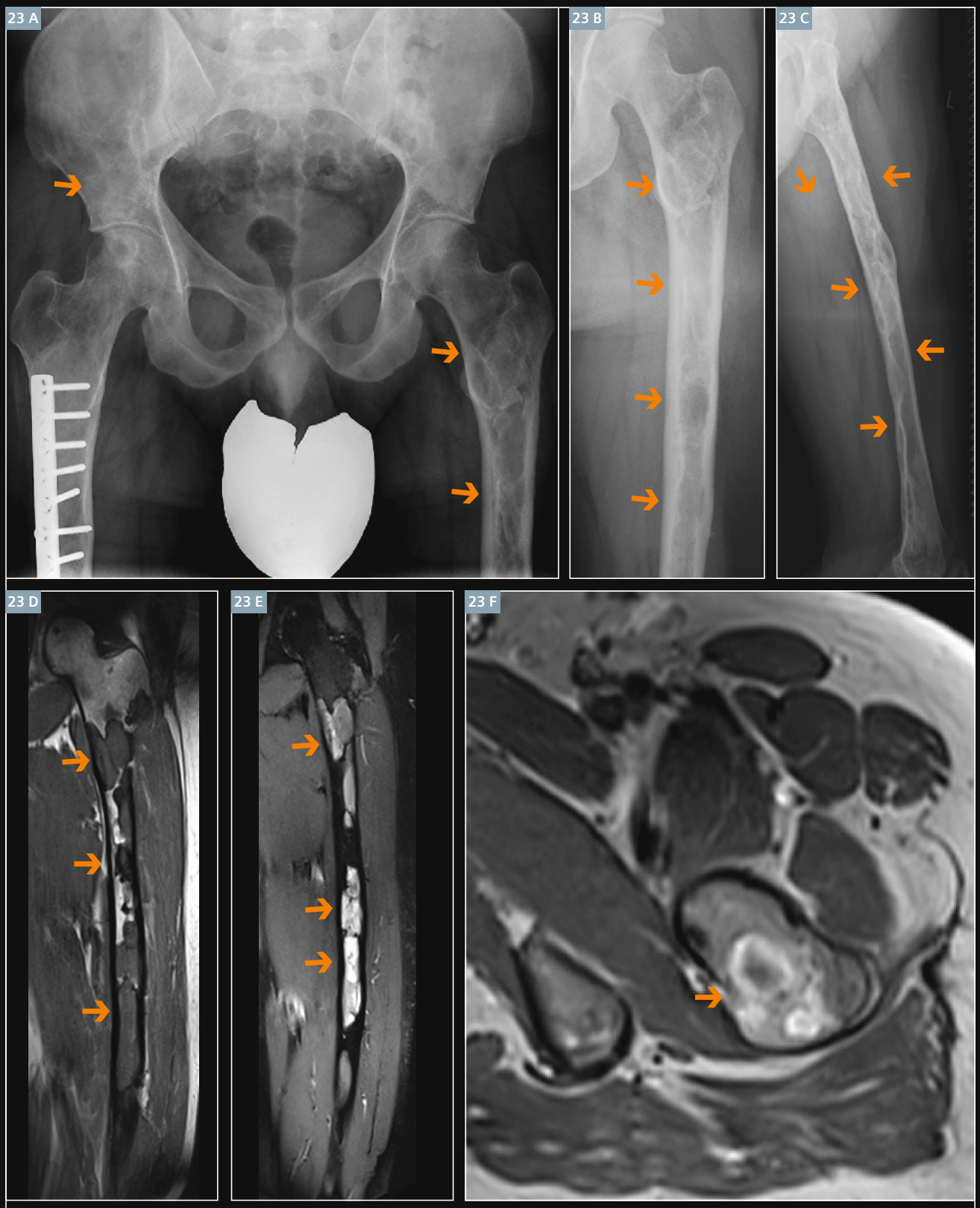

23 34-year-old male patient with a polyostotic fibrous dysplasia in pelvis and proximal femur (Albright-syndrome). **(23A)** Antero-posterior radiograph of the pelvis, **(23B)** antero-posterior radiograph of the left femur and **(23C)** lateral radiograph of the left femur show lots of lesions with smoky appearance in the right os ileum and the left femur (orange arrow). **(23D)** Coronal T1-weighted MR image of the left femur shows a low signal of the lesions (orange arrow). **(23E)** Coronal STIR MR image of the left femur shows an intermediate to high signal of the lesions (orange arrow) and **(23F)** axial contrast-enhanced T1-weighted MR image shows an inhomogeneous contrast-enhancement of the fibrous tissue (orange arrow).

Lipoid/fatty type

Calcaneus lipoma (Fig. 24)
A common location is the calcaneus. It is a rare entity and a so-called 'leave-me-alone lesion'. Key to diagnosis: Fat signal in all MRI sequences.

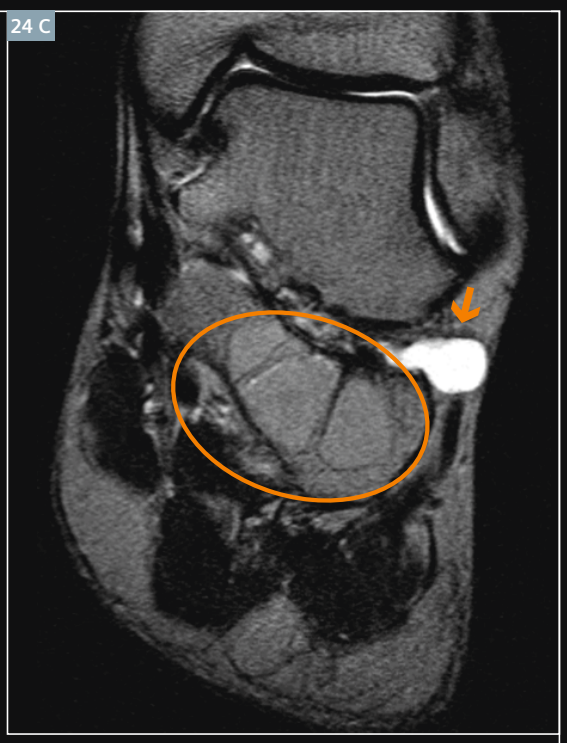

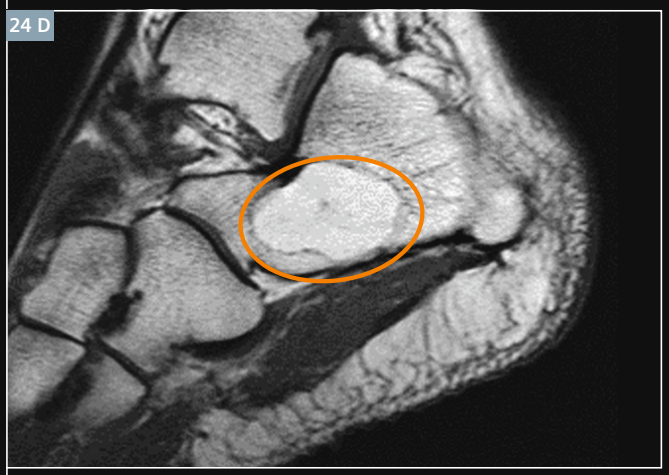

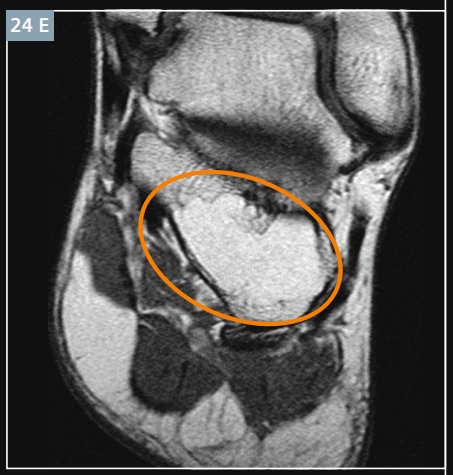

24 49-year-old male patient with an intra-osseous lipoma of the calcaneus as typical location. **(24A)** Lateral radiograph of the calcaneus shows the geographic lesion with sclerotic rim, Lodwick IA (orange arrow). **(24B)** Axial contrast-enhanced T1w MRI with fat saturation, **(24C)** coronal T2w MRI, **(24D)** sagittal T1w MRI and **(24E)** coronal contrast-enhanced T1w MRI. MR images show well that the lesion contains fat, especially seen in 24B and E (orange circle). Notice the synovial cyst between calcaneus and talus in 24C as auxiliary diagnosis (orange arrow).

Other types

Solitary bone cyst (Figs. 25, 26)
Patients are usually younger than 20 years. Common location: calcaneus, proximal humerus and femur with central location of the lesion. Patients have no pain or periosteal reaction unless they suffer a fracture through this lesion. The fracture often produces fragments that sink to the bottom of the lesion, well known as the 'fallen fragment sign' visible on radiographs.

Key to diagnosis: Lytic centrally located lesion, well-defined with sclerotic rim (Lodwick type IA). The MRI shows non-enhancing pure fluid (in contrary to aneurysmal bone cyst).

If the lesion is located in the calcaneus think about the differential diagnosis of an intra-osseous lipoma. A differentiation by X-ray is then only possible if the lipoma has a central calcification. But this differentiation is not relevant, because both lesions are 'leave-me-alone lesions' [11].

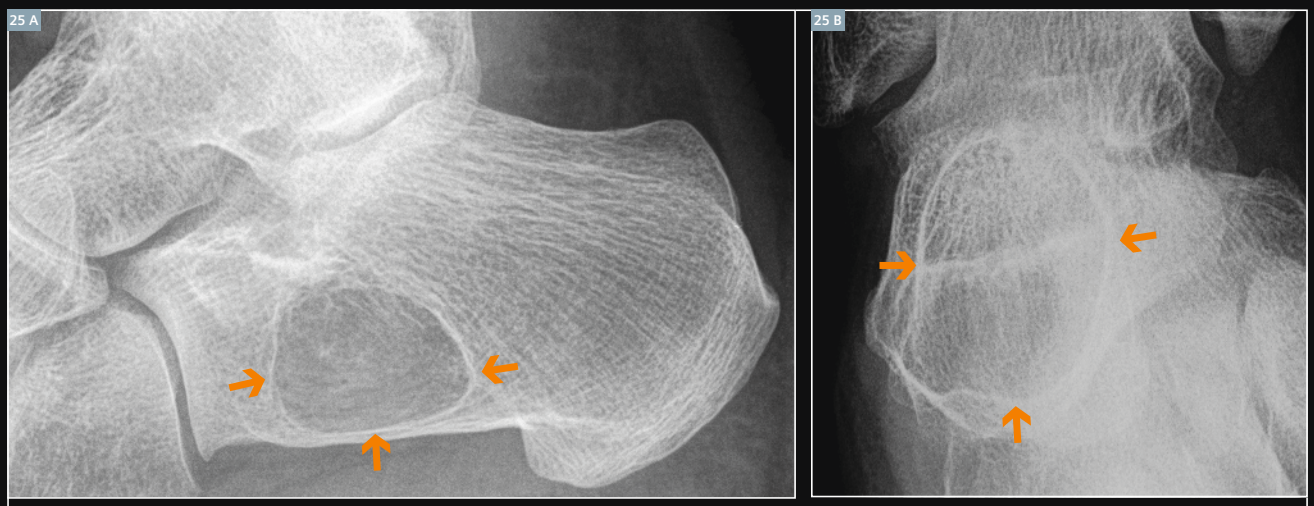

25 25-year-old male patient with a solitary bone cyst of the calcaneus. **(25A)** Lateral and **(25B)** antero-posterior radiographs of the calcaneus show both the geographic lesion with sclerotic rim, Lodwick IA (orange arrows). Typically for the location in the anterior to the midportion of the calcaneus and on the inferior border is: only in this position the solitary bone cyst has a characteristic triangular appearance.

Save the Date
3rd Heidelberg Summer School
Musculoskeletal Cross Sectional Imaging 2014

July 25/26, 2014
Heidelberg, Germany

Please visit:
www.heidelbergsummerschool.de

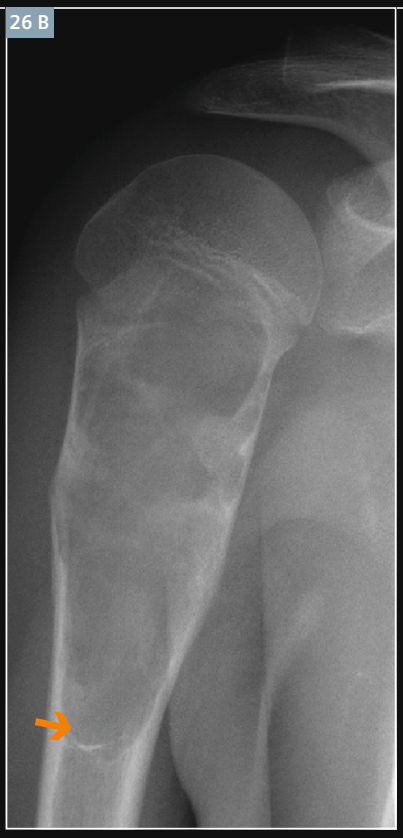

26

Image gallery of solitary bone cyst with the 'fallen fragment sign'. **(26A)** Antero-posterior radiograph of the right shoulder of a 9-year-old female patient with the 'fallen fragment sign' in a solitary bone cyst of the humerus (orange arrow).
Figures 26B–E show the case of an 11-year-old patient with a solitary bone cyst also in the right humerus. **(26B)** Antero-posterior radiograph of the right shoulder demonstrates well the pathognomonic 'fallen fragment sign' of the cystic lesion.

(26C) Shows a coronal T1w MRI with low signal of the lesion and **(26E)** shows an axial T2w MRI with a small fluid level between the cystic fluid and the blood after the occurred fracture (orange arrow). Usually solitary bone cysts show no fluid-fluid levels as it is typical for the aneurysmal bone cyst.
(26D) Coronal contrast-enhanced T1w MRI with fat saturation shows non-enhancing pure fluid.

Aneurysmal bone cyst (ABC) (Fig. 27)
The patients are usually younger than 20 years. At the vertebral column, this entity often occurs at the posterior elements of the vertebral bodies. It shows an aneurysmal, expansive growth with thinned cortex or neocortex (ballooned cortices) called 'blow-out' phenomenon in CT.

Key to diagnosis: The aneurysmal bone cyst is a lytic geographic lesion, eccentrically located with extensive thinning of the cortex. Sedimentation effects of blood-filled cysts with fluid-fluid levels and contrast-enhancement of the cystic wall and the septa are typical signs in MRI. If there are solid contrast-enhancing parts consider secondary ABC with other tumors (e.g. giant cell tumor, osteosarcoma, chondrosarcoma, chondroblastoma).

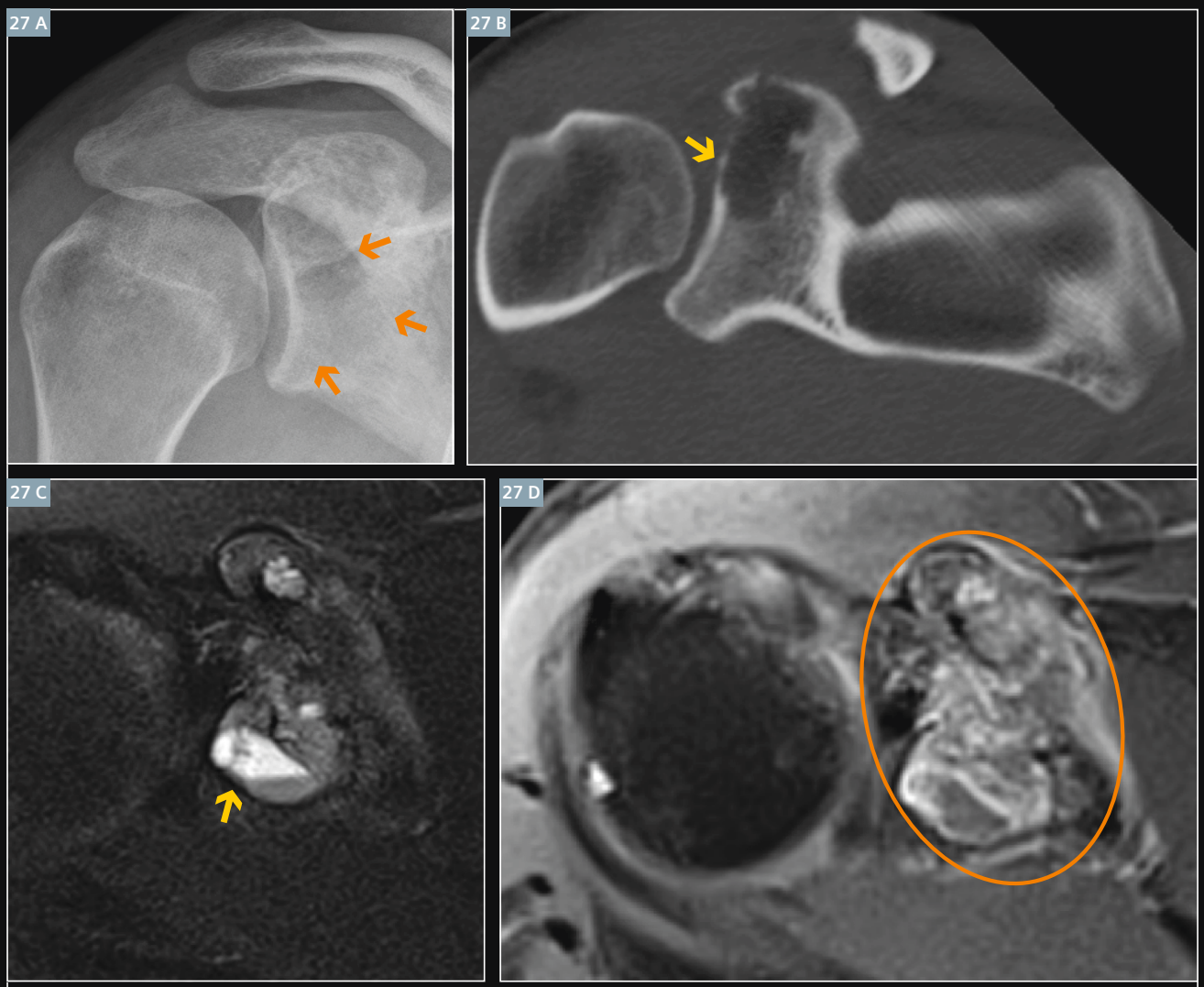

27 17-year-old male patient with an aneurysmal bone cyst of the right glenoid. **(27A)** Lateral radiograph of the right shoulder shows a geographic lesion in the glenoid without sclerotic rim, Lodwick IB (orange arrows). **(27B)** Coronal CT of the right shoulder shows a lytic expansible lesion with a thinned cortex (yellow arrow). **(27C)** Axial T2-weighted MRI shows the cystic parts with fluid-fluid level (yellow arrow). **(27D)** Axial contrast-enhanced T1w MRI shows the enhancement of the septa (orange circle).

Giant cell tumor (Fig. 28)
A precondition is that the epiphysis is closed. This tumour often abuts the articular surface and most often has an eccentric localization. This is often a well defined lesion with a non-sclerotic margin (Lodwick IB). Local aggressive growth and lung metastasis in 5–10% occur.

Key to diagnosis: Osteolytic eccentric, epiphyseal lesion without matrix calcification and extensive thinning of the cortex. The tumor shows low signal in T1-weighting, inhomogeneous or low signal in T2-weighting and contrast-enhancement. If the tumor contains necrosis and hemosiderin, this results in an inhomogeneous contrast-enhancement pattern.

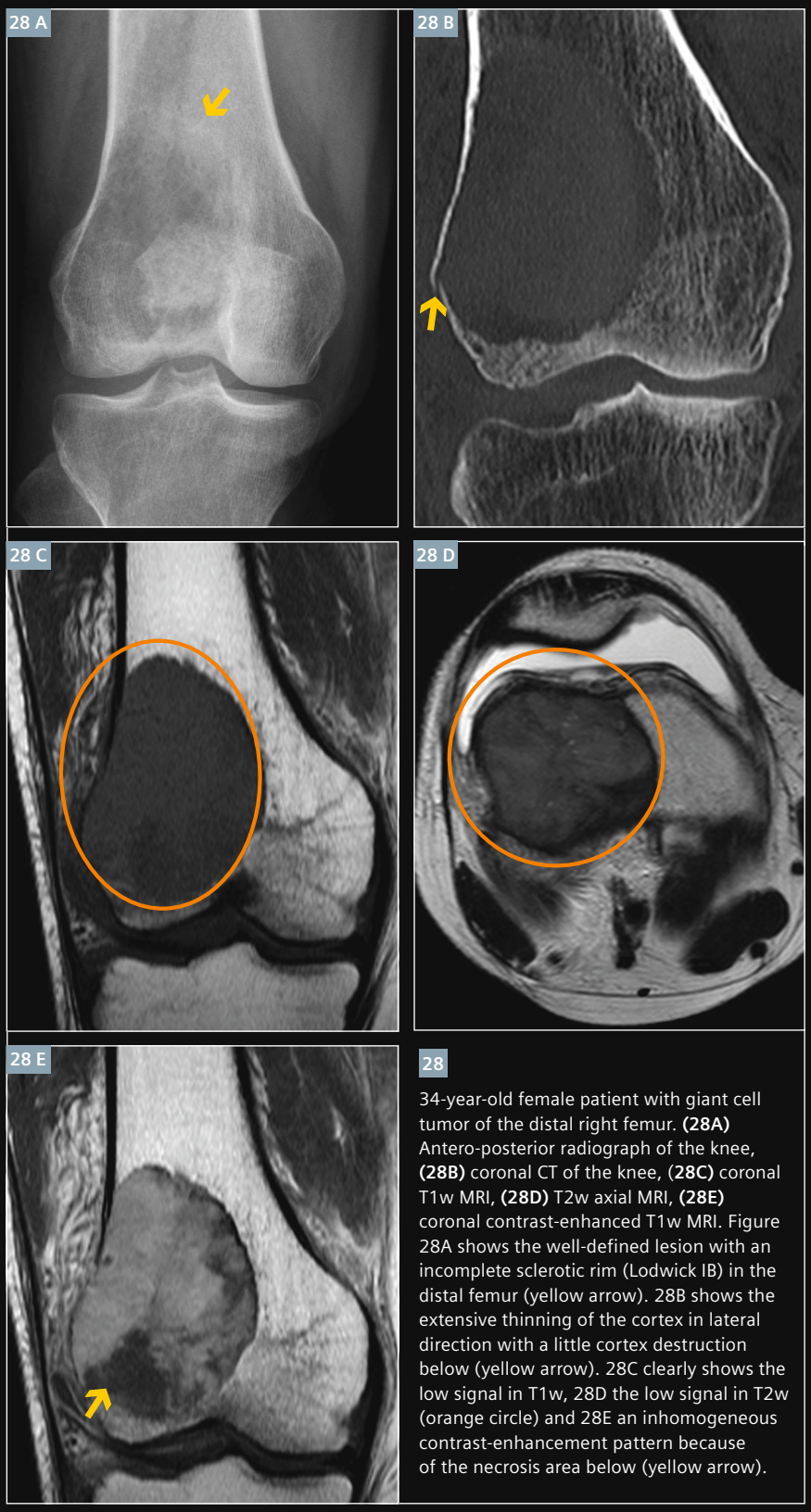

28

34-year-old female patient with giant cell tumor of the distal right femur. **(28A)** Antero-posterior radiograph of the knee, **(28B)** coronal CT of the knee, **(28C)** coronal T1w MRI, **(28D)** T2w axial MRI, **(28E)** coronal contrast-enhanced T1w MRI. Figure 28A shows the well-defined lesion with an incomplete sclerotic rim (Lodwick IB) in the distal femur (yellow arrow). 28B shows the extensive thinning of the cortex in lateral direction with a little cortex destruction below (yellow arrow). 28C clearly shows the low signal in T1w, 28D the low signal in T2w (orange circle) and 28E an inhomogeneous contrast-enhancement pattern because of the necrosis area below (yellow arrow).

Ewing's sarcoma (Figs. 29, 30)
The classic Ewing's sarcoma is a, 'permeative lesion in the diaphysis of long bone in a child', [11], with osteodestruction in CT and a very high signal in T2-weighted imaging indicating infiltration of bone marrow. The location of Ewing's sarcoma tends to follow the distribution of red marrow. In histology small round blue cells are visible. A large soft tissue mass is possible. Important differential diagnoses are osteomyelitis and eosinophilic granuloma, which have a benign periosteal reaction and sometimes a sequestrum.

Keys to diagnosis are: A permeative lesion or lesion with sclerotic and patchy appearance and periosteal reaction which can be onion-skinned (multilamellated), sunburst or amorphous. Low signal in T1-weighted MR images, high signal in T2-weighted MR imaging with strong contrast-enhancement. More than 50% are osteolytic lesions. Edema and large soft tissue mass often occur.

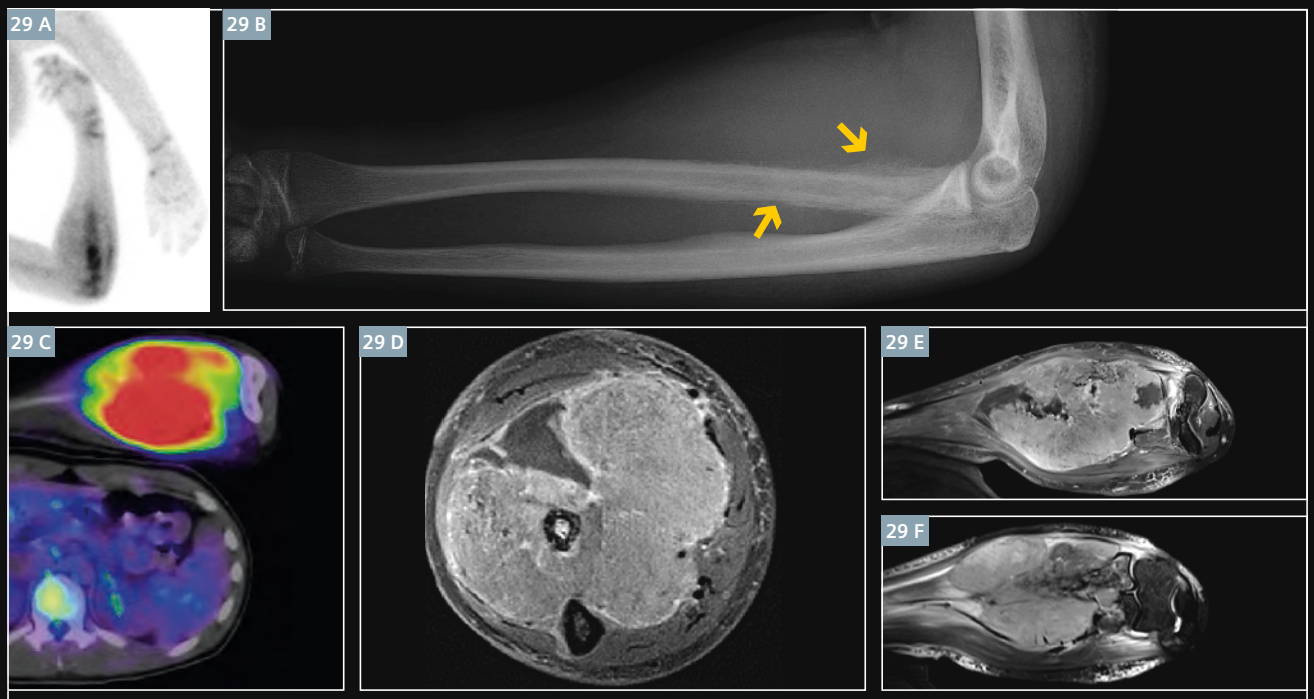

29 16-year-old male patient with Ewing's sarcoma of the proximal left forearm. **(29A)** Bone scan shows an overview of the involvement of the proximal radius, the ulna and parts of the distal humerus. **(29B)** Lateral radiograph of the forearm shows the onion-skinned, multilamellated periosteal reaction of the proximal radius (yellow arrows). **(29C)** Three-phase radionuclide bone scan with Tc-99m MDP shows the tracer uptake in the big tumor mass. **(29D, E)** Contrast-enhanced T1-weighted MRI with fat saturation axial (D) and coronal (E) and **(29F)** coronal STIR MRI shows the big tumor involving radius and ulna.

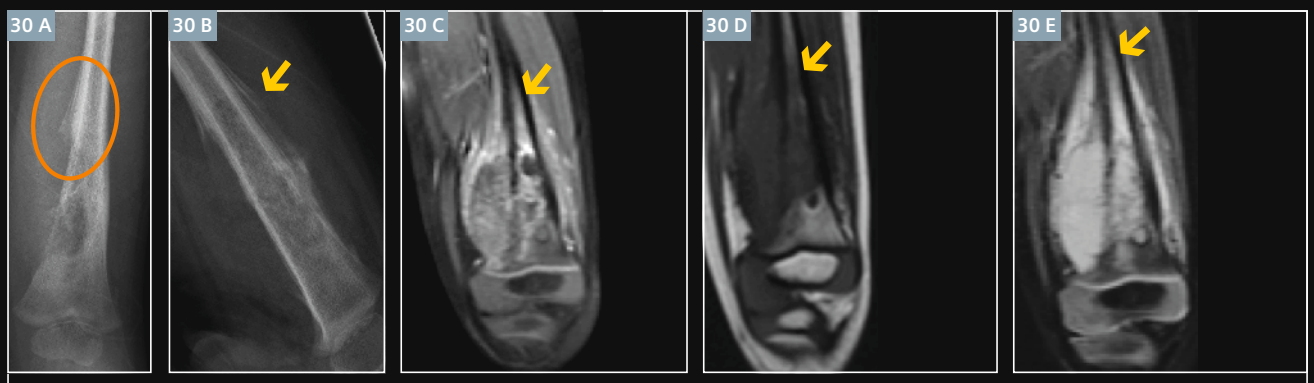

30 3-year-old male patient with Ewing's sarcoma of the left distal femur. **(30A)** Antero-posterior radiograph of the femur, **(30B)** lateral radiograph of the femur, **(30C)** coronal contrast-enhanced T1-weighted MRI with fat saturation, **(30D)** coronal T1-weighted MRI, **(30E)** coronal STIR MRI. Figure 30A clearly shows the Codman-triangle, whereby the elevated periosteum forms an angle with the cortex, (orange circle) and 30B the onion-skinned periosteal reaction (yellow arrow). Figures 30C–E show the T1w hypo-, T2w hyperintense signal character of the tumor with contrast-enhancement, the large soft tissue component (yellow arrows) and also the Codman triangle.

Multiple myeloma (Fig. 31)
In multiple myeloma, a proliferation of monoclonal plasma cells within the bone marrow occurs. The vertebral column is mostly affected and 70% of patients are older than 60 years. Multiple lytic lesions in an adult older than 40 years almost always suggest metastases or multiple myeloma. Bone sarcomas are rare, and the most common cause of a solitary destructive lesion in an adult is a metastasis. Low-dose CT is important for proving osteolytic lesions and MRI [22] for proving bone marrow affection: Decrease of T1-weighted signal in bone marrow infiltration compared to the disks, and a signal increase in the STIR images compared to muscle tissue. Whole-body MRI is suitable for demonstration of the tumor burden. It is important to think of patient's age when interpreting T1-weighted MR imaging, because young patients still have a cell-rich red bone marrow and therefore also a low T1 signal. We differentiate three patterns of bone marrow infiltration: diffuse, multifocal, or 'salt-and-pepper' pattern. Salt-and-pepper pattern indicates a low grade disease stadium. A single lesion is called plasmacytoma [22, 23].

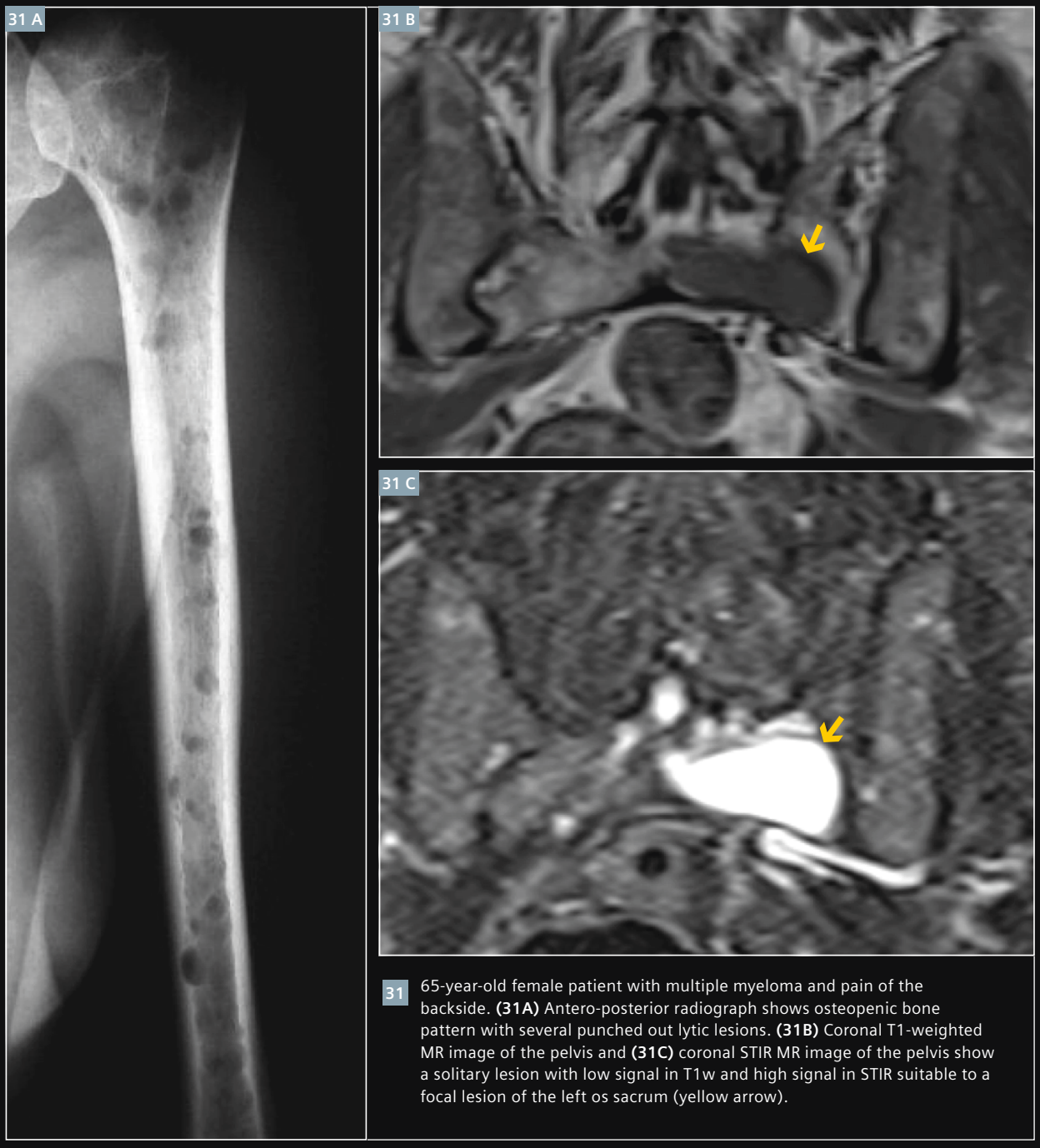

31 65-year-old female patient with multiple myeloma and pain of the backside. **(31A)** Antero-posterior radiograph shows osteopenic bone pattern with several punched out lytic lesions. **(31B)** Coronal T1-weighted MR image of the pelvis and **(31C)** coronal STIR MR image of the pelvis show a solitary lesion with low signal in T1w and high signal in STIR suitable to a focal lesion of the left os sacrum (yellow arrow).

Metastases (Fig. 32)
40% of all metastases are located in the vertebral column. The most frequent primary tumors are lung, breast, prostate, renal cell, gastrointestinal and thyroid carcinomas. Bone marrow infiltration happens before osseous destruction. It is important to pay attention to fractures, spinal canal invasion and myelon compression.

Key to diagnosis: For the diagnosis of bone metastases a low signal in T1-weighted MR images is more sensitive than osteolysis in CT [24]. Osteolytic metastases have a high signal in T2-weighted images, whereas osteoblastic metastases have a low to isointense signal in T2-weighted images. Take into account these factors in older patients and consider several osteoblastic and/or osteolytic lesions.

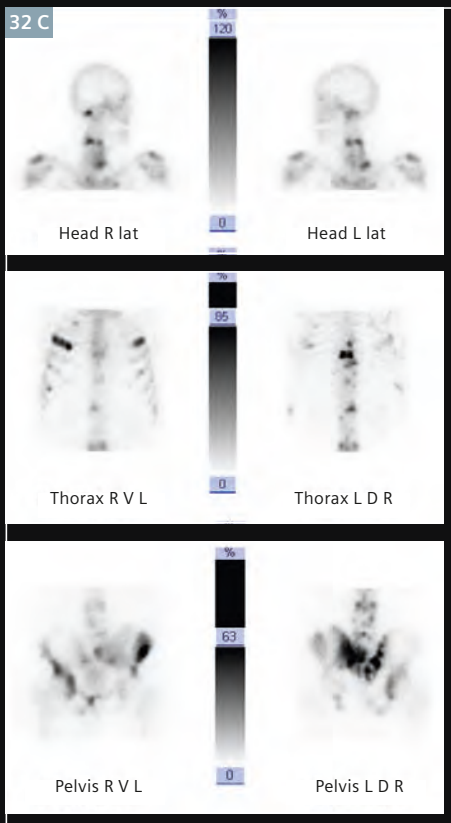

32

55-year-old man with osteoblastic metastases of vertebral column and pelvis in prostate cancer. **(32A)** Lateral radiograph of the vertebral column, **(32B)** antero-posterior radiograph of the lower vertebral column and os sacrum show several osteoblastic metastases of the vertebral bodies and the os sacrum. **(32C)** Scintigraphic bone scan shows more skeletal metastases.

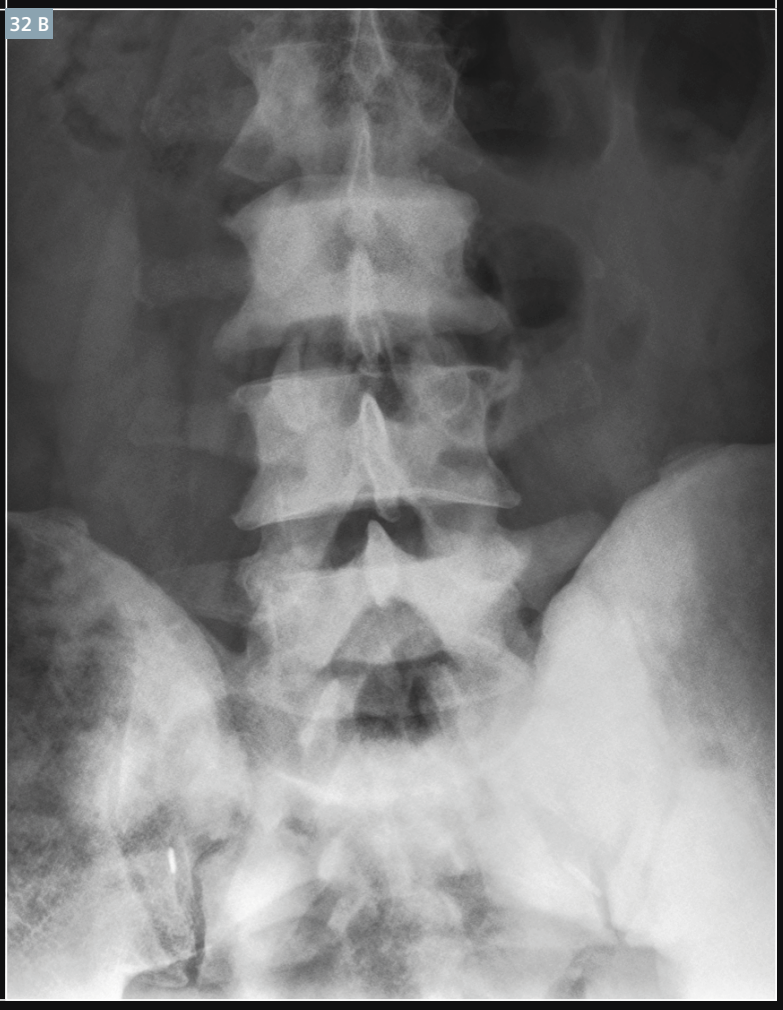

Summary

Role of X-ray

In addition to patient history and clinical findings, a radiograph in two orthogonal planes is still of great importance for determining the Lodwick classification and the tumor matrix, whereas the bone matrix is only poorly visualized in X-ray: You cannot differentiate between lesions containing fluid and solid lesions without mineralized matrix. In general, conventional X-ray radiography is the starting point and CT and MR images should only be interpreted with concurrent radiographic correlation.

Role of CT

CT is superior to MRI for the assessment of mineralized structures especially cortical integrity, matrix mineralization, and periosteal reactions [21]. Small lucency of the cortex, localized involvement of the soft tissues, and thin peripheral periosteal reaction can be best seen with CT [16]. CT is the examination of choice in the diagnosis of the nidus of osteoid osteoma in dense bone [17]. CT is valuable in the diagnosis of tumors of the axial skeleton such as spinal metastasis as well as in systemic staging.

Role of MRI [18-21]

Without any radiation MRI can be helpful while evaluating lesions that represent a differential diagnosis dilemma between benign and malignant lesions before a biopsy. For example in aneurysmal bone cysts MRI can display fluid levels in blood filled cavities better than CT. Another example, MRI before biopsy for staging all suspected sarcomas of bone could help identifying extraosseous sarcoma better. MRI plays an important role in planning limb salvage surgeries because of its superior role for soft tissue evaluation including the presence or absence of neurovascular invasion [21]. MRI helps by identifying skip lesions and helps measure the thickness of cartilage cap. The cap is thin in benign lesions and thicker in chondrosarcomas [14, 15]. This aids evaluation of the entire compartment of long bones in acceptable time. (Important here is a large field-of- view of the MR sequence, see Fig. 33.) This in turn helps to improve the quality of life by reducing morbidity without affecting survival. MRI is most useful in evaluation of spine metastasis differentiating osteoporotic and metastatic compression fractures. In Multiple Myeloma cases whole-body MRI scans are suitable for demonstration of the tumor burden. Though not yet in clinical routine, newer techniques such as diffusion-weighted imaging and DCE-MRI may support assessment of tumor response. More studies are being conducted.

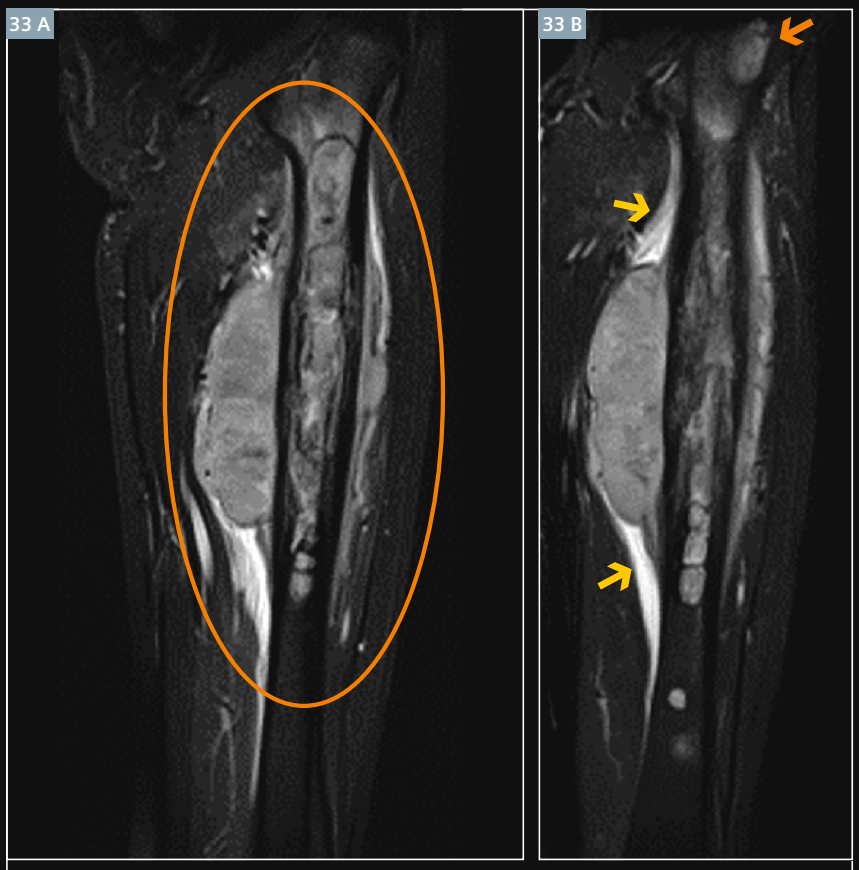

33 13-year-old female patient with Ewing's sarcoma. **(33A, B)** Coronal STIR MR images show the tumor in the left femur diaphysis (orange circle) with a large soft tissue mass surrounded by a soft tissue edema (yellow arrows) and a skip lesion in the femoral neck (orange arrow).

Proposed tumor MRI protocol

Sequences unenhanced

- coronal STIR with a large field-of-view
- coronal T1-weighted TSE (turbo spin echo)
- axial T2-weighted TSE with fat saturation
- sagittal T2-weighted TSE

Contrast-agent (0.1 mmol/kg body weight)

- axial contrast-enhanced T1-weighted TSE with fat saturation
- coronal contrast-enhanced T1-weigthed TSE + subtraction (contrast-enhanced minus native T1-weighted MRI scan)

The contrast-enhanced sequences are important in biopsy planning for identifying necrotic and viable tumor tissue. The biopsy should be targeted to the viable tumor area.

Optional

- MR-angiography
- Dynamic T1-weighted contrast-enhanced MRI (DCE-MRI)

Dynamic sequences are important for biopsy planning to identify vital tumor tissue [19-21], to which the biopsy should be guided.

References

1 WHO classification of bone tumours 2006.
2 Vanel D, Ruggieri P, Ferrari S, Picci P, Gambarotti M, Staals E, Alberghini M. The incidental skeletal lesion: ignore or explore? Cancer Imaging. 2009 Oct 2; 9 Spec No A: S38-43.
3 Lodwick GS, Wilson AJ, Farrell C, Virtama P, Dittrich F. Determining growth rates of focal lesions of bone from radiographs. Radiology 1980; 134: 577-583.
4 Erlemann R. Basic diagnostics of bone tumors. Radiologe 2009; 49: 257–267.
5 Oudenhoven LF, Dhondt E, Kahn S, Nieborg A, Kroon HM, Hogendoorn PC, Gielen JL, Bloem JL, De Schepper A. Accuracy of radiography in grading and tissue-specific diagnosis-a study of 200 consecutive bone tumors of the hand. Skeletal Radiol. 2006; 35: 78-87.
6 Miller T. Bone tumors and tumorlike conditions: analysis with conventional radiography. Radiology 2008; 246: 662-674.
7 Lucas DR, Unni KK, McLeod RA, O'Connor MI, Sim FH. Osteoblastoma: clinicopathologic study of 306 cases. Hum Pathol. 1994 Feb;25(2):117-34.
8 Rehnitz C, Sprengel SD, Lehner B, Ludwig K, Omlor G, Merle C, Kauczor HU, Ewerbeck V, Weber MA. CT-guided radiofrequency ablation of osteoid osteoma and osteoblastoma: clinical success and long-term follow up in 77 patients. Eur J Radiol 2012 Nov;81(11):3426-34. doi: 10.1016/j.ejrad.2012.04.037. Epub 2012 Jul 6.
9 Rehnitz C, Sprengel SD, Lehner B, Ludwig K, Omlor G, Merle C, Kauczor HU, Ewerbeck V, Weber MA. CT-guided radiofrequency ablation of osteoid osteoma: correlation of clinical outcome and imaging features. Diagn Interv Radiol. 2013 Jul-Aug;19(4):330-9. doi: 10.5152/dir.2013.096.
10 Omlor GW, Lehner B, Wiedenhöfer B, Deininger C, Weber MA, Rehnitz C. [Radiofrequency ablation in spinal osteoid osteoma. Options and limits]. [Article in German]. Orthopade. 2012 Aug;41(8):618-22. doi: 10.1007/s00132-012-1907-x.
11 Clyde A. Helms, Fundamentals of Skeletal Radiology (2005),3. Edition, Elsevier inc.
12 Murphey MD, Robbin MR, McRae GA, Flemming DJ, Temple HT, Kransdorf MJ. The many faces of osteosarcoma. Radiographics 1997; 17: 1205-1231.
13 Kloth JK, Wolf M, Rehnitz C, Lehner B, Wiedenhöfer B, Weber MA. [Radiological diagnostics of spinal tumors. Part 1: general tumor diagnostics and special diagnostics of extradural tumors]. Orthopade. 2012 Aug;41(8):595-607. doi: 10.1007/s00132-012-1978-8. [Article in German].
14 Murphey MD, Choi JJ, Kransdorf MJ, Flemming DJ, Gannon FH. Imaging of osteochondroma: variants and complications with radiologic-pathologic correlation. Radiographics. 2000 Sep-Oct;20(5):1407-34.
15 Bernard SA, Murphey MD, Flemming DJ, Kransdorf MJ. Improved differentiation of benign osteochondromas from secondary chondrosarcomas with standardized measurement of cartilage cap at CT and MR imaging. Radiology 2010 Jun;255(3):857-65.
16 Brown KT, Kattapuram SV, Rosenthal DI. Computed tomography analysis of bone tumors: patterns of cortical destruction and soft tissue extension. Skeletal Radiol 1986; 15: 448-451).
17 Glass RB, Poznanski AK, Fisher MR, Shkolnik A, Dias L. MR imaging of osteoid osteoma. J Comput Assist Tomogr 1986; 10: 1065-1067.
18 Anderson SE, Steinbach LS, Schlicht S, Powell G, Davies M, Choong P. Magnetic resonance imaging of bone tumors and joints. Top Magn Reson Imaging. 2007 Dec; 18(6):457-65.
19 Fayad LM, Jacobs MA, Wang X, Carrini JA, Bluemke DA. Musculoskeletal tumours: how to use anatomic, functional, and metabolic MR techniques. Radiology 2012; 265: 340-356.
20 Alyas F, James SL, Davies AM, Saifuddin A. The role of MR imaging in the diagnostic characterisation of appendicular bone tumours and tumour-like conditions. Eur Radiol 2007; 17: 2675-2686.
21 Roberts CC, Liu PT, Wenger DE. Musculoskeletal tumor imaging, biopsy, and therapies: self-assessment module. AJR Am J Roentgenol. 2009; 193(6 Suppl): S74-78.
22 Fechtner K, Hillengass J, Delorme S, Heiss C, Neben K, Goldschmidt H, Kauczor HU, Weber MA. Staging monoclonal plasma cell disease: comparison of the Durie-Salmon and the Durie-Salmon PLUS staging systems. Radiology. 2010 Oct; 257(1):195-204. doi: 10.1148/radiol.10091809.
23 Bäuerle T, Hillengass J, Fechtner K, Zechmann CM, Grenacher L, Moehler TM, Christiane H, Wagner-Gund B, Neben K, Kauczor HU, Goldschmidt H, Delorme S. Multiple myeloma and monoclonal gammopathy of undetermined significance: importance of whole-body versus spinal MR imaging. Radiology. 2009 Aug; 252(2):477-85. doi: 10.1148/radiol.2522081756.
24 Bohndorf K, et al. Radiologische Diagnostik der Knochen und Gelenke. (2006) 2nd edition, Thieme.

Contact

Katharina Grünberg, M.D.
Section Musculoskeletal Radiology
Diagnostic and Interventional Radiology
University Hospital Heidelberg
Schlierbacher Landstraße 200a
69118 Heidelberg
Germany
Katharina.Gruenberg@med.uni-heidelberg.de

Combined ^{18}F-FDG PET and MRI Evaluation of a case of Hypertrophic Cardiomyopathy Using Simultaneous MR-PET

Ihn-ho Cho, M.D.; Eun-jung Kong, M.D.

Department of Nuclear Medicine, Yeungnam University Hospital, Daegu, South Korea

Introduction

Hypertrophic cardiomyopathy (HCM) is a common condition causing left ventricular outflow obstruction, as well as cardiac arrhythmias. Cardiac MRI is a key modality for evaluation of HCM. Apart from estimating left ventricular (LV) wall thickness, LV function and aortic flow, MRI is capable of estimating the late gadolinium enhancement in affected myocardium, which has been shown to have a direct correlation with incidence and severity of arrhythmias in HCM [1]. In patients with HCM, late gadolinium enhancement (LGE) on CE-MRI is presumed to represent intramyocardial fibrosis. PET myocardial perfusion studies have shown slight impairment of myocardial blood flow with pharmacological stress in hypertrophic myocardium in HCM, presumably related to microvascular disease [2]. ^{18}F-FDG PET has been sporadically studied in HCM, mostly for evaluation of the metabolic status of the hypertrophic myocardial segment, especially after interventions such as transcoronary ablation of septal hypertrophy (TASH) [3] or to demonstrate partial myocardial fibrosis [4]. This clinical example illustrates the value of integrated simultaneous ^{18}F-FDG PET and MRI acquisition performed on the Biograph mMR system.

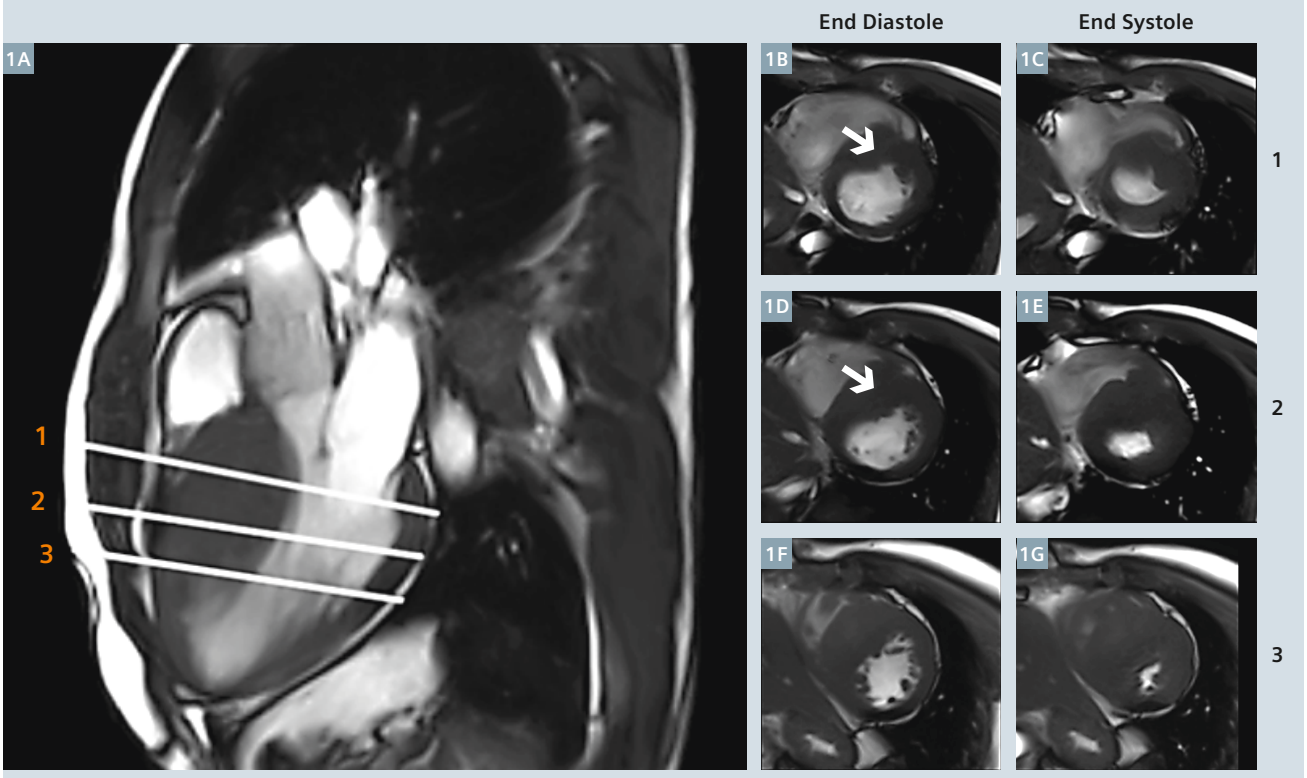

1 Short-axis views of end diastole and end systole at 3 different sections in the left ventricle obtained from gated TrueFISP cine MRI acquisitions performed on Biograph mMR. Note the thick hypertrophic septum (white arrow), which demonstrates the degree of asymmetric septal hypertrophy.

Patient history

A 25-year-old man presented to the cardiology department with incidental ECG abnormality after fractures to his left 2nd and 4th fingers. Although he had not consulted a doctor, he had been suffering from mild dyspnea with chest discomfort at rest and exacerbation at exercise since May 2012. Echocardiography revealed non-obstructive hypertrophic cardiomyopathy (Maron III) with trivial MR. The patient was referred for a simultaneous MR-PET study for ^{18}F-FDG PET and cardiac MRI with Gadolinium (Gd) contrast for evaluation of the morphological and metabolic status of the hypertrophic myocardium.

The patient was injected with 10 mCi ^{18}F-FDG following glucose loading. Simultaneous MR-PET study performed on a Biograph mMR was started one hour following tracer injection. Following standard Dixon sequence acquisition for attenuation correction, the comprehensive cardiac MRI sequences were acquired including MR perfusion after Gd contrast infusion, as well as post contrast late Gd enhancement studies. Static ^{18}F-FDG PET was acquired simultaneously during the MRI acquisition.

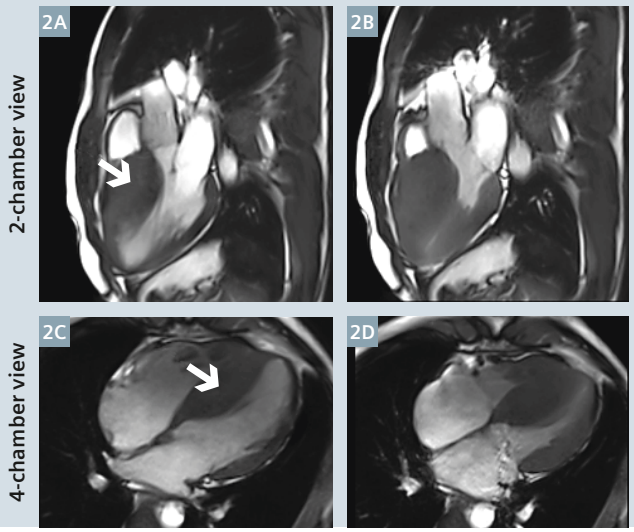

2 End diastolic and end systolic views of 2-chamber and 4-chamber views obtained from gated cine TrueFISP acquisitions showing thickness of the asymmetric septal hypertrophy (white arrow).

Discussion

The late Gd enhancement within the hypertrophic septum along with the non-uniform glucose metabolism demonstrated by the patchy ^{18}F-FDG uptake within the hypertrophic septum exactly corresponding to the area of Gd enhancement reflect myocardial fibrosis within the asymmetric septal hypertrophy. Myocardial fibrosis and the presence of late Gd enhancement on MRI has been shown to be associated with increased risk of cardiac arrhythmia [1] as evident from the symptoms of this patient.

Simultaneous MR-PET acquisition provides combined acquisition of both modalities, thereby ensuring accurate fusion between morphological and functional images due to simultaneous PET acquisition for every MR sequence. The exact coregistration of the patchy ^{18}F-FDG uptake in the area of Gd enhancement within the hypertrophic upper septum reflects the advantage of simultaneous acquisition.

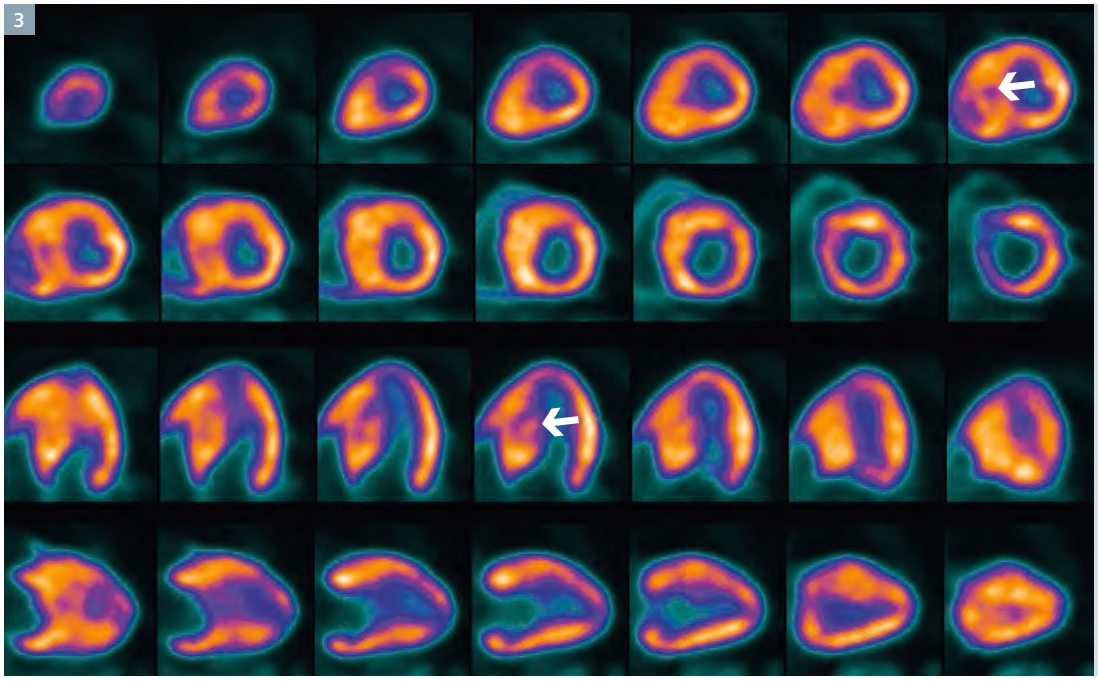

3 Static ^{18}F-FDG PET images in short-axis, horizontal long-axis and vertical long-axis views demonstrating normal uptake in the LV myocardium except the non-uniform uptake pattern in the hypertrophied septum (white arrows). LV cavity size appears normal.

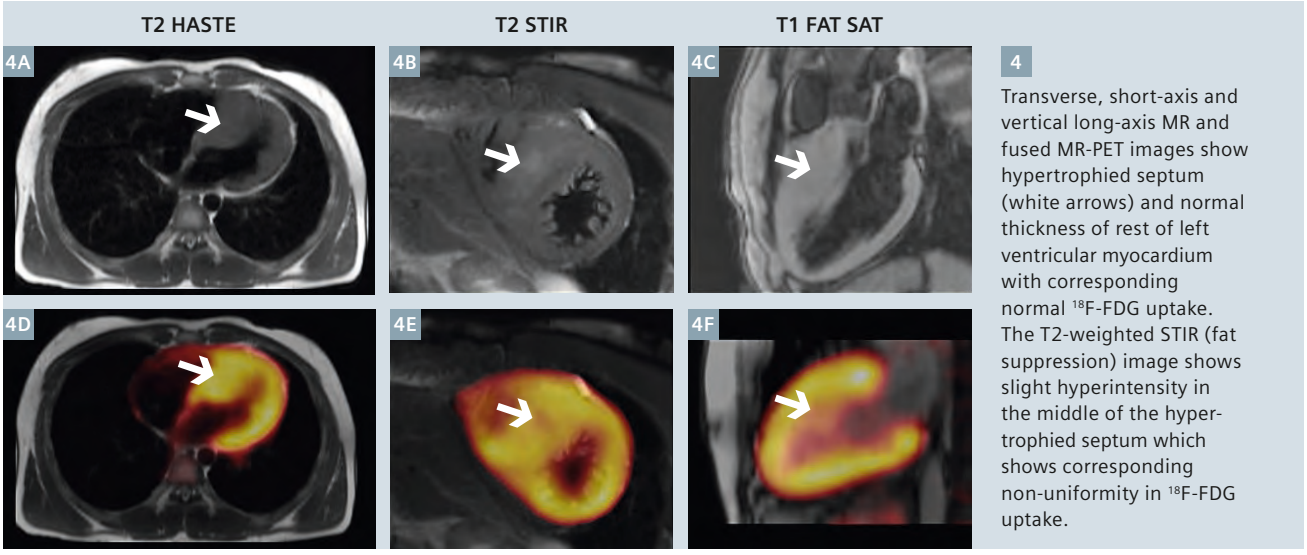

4

Transverse, short-axis and vertical long-axis MR and fused MR-PET images show hypertrophied septum (white arrows) and normal thickness of rest of left ventricular myocardium with corresponding normal ^{18}F-FDG uptake. The T2-weighted STIR (fat suppression) image shows slight hyperintensity in the middle of the hypertrophied septum which shows corresponding non-uniformity in ^{18}F-FDG uptake.

5

Post-contrast MR short-axis images demonstrate late Gd enhancement within the hypertrophied septum (white arrow), which shows corresponding non-uniform patchy uptake of ^{18}F-FDG.

References

1 Rubinstein et al. Characteristics and Clinical Significance of Late Gadolinium Enhancement by Contrast-Enhanced Magnetic Resonance Imaging in Patients With Hypertrophic Cardiomyopathy. Circ Heart Fail. 2010;3:51-58.

2 Bravo et al. PET/CT Assessment of Symptomatic Individuals with Obstructive and Nonobstructive Hypertrophic Cardiomyopathy. J Nucl Med 2012; 53:407–414.

3 Kuhn et al. Changes in the left ventricular outflow tract after transcoronary ablation of septal hypertrophy (TASH) for hypertrophic obstructive cardiomyopathy as assessed by transoesophageal echocardiography and by measuring myocardial glucose utilization and. perfusion. European Heart Journal (1999) 20, 1808–1817.

4 Funabashi N et al. Partial myocardial fibrosis in hypertrophic cardiomyopathy demonstrated by ^{18}F-fluoro-deoxy-glucose positron emission tomography and multislice computed tomography. Int J Cardiol. 2006 Feb 15;107(2):284-6.

Contact

Ihn-ho Cho, M.D.
Department of Nuclear Medicine
Yeungnam University
College of Medicine
Daegu Hyunchungro 170
South Korea
nuclear126@ynu.ac.kr

What's your favorite Dot Feature?

Dot (Day optimizing throughput) is the most comprehensive MRI workflow solution, and it helps take the complexity out of MRI. Dot has now established itself in the field and our customers have told us what they like best about Dot:

"Within our environment, we just could not provide a cardiac MRI service without the Cardiac Dot Engine."

Dr. Russell Bull, MRCP, FRCR
Consultant Radiologist
Royal Bournemouth Hospital, Bournemouth, UK

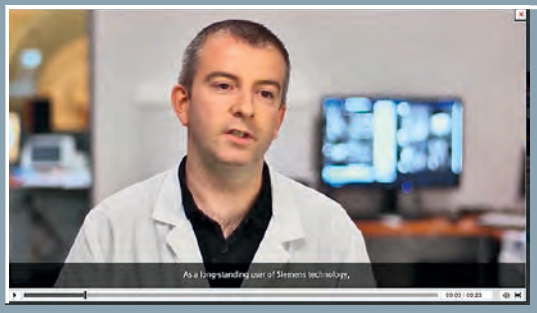

"The Dot Decisions functionality in Abdomen Dot has enabled us to schematize and simplify these protocols. With Dot, we can now ensure our examinations are far more reproducible and of excellent quality."

Arnaud Lambert
Technologist
Imagerie Médicale Saint Marie, Osny, France

"Cardiac Dot (Engine) allows us to obtain automatic positioning of the main slices necessary to evaluate cardiac function with a high degree of reproducibility."

Professor Philippe Cluzel, MD, PhD
Service de Radiologie Polyvalente Diagnostique et Interventionnelle Hôpital Pitié-Salpêtrière, Paris, France

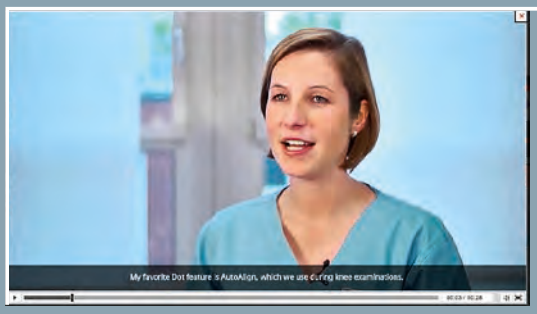

"AutoAlign is helpful especially for colleagues who rarely perform knee examinations because the slices are positioned automatically, which saves a lot of time. Furthermore, our knee examinations have become reproducible."

Linda Willeke
Technologist
St. Franziskus Hospital, Münster, Germany

Experience a Dot workflow yourself and hear from more users at

www.siemens.com/Dot

Visit our site optimized for tablets and smartphones

New Generation Cardiac Parametric Mapping: the Clinical Role of T1 and T2 Mapping

Viviana Maestrini; Amna Abdel-Gadir; Anna S. Herrey; James C. Moon

The Heart Hospital Imaging Centre, University College London Hospitals, London, UK

Introduction

Cardiovascular magnetic resonance (CMR) is an essential tool in cardiology and excellent for cardiac function and perfusion. However, a key, unique advantage is its ability to directly scrutinize the fundamental material properties of myocardium – 'myocardial tissue characterization'.

Between 2001 and 2011, the key methods for tissue characterization have been sequences 'weighted' to a magnetic property – T1-weighted imaging for scar (LGE) and T2-weighted for edema (area at risk, myocarditis). These, particularly LGE imaging, have changed our understanding and clinical practice in cardiology.

However, there are limitations to these approaches: Both are difficult to quantify – the LGE technique in particular is very robust in infarction, but harder to quantify in non-ischemic cardiomyopathy. A more fundamental difference is that sequences are designed to optimize contrast between 'normal' and abnormal – a dichotomy of health and disease. As a result, global myocardial pathologies such as diffuse infiltration (fibrosis, amyloid, iron, fat, pan-inflammation) are missed.

Recently, rapid technical innovations have generated new 'mapping' techniques. Rather than being 'weighted', these create a pixel map where each pixel value is the T1 or T2 (or T2*), displayed in color. These new sequences are single breath-hold, increasingly robust and now widely available. With T1 mapping, clever contrast agent use also permits the measurement of the extracellular volume (ECV), quantifying the interstitium (odema, fibrosis or amyloid), also as a map. Early results with these methodologies are exciting – potentially representing a new era of CMR.

T1 mapping

Initial T1 measurement methods were multi-breath-hold. These were time consuming and clunky, but were able to measure well diffuse myocardial fibrosis, a fundamental myocardial property with high potential clinical significance [1]. Healthy volunteers and those with disease had different extents of diffuse fibrosis [2], and these were shown to be clinically significant in a number of diseases. T1 mapping methods based on the MOLLI* approach with modifications for shorter breath-holds, better heart rate independence and better image registration for cleaner maps, however, transformed the field – albeit still with a variety of potential sequences in use [3-5]. There are two key ways of using T1 mapping: Without (or

* The product is currently under development; is not for sale in the U.S. and other countries, and its future availability cannot be ensured.

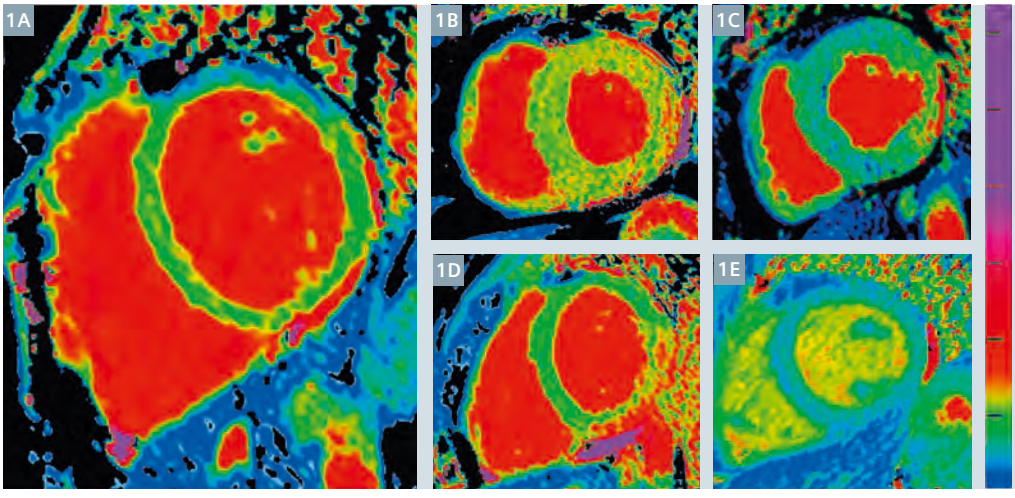

1
Native T1 maps of **(1A)** healthy volunteer (author VM): the myocardium appears homogenously green and the blood is red; **(1B)** cardiac amyloid: the myocardium has a higher T1 (red); **(1C)** Anderson Fabry disease: the myocardium has a lower T1 (blue) from lipid – except the inferolateral wall where there is red from fibrosis; **(1D)** myocarditis, the myocardium has a higher T1 (red) from edema, which is regional; **(1E)** iron overload: the myocardium has a lower T1 (blue) from iron.

before) contrast – Native T1 mapping; and with contrast, typically by subtracting the pre and post maps with hematocrit correction to generate the ECV [6].

Native T1

Native T1 mapping (pre-contrast T1) can demonstrate intrinsic myocardial contrast (Fig. 1). T1, measured in milliseconds, is higher where the extracellular compartment is increased. Fibrosis (focal, as in infarction, or diffuse) [7-8], odema [9-10] and amyloid [11], are examples. T1 is lower in lipid (Anderson Fabry disease, AFD) [12], and iron [13] accumulation.

These changes are large in some rare disease. Global myocardial changes are robustly detectable without contrast, even in early disease. In iron, AFD and amyloid, changes appear before any other abnormality – there may be no left ventricular hypertrophy, a normal electrocardiogram, and normal conventional CMR, for example – genuinely new information. In established disease, low T1 values in AFD appear to absolutely distinguish it from other causes of left ventricular hypertrophy [12] whilst in established amyloid T1 elevation tracks known markers of cardiac severity [11].

A note of caution, however. Native T1, although stable between healthy volunteers to 1 part in 30, is dependent on platform (magnet manufacturer, sequence and sequence variant, field strength) [14]. Normal reference ranges for your setup are needed.

2

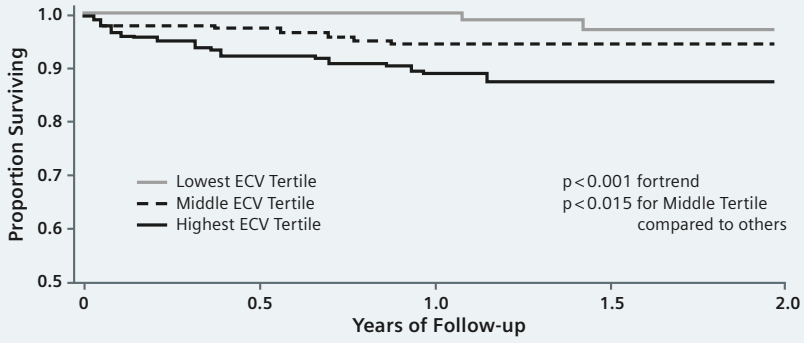

2 ECV in non scar areas (LGE excluded) is associated with all-cause mortality [21].

The signal acquired is also a composite signal – generated by both interstitium and myocytes. The use of an extracellular contrast agent adds another dimension to T1 mapping and the ability to characterize the extracellular compartment specifically.

Extracellular volume (ECV)

Initially, post-contrast T1 was measured, but this is confounded by renal clearance, gadolinium dose, body composition, acquisition time post bolus, and hematocrit. Better is measuring the ECV. The ratio of change of T1 between blood and myocardium after contrast, at sufficient equilibrium (e.g. after 15 minutes post-bolus – no infusion generally needed) [15, 16], represents the contrast agent partition coefficient [17], and if corrected for the hematocrit, the myocardial extracellular space – ECV [1]. The ECV is specific for extracellular expansion, and well validated. Clinically this occurs in fibrosis, amyloid and odema. To distinguish, the degree of ECV change and the clinical context is important. A multiparametric approach (e. g. T2 mapping or T2-weighted imaging in addition) may therefore be useful. Amyloid can have far higher ECVs than any other disease [18] whereas ageing has small changes – near the detection limits, but of high potential clinical importance [19, 20]. For low ECV expansion diseases, biases from blood pool partial volume errors need to be meticulously addressed. Nevertheless, even modest ECV changes appear prognostic. In 793 consecutive patients (all-comers but excluding amyloid and HCM, measuring outside LGE areas) followed over 1 year, global ECV predicted short term-mortality (Fig. 2)

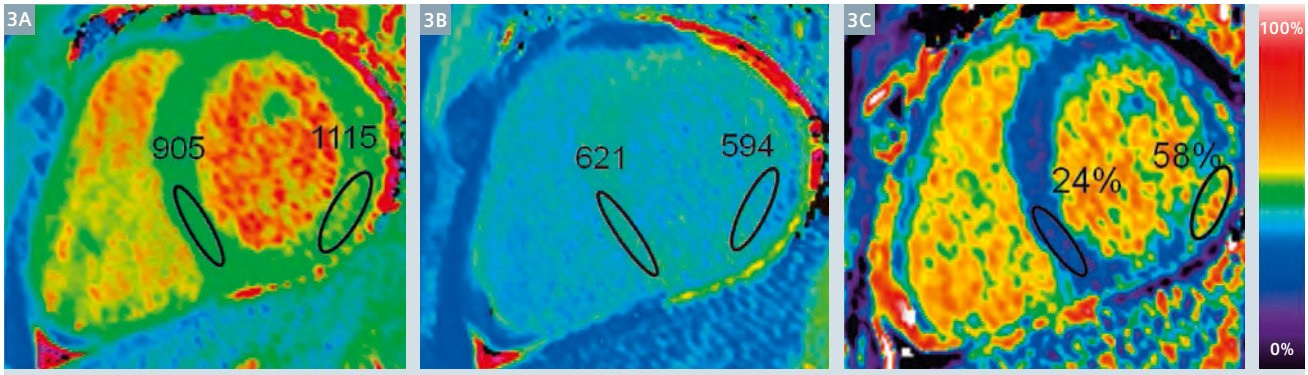

3 A patient with myocarditis. On the left side a native T1 map showing the higher T1 value in the inferolateral wall (1115 ms); in the centre, a post-contrast T1 map showing the shortened T1 value after contrast administration (594 ms); on the right side the derived ECV map showing higher value of ECV (58%) compared to remote myocardium.

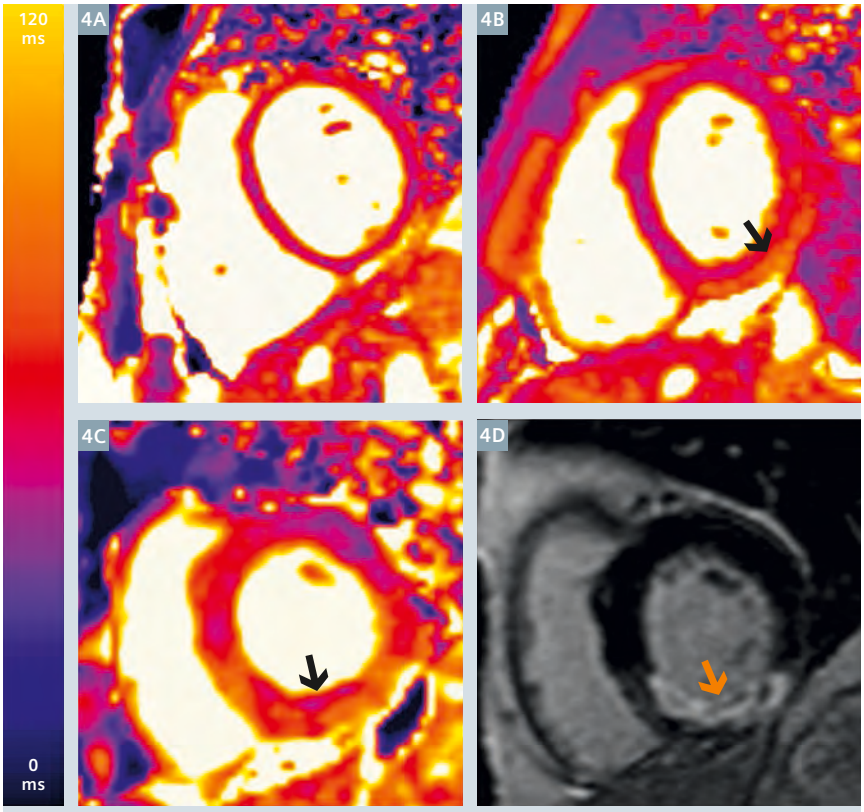

4 **(4A)** T2 mapping in a normal volunteer (author VM). **(4B)** High T2 value in patient with myocarditis – here epicardial edema. **(4C)** Edema in acute myocardial infarction – here patchy due to microvascular obstruction – see LGE, **(4D)**.

[21]. The same group also found (n ~1000) higher ECVs in diabetics. Those on renin-angiotensin-aldosterone system blockade had lower ECVs. ECV also predicted mortality and/or incident hospitalization for heart failure in diabetics [22].

The use and capability of ECV quantification is growing. T1 mapping is getting better and inline ECV maps are now possible where each pixel carries directly the ECV value (Fig. 3) – a more biologically relevant figure than T1 [6].

T2 mapping

T2-weighted CMR identifies myocardial odema both in inflammatory pathologies and acute ischemia, delineating the area at risk. However, these imaging techniques (e. g. STIR) are fragile in the heart and can be challenging, both to acquire and to interpret. Preliminary advances were made with T2-weighted SSFP sequences, which reduce false negatives and positives [23, 24]. T2 mapping seems a further increment [25] (Fig. 4). As with T1 mapping, global diseases such as pan-myocarditis may now be identified by T2 mapping, and preliminary results are showing this in several rheumatologic diseases (lupus, systemic capillary leak syndrome) and transplant rejection, detecting early rejection missed by other modalities [26, 27].

Conclusion

Mapping – T1, T2, ECV mapping of myocardium is an emerging topic with the potential to be a powerful tool in the identification and quantification of diffuse myocardial processes without biopsy. Early evidence suggests that this technique detects early stage disease missed by other imaging methods and has potential as a prognosticator, as a surrogate endpoint in trials, and to monitor therapy. Progress is rapid; challenges remain. Delivery across sites and standardization is now beginning with new draft guidelines for T1 mapping in preparation. Watch this space.

References

1 Flett AS, Hayward MP, Ashworth MT, Hansen MS, Taylor AM, Elliott PM, McGregor C, Moon JC. Equilibrium Contrast Cardiovascular Magnetic Resonance for the measurement of diffuse myocardial fibrosis: preliminary validation in humans. Circulation 2010;122:138-144.

2 Sado DM, Flett AS, Banypersad SM, White SK, Maestrini V, Quarta G, Lachmann RH, Murphy E, Mehta A, Hughes DA, McKenna WJ, Taylor AM, Hausenloy DJ, Hawkins PN, Elliott PM, Moon JC. Cardiovascular magnetic resonance measurement of myocardial extracellular volume in health and disease. Heart 2012;98:1436-1441.

3 Piechnik SK, Ferreira VM, Dall'Armellina E, Cochlin LE, Greiser A, Neubauer S, Robson MD. Shortened Modified Look-Locker Inversion recovery (ShMOLLI) for clinical myocardial T1-mapping at 1.5 and 3 T within a 9 heartbeat breathhold. J Cardiovasc Magn Reson 2010;12:69.

4 Messroghli DR, Greiser A, Fröhlich M, Dietz R, Schulz-Menger J. Optimization and validation of a fully-integrated pulse sequence for modified look-locker inversion-recovery (MOLLI) T1 mapping of the heart. J Magn Reson Imaging 2007;26:1081–1086.

5 Fontana M, White SK, Banypersad SM, Sado DM, Maestrini V, Flett AS, Piechnik SK, Neubauer S, Roberts N, Moon JC. Comparison of T1 mapping techniques for ECV quantification. Histological validation and reproducibility of ShMOLLI versus multibreath-hold T1 quantification equilibrium contrast CMR. J Cardiovasc Magn Reson 201;14:88.

6 Kellman P, Wilson JR, Xue H, Ugander M, Arai AE. Extracellular volume fraction mapping in the myocardium, part 1: evaluation of an automated method. J Cardiovasc Magn Reson 2012;14:63.

7 Dass S, Suttie JJ, Piechnik SK, Ferreira VM, Holloway CJ, Banerjee R, Mahmod M, Cochlin L, Karamitsos TD, Robson MD, Watkins H, Neubauer S. Myocardial tissue characterization using magnetic resonance non contrast T1 mapping in hypertrophic and dilated cardiomyopathy. Circ Cardiovasc Imaging. 2012; 6:726-33.

8 Puntmann VO, Voigt T, Chen Z, Mayr M, Karim R, Rhode K, Pastor A, Carr-White G, Razavi R, Schaeffter T, Nagel E. Native T1 mapping in differentiation of normal myocardium from diffuse disease in hypertrophic and dilated cardiomyopathy. J Am Coll Cardiovasc Imgaging 2013;6:475–84.

9 Ferreira VM, Piechnik SK, Dall'Armellina E, Karamitsos TD, Francis JM, Choudhury RP, Friedrich MG, Robson MD, Neubauer S. Non-contrast T1-mapping detects acute myocardial edema with high diagnostic accuracy: a comparison to T2-weighted cardiovascular magnetic resonance. J Cardiovasc Magn Reson 2012; 14:42.

10 Dall'Armellina E, Piechnik SK, Ferreira VM, Si Ql, Robson MD, Francis JM, Cuculi F, Kharbanda RK, Banning AP, Choudhury RP, Karamitsos TD, Neubauer S. Cardiovascular magnetic resonance by non contrast T1-mapping allows assessment of severity of injury in acute myocardial infarction. J Cardiovasc Magn Reson 2012;14:15.

11 Karamitsos TD, Piechnik SK, Banypersad SM, Fontana M, MD, Ntusi NB, Ferreira VM, Whelan CJ, Myerson SG, Robson MD, Hawkins PN, Neubauer S, Moon JC. Non-contrast T1 Mapping for the Diagnosis of Cardiac Amyloidosis. J Am Coll Cardiol Img 2013;6:488–97.

12 Sado DM, White SK, Piechnik SK, Banypersad SM, Treibel T, Captur G, Fontana M, Maestrini V, Flett AS, Robson MD, Lachmann RH, Murphy E, Mehta A, Hughes D, Neubauer S, Elliott PM, Moon JC. Identification and assessment of Anderson-Fabry Disease by Cardiovascular Magnetic Resonance Non-contrast myocardial T1 Mapping clinical perspective. Circ Cardiovasc Imaging 2013;6:392-398.

13 Pedersen SF, Thrys SA, Robich MP, Paaske WP, Ringgaard S, Bøtker HE, Hansen ESS, Kim WY. Assessment of intramyocardial hemorrhage by T1-weighted cardiovascular magnetic resonance in reperfused acute myocardial infarction. J Cardiovasc Magn Reson 2012; 14:59.

14 Raman FS, Kawel-Boehm N, Gai N, Freed M, Han J, Liu CY, Lima JAC, Bluemke DA, Liu S. Modified look-locker inversion recovery T1 mapping indices: assessment of accuracy and reproducibility between magnetic resonance scanners. J Cardiovasc Magn Reson 2013; 15:64.

15 White SK, Sado DM, Fontana M, Banypersad SM, Maestrini V, Flett AS, Piechnik SK, Robson MD, Hausenloy DJ, Sheikh AM, Hawkins PN, Moon JC. T1 Mapping for Myocardial Extracellular Volume measurement by CMR: Bolus Only Versus Primed Infusion Technique, 2013 Apr 5 [Epub ahead of print].

16 Schelbert EB, Testa SM, Meier CG, Ceyrolles WJ, Levenson JE, Blair AJ, Kellman P, Jones BL, Ludwig DR, Schwartzman D, Shroff SG, Wong TC. Myocardial extravascular extracellular volume fraction measurement by gadolinium cardiovascular magnetic resonance in humans: slow infusion versus bolus. J Cardiovasc Magn Reson 2011, Mar 4;13-16.

17 Flacke SJ, Fischer SE, Lorenz CH. Measurement of the gadopentetate dimeglumine partition coefficient in human myocardium in vivo: normal distribution and elevation in acute and chronic infarction. Radiology 2001;218:703-10.

18 Banypersad SM, Sado DM, Flett AS, Gibbs SDG, Pinney JH, Maestrini V, Cox AT, Fontana M, Whelan CJ, Wechalekar AD, Hawkins PN, Moon JC. Quantification of myocardial extracellular volume fraction in systemic AL amyloidosis: An Equilibrium Contrast Cardiovascular Magnetic Resonance Study. Circ Cardiovasc Imaging 2013;6:34-39.

19 Ugander M, Oki AJ, Hsu LY, Kellman P, Greiser A, Aletras AH, Sibley CT, Chen MY, Bandettini WP, Arai AE. Extracellular volume imaging by magnetic resonance imaging provides insights into overt and sub-clinical myocardial pathology. Eur Heart J 2012; 33: 1268–1278.

20 Liu CY, Chang Liu Y, Wu C, Armstrong A, Volpe GJ, van der Geest RJ, Liu Y, Hundley WG, Gomes AS, Liu S, Nacif M, Bluemke DA, Lima JAC. Evaluation of age related interstitial myocardial fibrosis with Cardiac Magnetic Resonance Contrast-Enhanced T1 Mapping in the Multi-ethnic Study of Atherosclerosis (MESA). J Am Coll Cardiol 2013 Jul 3 [Epub ahead of print].

21 Wong TC, Piehler K, Meier CG, Testa SM, Klock AM, Aneizi AA, Shakesprere J, Kellman P, Shroff SG, Schwartzman DS, Mulukutla SR, Simon MA, Schelbert EB. Association between extracellular matrix expansion quantified by cardiovascular magnetic resonance and short-term mortality. Circulation 2012 Sep 4;126(10):1206-16.

22 Wong TC, Piehler KM, Kang IA, Kadakkal A, Kellman P, Schwartzman DS, Mulukutla SR, Simon MA, Shroff SG, Kuller LH, Schelbert EB. Myocardial extracellular volume fraction quantified by cardiovascular magnetic resonance is increased in diabetes and associated with mortality and incident heart failure admission. Eur Heart J 2013 Jun 11 [Epub ahead of print].

23 Giri S, Chung YC, Merchant A, Mihai G, Rajagopalan S, Raman SV, Simonetti OP. T2 quantification for improved detection of myocardial edema. J Cardiovasc Magn Reson 2009; 11:56.

24 Verhaert D, Thavendiranathan P, Giri S, Mihai G, Rajagopalan S, Simonetti OP, Raman SV. Direct T2 Quantification of Myocardial Edema in Acute Ischemic Injury. J Am Coll Cardiol Img 2011;4: 269-78.

25 Ugander M, Bagi PS, Oki AB, Chen B, Hsu LY, Aletras AH, Shah S, Greiser A, Kellman P, Arai AE. Myocardial oedema as detected by Pre-contrast T1 and T2 CMR delineates area at risk associated with acute myocardial infarction. J Am Coll Cardiol Img 2012;5:596–603.

26 ThavendiranathanP, Walls M, Giri S, Verhaert D, Rajagopalan S, Moore S, Simonetti OP, Raman SV. Improved detection of myocardial involvement in acute inflammatory cardiomyopathies using T2 Mapping. Circ Cardiovasc Imaging 2012;5:102-110.

27 Usman AA, Taimen K, Wasielewski M, McDonald J, Shah S, Shivraman G, Cotts W, McGee E, Gordon R, Collins JD, Markl M, Carr JC. Cardiac Magnetic Resonance T2 Mapping in the monitoring and follow-up of acute cardiac transplant rejection: A Pilot Study. Circ Cardiovasc Imaging. 2012; 6:782-90.

Contact

Dr. James C. Moon
The Heart Hospital Imaging Centre
University College London Hospitals
16–18 Westmoreland Street
London W1G 8PH
UK
Phone: +44 (20) 34563081
Fax: +44 (20) 34563086
james.moon@uclh.nhs.uk

Preliminary Experiences with Compressed Sensing Multi-Slice Cine Acquisitions for the Assessment of Left Ventricular Function: CV_sparse WIP

G. Vincenti, M.D.[1]; D. Piccini[2,4]; P. Monney, M.D.[1]; J. Chaptinel[3]; T. Rutz, M.D.[1]; S. Coppo[3]; M. O. Zenge, Ph.D.[4]; M. Schmidt[4]; M. S. Nadar[5]; Q. Wang[5]; P. Chevre[1, 6]; M.; Stuber, Ph.D.[3]; J. Schwitter, M.D.[1]

[1] Division of Cardiology and Cardiac MR Center, University Hospital of Lausanne (CHUV), Lausanne, Switzerland
[2] Advanced Clinical Imaging Technology, Siemens Healthcare IM BM PI, Lausanne, Switzerland
[3] Department of Radiology, University Hospital (CHUV) and University of Lausanne (UNIL) / Center for Biomedical Imaging (CIBM), Lausanne, Switzerland
[4] MR Applications and Workflow Development, Healthcare Sector, Siemens AG, Erlangen, Germany
[5] Siemens Corporate Technology, Princeton, USA
[6] Department of Radiology, University Hospital Lausanne, Switzerland

Introduction

Left ventricular (LV) ejection fraction is one of the most important measures in cardiology and part of every cardiac imaging evaluation as it is recognized as one of the strongest predictors of outcome [1]. It allows to assess the effect of established or novel treatments [2], and it is crucial for decision making [3] e.g. to start [4] or stop [5] specific drug treatments or to implant devices [6]. CMR is generally accepted as the gold standard method to yield most accurate measures of LV ejection fraction and LV volumes. This capability and the additional value of CMR to characterize pathological myocardial tissue was the basis to assign a class 1 indication for patients with known or suspected heart failure to undergo CMR in the new Heart Failure Guidelines of the European Society of Cardiology [3].

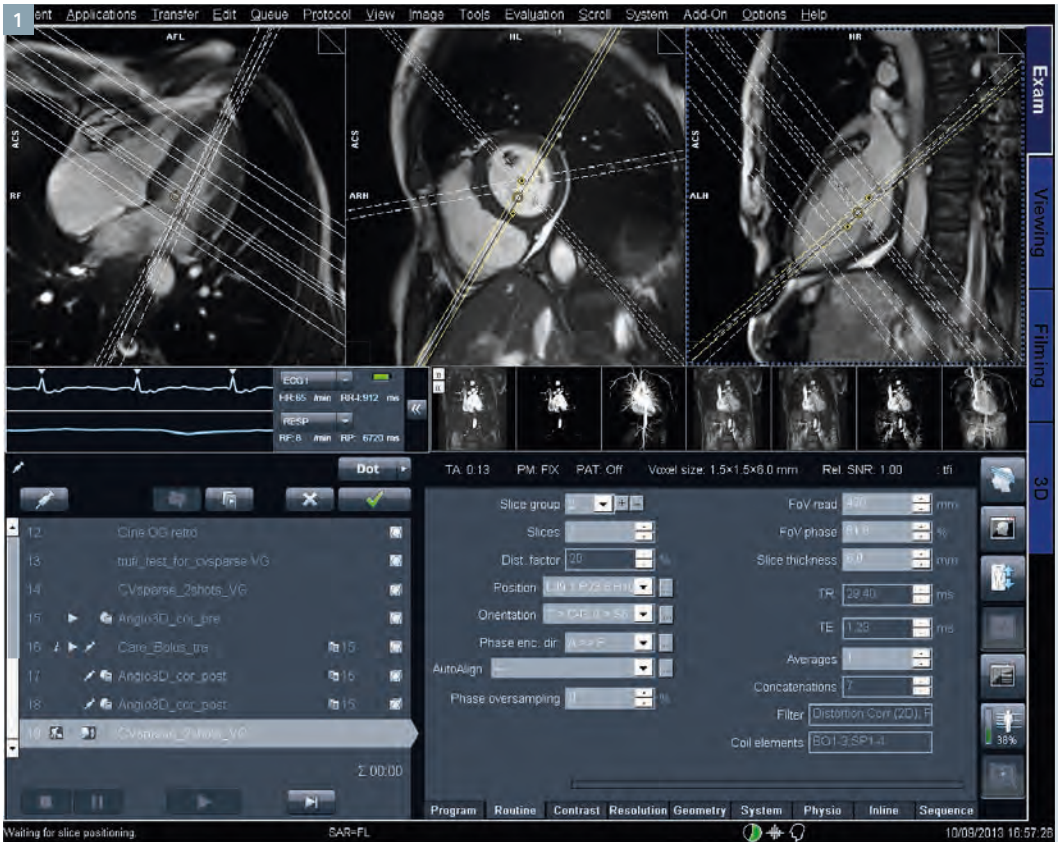

1 Display of the planning of the 7 slices (4 short axis and 3 long axis slices) acquired within a single breath-hold with the three localizers.

The evaluation of LV volumes and LV ejection fraction are based on well-defined protocols [7] and it involves the acquisition of a stack of LV short axis cine images from which volumes are calculated by applying Simpson's rule. These stacks are typically acquired in multiple breath-holds. Quality criteria [8] for these functional images are available and are implemented e.g. for the quality assessment within the European CMR registry which currently holds approximately 33,000 patients and connects 59 centers [9].

Recently, compressed sensing (CS) techniques emerged as a means to considerably accelerate data acquisition without compromising significantly image quality. CS has three requirements:

1) transform sparsity,
2) incoherence of undersampling artifacts, and
3) nonlinear reconstruction (for details, see below).

Based on these prerequisites, a CS approach for the acquisition of cardiac cine images was developed and tested*. In particular, the potential to acquire several slices covering the heart in different orientations within a single breath-hold would allow to apply model-based analysis tools which theoretically could improve the motion assessment at the base of the heart, where considerable through-plane motion on short-axis slices can introduce substantial errors in LV volume and LV ejection fraction calculations. Conversely, with a multi-breath-hold approach, there are typically small differences in breath-hold positions which can introduce errors in volume and function calculations. The pulse sequence tested here allows for the acquisition of 7 cine slices within 14 heartbeats with an excellent temporal and spatial resolution.

Such a pulse sequence would also offer the advantage to obtain functional information in at least a single plane in patients unable to hold their breath for several heartbeats or in patients with frequent extrasystoles or atrial fibrillation. However, it should be mentioned that accurate quantitative measures of LV volumes and function cannot be obtained in highly arrhythmic hearts or in atrial fibrillation, as under such conditions volumes and ejection fraction change from beat to beat due to variable filling conditions. Nevertheless, rough estimates of LV volumes and function would still be desirable in arrhythmic patients.

*Work in progress: The product is still under development and not commercially available yet. Its future availability cannot be ensured.

In a group of healthy volunteers and patients with different LV pathologies, the novel single-breath-hold CS cine approach was compared with the standard multi-breath-hold cine technique with respect to measure LV volumes and LV ejection fraction.

The CV_sparse work-in-progress (WIP)

The CV_sparse WIP package implements sparse, incoherent sampling and iterative reconstruction for cardiac applications. This method in principle allows for high acceleration factors which enable triggered 2D real-time cine CMR while preserving high spatial and/or temporal resolution of conventional cine acquisitions. Compressed sensing methods exploit the potential of image compression during the acquisition of raw input data. Three components [10] are crucial for the concept of compressed sensing to work

I. Sparsity: In order to guarantee compressibility of the input data, sparsity must be present in a specific transform domain. Sparsity can be computed e.g. by calculating differences between neighboring pixels or by calculating finite differences in angiograms which then detect primarily vessel contours which typically represent a few percent of the

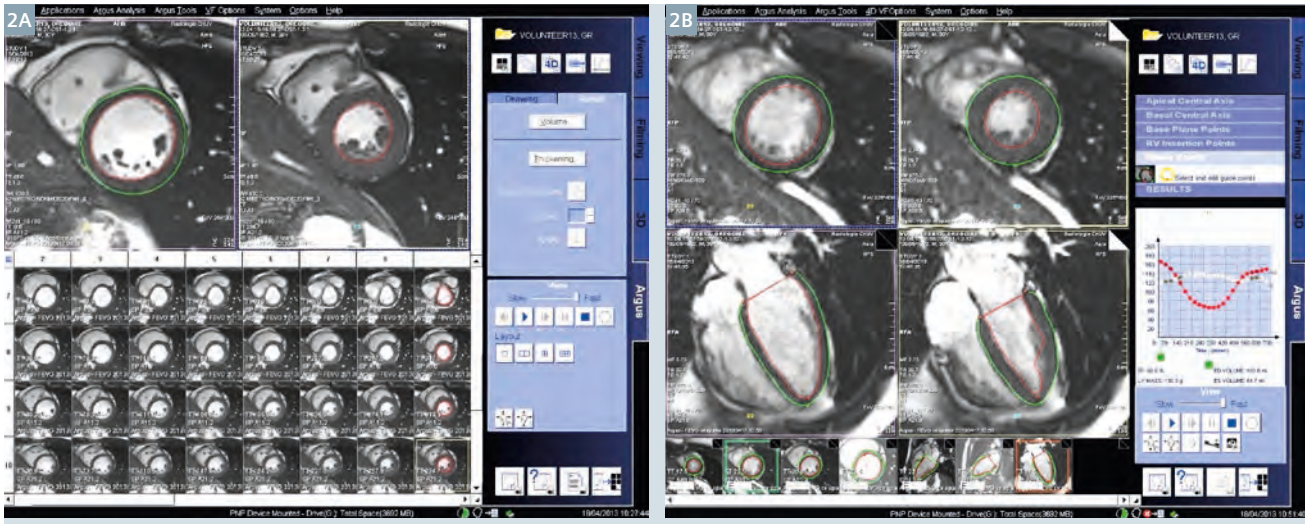

2 Displays of the data analysis tools for the conventional short axis stack of cine images covering the entire LV **(2A)** and the 4D analysis tool **(2B)**, which is model-based and takes long axis shortening of the LV, i.e. mitral annulus motion into account. Note that with both analysis tools, LV trabeculations are included into the LV volume, particularly in the end-diastolic images (corresponding images on the left of top row in 2A and 2B).

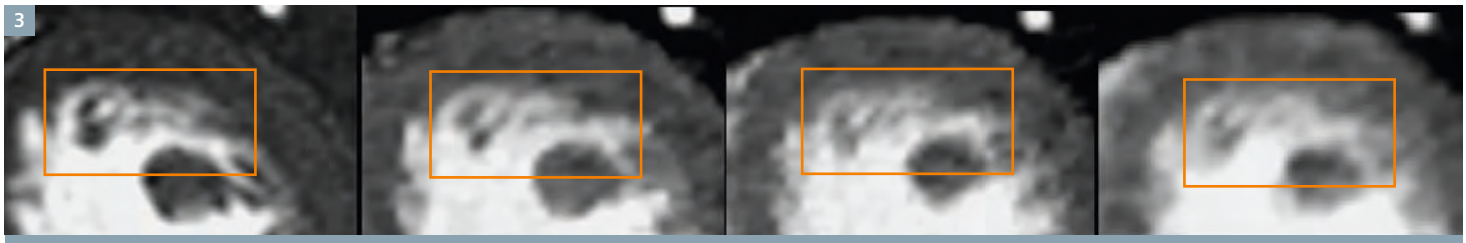

3 Examples of visualization of small trabecular structures in the LV (in the rectangle) with the standard cine SSFP sequence (image on the left) and the accelerated compressed sensing sequences (images on the right). Despite increasing acceleration most information on small intraluminal structures remains visible.

entire image data only. Furthermore, sparsity is not limited to the spatial domain: the acquisition of cine images of the heart can be highly sparsified in the temporal dimension.

II. Incoherent sampling: The aliasing artifacts due to *k*-space undersampling must be incoherent, i.e. noise-like, in that transform domain. Here, it is to mention that fully random *k*-space sampling is suboptimal as *k*-space trajectories should be smooth for hardware and physiological considerations. Therefore, incoherent sampling schemes must be designed to avoid these concerns while fulfilling the condition of random, i.e. incoherent sampling.

III. Reconstruction: A non-linear iterative optimization corrects for subsampling artifacts during the process of image reconstruction yielding to a best solution with a sparse representation in a specific transform domain and which is consistent with the input data. Such compressed sensing techniques can also be combined with parallel imaging techniques [11].

WIP CV_sparse Sequence

The current CV_sparse sequence [12] realizes incoherent sampling by initially distributing the readouts pseudo-randomly on the Cartesian grid in *k*-space. In addition, for cine-CMR imaging, a pseudo-random offset is applied from frame-to-frame which results in an incoherent temporal jitter. Finally, a variable sampling density in *k*-space stabilizes the iterative reconstruction. To avoid eddy current effects for balanced steady-state free precession (bSSFP) acquisitions, pairing [13] can also be applied. Thus, the tested CV_sparse sequence is characterized by sparse, incoherent sampling in space and time, non-linear iterative reconstruction integrating SENSE, and L1 wavelet regularization in the phase encoding direction and/or the temporal dimension. With regard to reconstruction, the ICE program runs a non-linear iterative reconstruction with *k-t* regularization in space and time specifically modified for compressed sensing. The algorithm derives from a parallel imaging type reconstruction which takes coil sensitivity maps into account, thus supporting predominantly high acceleration factors. For cine CMR, no additional reference scans are needed because – similar to TPAT – the coil sensitivity maps are calculated from the temporal average of the input data in a central region of *k*-space consisting of not more than 48 reference lines. The extensive calculations for image reconstruction typically running 80 iterations are performed online on all CPUs on the MARS computer in parallel, in order to reduce reconstruction times.

Volunteer and Patient studies

In order to obtain insight into the image quality of single-breath-hold multi-slice cine CMR images acquired with the compressed sensing (CS) approach, we studied a group of healthy volunteers and a patient group with different pathologies of the left ventricle. In addition to the evaluation of image quality, the robustness and the precision of the CS approach for LV volumes and LV ejection fraction was also assessed in comparison with a standard high-resolution cine CMR approach. All CMR examinations were performed on a 1.5T MAGNETOM Aera (Siemens Healthcare, Erlangen, Germany). The imaging protocol consisted of a set of cardiac localizers followed by the acquisition of a stack of conventional short-axis SSFP cine images covering the entire LV with a spatial and tem-

poral resolution of 1.2 x 1.6 mm², and approximately 40 ms, respectively (slice thickness: 8 mm; gap between slices: 2 mm). LV 2-chamber, 3-chamber, and 4-chamber long-axis acquisitions were obtained for image quality assessment but were not used for LV volume quantifications. As a next step, to test the new CS-based technique, slice orientations were planned to cover the LV with 4 short-axis slices distributed evenly over the LV long axis complemented by 3 long-axis slices (i.e. a 2-chamber, 3-chamber, and 4-chamber slice) (Fig. 1). These 7 slices were then acquired in a single breath-hold maneuver lasting 14 heart beats (i.e. 2 heart beats per slice) resulting in an acceleration factor of 11.0 with a temporal and spatial resolution of 30 ms and 1.5 x 1.5 mm², respectively (slice thickness: 6 mm). As the reconstruction algorithm is susceptible to aliasing in the phase-encoding direction, the 7 slices were first acquired with a non-cine acquisition to check for correct phase-encoding directions and, if needed, to adjust the field-of-view to avoid fold-over artifacts. After confirmation of correct imaging parameters, the 7-slice single-breath-hold cine CS-acquisition was performed. In order to obtain a reference for the LV volume measurement, a phase-contrast flow measurement in the ascending aorta was performed to be compared with the LV stroke volumes calculated from the standard and CS cine data.

The conventional stack of cine SSFP images was analyzed by the Argus software (Siemens Argus 4D Ventricular Function, Fig. 2A). The CS cine data were analyzed by the 4D-Argus software (Siemens Argus, Fig. 2B). Such software is based on an LV model and, with relatively few operator interactions, the contours for the LV endocardium and epicardium are generated by the analysis tool. Of note, this 4D analysis tool automatically tracks the 3-dimensional motion of the mitral annulus throughout the cardiac cycle which allows for an accurate volume calculation particularly at the base of the heart.

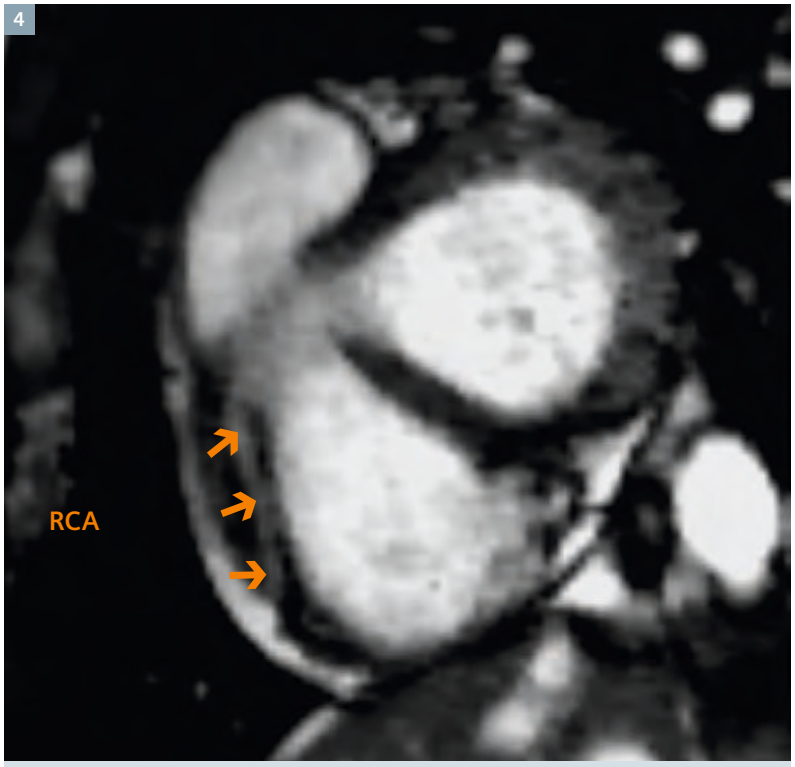

4 Example demonstrating the performance of the compressed sensing technique visualizing small structures such as the right coronary artery (RCA) with high temporal and spatial resolution acquired within 2 heartbeats. Short-axis view of the base of the heart (1 out of 17 frames).

Results and discussion

Image quality – robustness of the technique

Overall, a very good image quality of the single-breath-hold multi-slice CS acquisitions was obtained in the 12 volunteers and 14 patient studies. All CS data sets were of adequate quality to undergo 4D analysis. Small structures such as trabeculations were visualized in the CS data sets as shown in Figures 3 and 4. However, very small structures, detectable by the conventional cine acquisitions, were less well discernible by the CS images. Therefore, it should be mentioned here, that this accelerated single-breath-hold CS approach would be adequate for functional measurements, i.e. LV ejection fraction assessment (see also results below), whereas assessment of small structures as present in many cardiomyopathies is more reliable when performed on conventional cine images. Temporal resolution of the new technique appears adequate to even detect visually the dyssynchroneous contraction pattern in left bundle branch block. Also, the image contrast between the LV myocardium and the blood pool was high on the CS images allowing for an easy assessment of the LV motion pattern. As a result, the single-breath-hold cine approach permits to reconstruct the LV in 3D space with high temporal resolution as illustrated in Figure 5. Since these data allow to correctly include the 3D motion of the base of the heart during the cardiac cycle, the LV stroke volume appears to be measurable by the CS approach with higher accuracy than with the conventional multi-breath-hold approach (see results below). With an accurate measurement of the LV stroke volume, the quantification of a mitral insufficiency should theoretically benefit (when calculating mitral regurgitant volume as 'LV stroke volume minus aortic forward-flow volume').

As a current limitation of the CS approach, its susceptibility for fold-over artifacts should be mentioned (Figs. 6A). Therefore, the field-of-view must cover the entire anatomy and thus, some penalty in spatial res-

olution may occur in relation to the patient's anatomy. In addition, the sparsity in the temporal domain may be limited in anatomical regions of very high flow, and therefore, in some acquisitions, flow-related artifacts occurred in the phase-encoding direction during systole (Figs. 6B, C). Also, in its current version, the sequence is prospective, thus it does not cover the very last phases of the cardiac cycle and the reconstruction times for the CS images lasted several minutes precluding an immediate assessment of the image data quality or using this image information to plan next steps of a CMR examination.

Performance of the single-breath-hold CS approach in comparison with the standard multi-breath-hold cine approach

From a quantitative point-of-view, the accurate and reliable measurement of LV volumes and function is crucial as many therapeutic decisions directly depend on these measures [3–6]. In this current relatively small study group, LV end-diastolic and end-systolic volumes measured by the single-breath-hold CS approach were comparable with those calculated from the standard multi-breath-hold cine SSFP approach. LVEDV and LVESV differed by 10 ml ± 17 ml and 2 ml ± 12 ml, respectively. Most importantly, LV ejection fraction differed by only 1.3 ± 4.7% (50.6% vs 49.3% for multi-breath-hold and single-breath-hold, respectively, $p = 0.17$; regression: $r = 0.96$, $p < 0.0001$; $y = 0.96x + 0.8$ ml). Thus, it can be concluded that the single-breath-hold CS approach could potentially replace the multi-breath-hold standard technique for the assessment of LV volumes and systolic function.

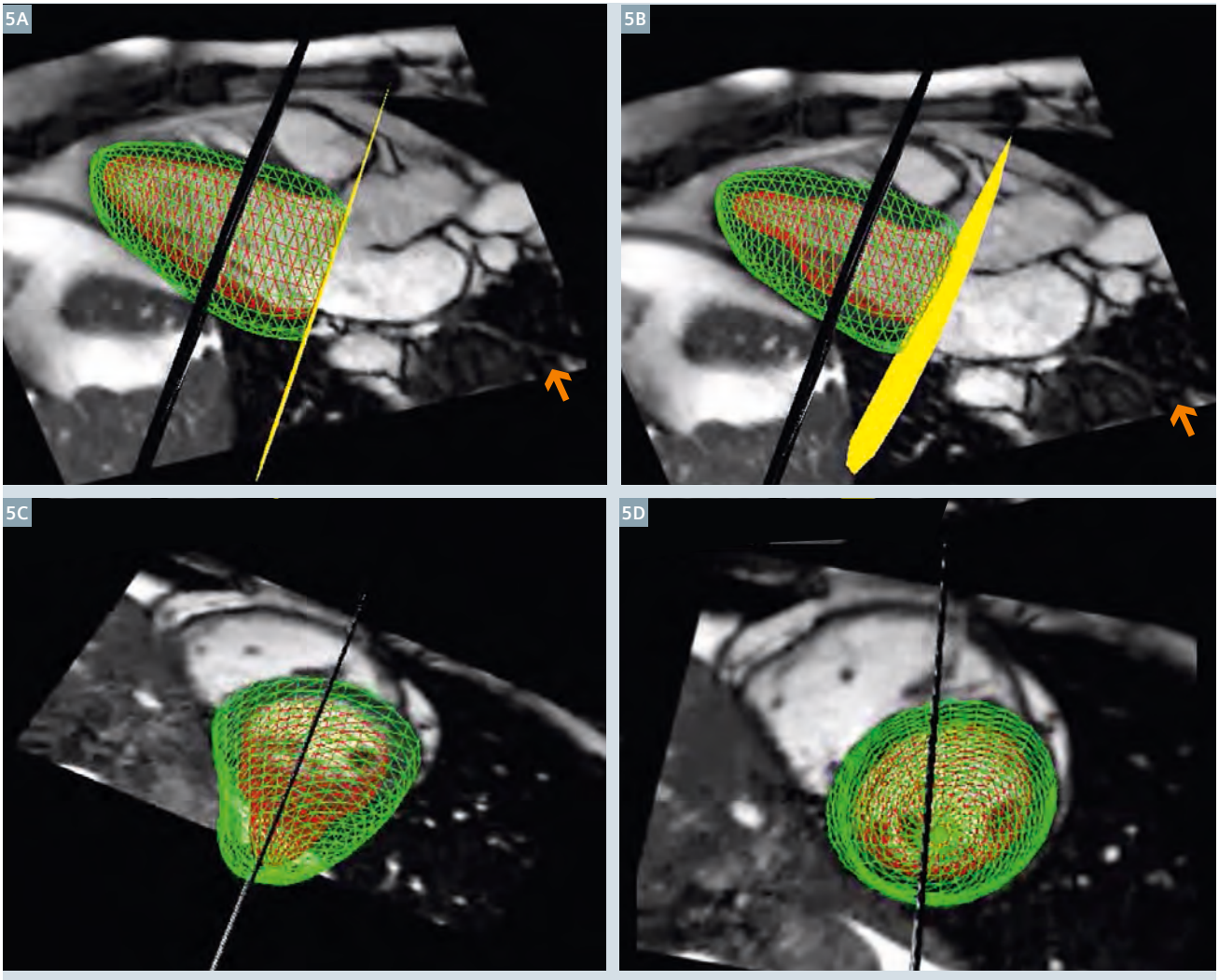

5 Display of the 3D reconstruction derived from the 7 slices acquired within a single breath-hold. Note the long-axis shortening of the LV during systole allowing for accurate LV volume measurements (**5A, 5B**, yellow plane). Any orientation of the 3D is available for inspection of function **(5A–D)**.

What about the accuracy of the novel single-breath-hold CS technique?

To assess the accuracy of the LV volume measurements, LV stroke volume was compared with the LV output measured in the ascending aorta with phase-contrast MR. As the flow measurements were performed distally to the coronary arteries, flow in the coronaries was estimated as the LV mass multiplied by 0.8 ml/min/g. An excellent agreement was found with a mean of 86.8 ml/beat for the aortic flow measurement and 91.9 ml/beat for the LV measurements derived from the single-breath-hold CS data ($r = 0.93$, $p < 0.0001$). By Bland-Altman analysis, the stroke volume approach overestimated by 5.2 ml/beat versus the reference flow measurement. For the conventional stroke volume measurements, this difference was 15.6 ml/beat (linear regression analysis vs aortic flow: $r = 0.69$, $p < 0.01$). More importantly, the CS LV stroke data were not only more precise with a smaller mean difference, the variability of the CS data vs the reference flow data was less with a standard deviation as low as 6.8 ml/beat vs 12.9 ml/beat for the standard multi-breath-hold approach (Fig. 7). Several explanations may apply for the higher accuracy of the single-breath-hold multi-slice CS approach in comparison to the conventional multi-breath-hold approach:

1) With the single-breath-hold approach, all acquired slices are correctly co-registered, i.e. they are correctly aligned in space, a prerequisite for the 4D-analysis tool to work properly.

2) This 4D-analysis tool allows for an accurate tracking of the mitral valve plane motion during the cardiac cycle as shown in Figure 5, which is important as the cross-sectional area of the heart at its base is large and thus, inaccurate slice positioning at the base of

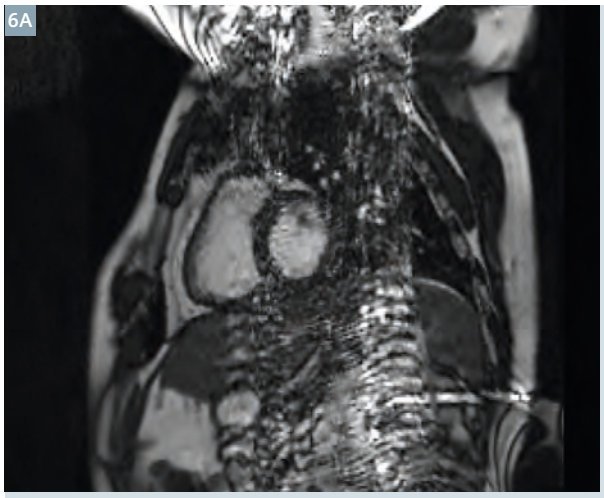

6A
A typical fold-over artifact along the phase-encoding direction in a short axis slice, oriented superior-inferior for demonstrative purpose.

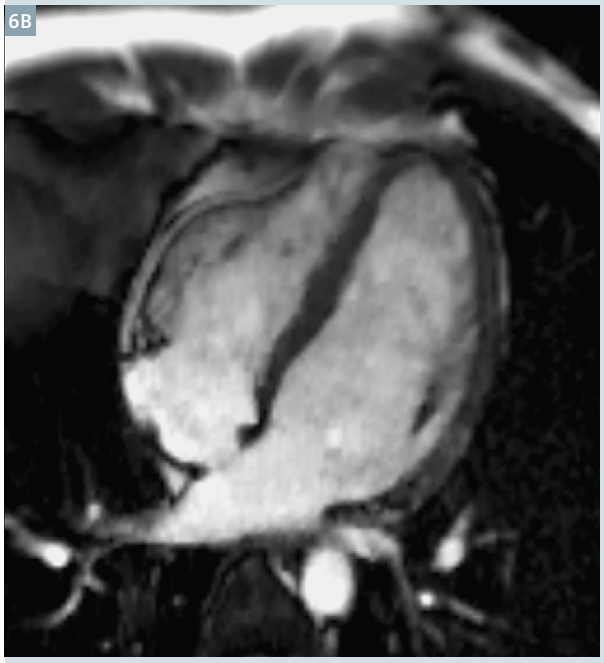

6B
No flow-related artifacts are visible on the end-diastolic phases, while small artifacts in phase-encoding direction (Artif, arrows) occur in mid-systole projecting over the mitral valve **(6C).**

7

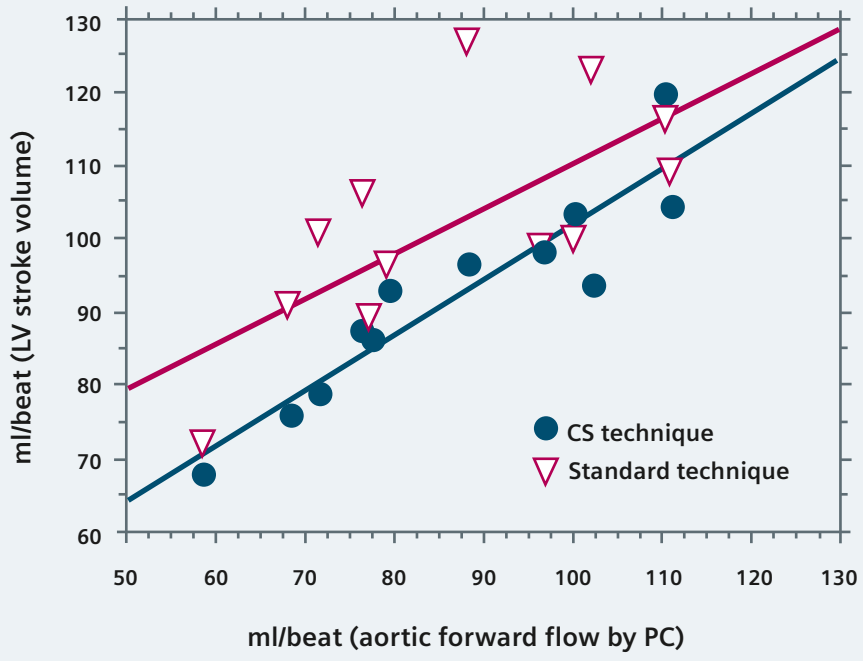

7
An excellent correlation is obtained for the LV stroke volume calculated from the compressed sensing data with the flow volume in the aorta measured by phase-contast technique. Variability of the conventional LV stroke volume data appears higher than for the compressed sensing data.

the heart with conventional short-axis slices typically translate in relatively large errors. Nevertheless, we observed a systematic overestimation of the stroke volume by the CS approach of 5.2 ml/beat in comparison to the flow measurements. In normal hearts with tricuspid aortic valves, an underestimation of aortic flow by the phase-contrast technique is very unlikely [14]. Thus, overestimation of stroke volume by the volume approach is to consider. In the volume contours, the papillary muscles are excluded as illustrated in Figure 8. As these papillary muscles are excluded in both the diastolic and systolic contours, this aspect should not affect net LV stroke volume. However, as shown in Figure 8, smaller trabeculations of the LV wall are included into the LV blood pool contour in the diastolic phase, while these trabeculations, when compacted in the end-systolic phase, are excluded from the blood pool resulting in a small overestimation of the end-diastolic volume, and thus, LV stroke volume. This explanation is likely as Van Rossum et al. demonstrated a slight underestimation of the LV mass when calculated on end-diastolic phases versus end-systolic phases, as trabeculations in end-diastole are typically excluded from the LV walls [15].

In summary, this novel very fast acquisition strategy based on a CS technique allows to cover the entire LV with high temporal and spatial resolution within a single breath-hold. The image quality based on these preliminary results appears adequate to yield highly accurate measures of LV volumes, LV stroke volume, LV mass, and LV ejection fraction.

Testing of this very fast multi-slice cine approach for the atria and the right ventricle is currently ongoing. Finally, these preliminary data show that compressed sensing MR acquisitions in the heart are feasible in humans and compressed sensing might be implemented for other important cardiac sequences such as fibrosis/viability imaging, i.e. late gadolinium enhancement, coronary MR angiography, or MR first-pass perfusion.

The Cardiac MR Center of the University Hospital Lausanne

The Cardiac Magnetic Resonance Center (CRMC) of the University Hospital of Lausanne (Centre Hospitalier Universitaire Vaudois; CHUV) was established in 2009. The CMR center is dedicated to high-quality clinical work-up of cardiac patients, to deliver state-of-the-art

training in CMR to cardiologists and radiologists, and to pursue research. In the CMR center education is provided for two specialties while focusing on one organ system. Traditionally, radiologists have focussed on using one technique for different organs, while cardiologists have concentrated on one organ and perhaps one technique. Now in the CMR center the focus is put on a combination of specialists with different background on one organ. Research at the CMR center is devoted to four major areas: the study of

1.) cardiac function and tissue characterization, specifically to better understand diastolic dysfunction,
2.) the development of MR-compatible cardiac devices such as pacemakers and ICDs;
3.) the utilization of hyperpolarized ^{13}C-carbon contrast media to investigate metabolism in the heart, and

4.) the development of ^{19}F-fluorine-based CMR techniques to detect inflammation and to label and track cells non-invasively.

For the latter two topics, the CMR center established tight collaborations with the Center for Biomedical Imaging (CIBM), a network around Lake Geneva that includes the Ecole Polytechnique Fédérale de Lausanne (EPFL), and the universities and university hospitals of Lausanne and Geneva. In particular, strong collaborative links are in place with the CVMR team of Prof. Matthias Stuber, a part of the CIBM and located at the University Hospital Lausanne and with Prof. A. Comment, with whom we perform the studies on real-time metabolism based on the ^{13}C-carbon hyperpolarization (DNP) technique. In addition, collaborative studies are ongoing with the Heart Failure and Cardiac Transplantation Unit led by Prof. R. Hullin (detection of graft rejection by tissue characterization) and the Oncology Department led by Prof. Coukos (T cell tracking by ^{19}F-MRI in collaboration with Prof. Stuber, R. van Heeswijk, CIBM, and Prof. O. Michielin, Oncology). This structure allows for a direct interdisciplinary interaction between physicians, engineers, and basic scientists on a daily basis with the aim to enable innovative research and fast translation of these techniques from bench to bedside.

The CMRC is also the center of competence for the quality assessment of the European CMR registry which holds currently approximately 33,000 patient studies acquired in 59 centers across Europe.

The members of the CRMC team are: Prof. J. Schwitter (director of the center), PD Dr. X. Jeanrenaud, Dr. D. Locca, MER, Dr. P. Monney, Dr. T. Rutz, Dr. C. Sierro, and Dr. S. Koestner (cardiologists, staff members),

LV short-axis slice: CV_SPARSE

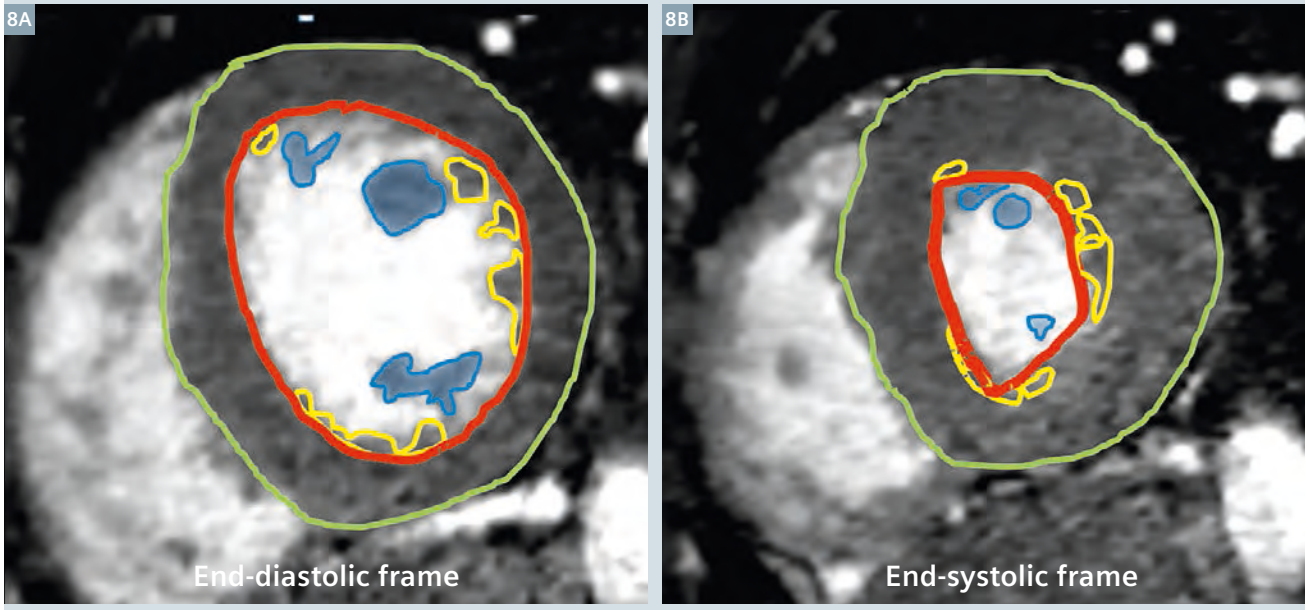

8 Overestimation of end-diastolic LV volumes by volumetric measurements. In comparison to ejected blood from the LV as measured with phase-contrast techniques, the volumetric measurements of LV stroke volume overestimated by approximately 5 ml, most likely by overestimation of LV end-diastolic volume. Small trabculations (yellow contours in 8A) are included into the LV blood volume (red contour in 8A) in diastole, while these trabeculations (yellow contours in 8B) are typically included in the end-systolic phase (red contours in 8B). For the same reasons, LV mass (= green contour minus red contour) is often slightly underestimated in diastole vs systole.

Dr. G. Vincenti (cardiologist) and Dr. N. Barras (cardiologist in training, rotation), PD. Dr. S. Muzzarellli (affiliated cardiologist), Prof. C. Beigelman and Dr. X. Boulanger (radiologists, staff members), Dr. G.L. Fetz (radiologist in training, rotation), C. Gonzales, PhD (^{19}F-fluorine project leader), H. Yoshihara, PhD (^{13}C-carbon project leader), V. Klinke (medical student, doctoral thesis), C. Bongard (medical student, master thesis), P. Chevre (chief CMR technician), and F. Recordon and N. Lauriers (research nurses).

Acknowledgements

The authors would like to thank all the members of the team of MR technologists at the CHUV for their highly valuable participation, helpfulness and support during the daily clinical CMR examinations and with the research protocols. Finally, a very important acknowledgment goes to Dr. Michael Zenge, Ms. Michaela Schmidt, and the whole Siemens MR Cardio team of Edgar Müller in Erlangen.

References

1 Curtis JP, Sokol SI, Wang Y, Rathore SS, Ko DT, Jadbabaie F, Portnay EL, Marshalko SJ, Radford MJ, Krumholz HM. The association of left ventricular ejection fraction, mortality, and cause of death in stable outpatients with heart failure. Journal of the American College of Cardiology. 2003;42(4):736-42.

2 Sürder D, Manka R, Lo Cicero V, Moccetti T, Rufibach K, Soncin S, Turchetto L, Radrizzani M, Astori G, Schwitter J, Erne P, Jamshidi P, Auf Der Maur C, Zuber M, Windecker S, Moschovitis A, Wahl A, Bühler I, Wyss C, Landmesser U, Lüscher T, Corti R. Intracoronary injection of bone marrow derived mononuclear cells, early or late after acute myocardial infarction: Effects on global LV-function: 4 months results of the SWISS-AMI trial. Circulation. 2013;127:1968-79.

3 McMurray JJV, Adamopoulos S, Anker SD, Auricchio A, Böhm M, Dickstein K, Falk V, Filippatos G, Fonseca C, Sanchez MAG, Jaarsma T, Køber L, Lip GYH, Maggioni AP, Parkhomenko A, Pieske BM, Popescu BA, Rønnevik PK, Rutten FH, Schwitter J, Seferovic P, Stepinska J, Trindade PT, Voors AA, Zannad F, Zeiher A. ESC Guidelines for the diagnosis and treatment of acute and chronic heart failure 2012. European Heart Journal. 2012 May 19, 2012(33):1787–847.

4 Zannad F, McMurray JJV, Krum H, van Veldhuisen DJ, Swedberg K, Shi H, Vincent J, Pocock SJ, Pitt B. Eplerenone in Patients with Systolic Heart Failure and Mild Symptoms. New England Journal of Medicine. 2011;364(1):11-21.

5 Gharib MI, Burnett AK. Chemotherapy-induced cardiotoxicity: current practice and prospects of prophylaxis. European Journal of Heart Failure. 2002 June 1, 2002;4(3):235-42.

6 Bardy GH, Lee KL, Mark DB, Poole JE, Packer DL, Boineau R, Domanski M, Troutman C, Anderson J, Johnson G, McNulty SE, Clapp-Channing N, Davidson-Ray LD, Fraulo ES, Fishbein DP, Luceri RM, Ip JH. Amiodarone or an Implantable Cardioverter–Defibrillator for Congestive Heart Failure. New England Journal of Medicine. 2005;352(3):225-37.

7 Schwitter J. CMR-Update. 2. Edition ed. Lausanne, Switzerland. www.herz-mri.ch.

8 Klinke V, Muzzarelli S, Lauriers N, Locca D, Vincenti G, Monney P, Lu C, Nothnagel D, Pilz G, Lombardi M, van Rossum A, Wagner A, Bruder O, Mahrholdt H, Schwitter J. Quality assessment of cardiovascular magnetic resonance in the setting of the European CMR registry: description and validation of standardized criteria. Journal of Cardiovascular Magnetic Resonance. 2013;15(1):55.

9 Bruder O, Wagner A, Lombardi M, Schwitter J, van Rossum A, Pilz G, Nothnagel D, Steen H, Petersen S, Nagel E, Prasad S, Schumm J, Greulich S, Cagnolo A, Monney P, Deluigi C, Dill T, Frank H, Sabin G, Schneider S, Mahrholdt H. European Cardiovascular Magnetic Resonance (EuroCMR) registry-multi national results from 57 centers in 15 countries. J Cardiovasc Magn Reson. 2013;15:1-9.

10 Lustig M, Donoho D, Pauly JM. Sparse MRI: The application of compressed sensing for rapid MR imaging. Magnetic Resonance in Medicine. 2007;58(6):1182-95.

11 Liang D, Liu B, Wang J, Ying L. Accelerating SENSE using compressed sensing. Magnetic Resonance in Medicine. 2009;62(6): 1574-84.

12 Liu J. Dynamic cardiac MRI reconstruction with weighted redundant Haar wavelets. Magn Reson Med. 2012;Proc. ISMRM 2012,abstract.

13 Bieri O, Markl M, Scheffler K. Analysis and compensation of eddy currents in balanced SSFP. Magn Reson Med. 2005;54:129-37.

14 Muzzarelli S, Monney P, O'Brien K, Faletra F, Moccetti T, Vogt P, Schwitter J. Quantification of aortic valve regurgitation by phase-contrast magnetic resonance in patients with bicuspid aortic valve: where to measure the flow? . Eur Heart J - CV Imaging. 2013:in press.

15 Papavassiliu T, Kühl HP, Schröder M, Süselbeck T, Bondarenko O, Böhm CK, Beek A, Hofman MMB, van Rossum AC. Effect of Endocardial Trabeculae on Left Ventricular Measurements and Measurement Reproducibility at Cardiovascular MR Imaging1. Radiology. 2005 July 1, 2005;236(1):57-64.

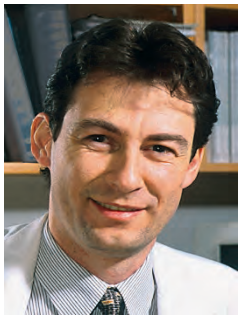

Contact

Professor Juerg Schwitter
Médecin Chef Cardiologie
Directeur du Centre de la RM
Cardiaque du CHUV
Centre Hospitalier
Universitaire Vaudois – CHUV
Rue du Bugnon 46
1011 Lausanne
Suisse
Phone: +41 21 314 0012
jurg.schwitter@chuv.ch
www.cardiologie.chuv.ch

Accelerated Segmented Cine TrueFISP of the Heart on a 1.5T MAGNETOM Aera Using *k-t*-sparse SENSE

Maria Carr[1]; Bruce Spottiswoode[2]; Bradley Allen[1]; Michaela Schmidt[2]; Mariappan Nadar[4]; Qiu Wang[4]; Jeremy Collins[1]; James Carr[1]; Michael Zenge[2]

[1]Northwestern University, Feinberg School of Medicine, Chicago, IL, USA
[2]Siemens Healthcare
[3]Siemens Corporate Technology, Princeton, United States

Introduction

Cine MRI of the heart is widely regarded as the gold standard for assessment of left ventricular volume and myocardial mass and is increasingly utilized for assessment of cardiac anatomy and pathology as part of clinical routine. Conventional cine imaging approaches typically require 1 slice per breath-hold, resulting in lengthy protocols for complete cardiac coverage. Parallel imaging allows some shortening of the acquisition time, such that 2–3 slices can be acquired in a single breath-hold. In cardiac cine imaging artifacts become more prevalent with increasing acceleration factor. This will negatively impact the diagnostic utility of the images and may reduce accuracy of quantitative measurements. However, regularized iterative reconstruction techniques can be used to considerably improve the images obtained from highly undersampled data. In this work, L1-regularized iterative SENSE as proposed in [1] was applied to reconstruct under-sampled *k*-space data. This technique* takes advantage of the de-noising characteristics of Wavelet regularization and promises to very effectively suppress subsampling artifacts. This may allow for high acceleration factors to be used, while diagnostic image quality is preserved.

The purpose of this study was to compare segmented cine TrueFISP images from a group of volunteers and patients using three acceleration and reconstruction approaches: iPAT factor 2 with conventional reconstruction; T-PAT factor 4 with conventional reconstruction; and T-PAT factor 4 with iterative *k-t*-sparse SENSE reconstruction.

Technique

Cardiac MRI seems to be particularly well suited to benefit from a group of novel image reconstruction methods known as compressed sensing [2] which promise to significantly speed up data acquisition. Compressed sensing methods were introduced to MR imaging [3, 4] just a few years ago and have since been successfully combined with parallel imaging [5, 6]. Such methods try to utilize the

*Work in progress: The product is still under development and not commercially available yet. Its future availability cannot be ensured.

Table 1: MRI conventional and iterative imaging parameters

Parameters	Conventional iPAT 2	Conventional T-PAT 4	Iterative T-PAT 4
Iterative recon	No	No	Yes
Parallel imaging	iPAT2 (GRAPPA)	TPAT4	TPAT4
TR/TE (ms)	3.2 / 1.6	3.2 / 1.6	3.2 / 1.6
Flip angle (degrees)	70	70	70
Pixel size (mm²)	1.9 × 1.9	1.9 × 1.9	1.9 × 1.9
Slice thickness (mm)	8	8	8
Temp. res. (msec)	38	38	38
Acq. time (sec)	7	3.2	3.2

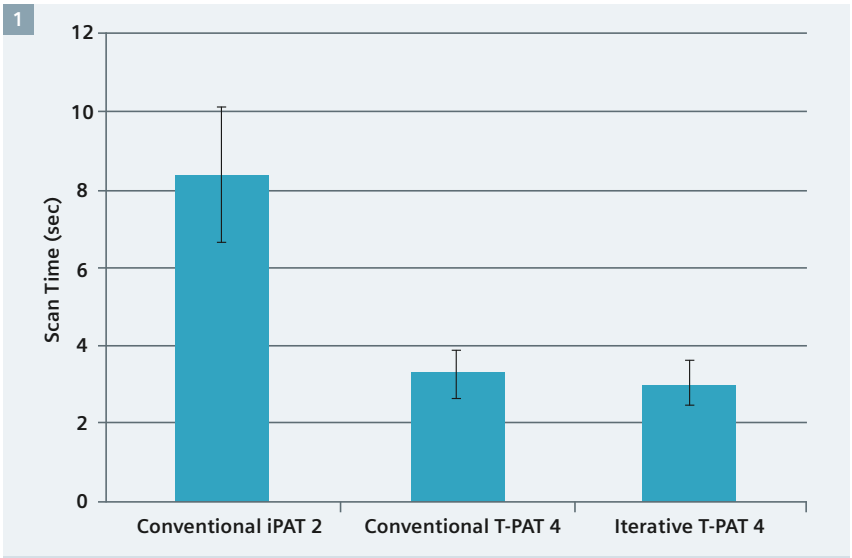

1 Single slice scan time in patients and volunteers. There was a statistically significant reduction in scan time compared to the standard iPAT2 for both TPAT4 acceleration and iterative reconstruction TPAT4 acceleration.

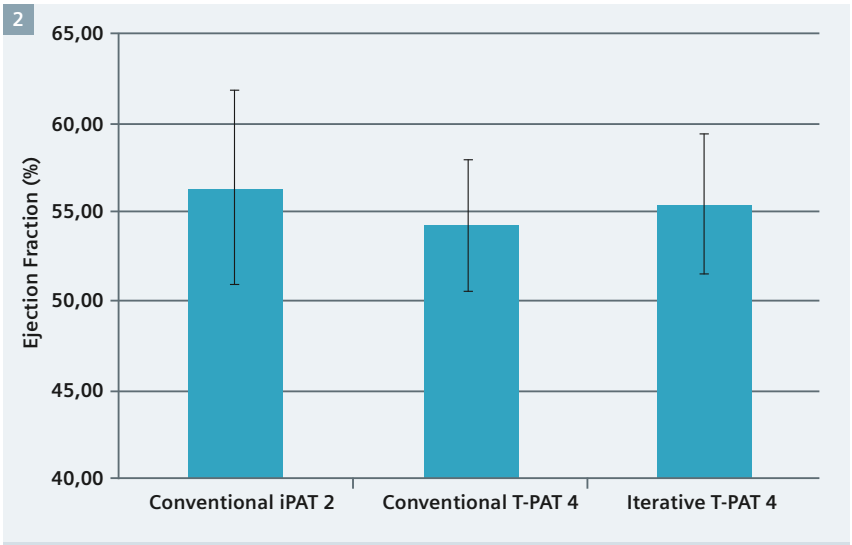

2 Ejection fraction in volunteers. Quantitatively measured ejection fractions were comparable across all three techniques.

full potential of image compression during the acquisition of raw input data. In the case of highly subsampled input data, a non-linear iterative optimization avoids sub-sampling artifacts during the process of image reconstruction. The resulting images represent the best solution consistent with the input data, which have a sparse representation in a specific transform domain. In the most favorable case, residual artifacts are not visibly perceptible or are diagnostically irrelevant.

As outlined by Liu et al. in [1], the image reconstruction can be formulated as an unconstrained optimization problem. In the current implementation, this optimization is solved using a Nesterov-type algorithm [7]. The L1-regularization with a redundant Haar transform is efficiently solved using a Dykstra-type algorithm [8]. This allowed a smooth integration into the current MAGNETOM platform and, therefore, facilitates a broad clinical evaluation.

Materials and methods

Nine healthy human volunteers (57.4 male/56.7 female) and 20 patients (54.4 male/40.0 female) with suspected cardiac disease were scanned on a 1.5T MAGNETOM Aera system under an approved institutional review board protocol. All nine volunteers and 16 patients were imaged using segmented cine TrueFISP sequences with conventional GRAPPA factor 2 acceleration (conventional iPAT 2) T-PAT factor 4 acceleration (conventional T-PAT 4), and T-PAT factor 4 acceleration with iterative *k-t*-sparse SENSE reconstruction (iterative T-PAT 4). The remaining 4 patients were scanned using only conventional iPAT 2 and iterative T-PAT 4 techniques. Note that the iterative technique is fully integrated into the standard reconstruction environment.

The imaging parameters for each imaging sequence are provided in Table 1. All three sequences were run in 3 chamber and 4 chamber views, as well as a stack of short axis slices.

Quantitative analysis was performed on all volunteer data sets at a *syngo* MultiModality Workplace (Leonardo) using Argus post-processing software (Siemens Healthcare, Erlangen, Germany) by an experienced cardiovascular MRI technician. Ejection fraction, end-diastolic volume, end-systolic volume, stroke volume, cardiac output, and myocardial mass were calculated. In all volunteers and patients,

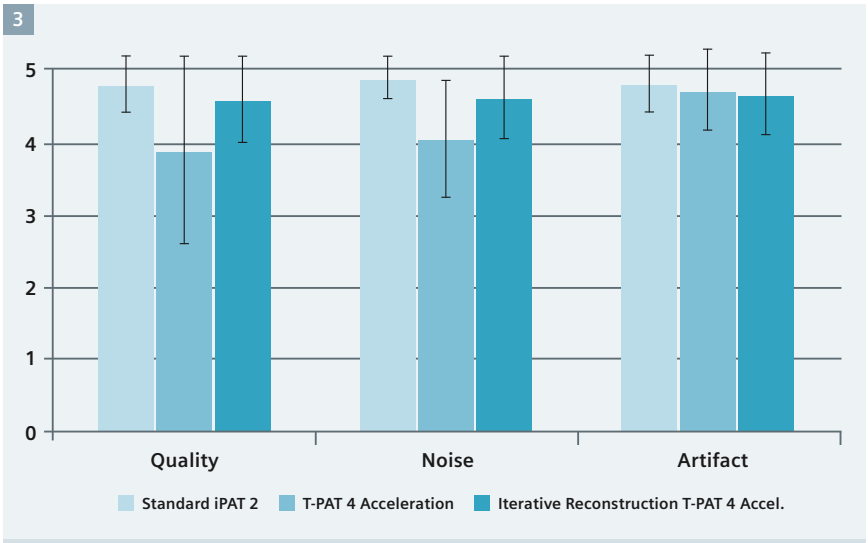

3 Qualitative scores in patients and volunteers. Image quality was highest and noise and artifact were lowest with iterative T-PAT 4 and conventional iPAT 2 compared to conventional T-PAT 4.

blinded qualitative scoring was performed by a radiologist using a 5 point Likert scale to assess overall image quality (1 – non diagnostic; 2 – poor; 3 – fair; 4 – good; 5 – excellent). Images were also scored for artifact and noise (1 – severe; 2 – moderate; 3 – mild; 4 – trace; 5 – none).

All continuous variables were compared between groups using an unpaired t-test, while ordinal qualitative variables were compared using a Wilcoxon signed-rank test.

Results

All images were acquired successfully and image quality was of diagnostic quality in all cases. The average scan time per slice for conventional iPAT 2, conventional T-PAT 4 and iterative T-PAT 4 were for patients 7.7 ± 1.5 sec, 5.6 ± 1.5 sec and 2.9 ± 1.5 sec and for the volunteers 9.8 ± 1.5 sec, 3.2 ± 1.5 sec and 3.0 ± 1.5 sec, respectively. The results in scan time are illustrated in Figure 1. In both patients and volunteers, conventional iPAT 2 were significantly longer than both conventional T-PAT 4 and iterative T-PAT 4 techniques ($p < 0.001$ for each group).

The results for ejection fraction (EF) for all three imaging techniques are provided in Figure 2. The average EF for conventional T-PAT 4 was slightly lower than that measured for conventional iPAT 2 and iterative T-PAT, but the group size is relatively small (9 subjects) and this difference was not significant ($p = 0.34$ and $p = 0.22$ respectively).There was no statistically significant difference in ejection fraction between the conventional iPAT 2 and the iterative T-PAT 4 sequences ($p = 0.48$).

The results for image quality, noise and artifact are provided in Figure 3. The iterative T-PAT 4 images had comparable image quality, noise and artifact scores compared to the conventional iPAT 2 images. The conventional T-PAT 4 images had lower image quality, more artifacts and higher noise compared to the other techniques.

Figures 4 and 5 show an example of 4-chamber and mid-short axis images from all three techniques in a patient with basal septal hypertrophy. In both series', the conventional iPAT 2 and iterative T-PAT 4 images are comparable in quality, while the conventional T-PAT 4 image is visibly noisier.

Discussion

This study compares a novel accelerated segmented cine TrueFISP technique to conventional iPAT 2 cine TrueFISP and T-PAT 4 cine TrueFISP in a cohort of normal subjects and patients. The iterative reconstruction technique provided comparable measurements of ejection fraction to the clinical gold standard (conventional iPAT 2). The accelerated segmented cine TrueFISP with T-PAT 4, which was used as comparison technique, produced slightly lower EF values compared to the other techniques, although this was not found to be statistically significant. The iterative reconstruction produced comparable image quality, noise and artifact scores to the conventional reconstruction using iPAT 2. The conventional T-PAT 4 technique had lower image quality and higher noise scores compared to the other two techniques.

The iterative T-PAT 4 segmented cine technique allows for greater than 50% reduction in acquisition time for comparable image quality and spatial resolution as the clinically used iPAT 2 cine TrueFISP technique. This iterative technique could be extended to permit complete heart coverage in a single breath-hold thus greatly simplifying and shortening routine clinical cardiac MRI protocols, which has been one of the biggest obstacles to wide acceptance of cardiac MRI. With a shorter cine acquisition, additional advanced imaging techniques, such as perfusion and flow, can be more readily added to patient scans within a reasonable protocol length.

There are currently some limitations to the technique. Firstly, the use of SENSE implies that aliasing artifacts can occur if the field-of-view is smaller than the subject, which is sometimes difficult to avoid in the short axis orientation. But a solution to this is promised to be part of a future release of the current prototype. Secondly, the image reconstruction times of the current implementation seems to be prohibitive for routine clinical use. However, we anticipate future algorithmic improvements with increased computational power to reduce the reconstruction time to clinically acceptable values.

Of course, iterative reconstruction techniques are not just limited to cine imaging of the heart. Future work may see this technique applied to time intense techniques such as 4D flow phase contrast MRI and 3D coronary MR angiography, making them more clinically applicable. Furthermore, higher acceleration rates might be achieved by using an incoherent sampling pattern [9].

With sufficiently high acceleration, the technique can also be used effectively for real time cine cardiac imaging in patients with breath-holding difficulties or arrhythmia. Figure 6 shows that real-time acquisition with T-PAT 6 and *k-t* iterative reconstruction still results in excellent image quality.

In conclusion, cine TrueFISP of the heart with inline *k-t*-sparse iterative reconstruction is a promising technique for obtaining high quality cine images at a fraction of the scan time compared to conventional techniques.

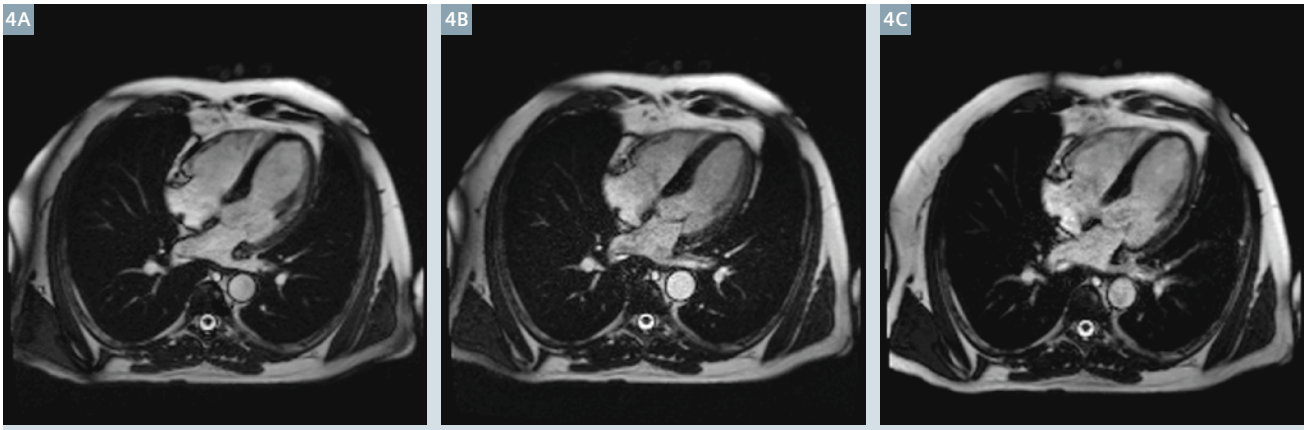

4 Four chamber cine TrueFISP from a normal volunteer. **(4A)** Conventional iPAT 2, acquisition time 8 s. **(4B)** Conventional T-PAT 4, acquisition time 3 seconds. **(4C)** Iterative T-PAT 4, acquisition time 3 seconds.

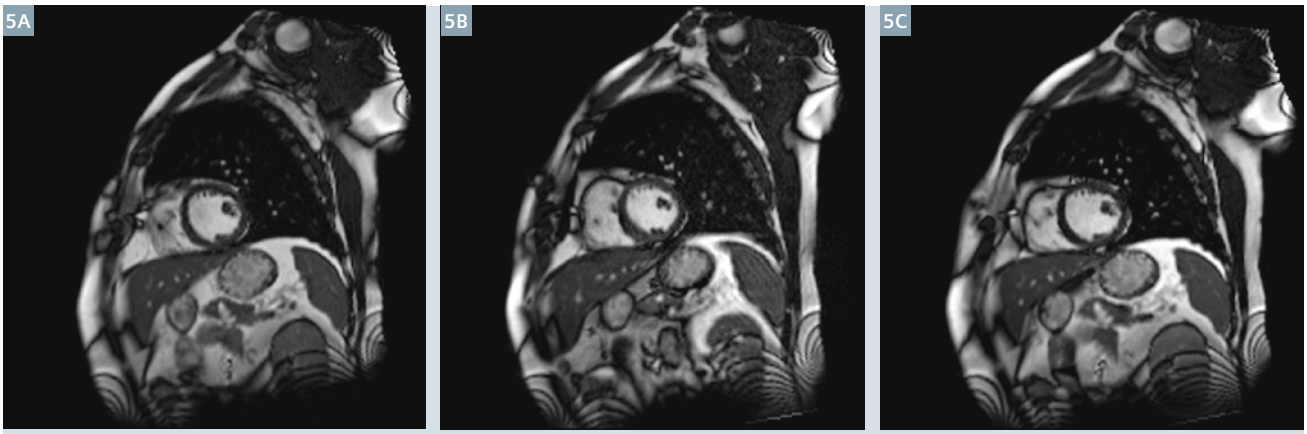

5 End-systolic short axis cine TrueFISP images from a patient with a history of myocardial infarction. A metal artifact from a previous sternotomy is noted in the sternum. There is wall thinning in the inferolateral wall with akinesia on cine views, consistent with an old infarct in the circumflex territory. **(5A)** Conventional iPAT 2, **(5B)** conventional T-PAT 4, **(5C)** iterative T-PAT 4.

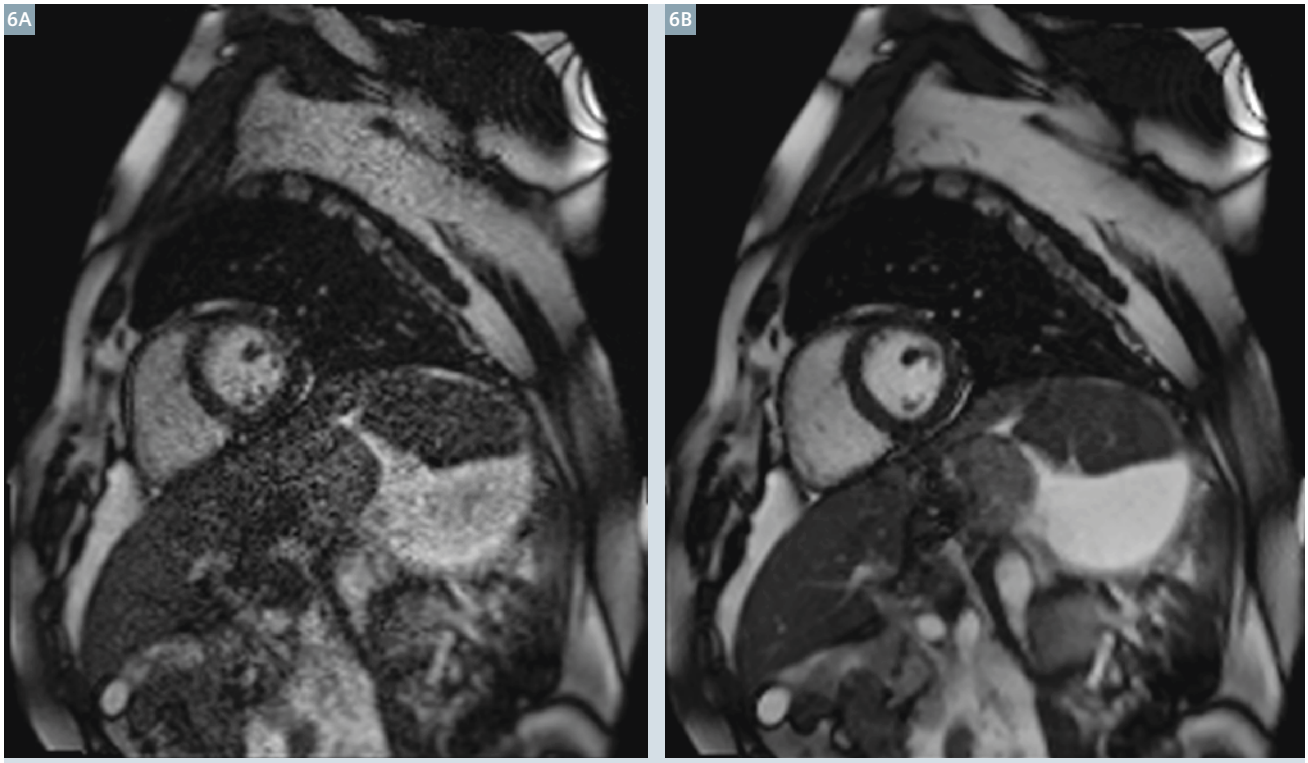

6 Real-time cine TrueFISP T-PAT 6 images reconstructed using **(6A)** conventional, and **(6B)** iterative techniques.

Acknowledgement

The authors would like to thank Judy Wood, Manger of the MRI Department at Northwestern Memorial Hospital, for her continued support and collaboration with our ongoing research through the years. Secondly, we would like to thank the magnificent Cardiovascular Technologist's Cheryl Jarvis, Tinu John, Paul Magarity, Scott Luster for their patience and dedication to research. Finally, the Resource Coordinators that help us make this possible Irene Lekkas, Melissa Niemczura and Paulino San Pedro.

References

1 Liu J, Rapin J, Chang TC, Lefebvre A, Zenge M, Mueller E, Nadar MS. Dynamic cardiac MRI reconstruction with weighted redundant Haar wavelets. In Proceedings of the 20th Annual Meeting of ISMRM, Melbourne, Australia, 2002. p 4249.

2 Candes EJ, Wakin MB. An Introduction to compressive sampling. IEEE Signal Processing Magazine 2008. 25(2):21-30. doi: 10.1109/MSP.2007.914731.

3 Block KT, Uecker M, Frahm J. Undersampled Radial MRI with Multiple Coils. Iterative Image Reconstruction Using a Total Variation Constraint. Magn Reson Med 2007. 57(6):1086-98.

4 Lustig M, Donoho D, Pauly JM. Sparse MRI: The application of compressed sensing for rapid MR imaging. Magn Reson Med 2007. 58(6):1182-95.

5 Liang D, Liu B, Wang J, Ying L. Accelerating SENSE using compressed sensing. Magn Reson Med 2009. 62(6):154-84. doi: 10.1002/mrm.22161.

6 Lustig M, Pauly, JM. SPIRiT: Iterative self-consistent parallel imaging reconstruction from arbitrary k-space. Magn Reson Med 2010. 64(2):457-71. doi: 10.1002/mrm.22428.

7 Beck A, Teboulle M. A fast iterative shrinkage-thresholding algorithm for linear inverse problems. SIAM J Imaging Sciences 2009. 2(1): 183-202.

8 Dykstra RL. An algorithm for restricted least squares regression. J Amer Stat Assoc 1983 78(384):837-842.

9 Schmidt M, Ekinci O, Liu J, Lefebvre A, Nadar MS, Mueller E, Zenge MO. Novel highly accelerated real-time CINE-MRI featuring compressed sensing with *k-t* regularization in comparison to TSENSE segmented and real-time Cine imaging. J Cardiovasc Magn Reson 2013. 15(Suppl 1):P36.

Contact

Maria Carr, RT (CT)(MR)
CV Research Technologist
Department of Radiology
Northwestern University
Feinberg School of Medicine
737 N. Michigan Ave.
Suite 1600
Chicago, IL 60611
USA
Phone: +1 312-926-5292
m-carr@northwestern.edu

Siemens Healthcare Publications

Our publications offer the latest information and background for every healthcare field. From the hospital director to the radiological assistant – here, you can quickly find information relevant to your needs.

MAGNETOM Flash
Everything from the world of magnetic resonance imaging.

SOMATOM Sessions
Everything from the world of computed tomography.

Imaging Life
Everything from the world of molecular imaging innovations.

AXIOM Innovations
Everything from the world of interventional radiology, cardiology, and surgery.

Heartbeat
Everything from the world of sustainable cardiovascular care.

Medical Solutions Online
The online version includes additional video features and greater depth to the articles in the printed healthcare leadership magazine. Read online at:
www.siemens.com/medical-solutions

For current and past issues and to order the magazines, please visit
www.siemens.com/healthcare-magazine

The entire editorial staff at Duke University Medical Center and at Simens Healthcare extends their appreciation to all the radiologists, technologists, physicists, experts and scholars who donate their time and energy – without payment – in order to share their expertise with the readers of MAGNETOM Flash.

MAGNETOM Flash – Imprint

© 2013 by Siemens AG,
Berlin and Munich,
All Rights Reserved

Publisher:
Siemens AG
Medical Solutions
Business Unit Magnetic Resonance,
Karl-Schall-Straße 6, D-91052 Erlangen,
Germany

Guest Editor:
Mustafa R. Bashir, M.D.
Director of MRI
Assistant Professor of Radiology
Division of Abdominal Imaging
Duke University Medical Center
Durham, NC, USA

Associate Editor: Antje Hellwich
(antje.hellwich@siemens.com)

Editorial Board: Wellesley Were;
Ralph Strecker; Sven Zühlsdorff, Ph.D.;
Gary R. McNeal, MS (BME);
Peter Kreisler, Ph.D.

Production: Norbert Moser, Siemens AG,
Medical Solutions

Layout: independent Medien-Design
Widenmayerstrasse 16, D-80538 Munich,
Germany

Printer: G. Peschke Druckerei GmbH,
Schatzbogen 35, D-81829 Munich,
Germany

Note in accordance with § 33 Para.1 of the German Federal Data Protection Law: Despatch is made using an address file which is maintained with the aid of an automated data processing system.

MAGNETOM Flash is sent free of charge to Siemens MR customers, qualified physicians, technologists, physicists and radiology departments throughout the world. It includes reports in the English language on magnetic resonance: diagnostic and therapeutic methods and their application as well as results and experience gained with corresponding systems and solutions. It introduces from case to case new principles and procedures and discusses their clinical potential. The statements and views of the authors in the individual contributions do not necessarily reflect the opinion of the publisher.

The information presented in these articles and case reports is for illustration only and is not intended to be relied upon by the reader for instruction as to the practice of medicine. Any health care practitioner reading this information is reminded that they must use their own learning, training and expertise in dealing with their individual patients. This material does not substitute for that duty and is not intended by Siemens Medical Solutions to be used for any purpose in that regard. The drugs and doses mentioned herein are consistent with the approval labeling for uses and/or indications of the drug. The treating physician bears the sole responsibility for the diagnosis and treatment of patients, including drugs and doses prescribed in connection with such use. The Operating Instructions must always be strictly followed when operating the MR system. The sources for the technical data are the corresponding data sheets. Results may vary.

Partial reproduction in printed form of individual contributions is permitted, provided the customary bibliographical data such as author's name and title of the contribution as well as year, issue number and pages of MAGNETOM Flash are named, but the editors request that two copies be sent to them. The written consent of the authors and publisher is required for the complete reprinting of an article.

We welcome your questions and comments about the editorial content of MAGNETOM Flash. Please contact us at magnetomworld.med@siemens.com.

Manuscripts as well as suggestions, proposals and information are always welcome; they are carefully examined and submitted to the editorial board for attention. MAGNETOM Flash is not responsible for loss, damage, or any other injury to unsolicited manuscripts or other materials. We reserve the right to edit for clarity, accuracy, and space. Include your name, address, and phone number and send to the editors, address above.

MAGNETOM Flash is also available on the internet:

www.siemens.com/magnetom-world

SIEMENS

MAGNETOM Flash

The Magazine of MRI

Issue Number 5/2013 | RSNA Edition

Not for distribution in the US.

55

New Generation Cardiac Parametric Mapping: The Clinical Role of T1 and T2 Mapping
Page 104

Acute MR Stroke Protocol in 6 Minutes
Page 44

Clinical T1w MRI using Radial VIBE
Page 6

Please enter your business address

Institution

Department

Function

Title

Name

Street

Postal Code

City

State

Country

MR system used

Please include me in your mailing list for the following Siemens Healthcare customer magazine(s):

☐ Medical Solutions

☐ MAGNETOM Flash

☐ SOMATOM Sessions

☐ AXIOM Innovations

Stay up to date with the latest information

Register for:

E-mail

☐ Yes, I consent to the above information being used for future contact regarding product updates and other important news from Siemens.

☐ unsubscribe from info service

Please print clearly!

→Visit www.siemens.com/magnetom-world for case reports, clinical methods, application tips, talks and much more clinical information.

SUBSCRIBE NOW!

– and get your free copy of future MAGNETOM Flash! Interesting information from the world of magnetic resonance – gratis to your desk. Send us this postcard, or subscribe online at www.siemens.com/MAGNETOM-World

Siemens AG
Healthcare Sector
Magnetic Resonance
Antje Hellwich – Marketing
P.O. Box 32 60
D-91050 Erlangen
Germany

MAGNETOM Flash

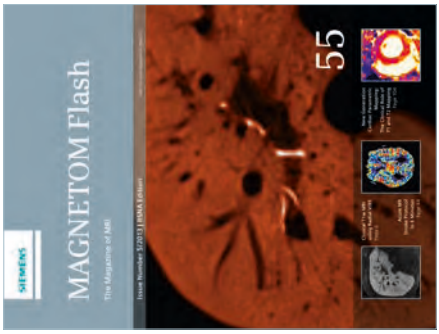

On account of certain regional limitations of sales rights and service availability, we cannot guarantee that all products included in this brochure are available through the Siemens sales organization worldwide. Availability and packaging may vary by country and is subject to change without prior notice. Some/All of the features and products described herein may not be available in the United States.

The information in this document contains general technical descriptions of specifications and options as well as standard and optional features which do not always have to be present in individual cases.

Siemens reserves the right to modify the design, packaging, specifications, and options described herein without prior notice.
Please contact your local Siemens sales representative for the most current information.

Note: Any technical data contained in this document may vary within defined tolerances. Original images always lose a certain amount of detail when reproduced.

Not for distribution in the US

Global Business Unit

Siemens AG
Medical Solutions
Magnetic Resonance
Henkestrasse 127
DE-91052 Erlangen
Germany
Phone: +49 9131 84-0
www.siemens.com/healthcare

Local Contact Information

Asia/Pacific:
Siemens Medical Solutions
Asia Pacific Headquarters
The Siemens Center
60 MacPherson Road
Singapore 348615
Phone: +65 6490 6000

Canada:
Siemens Canada Limited
Healthcare Sector
1550 Appleby Lane
Burlington, ON L7L 6X7, Canada
Phone +1 905 315-6868

Europe/Africa/Middle East:
Siemens AG, Healthcare Sector
Henkestr. 127
91052 Erlangen, Germany
Phone: +49 9131 84-0

Latin America:
Siemens S.A., Medical Solutions
Avenida de Pte. Julio A. Roca No 516, Piso
C1067 ABN Buenos Aires, Argentina
Phone: +54 11 4340-8400

USA:
Siemens Medical Solutions USA, Inc.
51 Valley Stream Parkway
Malvern, PA 19355-1406, USA
Phone: +1 888 826-9702

Global Siemens Headquarters

Siemens AG
Wittelsbacherplatz 2
80333 Munich
Germany

Global Siemens Healthcare Headquarters

Siemens AG
Healthcare Sector
Henkestrasse 127
91052 Erlangen
Germany
Phone: +49 9131 84-0
www.siemens.com/healthcare

Order No. A91MR-1000-102C-7600 | Printed in Germany | CC MR 1661 111320. |

© 11.13, Siemens AG

www.siemens.com/magnetom-world